NASA TECHNICAL REPORT

NASA TR R-444

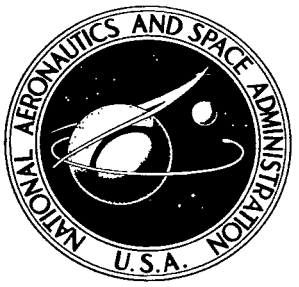

NASA TR R-444

EFFECTS OF JET EXHAUST GAS PROPERTIES ON EXHAUST SIMULATION AND AFTERBODY DRAG

William B. Compton III

Langley Research Center
Hampton, Va. 23665

NATIONAL AERONAUTICS AND SPACE ADMINISTRATION • WASHINGTON, D. C. • OCTOBER 1975

1. Report No.	2. Government Accession No.	3. Recipient's Catalog No.
NASA TR R-444		

4. Title and Subtitle
EFFECTS OF JET EXHAUST GAS PROPERTIES ON EXHAUST SIMULATION AND AFTERBODY DRAG

5. Report Date
October 1975

6. Performing Organization Code

7. Author(s)
William B. Compton III

8. Performing Organization Report No.
L-10183

9. Performing Organization Name and Address
NASA Langley Research Center
Hampton, Va. 23665

10. Work Unit No.
505-04-11-01

11. Contract or Grant No.

12. Sponsoring Agency Name and Address
National Aeronautics and Space Administration
Washington, D.C. 20546

13. Type of Report and Period Covered
Technical Report

14. Sponsoring Agency Code

15. Supplementary Notes
The information presented in this report is based on a thesis submitted in partial fulfillment of the requirements for the degree of Master of Science, George Washington University, Washington, D.C., August 1973.

16. Abstract

The effect of varying the jet exhaust's ratio of specific heats, gas constant, and temperature on airplane afterbody drag was investigated. Jet exhaust simulation parameters were evaluated also. Subsonic and transonic tests were made using a single nacelle model with afterbodies having boattail angles of 10° and 20°. Besides air, three other jet exhaust gases were investigated. The ratios of specific heats, gas constants, and total temperatures of the four exhaust gases ranged from 1.40 to 1.26, 287 to 376 J/kg-K, and 300 to 1013 K, respectively.

For steep boattail angles, and transonic speeds and typical turbojet pressure ratios, the current data indicate that the use of air to simulate a dry turbojet exhaust can result in an overprediction of afterbody drag as high as 17 percent of the dry turbojet value.

17. Key Words (Suggested by Author(s))
Jet simulation
Afterbody drag
Jet temperature effects
Jet interference
Jet plume
Entrainment
Jet exhaust gas properties

18. Distribution Statement
Unclassified – Unlimited

Subject Category 02

19. Security Classif. (of this report)	20. Security Classif. (of this page)	21. No. of Pages	22. Price*
Unclassified	Unclassified	126	$5.75

*For sale by the National Technical Information Service, Springfield, Virginia 22161

EFFECTS OF JET EXHAUST GAS PROPERTIES ON EXHAUST SIMULATION AND AFTERBODY DRAG*

William B. Compton III
Langley Research Center

SUMMARY

Afterbody drag predictions for jet airplanes are usually made experimentally with the jet exhaust flow simulated. The physical gas properties of the fluid used for the model jet exhaust can affect the accuracy of simulation of the airplane's jet exhaust plume. The effect of the accuracy of jet plume simulation on afterbody drag was investigated by making wind-tunnel tests on a single engine nacelle model. In addition to unheated air as the exhaust gas, the decomposition products of three different concentrations of hydrogen peroxide were utilized.

The air jet simulation consistently resulted in higher boattail drag than the hydrogen peroxide simulation. The largest differences in drag due to exhaust gas properties were obtained for the combination of high transonic Mach numbers and steep boattail angles. For these conditions, the current data indicate that the use of air to simulate a nonafterburning turbojet exhaust can result in an overprediction of afterbody drag as high as 17 percent of the real nonafterburning turbojet exhaust value.

The differences between the drags obtained for the various exhaust gases are attributed to different plume shapes and entrainment properties of the gases. Corrections for the plume shape differences can be made by relating the drag to the computed initial inclination angle of the jet plume. Although the entrainment differences are difficult to predict, they seem to be nearly a linear function of the product of the jet exhaust gas constant and local temperature, the local jet exhaust kinetic energy per unit mass, and the internal energy per unit mass.

INTRODUCTION

Experience has shown that the complex flow field in the vicinity of a jet airplane's exhaust nozzles has made calculation of transonic nozzle drag difficult. (See refs. 1 and 2, for example.) The jet exhaust, which influences nozzle drag by plume blockage and

*The information presented in this report is based on a thesis submitted in partial fulfillment of the requirements for the degree of Master of Science, George Washington University, Washington, D.C., August 1973.

entrainment, is a major factor contributing to the complexity of the flow and hence the difficulty in calculating the drag. Therefore, transonic performance predictions are made experimentally with the exhaust flow simulated. Usually because of technical reasons, costs, or safety considerations, the fluid simulating the jet exhaust of the wind-tunnel model is not the same as the exhaust gas of the full-scale airplane. Thus, the difference in the temperatures, specific heats, and gas constants between the model and airplane exhausts can result in a difference in jet plume shapes and entrainments. The problem, therefore, is to determine if the magnitude of the jet interference on afterbody drag is the same for different jet exhaust gases; and if not, to find a logical way to adjust for the differences.

Early investigations which have been conducted to determine the effect of varying the exhaust gas parameters on jet interference (refs. 3 to 8) generally utilized afterbody configurations which are not typical of airplanes today. Usually, they lacked information such as jet exit profiles, afterbody skin temperatures, and boundary-layer profiles which precluded determining precise differences in drag due solely to the jet interference of the various exhaust gases. However, the investigations did tend to show that with cold air simulating the jet exhaust, base and boattail pressures were generally lower than for the other gases. In reference 9, attention was especially given to the problem of correlating the jet interference for different exhaust gases. In that reference, several jet simulation parameters were proposed which, if matched for different jet exhausts, would hopefully give the same jet interference for each exhaust gas.

The present investigation was conducted to get a clear understanding of the relative magnitude of jet interference for various exhaust gases. It also was conducted to determine at which conditions any differences between the jet interference of the various gases occur, the cause of the differences, and to evaluate the simulation parameters suggested in reference 9. This particular investigation concentrated on studying the problem of jet interference on surfaces forward of the nozzle exit. Therefore, only those correlation parameters which were considered most likely to influence the jet interference in this region were evaluated.

Two afterbodies, one with a boattail angle of 20° and one with an angle of 10°, were investigated. Each was investigated for jet exit Mach numbers of 1 and 2. Air and the decomposition products of three concentrations of hydrogen peroxide were used for the jet exhaust. Afterbody pressures and skin temperatures, jet exit pressure and temperature profiles, and afterbody boundary-layer profiles were measured.

SYMBOLS

A area, meters squared

A_{max} maximum cross-sectional area of model, meters squared

a	speed of sound, meters per second
B	jet total temperature weighting factor
C	entrainment constant
C_D	uncorrected afterbody pressure-drag coefficient
$C_{D,aft}$	corrected afterbody pressure-drag coefficient (see eq. (1))
$C_{D,jet\ off}$	afterbody pressure-drag coefficient at jet-off conditions
$C_{D,jet\ on}$	afterbody pressure-drag coefficient at jet-on conditions
C_p	pressure coefficient, $\frac{p - p_\infty}{q_\infty}$
C_v	specific heat at constant volume, joules per kilogram-kelvin
d	diameter, meters
d_{max}	maximum diameter of model, meters
F	jet total pressure weighting factor
f	distance from nozzle throat to exit (see fig. 4), meters
H	momentum, kilogram-meters per second
i,n	integers
l	length of afterbody, meters
M	Mach number
m_{ent}	mass of fluid entrained, kilograms
N_{Re}	Reynolds number
p	pressure, newtons per meter squared

q_∞	free-stream dynamic pressure, newtons per meter squared
R	gas constant, joules per kilogram-kelvin
r	radial distance from model center line, meters
r_e	radius of nozzle exit, meters
s	length of convergent portion of nozzle (see fig. 4), meters
T	temperature, kelvin
T_{dp}	free-stream dewpoint temperature, kelvin
V	velocity, meters per second
V_e	speed of jet exhaust at jet exit, meters per second
$V_{j,l}$	local speed of jet exhaust, meters per second
V_∞	speed of free stream, meters per second
w	axial distance from nozzle exit, positive aft, meters
x	axial distance from tangent point of afterbody radius to forward section of model, positive aft (see fig. 4), meters
y	radial distance from model surface, meters
z	axial distance from nozzle throat, positive aft (see fig. 4), meters
β	afterbody boattail angle, angle between axis of symmetry and generatrix of model afterbody (see fig. 4), degrees
β_j	$= \left(M_e^2 - 1\right)^{1/2}$
β_∞	$= \left(M_\infty^2 - 1\right)^{1/2}$
γ	ratio of specific heats

δ_j calculated initial inclination angle of the jet exhaust plume, degrees

θ angle the boundary-layer rake probes make with axis of symmetry of model (see fig. 7), degrees

$\Delta\nu$ difference between Prandtl-Meyer turning angles of the jet exhaust just inside the nozzle exit and just downstream of the nozzle exit, degrees

ρ density, kilograms per meter cubed

ϕ angular location measured in a plane perpendicular to axis of symmetry of model, clockwise direction positive when viewed from rear, 0° at top of model, degrees

Subscripts:

aft afterbody

b base

bl boundary layer

des design

e exit

edge conditions at the outside edge of the boundary layer

j jet

l local conditions just downstream of the jet exit

noz internal nozzle wall

r rake

s static

t total

te trailing edge

th nozzle throat

∞ free stream

EXPERIMENTAL APPARATUS AND PROCEDURE

Test Matrix and General Procedure

The jet interference on afterbody drag was investigated using four different jet exhaust gases for each of four afterbody configurations. The investigation was made on single nacelle models in the Langley 16-foot transonic tunnel which is a single-return, continuous, atmospheric wind tunnel with an octagonal, slotted test section. Further details of the tunnel are given in reference 10. Tests were conducted at free-stream Mach numbers from 0.60 to 1.20, at an angle of attack of 0°, and at Reynolds numbers per meter ranging from 10.06×10^6 to 14.05×10^6 depending on the Mach number. The blockage of the model and support system was 0.148 percent of the test section cross-sectional area. The jet exhaust physical gas properties are shown below.

Gas	Composition	Formed by decomposition of –	γ	R, J/kg-K	T_t, K
1	Air	--------	1.4	287.04	300
2	64.6% steam, 35.4% oxygen	75% H_2O_2	1.301	389.86	646
3	61.5% steam, 38.5% oxygen	82% H_2O_2	1.282	383.78	810
4	57.7% steam, 42.3% oxygen	90% H_2O_2	1.265	376.19	1013

The test matrix is shown in the following table:

Configuration				Jet exhaust gases	Free-stream Mach number range
Number	β, deg	l/d_{max}	Exit Mach number		
1	20	1.0	1	1, 2, 3, and 4	0.6 to 1.2
2	10	1.5	1	1, 2, 3, and 4	
3a and 3b	20	1.0	2	1, 2, 3, and 4	
4a and 4b	10	1.5	2	1, 2, 3, and 4	
5 (forward boundary layer)	20	1.0	1	2, 3, and 4	
6 (rear boundary layer)	20	1.0	1	2, 3, and 4	

The free-stream Mach number was held constant while a sweep of the jet pressure ratio was made with data being taken at discrete values of pressure ratio. All conditions were held essentially constant while data were being recorded. Data were taken at the highest Mach numbers first, and then at progressively lower Mach numbers to keep the variation in the tunnel total temperature small. The data reduction procedures are outlined in appendix A.

Model

General.- Two separate models were required for an air propellant system and a hydrogen peroxide propellant system. Both models had the same external contours within fabrication tolerance and were cylindrical nacelles with semiogive noses. The various afterbodies were attached to the basic models. Boundary-layer transition from laminar to turbulent flow on the model surface was fixed 2.54 cm from the nose by a strip of No. 100 grit 0.25 cm wide. The models were supported from the nose by a sting-strut arrangement which positioned the center line of the models on the center line of the tunnel. (See sketch (a). All linear dimensions are in centimeters unless otherwise noted.) Photographs of the model installed in the tunnel are presented as figure 1. Figure 2 shows the general arrangement of the model in greater detail than sketch (a).

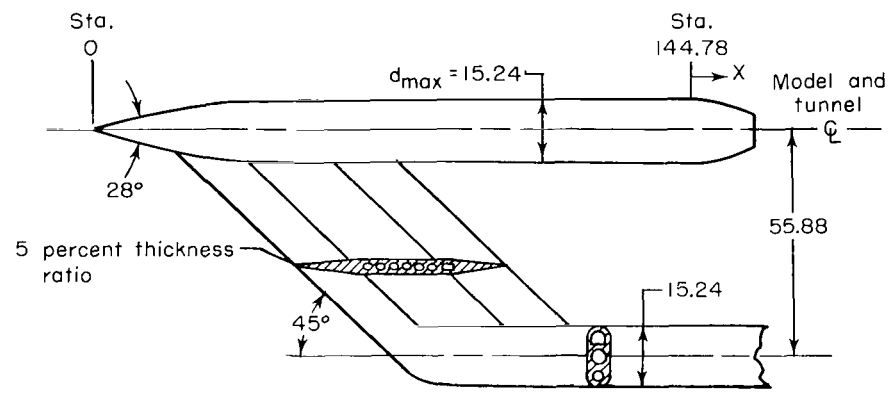

Conf.	β	M_e	Sta. E
1	20°	1	160.02
2	10°	1	167.64
3	20°	2	160.02
4	10°	2	167.64

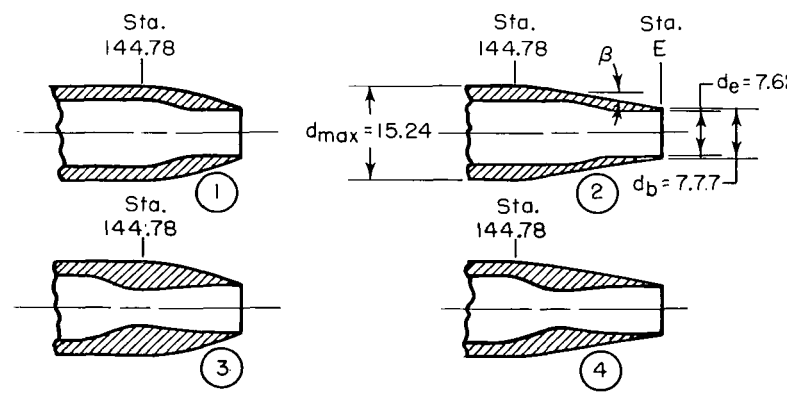

Sketch (a) Model.

Air model.- The arrangement of the air model is shown in figure 2(a). Room temperature air for the jet exhaust is introduced into the model through eight sonic nozzles equally spaced radially around a central core. The two flow smoothing plates each have a latticework of sharp edged holes drilled in an equilateral triangular pattern. The jet total temperature and pressure were obtained from a rake as illustrated. Details of the rake are shown in figure 3.

Hydrogen peroxide model.- The general arrangement of the hydrogen peroxide model is shown in figure 2(b). The hydrogen peroxide is decomposed by a silver screen catalyst bed, which produces a gas composed of a mixture of steam and oxygen. The mass ratio of the steam and oxygen, and hence the ratio of specific heats, gas constant, and total temperature of the mixture are determined by the concentration of the hydrogen peroxide.

The internal section of the hydrogen peroxide model from immediately forward of the flow smoothing plates (see fig. 2(b)) to the nozzle contour has the same dimensions as the air model. Insulation was installed between the inner and outer shells of the afterbody to minimize heat transfer and maintain the same external skin temperatures of the air and hydrogen peroxide models.

Afterbodies.- Four basic afterbodies were tested, the combinations of a 20° boattail, a 10° boattail, and a sonic and Mach 2 jet exit (see sketch (a) and fig. 4). The external contours of all the afterbodies began at model station 144.78, and the base and exit diameters were the same for all afterbodies. The rim at the base was kept as small as practical. Two internal, inviscid, isentropic contours were designed for the Mach 2 exits, one for the air nozzles, and one for the hydrogen peroxide nozzles. The method is described in reference 11. The internal contours at the exit were essentially parallel to the model axis for all configurations. Pressure orifices on both the external and internal contours were placed as close to the exit as physically practical. Tables 1 and 2 give the orifice locations.

Cross-sectional area distributions of the model with the 20° afterbody and of the support system are given in figure 5. Examples of theoretical pressure distributions calculated by an axisymmetric curved boattail method of characteristics and by an axisymmetric potential flow method in which the body is represented by sources and sinks distributed along its surface (ref. 12) are shown in figure 6.

Boundary-layer rakes.- The boundary layer was measured on the external surface of the 20° afterbody with measurements taken at the beginning of the boattail and near the trailing edge. Sketches of the boundary-layer rakes and their locations are presented in figure 7. The local flow angle at the rear rake was predicted from potential flow calculations described in reference 12. The probe tips were designed so that accurate total pressure readings could be obtained for misalinements of the probe with the local flow up to angles of 10°.

Instrumentation

Pressures were measured on the model, in the jet exhaust, and in the boundary layer with individual strain-gage pressure transducers. The accuracy of the transducers measuring the afterbody pressures was ± 293 N/m^2. Temperatures were measured with swagged wire thermocouples. Iron-constantan swagged wire with an accuracy of ± 0.6 K was used for the air model, while the higher temperature capacity chromel-alumel swagged wire with an accuracy of ± 2.2 K was used for the hydrogen peroxide model and the boundary-layer measurements. Wind-tunnel parameters were measured with the standard tunnel instrumentation described in reference 10.

ANALYSIS OF EXPERIMENTAL RESULTS

Factors Influencing Jet Interference

As the jet exhaust leaves the nozzle exit, it influences the afterbody pressures in two ways: by presenting a body which the external flow must negotiate, plume blockage, and by entraining fluid from the vicinity of the afterbody. These two effects oppose each other, with the plume blockage tending to raise the afterbody pressures, and the entrainment tending to lower them. Both these effects are strong functions of the gas properties of the jet exhaust. The manner in which the physical properties of the exhaust gas affect the jet plume shape and entrainment, and hence influence the jet interference on afterbody drag is the subject of this investigation. Sketch (b) illustrates plume blockage and

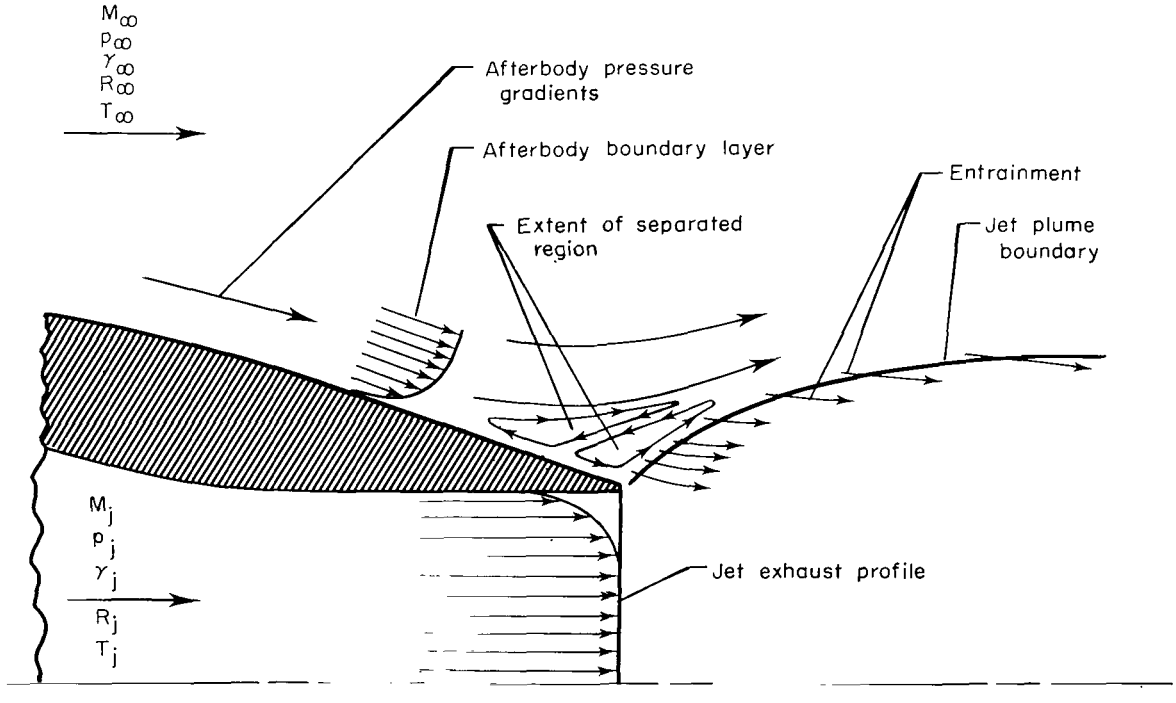

Sketch (b) Factors influencing jet interference.

entrainment, and includes other flow parameters (free-stream conditions, jet exhaust profiles, and afterbody boundary layers) which can influence the magnitude of the jet interference on the afterbody pressures.

During the investigation, the jet exhaust profiles and afterbody boundary layers were determined for each exhaust gas to insure that these flow conditions were constant. The variation in the free-stream parameters between tunnel runs was small, and the jet exhaust profiles for each exhaust gas were relatively flat and uniform. Also, the variation in the model external skin temperatures between the exhaust gases was generally small except very near the nozzle exit. The small skin temperature variations had no effect on the forward boundary layer, and only a slight, if any, effect on the one at the model trailing edge. Therefore, any differences in jet interference between the four exhaust gases should be due mainly to the effect of the properties of the exhaust gases on plume blockage and entrainment. A more thorough discussion of the additional parameters is given in appendix B.

Effect of Jet Exhaust Physical Gas Properties on Jet Interference

Typical afterbody pressure coefficient distributions at several values of jet pressure ratio are presented in figure 8. Examples of pressure-drag coefficients plotted as a function of jet total pressure ratio are presented in figure 9 for the four jet exhaust gases. There were small differences in the jet-off drag coefficients $\left(p_{t,j}/p_\infty \approx 1\right)$ for each jet exhaust gas tested. These small differences were mainly the result of increments between the jet-off afterbody drag of the air model and the hydrogen peroxide model. Therefore, to present the differences between the jet interference on afterbody drag of the four exhaust gases accurately, the data are presented as

$$C_{D,aft} = \left(\frac{C_{D,\text{jet on}} - C_{D,\text{jet off}}}{C_{D,\text{jet off}}}\right)\left(C_{D,\text{jet off}}\right)_{ave} + \left(C_{D,\text{jet off}}\right)_{ave}$$

$$C_{D,aft} = \left(\frac{C_D}{C_{D,\text{jet off}}}\right)\left(C_{D,\text{jet off}}\right)_{ave} \tag{1}$$

where $\left(C_{D,\text{jet off}}\right)_{ave}$ is the average jet-off drag of the four gases for the particular afterbody and Mach number in question.

This afterbody pressure-drag coefficient is presented for each afterbody in figures 10 to 13 as a function of jet total pressure ratio, jet static pressure ratio, and the computed initial inclination angle of the jet exhaust. Afterbody pressure coefficient distributions are presented in figures 14 to 17 for each exhaust gas at several values of jet total pressure

ratio. Each jet-on pressure coefficient is interpolated for exact values of jet total pressure ratio, but no correction was made for the jet-off level.

Sketch (c) summarizes the main effects of jet exhaust physical gas properties on afterbody drag. There are substantial differences between the afterbody pressure drags for the four exhaust gases. Air, when used as the jet exhaust, consistently results in the least favorable jet interference and therefore the highest drag. The exhaust gases having ratios of specific heats of 1.30, 1.28, and 1.26 and corresponding total temperatures of 646, 810, and 1013 K generally result in increasingly more favorable jet interference and less drag.

The magnitude of the differences between the afterbody drags for the various exhaust gases depends on the type of external flow conditions encountered. The differences between the afterbody drags for the various exhaust gases are greater for the high subsonic and transonic Mach numbers, M_∞ = 0.90 and 0.95, than for the lower Mach numbers. Also, the differences in drag are greater for the afterbody with a boattail angle of 20^o than for the one with an angle of 10^o. The greatest differences between the drags for the various exhaust gases were obtained for the combination of high transonic Mach numbers

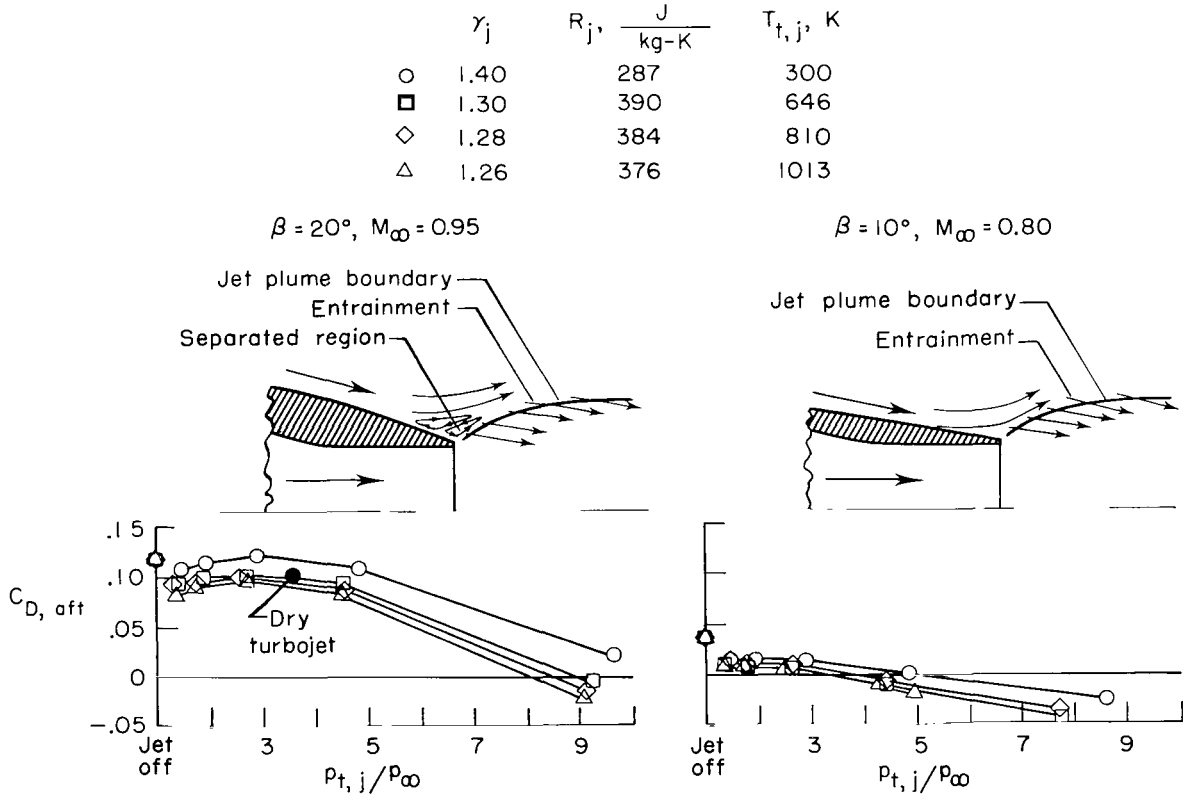

Sketch (c) Effect of exhaust gas properties on jet interference.

and a boattail angle of 20°. At these conditions, the strong adverse pressure gradients on the afterbody are probably easily influenced by plume blockage, and the large nonjet-induced separated regions near the exit (figs. 14(e) and 14(g)) could be easily influenced by entrainment. For the combination of low subsonic Mach numbers and a boattail angle of 10°, the differences between the drags for the four exhaust gases are small until high jet pressure ratios are reached. (See sketch (c) and also see the pressure distributions for this boattail angle presented in figs. 15 and 17.)

A dry turbojet value, determined by using the $R_j T_{j,l}$ ratio in the method described in the section "Correlation of Entrainment," is shown in sketch (c) for the high transonic Mach number and high boattail angle. The dry turbojet value indicates that for operating conditions typical of high nozzle drag (high boattail angles, and transonic speeds and corresponding jet pressure ratios), the use of air to simulate a dry turbojet exhaust can result in an overprediction of afterbody drag by as much as 17 percent of the dry turbojet value.

Based on percentage of jet-off drag, there are large differences between the jet interference of the various exhaust gases for all configurations and subsonic Mach numbers. Depending on the configuration and free-stream Mach number, the differences between the jet interference of the four exhaust gases generally ranged from 10 to 20 percent of the jet-off drag at the low jet pressure ratios, and up to 35 percent of the jet-off drag when compared at a jet exit static pressure ratio of 3. At a Mach number of 1.20, the increments between the drags for the various exhaust gases are small when based on the percentage of jet-off drag except for the sonic exit at the higher jet pressure ratios (figs. 10(e) and 11(e)). This results because the effect of the jet on the boattail pressures is limited to a small region at the rear of the boattail for the lower jet pressure ratios (figs. 14(i) and (j) and 15(i) and (j)). For the configurations with a jet exit Mach number of 2, the jet exit static pressure ratios were not high enough for the jet to expand very much. The differences between the drags for the various exhaust gases for these configurations (figs. 12 and 13) are similar to the differences for the configurations with the sonic exits at the lower jet pressure ratios (figs. 10 and 11).

Correlation of Exhaust Plume Blockage

As explained before, the jet exhaust influences the afterbody pressures by presenting a body which the external flow must negotiate and by entraining fluid from the vicinity of the afterbody. The plume blockage interference would obviously be a function of the shape of the jet exhaust boundary and, as discussed in reference 13, the most important factor determining the shape of the jet boundary is its initial inclination angle. It was verified in reference 14 that matching this angle for several exhaust gases in a quiescent atmosphere matched the initial jet plume shapes as well. Therefore, the initial inclination angle of the jet exhaust δ_j was calculated and used in an attempt to correlate the effect of jet plume blockage on afterbody drag. (See sketch (d).) To calculate δ_j, it was assumed that

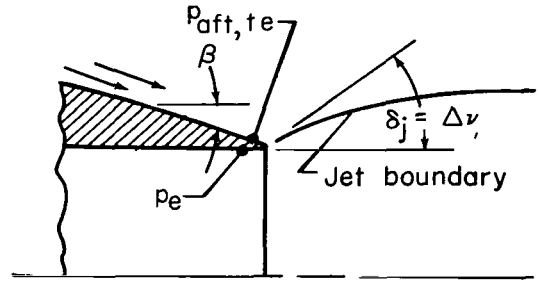

Sketch (d) Plume angle calculation.

$p_{aft,te}$ was the pressure to which the jet exhaust was expanding upon leaving the nozzle. Then, using the measured values of $p_{aft,te}$, p_e, and the jet total pressure, δ_j was calculated from the Prandtl-Meyer relations. The nozzle divergence half-angle was essentially zero for all configurations.

Sketch (e) presents an example of the afterbody pressure drag for each of the exhaust gases as a function of the jet total pressure ratio, the jet exit static pressure ratio, and the initial inclination angle of the jet exhaust plume. As discussed previously, differences exist between the afterbody drag coefficients for the various exhaust gases. As a function of jet total pressure ratio, the differences increase as pressure ratio is increased. When comparing the drag coefficients as a function of the jet exit static pressure ratio, the differences increase at a lower rate. A comparison of the drag coefficients as a function of

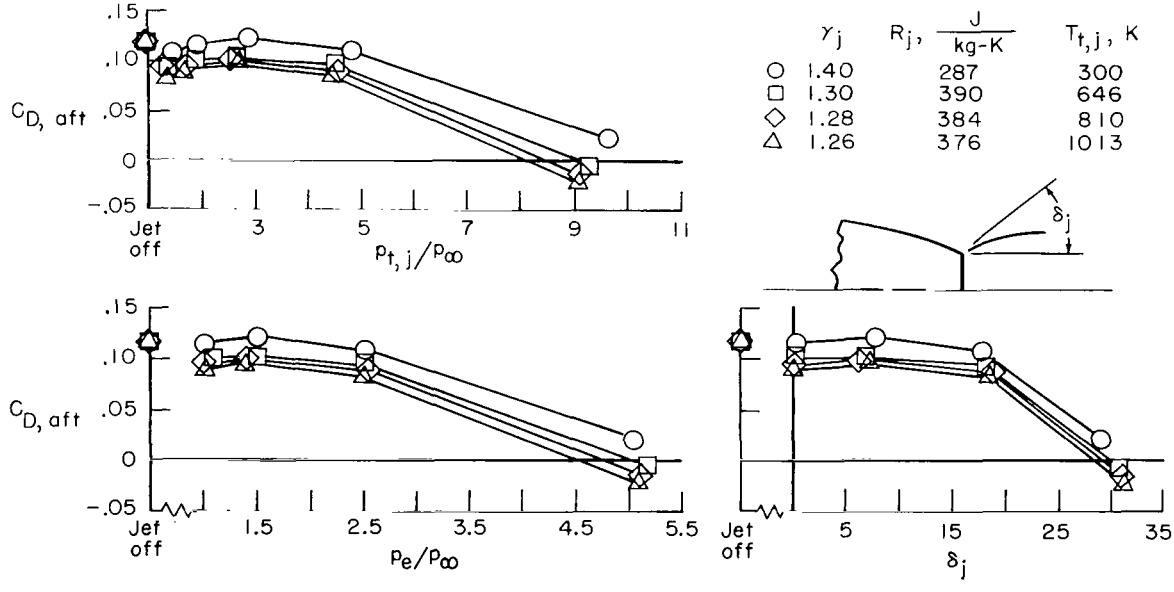

Sketch (e) Comparison of jet simulation parameters.

the initial inclination angle of the jet exhaust δ_j also shows differences between the afterbody drags for the four exhaust gases. However, at the high pressure ratios and hence high plume angles, the discrepancy is reduced even more than for the comparison using exit static pressure ratio. Similar correlations were obtained in reference 15 between room temperature air and hot exhaust gases by computing an effective jet pressure ratio based on the ratio of specific heats for each gas. Since the initial plume angle probably gives a good representation of the initial shape of the jet plume in a moving stream as it does in a quiescent atmosphere (ref. 14), the discrepancies between the jet interference of the four jet exhaust gases at a constant value of δ_j should be mainly due to entrainment. For each free-stream Mach number and configuration, these differences seem to be relatively consistent with δ_j.

The maximum values of exit pressure ratio or initial plume angle for the configurations with Mach 2 jet exits were not large enough to determine if the trends just mentioned were valid for these configurations (figs. 12 and 13). However, for these configurations, δ_j seems to be at least as good a parameter as jet pressure ratio with which to compare the jet interference of the various exhaust gases. Therefore, for underexpanded jets, the data seem to indicate that the initial inclination angle of the jet exhaust plume is a more relevant parameter for comparing the jet interference due to plume blockage than either $p_{t,j}/p_\infty$ or p_e/p_∞. The use of δ_j instead of p_e/p_∞ or $p_{t,j}/p_\infty$ would be more helpful when high jet exhaust plume angles are expected.

In reference 9, the first term of a series expansion of the ratio of p_l/p_e gives

$$\frac{p_l}{p_e} = 1 - \frac{\gamma_j M_e^2}{\beta_j}(\Delta\nu) + \cdots \tag{2}$$

where the subscript l denotes the conditions to which the jet is expanding, $\beta_j = \left(M_e^2 - 1\right)^{1/2}$, and $\Delta\nu$ is the difference in the Prandtl-Meyer turning angles for the jet exhaust in expanding from M_e to M_l. For small values of $\Delta\nu$, the following jet boundary simulation parameters, which would provide the same flow turning angle for the model and full-scale conditions, were suggested:

$$\left(1 - \frac{p_\infty}{p_e}\right)\left(\frac{\beta_j}{\gamma_j M_e^2}\right) \qquad \text{(Jet boundary in a quiescent medium)}$$

$$\frac{\left(p_e - p_l\right)p_\infty \beta_j \gamma_\infty M_\infty^2}{\left(p_l - p_\infty\right)p_e \beta_\infty \gamma_j M_e^2} \qquad \text{(Jet boundary in a moving stream)}$$

These parameters are compared with δ_j in figure 18 for the nozzle with a boattail angle of 20^o and an exit Mach number of 2. All three parameters seemed to give about equal results in comparing the drag for the various exhaust gases. However, due to the low plume angles obtained for the nozzles with supersonic exits, the results were inconclusive. Since these parameters are approximations for the initial plume angle, and since they can become very large or small for values of M_∞ and M_e near 1, δ_j would be the best of the three with which to compare the jet interference of various gases due to plume blockage.

Reference 14 indicates from quiescent atmosphere studies that excellent plume boundary simulation over a wider range of conditions and to much larger axial distances can be made by duplicating both δ_j and $M_j, l/\gamma_j$ instead of just δ_j. It also indicates that a small additional improvement can be made by duplicating the nozzle divergence half-angle. This may be important for very large pressure ratios or when surfaces downstream of the nozzle exit present such problems as pressurization or heating of adjacent surfaces. However, reference 13 indicates that the differences between boundaries for jets having the same jet exit Mach number and nozzle divergence angle are negligibly small when δ_j is duplicated and the difference in ratio of specific heats is not much greater than 0.1. Therefore for most jet airplane configurations and jet pressure ratios, the duplication of M_e, the nozzle divergence angle, and δ_j should give adequate correlation of jet interference on afterbody drag due to plume blockage for various exhaust gases.

Correlation of Entrainment

At supersonic Mach numbers, exhaust plume blockage usually accounts for nearly all the jet interference on nozzle boattails. However, at transonic Mach numbers, or when there are bases or large separated regions in the vicinity of the nozzle exit, entrainment of fluid from the region can significantly contribute to jet interference. In these situations, in addition to the proper simulation of the shape of the airplane's exhaust plume, corrections to wind-tunnel values for differences between the entrainment of the real airplane exhaust and the simulation gases used in the wind tunnel become important.

The amount of fluid entrained from the vicinity of the afterbody by the jet exhaust depends on, among other things, the momentums of the jet exhaust and local afterbody flow and the velocities, energies, and mixing characteristics of the two flows. The momentum of the entraining fluid is generally considered a major factor determining the quantity of fluid entrained. In reference 16 the following equation is given for the mass of fluid entrained by a jet in a quiescent atmosphere:

$$\frac{dm_{ent}}{dw} = C\left(H_j, l\right)^{1/2} \rho_\infty{}^{1/2} \tag{3}$$

In this equation, m_{ent} is the mass of the surrounding fluid entrained, $H_{j,\ell}$ is the momentum flux of the jet exhaust, ρ_∞ is the density of the surrounding fluid, w is the axial distance downstream of the nozzle exit, and C is a constant. Thus the equation predicts that the entrainment varies as the square root of the exhaust momentum.

In addition to the momentum ratio, the following simulation parameters suggested in reference 9 were considered the ones most likely to correlate the jet interference due to entrainment:

$$\frac{p_j \gamma_j{}^{1/2} M_j R_\infty{}^{1/2} T_\infty{}^{1/2} A_e}{p_\infty \gamma_\infty{}^{1/2} M_\infty R_j{}^{1/2} T_j{}^{1/2} A_\infty} = \frac{\rho_j A_e V_e}{\rho_\infty A_\infty V_\infty} \qquad \text{(Mass flow)}$$

$$\frac{\gamma_j M_j{}^2 R_j T_j}{\gamma_\infty M_\infty{}^2 R_\infty T_\infty} = \frac{V_e{}^2}{V_\infty{}^2} \qquad \text{(Kinetic energy per unit mass)}$$

$$\frac{\left(\gamma_\infty - 1\right) R_j T_j}{\left(\gamma_j - 1\right) R_\infty T_\infty} = \frac{C_{v,j} T_j}{C_{v,\infty} T_\infty} \qquad \text{(Internal energy per unit mass)}$$

The maximum cross-sectional area of the model A_{max} was substituted for A_∞ in these equations. The ratio

$$\frac{R_j T_{j,\ell}}{R_\infty T_\infty}$$

was also used to correlate entrainment. Since the jet exhaust interacts with the external flow downstream of the nozzle exit, the correlating parameters were computed for the conditions just behind the nozzle. For these calculations, the local jet static pressure was assumed to be equal to the afterbody trailing-edge pressure. Entrainment, in the sense used in this paper, refers to the effects of the mixing and aspiration of fluid by the jet exhaust in the region near the nozzle exit, as contrasted to the far downstream mixing region of the exhaust.

The entrainment correlation parameters are compared in sketches (f) and (g). Afterbody drag coefficient for the 20° boattail is cross-plotted versus the parameters for a constant initial plume angle of 0° (sketch (f)) and 5° (sketch (g)). Therefore, any differences in drag should be mainly due to differences in entrainment. For reference, since entrainment tends to lower the afterbody pressures, the greater the entrainment, the higher the drag. Entrainment is not a unique function of any of the parameters presented. For

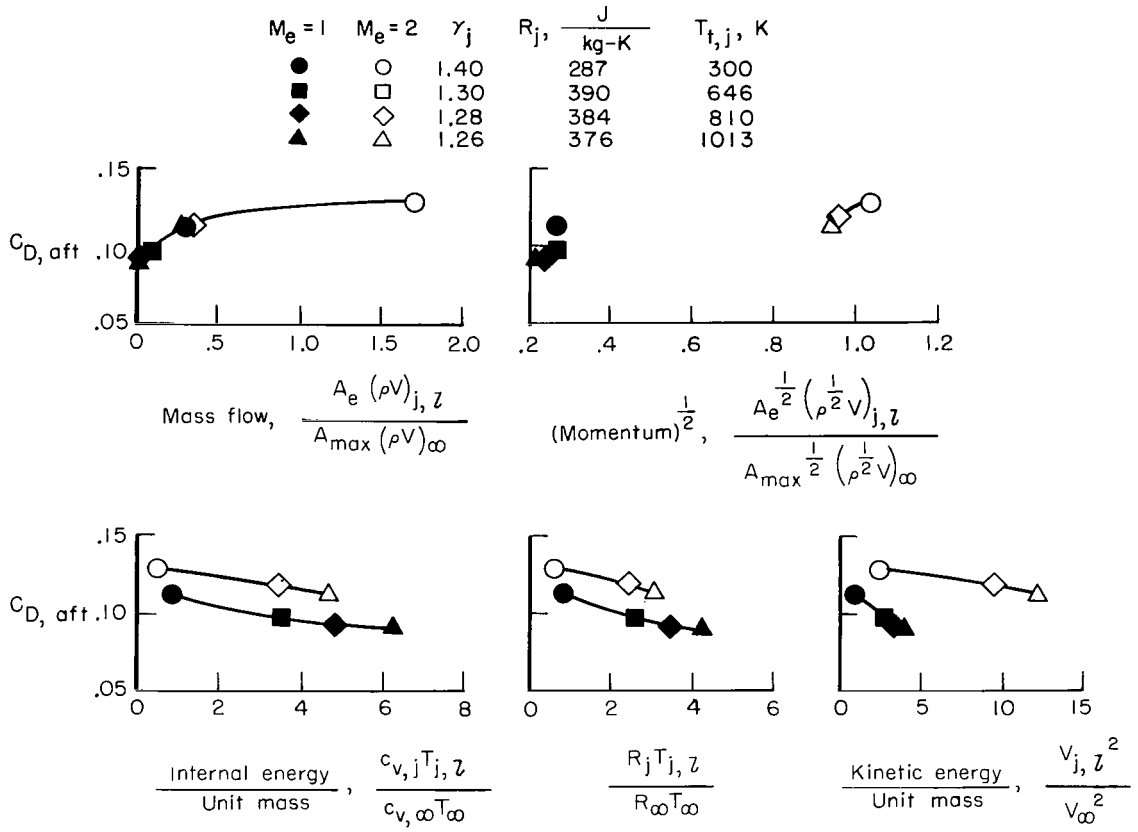

Sketch (f) Comparison of entrainment correlation parameters at $\delta_j = 0^o$.

example, the data for the afterbody with the Mach 2 exit do not fall on the same curve as the data for the afterbody with the Mach 1 exit when compared as a function of jet momentum. If entrainment were only a function of jet exhaust momentum, the data for each nozzle would lie on a single continuous curve.

For air, the jet exhaust Reynolds numbers based on the exit diameter of the nozzles ranged from 3.71×10^5 to 20.9×10^5 for the sonic nozzle, and from 5.60×10^5 to 25.7×10^5 for the Mach 2 nozzle. Reference 16 reports that for values greater than 3×10^4, the entrainment coefficient C in equation (3) is independent of nozzle Reynolds number. Then jet exhaust Reynolds number should not account for the fact that the entrainment of the two exits do not correlate. Therefore, sketches (f) and (g) indicate that entrainment is dependent on the jet exhaust Mach number, an observation also suggested in reference 17.

Although none of the parameters definitely correlated entrainment of the two nozzle exits, for each exit and for each plume angle, the effects of entrainment of the various gases are close to a straight line function of the parameters $R_j T_{j,l} / R_\infty T_\infty$, internal energy

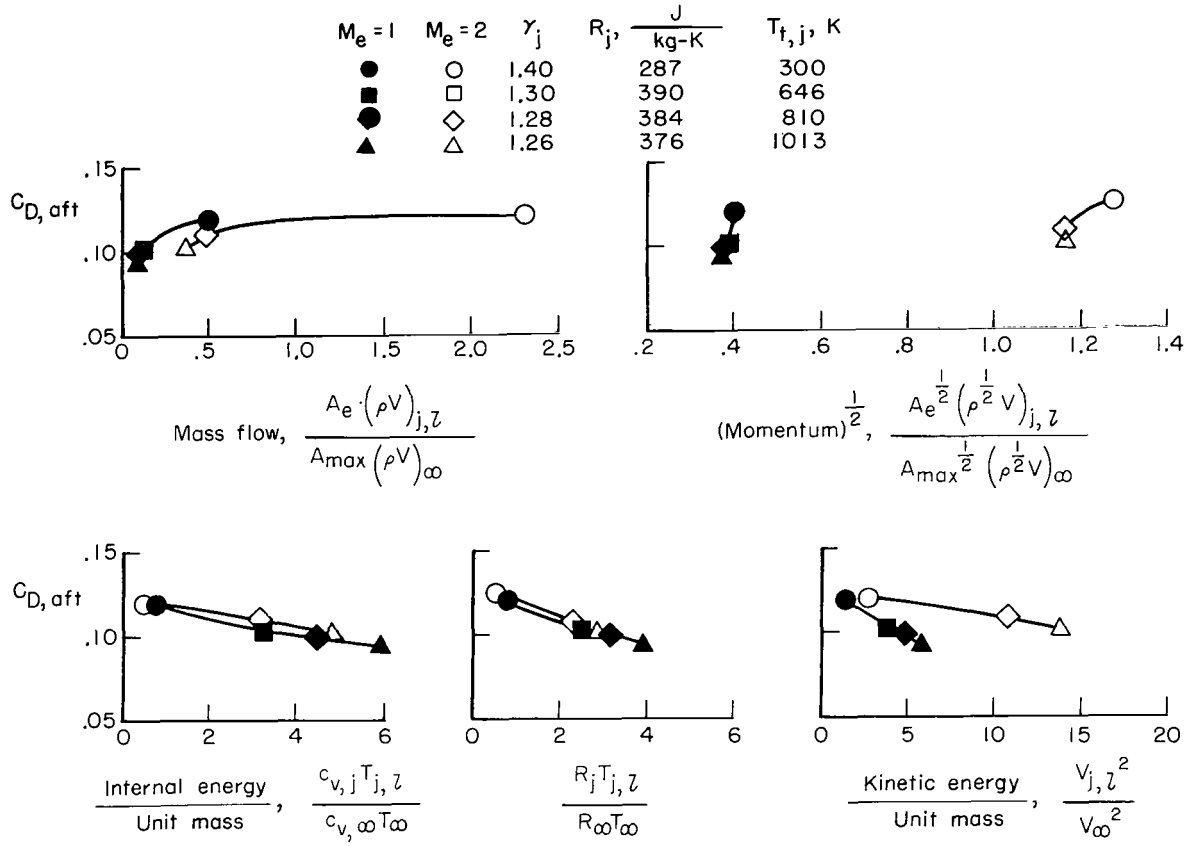

Sketch (g) Comparison of entrainment correlation parameters at $\delta_j = 5^o$.

per unit mass, and the local kinetic energy per unit mass, that is, $V_{j,\ell}^2/V_\infty^2$. Reference 18 also indicates the dependence of jet interference on the ratio $R_jT_{j,\ell}/R_\infty T_\infty$. Cross plots of incremental afterbody drag coefficient versus the ratio $R_jT_{j,\ell}/R_\infty T_\infty$ and the kinetic energy per unit mass parameters at constant values of δ_j are presented in figures 19 and 20. For subsonic jet exit conditions, the parameters are cross-plotted at a jet total pressure of 0.8 of the value required for sonic throat conditions.

The relatively straight-line variation of these parameters with drag suggests that they may be used to adjust for entrainment of various gases. Using either parameter, two points on the curve would have to be experimentally established at the proper plume angle for a particular configuration. Then a straight-line interpolation to the value of the parameter for the real jet exhaust gas may give an estimate to the real airplane drag. It should be emphasized though, since entrainment is dependent on the configuration and external flow conditions, that this is not a prediction method but only an interpolation method for adjusting the wind-tunnel values at the external flow conditions and for the model geometry tested.

Application of Jet Simulation Parameters

The preceding discussion has established the importance of simulating the jet plume blockage and entrainment effects. It has been demonstrated that the jet plume blockage effects can be duplicated for various exhaust gases by matching the initial inclination angle of the jet exhaust plume. Corrections to wind-tunnel values for entrainment, however, must be evaluated from results for at least two exhaust simulation gases. Sketch (h) shows an example of the procedure for adjusting the experimental value of jet interference to full-scale conditions. The data presented are for the following conditions: $M_\infty = 0.95$; $\beta = 20^o$; sonic exit. First, experimentally determine the variation of afterbody drag with jet pressure ratio for at least two jet exhaust gases. Then, correct for plume shape differences by relating the drag to the initial plume angle of the jet exhaust, and obtain a value of drag at the operating plume angle of the aircraft. Final adjustments to the jet interference for any discrepancies in entrainment could then be made by interpolating with the kinetic energy parameter, internal energy parameter, or the RT ratio as illustrated in sketch (h).

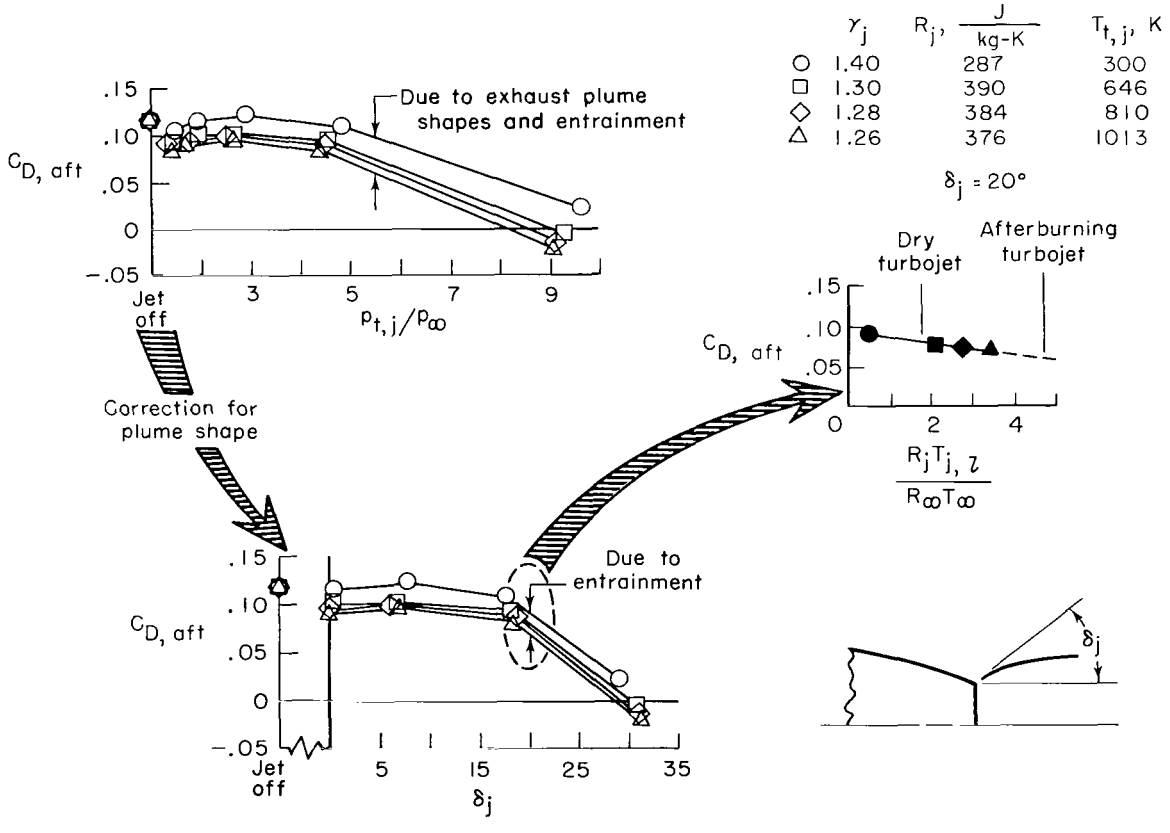

Sketch (h) Application of jet simulation parameters.

CONCLUDING REMARKS

Based on the jet exhaust gases tested and other variables of the investigation, the following effects of the jet exhaust physical gas properties on afterbody drag are indicated.

Substantial differences were obtained between the afterbody drags for the various jet exhaust gases. Air, when used as the jet exhaust, consistently gave the least favorable jet interference and therefore the highest drag. The exhaust gases having ratios of specific heats, gas constants, and total temperatures of 1.30, 390 J/kg-K, and 646 K; 1.28, 384 J/kg-K, and 810 K; and 1.26, 376 J/kg-K, and 1013 K generally resulted in increasingly more favorable jet interference and less drag.

The differences between the afterbody drags for the various exhaust gases were greatest for the combination of high boattail angles, 20°, and high subsonic or transonic Mach numbers. For the combination of the lower boattail angles, 10°, and lower Mach numbers, the differences were much less. At a free-stream Mach number of 1.20, the differences in drag were small until large values of jet pressure ratio were obtained. Based on percentage of jet-off drag, there were large increments between the afterbody drags for the various jet exhaust gases at all subsonic Mach numbers. Depending on the configuration and free-stream Mach number, the differences generally ranged from 10 to 20 percent of the jet-off drag at the low jet pressure ratios, and up to 35 percent of the jet-off drag at the jet exit static pressure ratio of 3. For operating conditions typical of high nozzle drag (high boattail angles and transonic speeds and corresponding pressure ratios), the current data indicate that the use of air to simulate a dry turbojet exhaust can result in an overprediction of afterbody drag as high as 17 percent of the dry turbojet value.

The differences in jet interference between the various exhaust gases are attributed to different plume shapes and entrainment properties of the gases. Corrections for the plume shape differences can be made by relating the drag to the computed initial inclination angle of the jet plume. Although the entrainment differences are difficult to predict, they seem to be a relatively straight-line function of the product of the jet exhaust gas constant and local temperature, of the local jet exhaust kinetic energy per unit mass, and also of the internal energy per unit mass.

Langley Research Center
National Aeronautics and Space Administration
Hampton, Va. 23665
June 16, 1975

APPENDIX A

DATA REDUCTION

This appendix describes the procedures used to reduce the measured quantities into coefficient form.

Jet Exhaust Conditions

The stagnation conditions of the jet were obtained from the rake located just behind the flow smoothing plates. (See fig. 2.) Incremental areas were assigned to the probes, and the total pressure and temperature were obtained from the equations

$$p_{t,j} = \sum_{i=1}^{10} F_i p_{t,j,i} \tag{A1}$$

and

$$T_{t,j} = \sum_{i=1}^{3} B_i T_{t,j,i} \tag{A2}$$

where $\sum_{i=1}^{10} F_i = 1$ and $\sum_{i=1}^{3} B_i = 1.$

The static pressure at the nozzle exit was assumed to be the average of measurements made with the two static pressure taps nearest the nozzle exit. Their exact locations are given in table 2. The afterbody with the boundary-layer rakes had no static orifices, so for conditions at which the nozzle was assumed choked, i.e., when

$$p_{t,j}\left(\frac{2}{\gamma_j + 1}\right)^{\frac{\gamma_j}{\gamma_j - 1}} > p_\infty \tag{A3}$$

p_e was calculated with the equation

$$p_e = p_{t,j}\left(\frac{2}{\gamma_j + 1}\right)^{\frac{\gamma_j}{\gamma_j - 1}} \tag{A4}$$

External Conditions

The afterbody drag coefficient was computed by assigning incremental areas to each pressure on the top row (at $\phi = 0^o$) and by using the equation

$$C_{D,aft} = \frac{-1}{A_{max}} \sum_{i=1}^{n} C_{p,aft,i} A_{aft,i} \tag{A5}$$

where n is the number of orifices in the top row and

$$\sum_{i=1}^{n} A_{aft,i} = A_{max} - A_e \tag{A6}$$

It was assumed that the top row of orifices would be the row most nearly free of strut interference.

The boundary-layer profiles were computed by substituting the pressure sensed by the rakes into either the equation

$$M_{bl,i} = \left\{5\left[\left(\frac{p_{t,r,i}}{p_{s,r}}\right)^{\frac{\gamma_\infty - 1}{\gamma_\infty}} - 1\right]\right\}^{1/2} \tag{A7}$$

if

$$\frac{p_{s,r}}{p_{t,r,i}} > \left(\frac{2}{\gamma_\infty + 1}\right)^{\frac{\gamma_\infty}{\gamma_\infty - 1}}$$

or the equation

$$M_{bl,i} = \left(\frac{p_{s,r}}{p_{t,r,i}}\right)\left(\frac{\gamma_\infty + 1}{2}\right)^{\frac{\gamma_\infty}{\gamma_\infty - 1}} \left(M_{bl,i}\right)^{\frac{3\gamma_\infty - 1}{\gamma_\infty - 1}} \left[\frac{\gamma_\infty + 1}{2\gamma_\infty \left(M_{bl,i}\right)^2 - \left(\gamma_\infty - 1\right)}\right]^{\frac{1}{\gamma_\infty - 1}} \tag{A8}$$

if

$$\frac{p_{s,r}}{p_{t,r,i}} \leq \left(\frac{2}{\gamma_\infty + 1}\right)^{\frac{\gamma_\infty}{\gamma_\infty - 1}}$$

The integer i indicates the particular rake total pressure measurement in question. The second equation for $M_{bl,i}$ was iterated until the residual was less than or equal to 0.0001 of the computed value of $M_{bl,i}$. The velocity profiles were computed by using the free-stream stagnation temperature as the stagnation temperature in the boundary layer. To check the validity of this assumption, boundary-layer temperatures were measured with another set of rakes. The ratio of the actual velocity in the boundary layer to the velocity computed by assuming the free-stream temperature would then be

$$\frac{V_{actual}}{V_{computed}} = \frac{M_{bl,i} a_{bl,i,actual}}{M_{bl,i} a_{bl,i,computed}} = \left(\frac{T_{bl,i}}{T_\infty}\right)^{1/2} = \left(\frac{T_{t,bl,i}}{T_{t,\infty}}\right)^{1/2} \tag{A9}$$

APPENDIX B

FACTORS INFLUENCING JET INTERFERENCE

As the jet exhaust leaves the nozzle exit, it influences the afterbody pressures by presenting a body which the external flow must negotiate and by entraining fluid from the vicinity of the afterbody. The magnitudes of these two effects are influenced by the free-stream conditions, jet exhaust profiles, and the condition of the flow on the afterbodies. There was a small variation of these parameters between the tests of each exhaust gas. The influence of these variations on drag is evaluated in this appendix. Therefore, an accurate assessment of the differences in drag due solely to differences in the jet exhaust physical gas parameters can be made.

Free-Stream Conditions

Since the Langley 16-foot transonic tunnel is an atmospheric wind tunnel, the free-stream conditions varied slightly during the investigation. Figure 21 shows the band of the free-stream parameters encountered during the test. The variation in Reynolds number at a particular Mach number is primarily due to the variation in free-stream total temperature. The break in the bands between Mach numbers 0.95 and 1.20 indicates that no data were taken in this Mach number range. The bandwidth of the free-stream parameters is small enough so that it does not substantially affect the jet interference.

Jet Exhaust Profiles

The shape of the jet exit profile is an important parameter affecting the influence of the jet exhaust on the external flow. Therefore, even though care was taken in the design of the model to insure flat and uniform profiles for each exhaust gas, the actual exit profiles were determined on a static test stand with rakes. This was especially important for the hydrogen peroxide nozzles because flat exit profiles are difficult to obtain without careful design of these gas generators. (See ref. 19.) The pressure distributions on the nozzle walls were also measured and are shown in figure 22 as a function of jet pressure ratio.

Figure 23 presents exit profiles of the total pressure, static pressure, and total temperature ratios for the $M_e = 1.0$ and $M_e = 2.0$ nozzles. The nozzle wall exit static pressures were obtained with the static pressure rake removed to avoid interference of the rake probes with the wall measurements. The exit profiles of the basic measured quantities were relatively flat and uniform for all the gases.

Exit velocity profiles computed from the basic measurements are presented in figure 24. These and the internal pressure distributions (fig. 22) indicate that the jet total pressure ratio for the supersonic nozzles must generally be greater than 0.6 of its design

value to insure a nominal exit Mach number of 2. Figure 24 shows that the exit velocity profiles for the various gases are also relatively flat and uniform. This indicates that nonuniformity of the exit profiles was not a major factor in the differences between the jet interference of the various exhaust gases.

Afterbody Flow Parameters

Entrainment of fluid from the region of the afterbody and the effect of the jet plume boundary on the afterbody pressures depend on the nature of the afterbody flow. Since afterbody skin temperature could affect the boundary-layer profiles and boattail pressures, each hydrogen peroxide nozzle was insulated to keep the external skin temperature distribution independent of the exhaust gas temperature. However, some variations between the afterbody skin temperature distributions for the four jet exhaust gases were obtained.

Figure 25 shows the jet-off pressure distributions, skin temperature distributions, and boundary-layer profiles for the afterbody with a boattail angle of 20°. The boundary-layer measurements were made on a special boundary-layer afterbody which duplicated the 20° afterbody with a sonic exit. Cold skin temperatures were obtained by making a tunnel run in which the jet was not operated. Data for the hot skin temperatures were taken immediately after the jet was turned off. The skin temperatures immediately after the jet was turned off were essentially the same as the hottest skin temperatures when the jet was operating. (See fig. 26.)

The Mach numbers in the boundary layer were computed by using the static pressures measured at the tips of the boundary-layer rakes. (See fig. 7.) A comparison of the coefficients of the pressures measured at the tips of the rakes with those measured on the model surface in the plane of the rake with the rake removed (fig. 27) shows that the static pressures used to compute the boundary-layer Mach numbers were in error. At the higher Mach numbers, a shock originating at the afterbody location where the boundary layer separates probably interferes with the rear rake static probe pressures. So these data were not faired. The profiles do serve the purpose, however, of giving an indication of the boundary-layer shapes and the extent of the separated region on the afterbody.

The velocities in the boundary layer were computed by assuming that the total temperature in the boundary layer was the same as the total temperature of the free stream. The square roots of the ratio of the total temperature in the boundary layer to that of the free stream show that this assumption gave very little error in that portion of the boundary layer which was not separated. The boundary-layer temperature measurements at a Mach number of 1.2 were unreliable due to a thermocouple malfunction and are not presented.

Figure 25 shows that the afterbody skin temperatures had no effect on the forward boundary-layer profiles. The rear profiles indicate that there is a slight tendency for the boundary layer at the trailing edge to separate earlier (see the data for $M_{\infty} = 0.90$,

fig. 25(f)) for the hotter skin temperatures. Trailing-edge boundary-layer profiles immediately before and after a jet pressure ratio sweep (cool and hot skin temperatures) do not always support this trend. It is supported at a free-stream Mach number of 1.20, but at $M_\infty = 0.90$ the opposite effect is seen (fig. 28). At other subsonic Mach numbers there was no difference between the profiles before and after a jet pressure ratio sweep.

The boundary-layer profiles (fig. 25) show that, for the test Mach numbers, the greatest amount of separated flow on the afterbody with $l/d_{max} = 1.0$ occurs at a free-stream Mach number of 0.95 and a smaller amount at Mach numbers of 1.20 and 0.90. At Mach numbers of 0.80 and 0.60 there appears to be no separation.

The data for the afterbody pressure distributions presented in figure 25 were taken just before and after each jet pressure ratio sweep to assess any effect of afterbody skin heating. At first, a comparison of the minimum values of the pressure coefficients in figure 25 for the air model with those for the hydrogen peroxide model seems to indicate that colder skin temperatures result in lower afterbody pressures. However, the pressure distributions for the hydrogen peroxide model seem to be consistent regardless of skin temperature, and some of those temperatures are at the same level as the temperatures for the air model. A check of the coordinates for the two afterbodies revealed a difference in model radius of up to 0.025 cm. Potential flow theory (ref. 12) only accounts for about one third of the pressure coefficient difference between the two models, but it does substantiate the variations obtained in the pressure coefficient distributions.

Summary of Factors Influencing Jet Interference

During the investigation, the width of the band of the various free-stream parameters was small. Also, the jet exit profiles were shown to be relatively flat and uniform for all the jet exhaust gases, and the flow field in the vicinity of the afterbody was negligibly affected by the model skin temperatures. Hence, any difference in jet interference between the four exhaust gases should be mainly due to the differences in the properties of the exhaust gases themselves.

REFERENCES

1. Runckel, Jack F.: Interference Between Exhaust System and Afterbody of Twin-Engine Fuselage Configurations. NASA TN D-7525, 1974.

2. Lee, Edwin E., Jr.; and Runckel, Jack F.: Performance of Closely Spaced Twin-Jet Afterbodies With Different Inboard-Outboard Fairings and Nozzle Shapes. NASA TM X-2329, 1971.

3. Cortright, Edgar M., Jr.; and Kochendorfer, Fred D.: Jet Effects on Flow Over Afterbodies in Supersonic Stream. NACA RM E53H25, 1953.

4. Hearth, Donald P.; and Wilcox, Fred A.: Thrust and Drag Characteristics of a Convergent-Divergent Nozzle With Various Exhaust Jet Temperatures. NACA RM E53L23b, 1954.

5. Henry, Beverly Z., Jr.; and Chan, Maurice S.: Preliminary Results of an Investigation at Transonic Speeds To Determine the Effects of a Heated Propulsive Jet on the Drag Characteristics of a Related Series of Afterbodies. NACA RM L55A24a, 1955.

6. Baughman, L. Eugene; and Kochendorfer, Fred D.: Jet Effects on Base Pressures of Conical Afterbodies at Mach 1.91 and 3.12. NACA RM E57E06, 1957.

7. Beke, Andrew; and Simon, Paul C.: Thrust and Drag Characteristics of Simulated Variable-Shroud Nozzles With Hot and Cold Primary Flows at Subsonic and Supersonic Speeds. NACA RM E54J26, 1955.

8. Lee, George: An Investigation of Transonic Flow Fields Surrounding Hot and Cold Sonic Jets. NASA TN D-853, 1961.

9. Pindzola, M.: Jet Simulation in Ground Test Facilities. AGARDograph 79, Nov. 1963.

10. Corson, Blake W., Jr.; Runckel, Jack F.; and Igoe, William B.: Calibration of the Langley 16-Foot Transonic Tunnel With Test Section Air Removal. NASA TR R-423, 1974.

11. Johnson, Charles B.; Boney, Lillian R.; Ellison, James C.; and Erickson, Wayne D.: Real-Gas Effects on Hypersonic Nozzle Contours With a Method of Calculation. NASA TN D-1622, 1963.

12. Hess, J. L.; and Smith, A. M. O.: Calculation of Potential Flow About Arbitrary Bodies. Progress in Aeronautical Sciences, Vol. 8, D. Küchemann, P. Carriere, B. Etkin, W. Fiszdon, N. Rott, J. Smolderen, I. Tani, and W. Wuest, eds., Pergamon Press, Inc., c.1967, pp. 1-138.

13. Love, Eugene S.; Grigsby, Carl E.; Lee, Louise P.; and Woodling, Mildred J.: Experimental and Theoretical Studies of Axisymmetric Free Jets. NASA TR R-6, 1959. (Supersedes NACA RM L54L31 by Love and Grigsby; RM L55J14 by Love; RM L56G18 by Love, Woodling, and Lee; and TN 4195 by Love and Lee.)

14. Herron, R. D.: An Investigation of Jet Boundary Simulation Parameters for Underexpanded Jets in a Quiescent Atmosphere. AIAA Paper No. 68-397, Apr. 1968.

15. Robinson, C. E.; and High, M. D.: Exhaust Plume Temperature Effects on Nozzle Afterbody Performance Over the Transonic Mach Number Range. AEDC-TR-74-9, U.S. Air Force, July 1974.

16. Hill, B. J.: Measurement of Local Entrainment Rate in the Initial Region of Axisymmetric Turbulent Air Jets. J. Fluid Mech., vol. 51, pt. 4, Feb. 22, 1972, pp. 773-779.

17. Berrier, Bobby Lee; and Wood, Frederick H., Jr.: Effect of Jet Velocity and Axial Location of Nozzle Exit on the Performance of a Twin-Jet Afterbody Model at Mach Numbers up to 2.2. NASA TN D-5393, 1969.

18. Jaarsma, F.: Engine-Airplane Interference in Transonic Tests. Report of the AGARD Ad Hoc Committee on Engine-Airplane Interference and Wall Corrections in Transonic Wind Tunnel Tests, AGARD-AR-36-71, Aug. 1971, pp. II-1 – II-116. (Available from DDC as AD 729 568.)

19. Salters, Leland B., Jr.; and Chamales, Nicholas C.: Studies of Flow Distortion in the Tailpipes of Hydrogen Peroxide Gas Generators Used for Jet-Engine Simulation. NASA TM X-1671, 1968.

TABLE 1.- EXTERNAL INSTRUMENTATION LOCATIONS

(a) Static pressure orifices

ϕ, deg (a)	x/d_{max} for boattails		ϕ, deg (a)	x/d_{max} for boattails	
	l/d_{max} = 1.0	l/d_{max} = 1.5		l/d_{max} = 1.0	l/d_{max} = 1.5
0	-0.833	-0.833	90	-0.500	-0.500
	-.500	-.500		0	0
	-.167	-.167		.200	.167
	0	0		.250	.220
	.125	.167		.300	.267
	.200	.200		.417	.147
	.250	.267		.567	.750
	.300	.417		.633	1.067
	.417	.583		.767	1.267
	.500	.750		.833	1.417
	.567	.917		.917	
	.633	1.000		.950	
	.700	1.067			
	.767	1.133	180	-.833	-.833
	.833	1.200		-.500	-.500
	.883	1.267		-.167	-.167
	.917	1.333		0	0
	.950	1.383		.125	.167
		1.417		.200	.220
				.250	.267
50	-.500	-.500		.300	.417
	0	0		.417	.750
	.125	.167		.567	1.000
	.200	.220		.633	1.133
	.250	.267		.767	1.267
	.300	.417		.833	1.383
	.417	.750		.917	1.417
	.567	1.607		.950	
	.633	1.267			
	.767	1.333			
	.833	1.417			
	.917				
	.950				

[a] ϕ is measured clockwise when model is viewed from the rear. 0^{o} is at the top of the model.

(b) Surface thermocouples: $\phi = 0^{o}$ and 180^{o}

x/d_{max} for boattails	
l/d_{max} = 1.0	l/d_{max} = 1.5
-0.833	-0.833
0	0
.500	.750
.833	1.200
.933	1.417

TABLE 2.- INTERNAL INSTRUMENTATION LOCATIONS

(a) Static pressure orifices; boattails with $l/d_{max} = 1.0$

ϕ, deg	z/d_{th}		
	Sonic nozzle	Supersonic nozzles	
		$\gamma = 1.4$	$\gamma = 1.283$
-5	-1.667	-2.164	-2.230
	-.333	-.433	-.446
	0	0	0
	.333	.433	.446
	[a] 1.267	1.299	1.784
		2.164	3.123
		3.030	4.015
		[a] 4.805	[a] 5.498
30	[a] 1.267	[a] 4.805	[a] 5.498

[a] For configurations with $l/d_{max} = 1.5$, substitute the following values:

Sonic nozzle	Supersonic nozzles	
	$\gamma = 1.4$	$\gamma = 1.283$
1.033	4.528	5.186

(b) Surface thermocouples; $\phi = 15^{\circ}$; boattails with $l/d_{max} = 1.0$

z/d_{th}		
Sonic nozzle	Supersonic nozzles	
	$\gamma = 1.4$	$\gamma = 1.283$
-1.667	-2.164	-2.230
0	0	0
[b] 1.267	2.164	3.123
	[b] 4.805	[b] 5.365

[b] For configuration with $l/d_{max} = 1.5$, substitute the following values:

Sonic nozzle	Supersonic nozzles	
	$\gamma = 1.4$	$\gamma = 1.283$
1.033	4.528	4.740

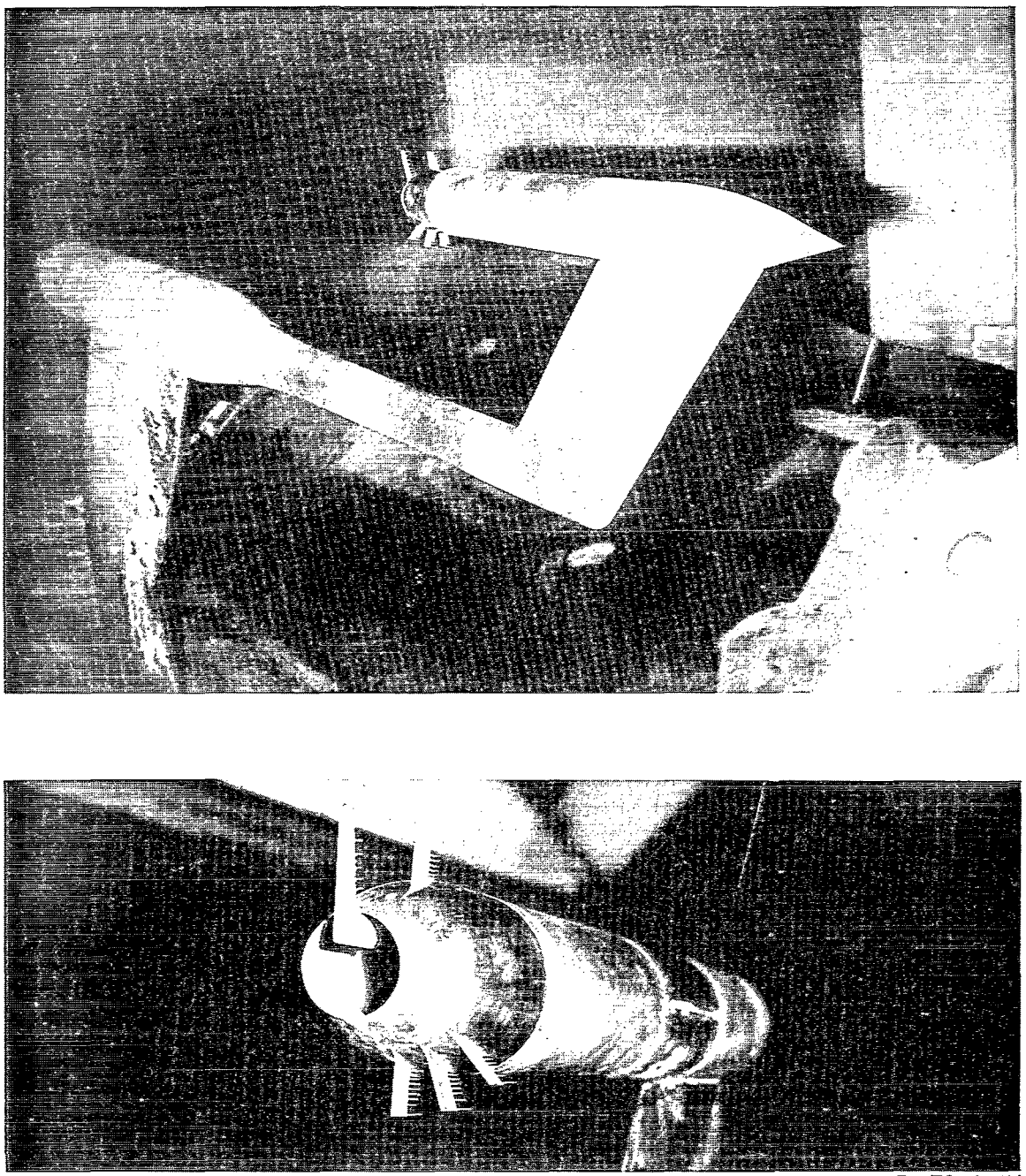

L-73-1951

Figure 1.- Model installed in wind tunnel. Boundary-layer rakes installed; forward rake configuration.

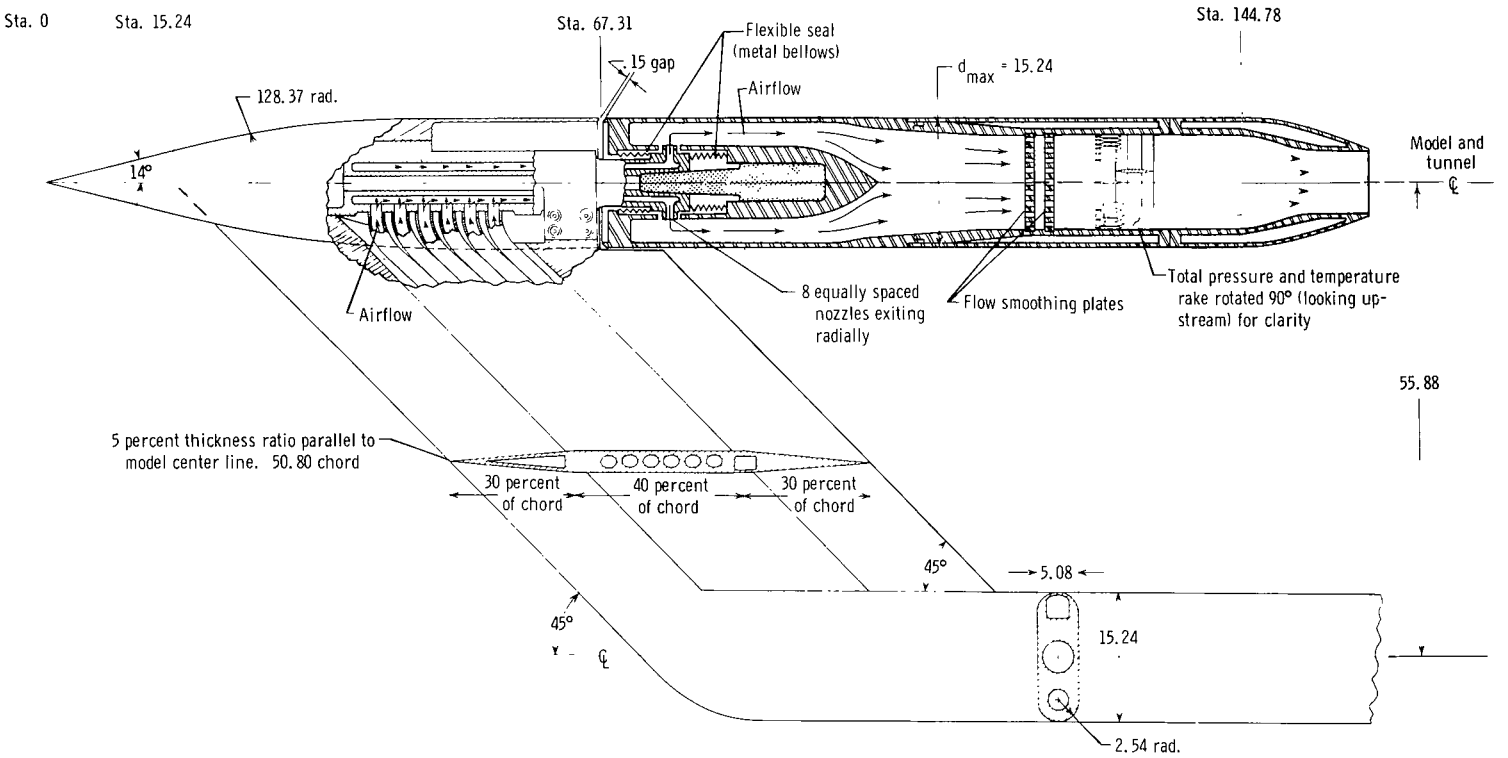

(a) Air model.

Figure 2.- General arrangement of model. (All linear dimensions are in centimeters unless otherwise noted.)

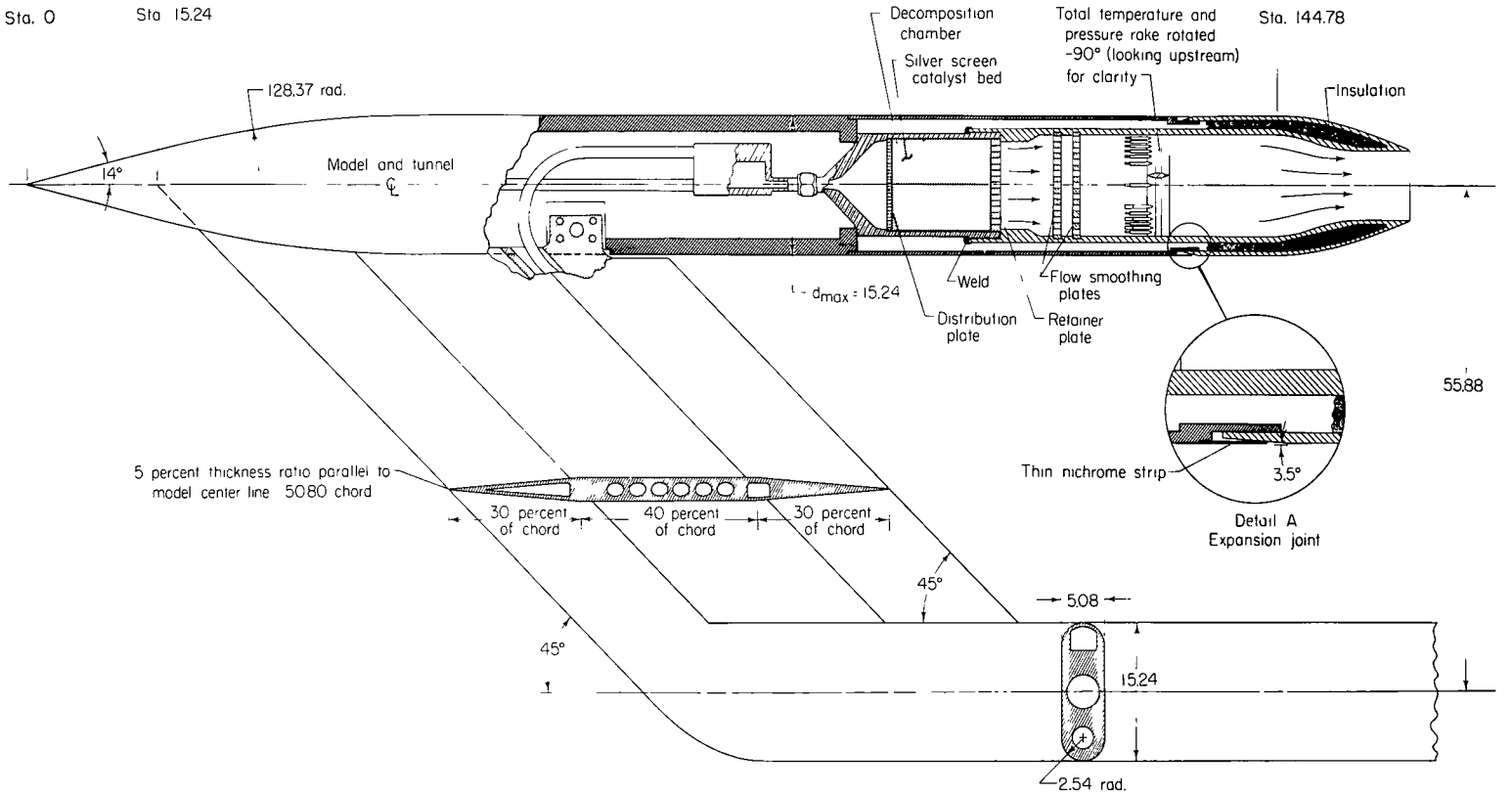

(b) Hydrogen peroxide model.

Figure 2.- Concluded.

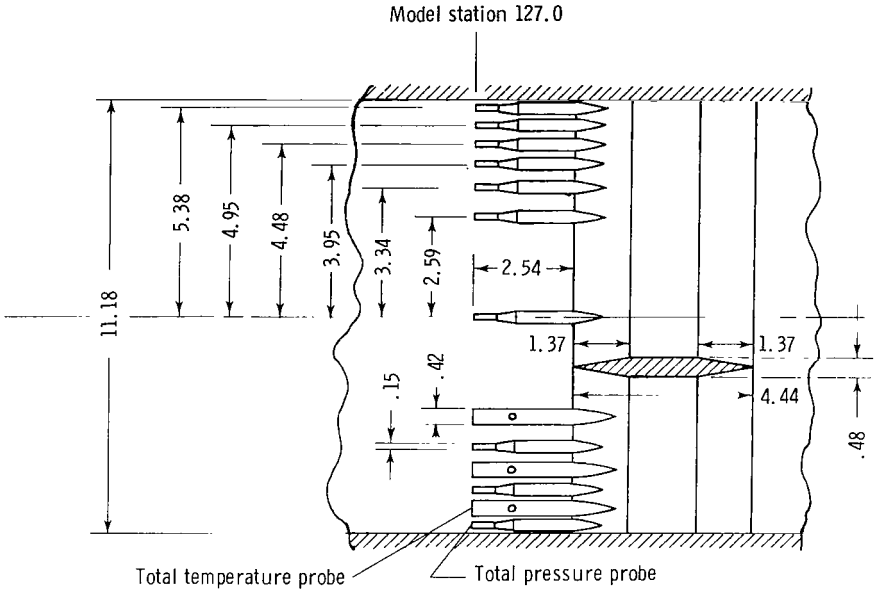

(a) Air model (top view).

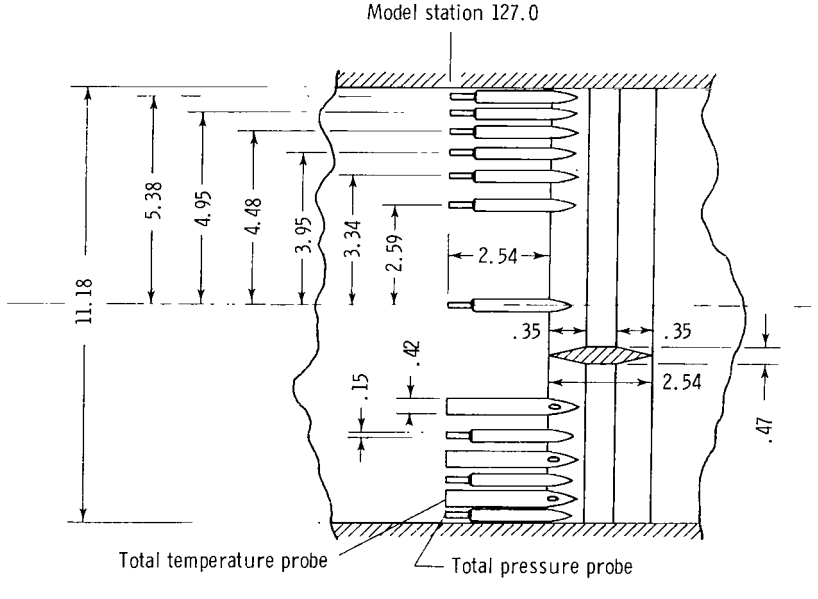

(b) Hydrogen peroxide model (top view).

Figure 3.- Details of internal flow rakes. (All linear dimensions are in centimeters unless otherwise noted.)

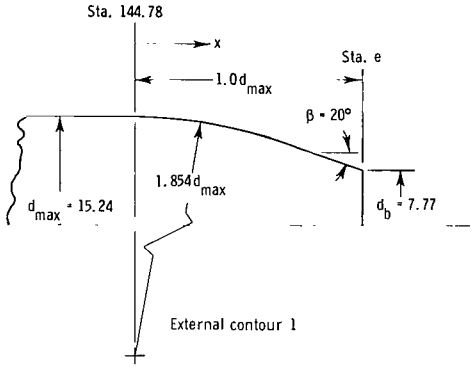

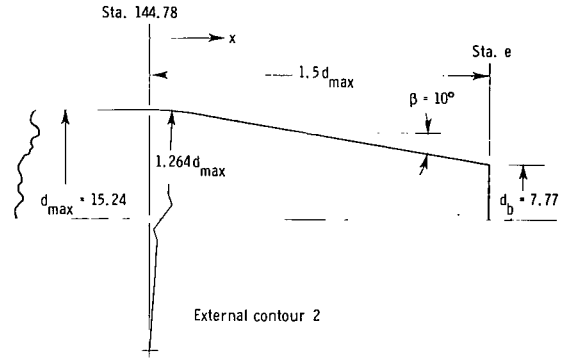

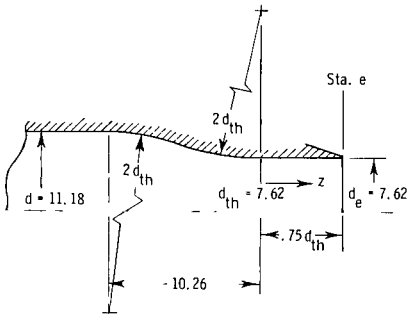

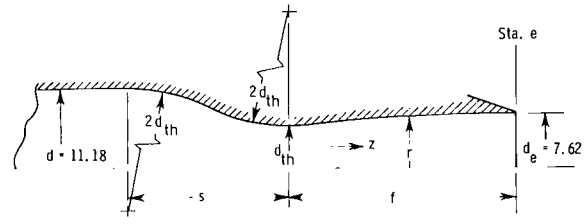

Configuration	External contour	Internal contour	Design parameters β	M_e	d_{th}	s	f
1	1	1	20^0	SONIC	7.62	-	
2	2	1	10^0	SONIC	7.62	-	
3a	1	2a(γ = 1.4)	20^0	2	5.87	10.84	15.06
3b	1	2b(γ = 1.283)	20^0	2	5.70	10.83	16.54
4a	2	2a(γ = 1.4)	10^0	2	5.87	10.84	15.06
4b	2	2b(γ = 1.283)	10^0	2	5.70	10.83	16.54

Coordinates for supersonic nozzles

Nozzle a(γ = 1.4) z	Nozzle a(γ = 1.4) r	Nozzle b(γ = 1.283) z	Nozzle b(γ = 1.283) r	Nozzle a(γ = 1.4) z	Nozzle a(γ = 1.4) r	Nozzle b(γ = 1.283) z	Nozzle b(γ = 1.283) r
0	2.934	0	2.847	7.699	3.602	7.584	3.439
0.455	2.957	0.307	2.850	8.148	3.630	8.110	3.485
0.566	2.964	0.493	2.850	8.626	3.655	8.677	3.531
1.034	3.000	0.998	2.855	9.124	3.680	9.154	3.564
1.544	3.043	1.516	2.873	9.652	3.706	9.662	3.599
2.037	3.089	2.009	2.901	10.201	3.729	10.193	3.632
2.550	3.139	2.588	2.946	10.630	3.744	10.612	3.655
3.071	3.193	3.033	2.884	11.229	3.762	11.194	3.686
3.561	3.244	3.574	3.035	11.692	3.774	11.646	3.708
4.087	3.299	4.054	3.081	12.154	3.785	12.121	3.726
4.567	3.348	4.580	3.137	12.865	3.797	12.774	3.752
5.052	3.393	5.103	3.193	13.604	3.805	13.627	3.774
5.591	3.442	5.568	3.241	14.348	3.810	14.364	3.790
6.104	3.485	6.144	3.302	15.062	3.810	15.110	3.802
6.563	3.520	6.639	3.350			15.839	3.807
7.160	3.563	7.097	3.396			16.543	3.810

Figure 4.- Geometry and dimensions of various nozzle configurations. (All linear dimensions are in centimeters unless otherwise noted.)

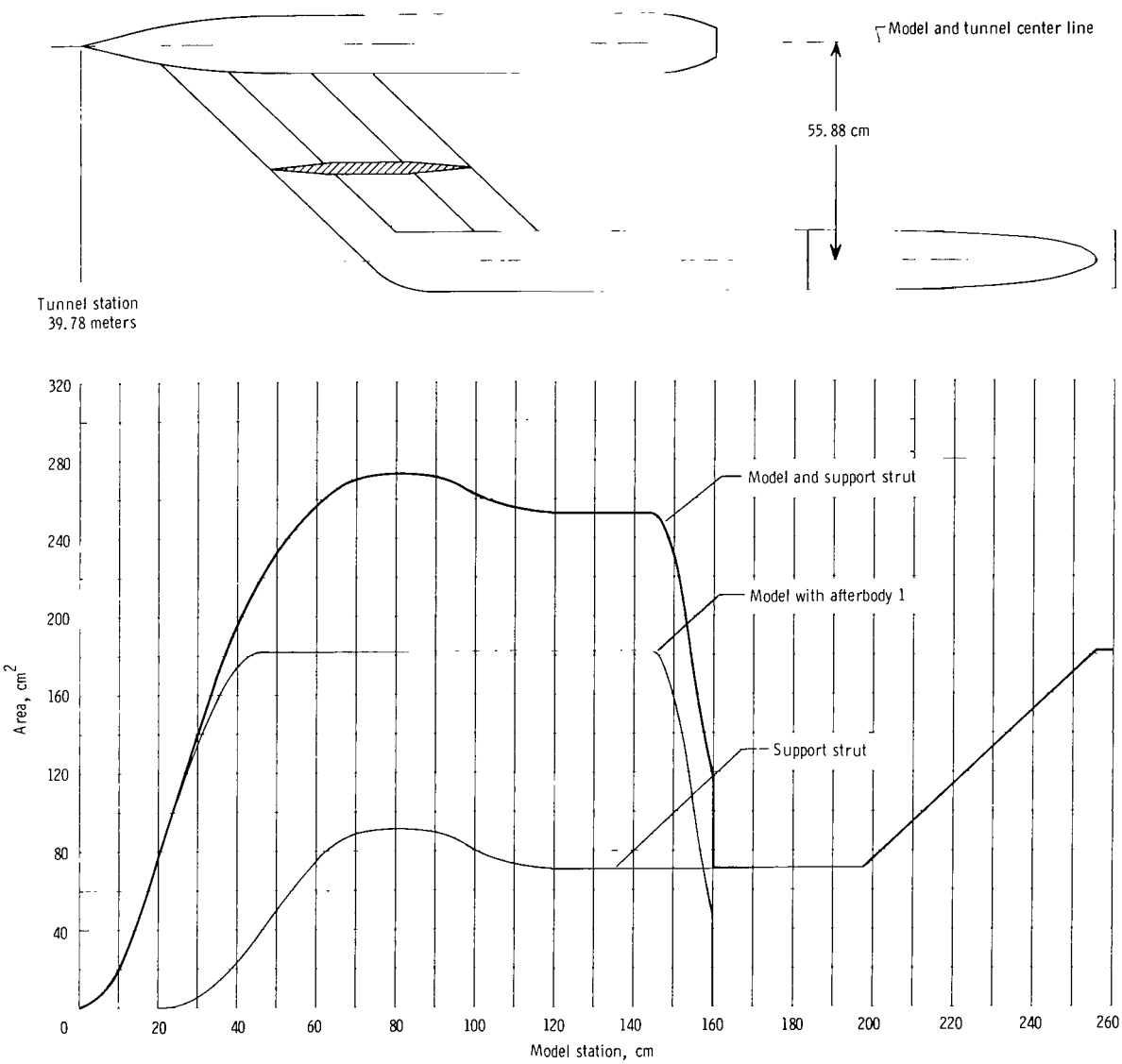

Figure 5.- Cross-sectional area distributions of model and support system.

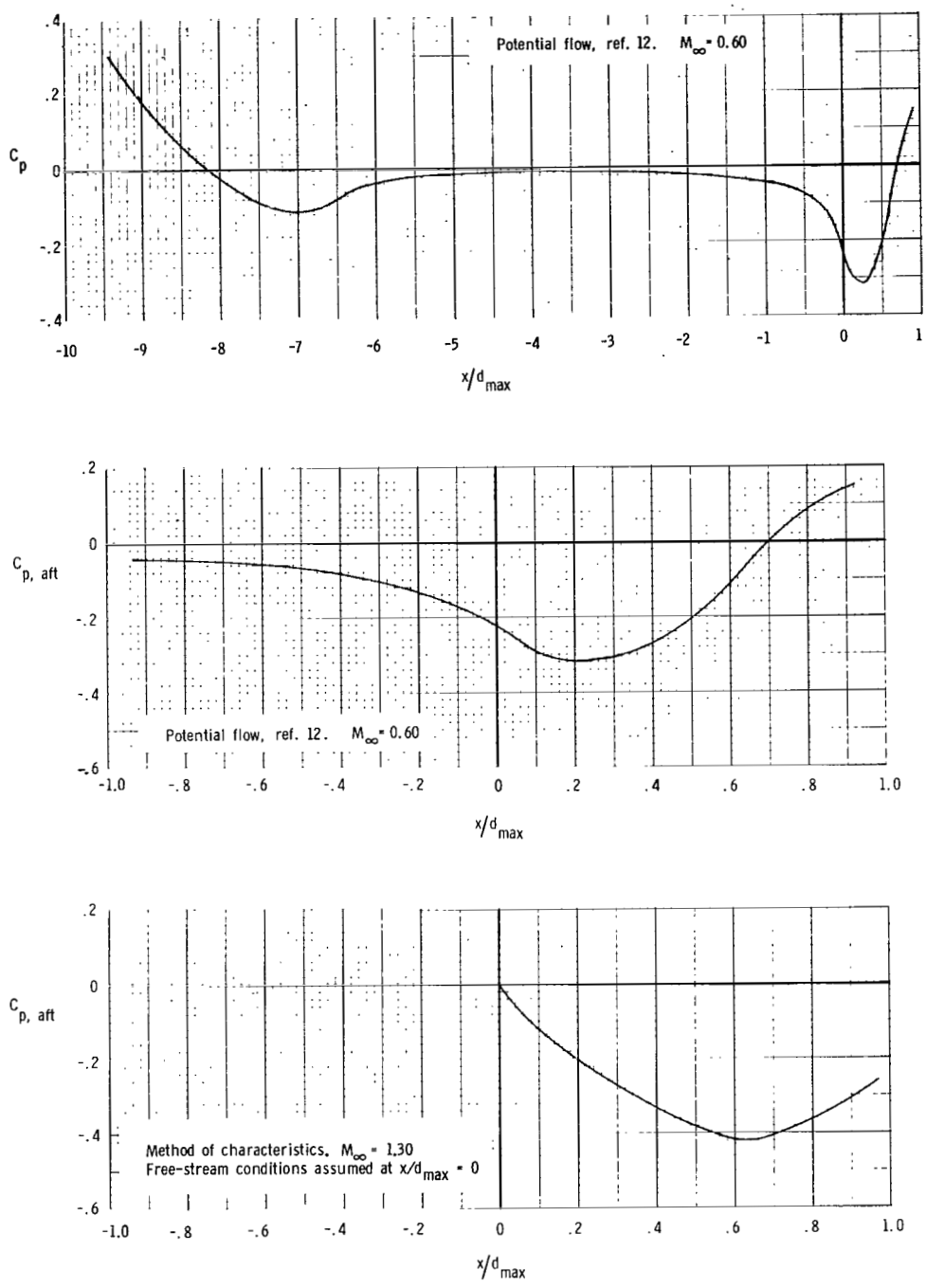

Figure 6.- Examples of theoretical pressure coefficient distributions. $\beta = 20^{o}$; $l/d_{max} = 1.0$.

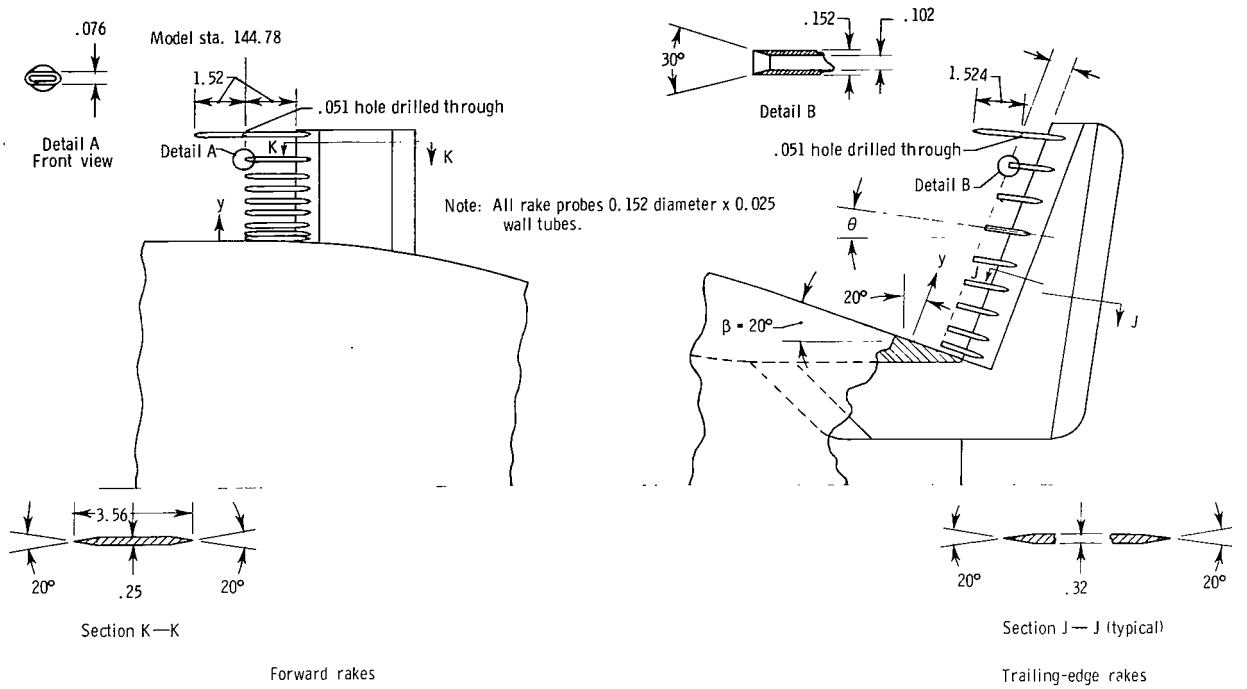

Forward rakes[a]	
Rake probe locations	
Probe	y
1	0.08
2	[b].25
3	[b].51
4	[b].89
5	[b]1.27
6	1.65
7	[b]2.03
8	2.54
9 (Static probe)	[b]3.30

Trailing-edge rakes		
Rake probe locations		
Probe	y	θ,deg
1	0.25	19.3
2	[b].76	16.8
3	[b]1.52	14.0
4	[b]2.29	11.8
5	[b]3.05	10.1
6	[b]4.06	8.3
7	5.08	7.0
8	[b]6.10	5.9
9 (Static Probe)	7.11	5.1

[a]Forward rakes located at angles of $\Phi = 0^{\circ}$, 135°, 157.5°, and 180°.
[b]Boundary-layer temperatures were measured at these values of y for the rakes located at angles $\Phi = 0^{\circ}$ and 180°.

Figure 7.- Boundary-layer rakes. (All linear dimensions are in centimeters unless otherwise noted.) Note: ϕ measured clockwise when the model is viewed from the rear; 0° is at the top of the model.

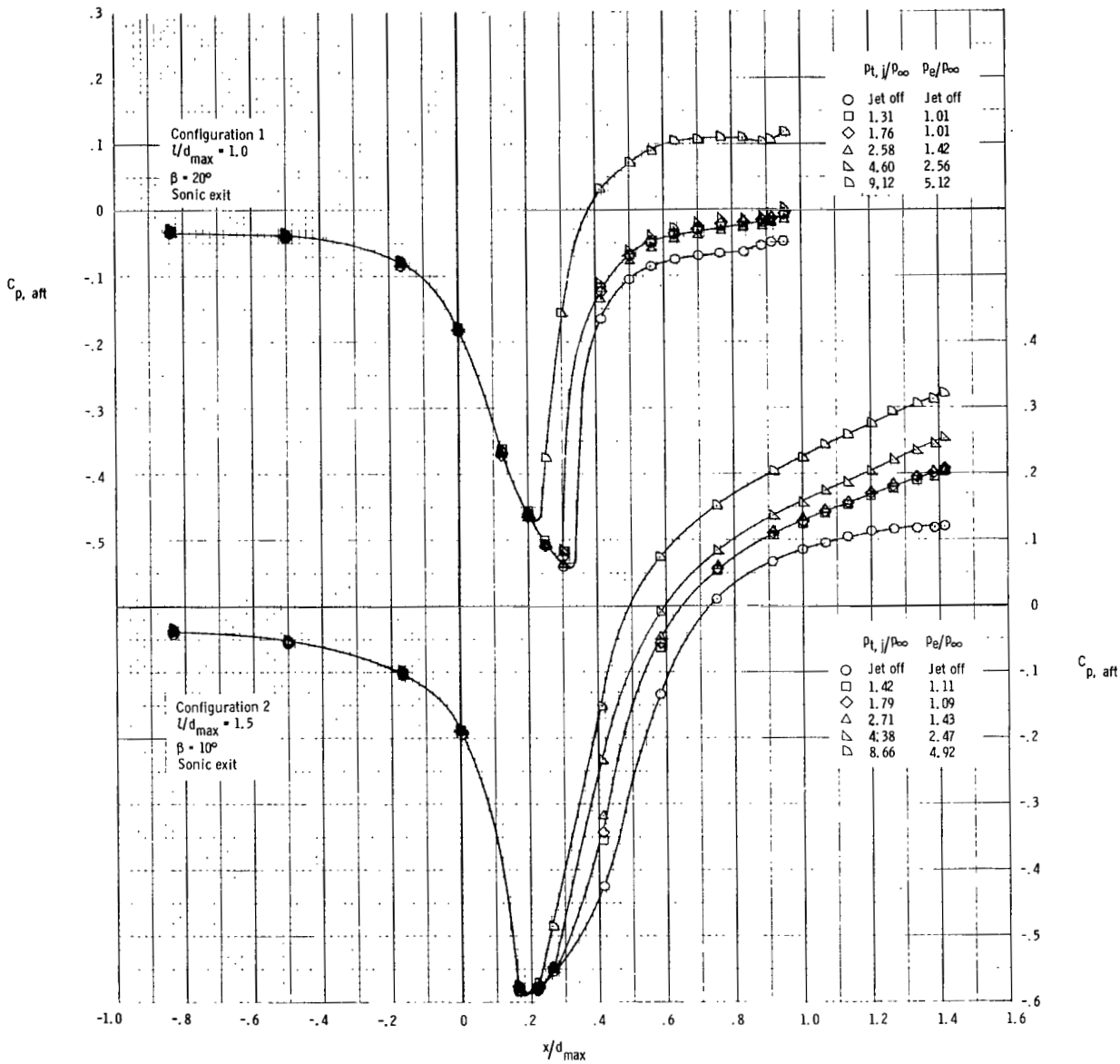

Figure 8.- Examples of jet interference on the afterbody pressures. $\gamma_j = 1.28$; $T_{t,j} = 810$ K; $R_j = 384$ J/kg-K; $M_\infty = 0.95$.

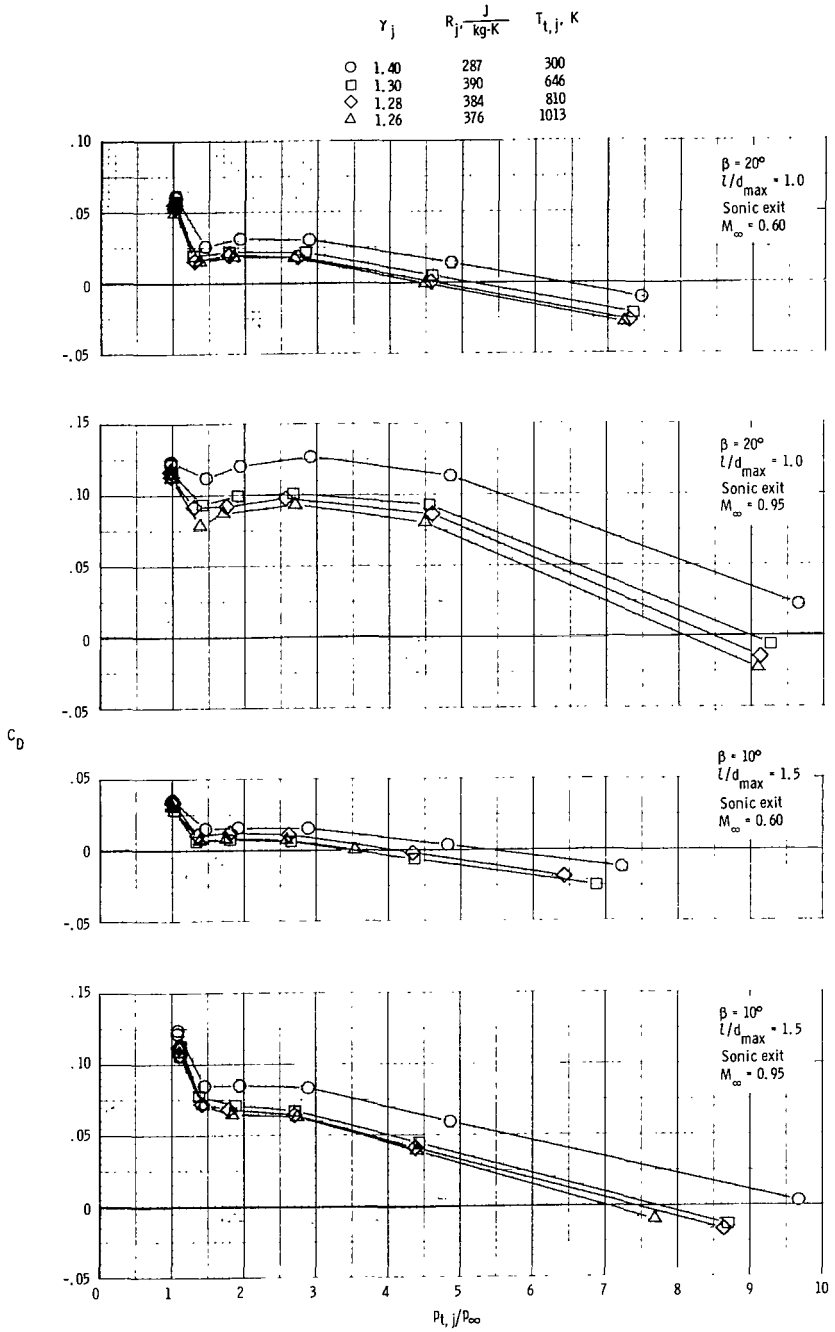

Figure 9.- Examples of afterbody drag as a function of jet total pressure ratio for the various jet exhaust gases.

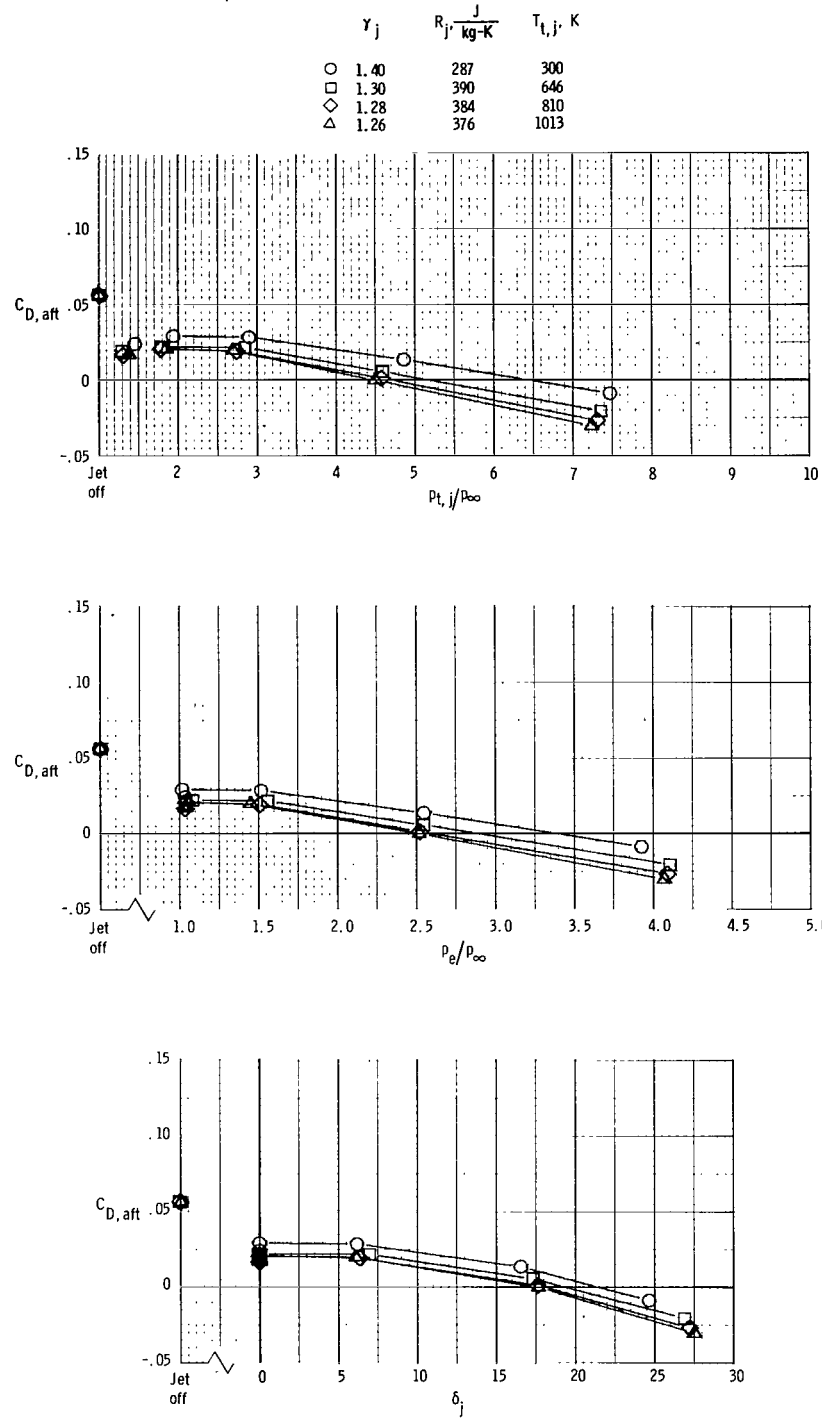

(a) $M_\infty = 0.60$.

Figure 10.- Corrected afterbody drag coefficient as a function of $p_{t,j}/p_\infty$, p_e/p_∞, and δ_j. $\beta = 20^o$; sonic exit.

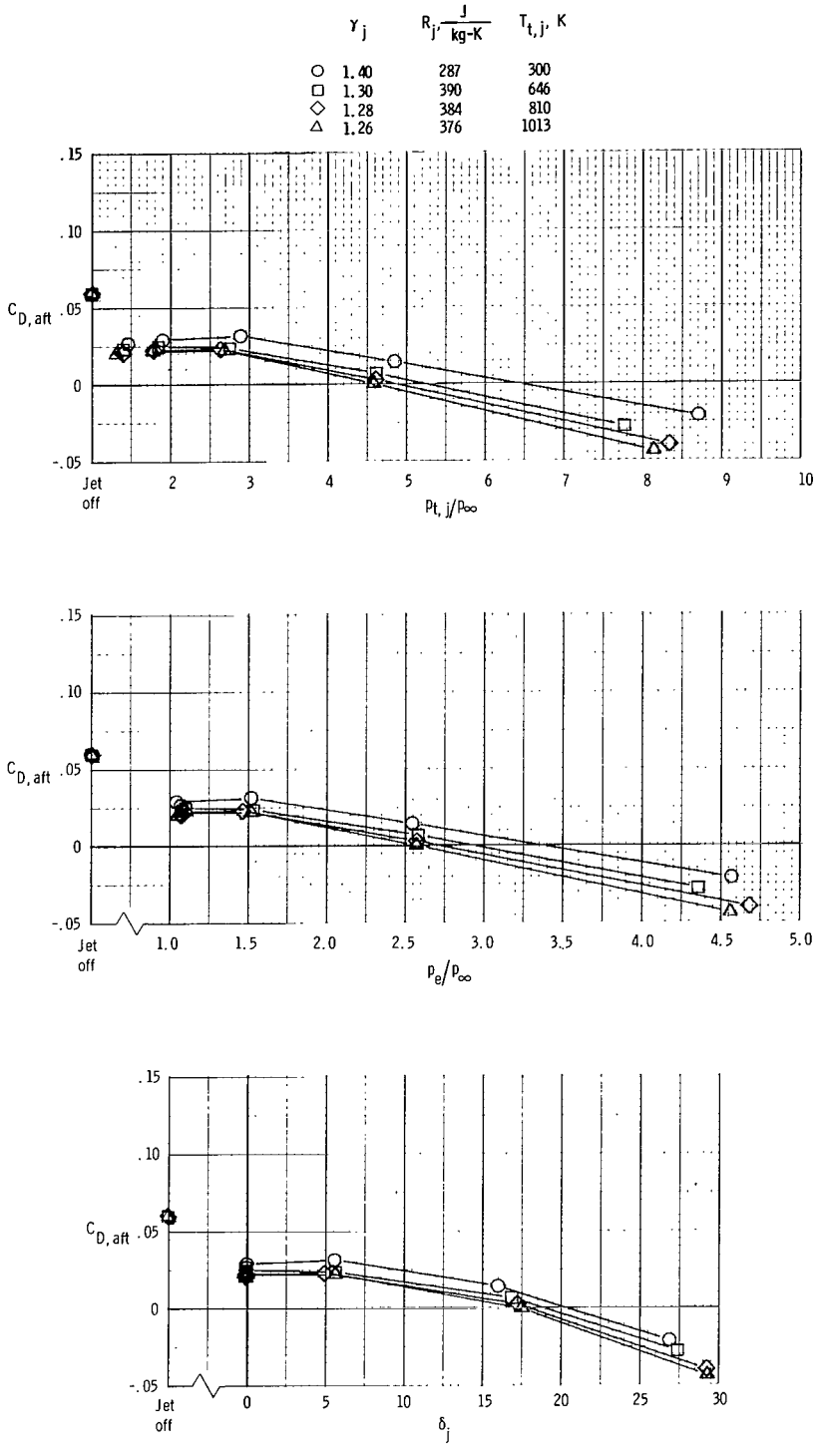

(b) $M_\infty = 0.80$.

Figure 10.- Continued.

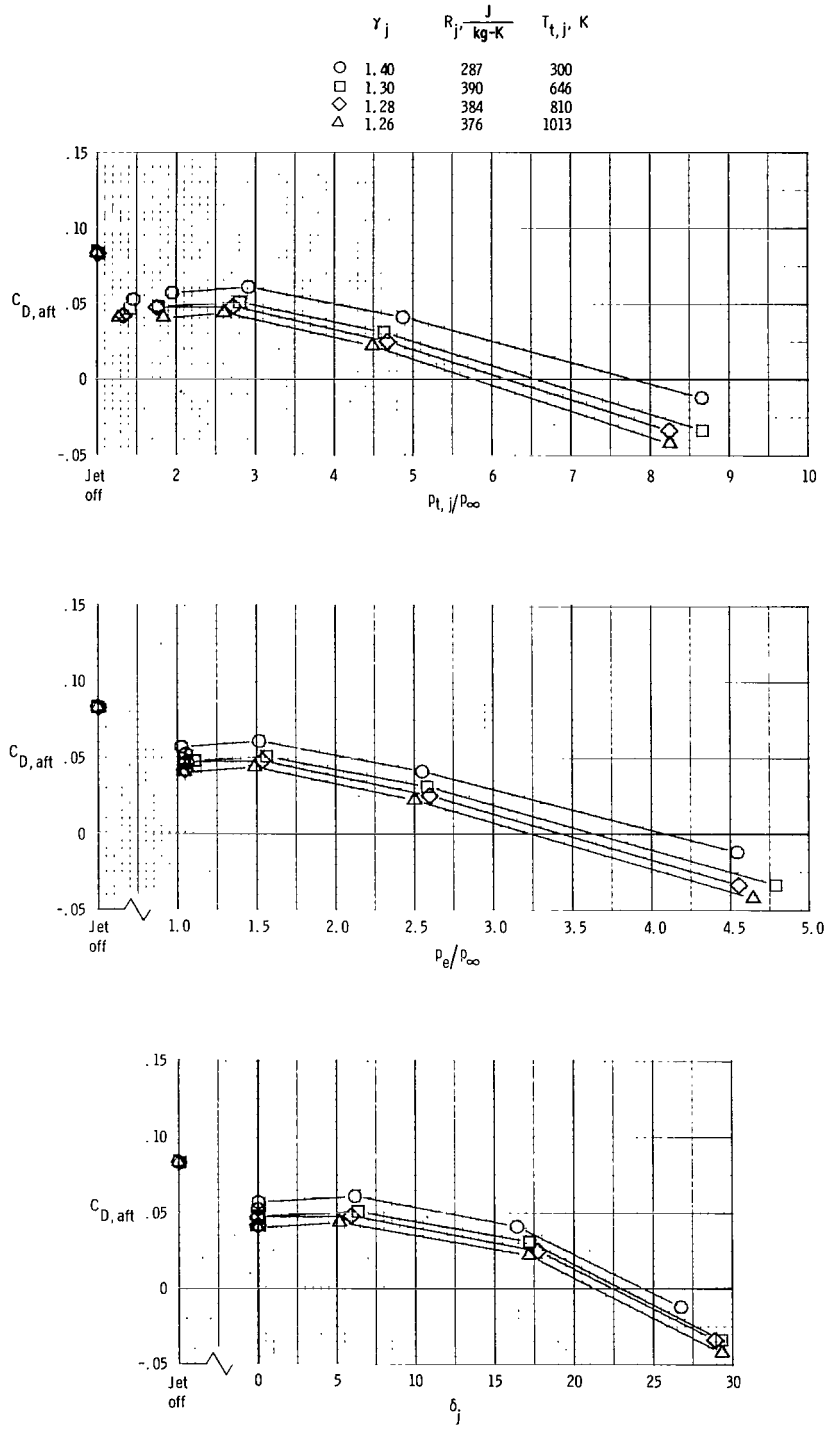

(c) $M_\infty = 0.90$.

Figure 10.- Continued.

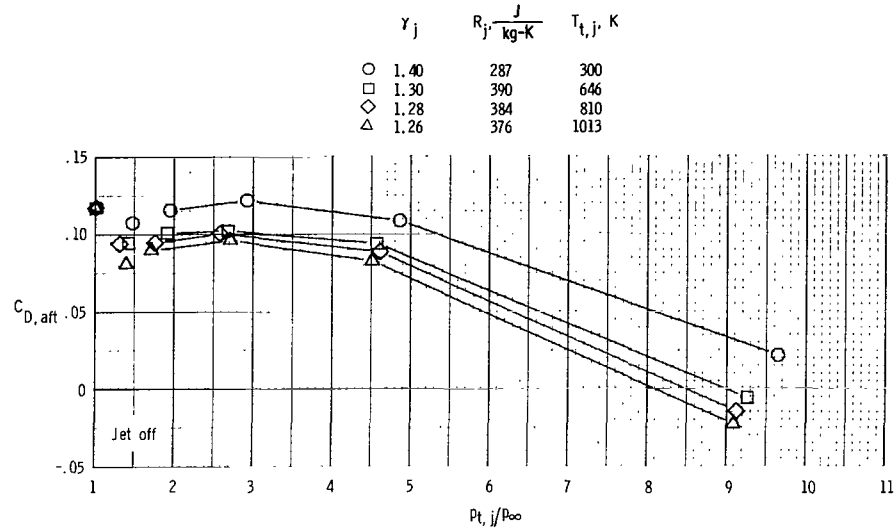

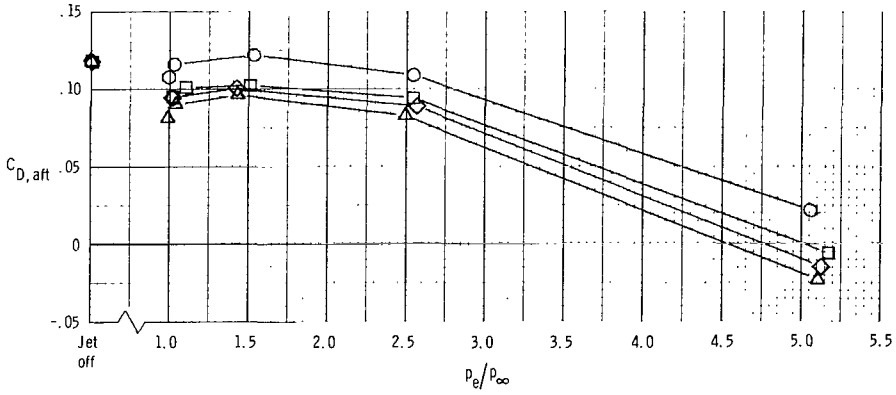

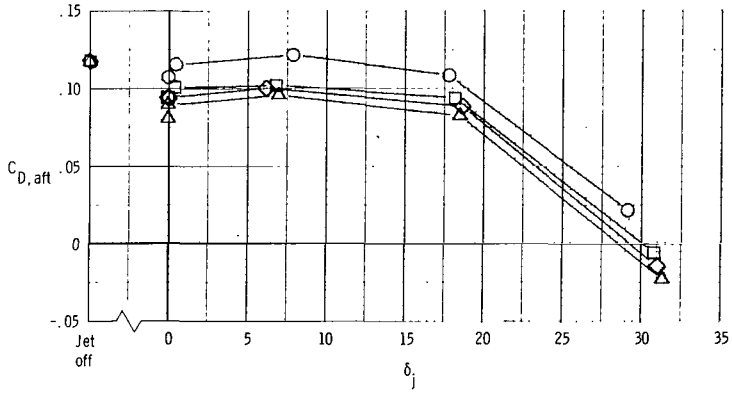

(d) $M_\infty = 0.95$.

Figure 10.- Continued.

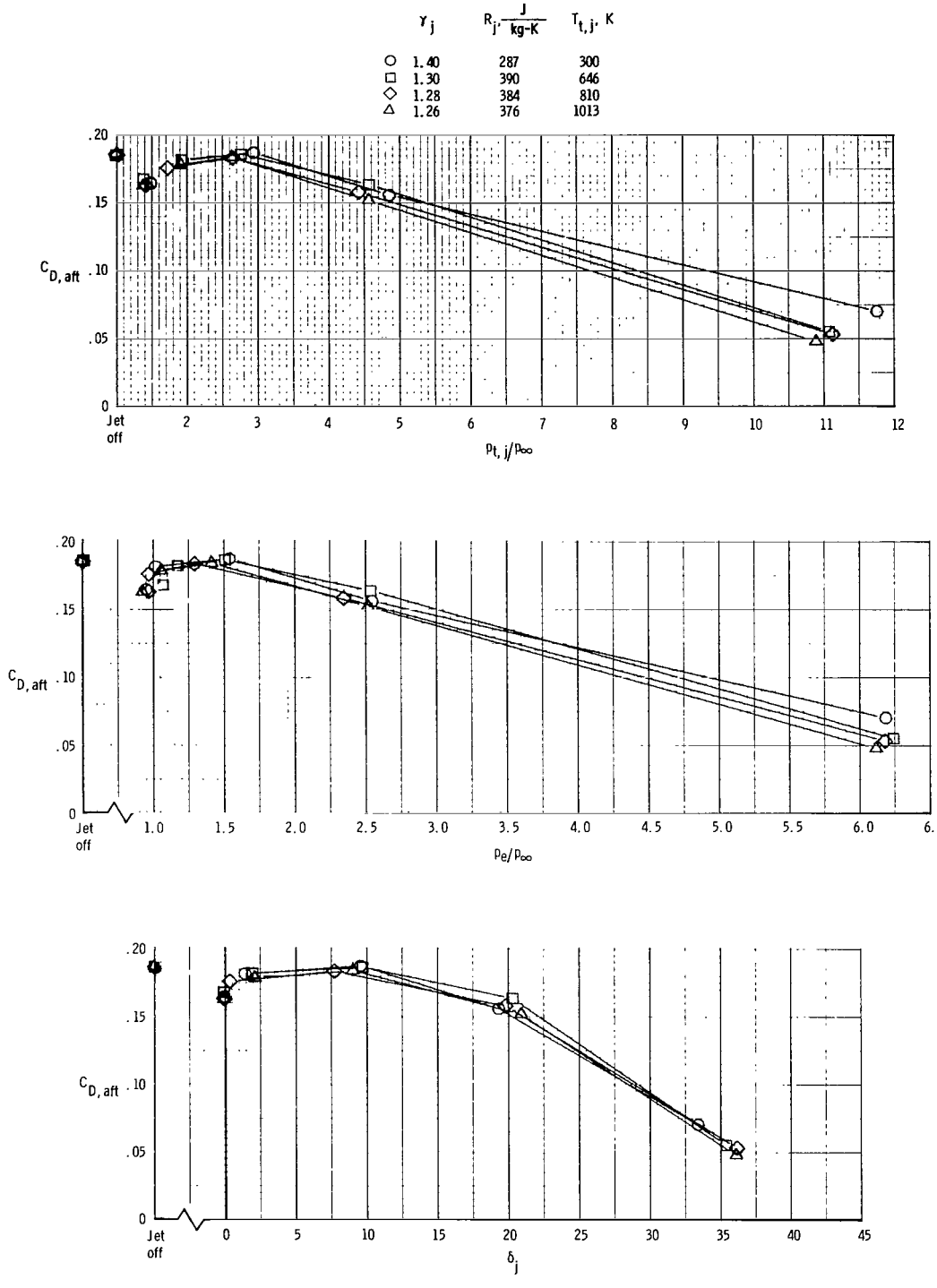

(e) $M_\infty = 1.20$.

Figure 10.- Concluded.

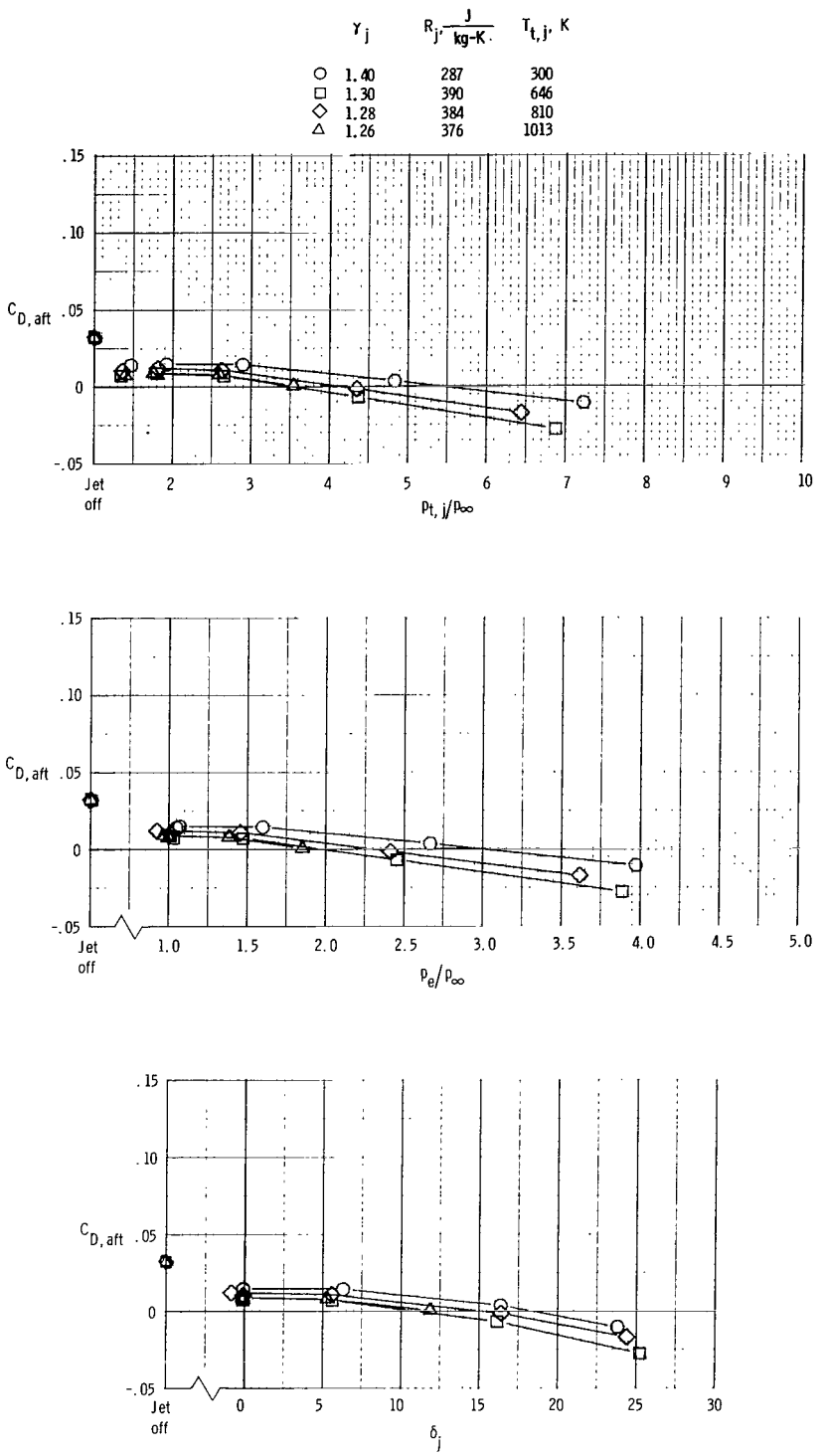

(a) $M_\infty = 0.60$.

Figure 11.- Corrected afterbody drag coefficient as a function of $p_{t,j}/p_\infty$, p_e/p_∞, and δ_j. $\beta = 10^o$; sonic exit.

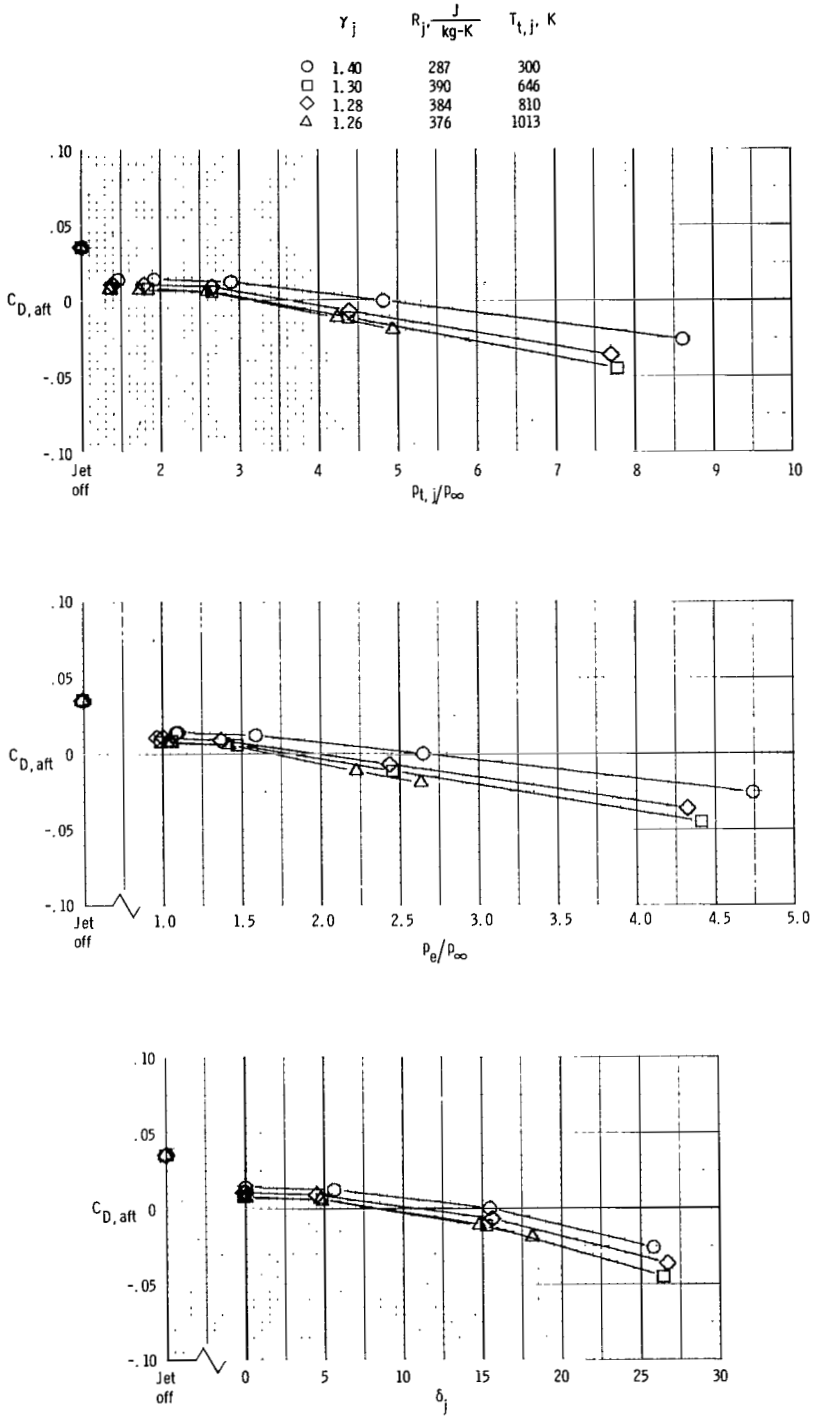

(b) $M_\infty = 0.80$.

Figure 11.- Continued.

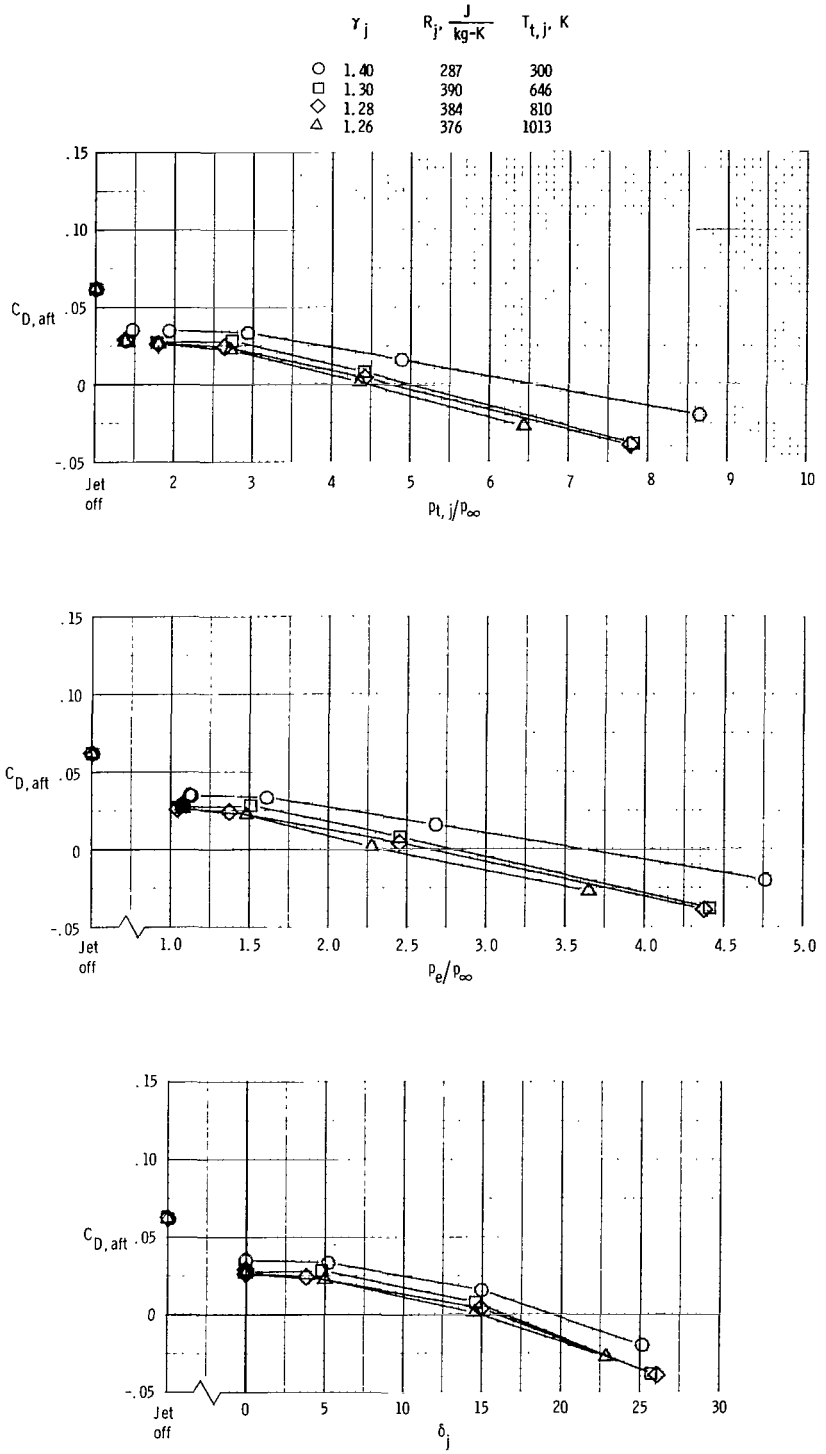

(c) $M_\infty = 0.90$.

Figure 11.- Continued.

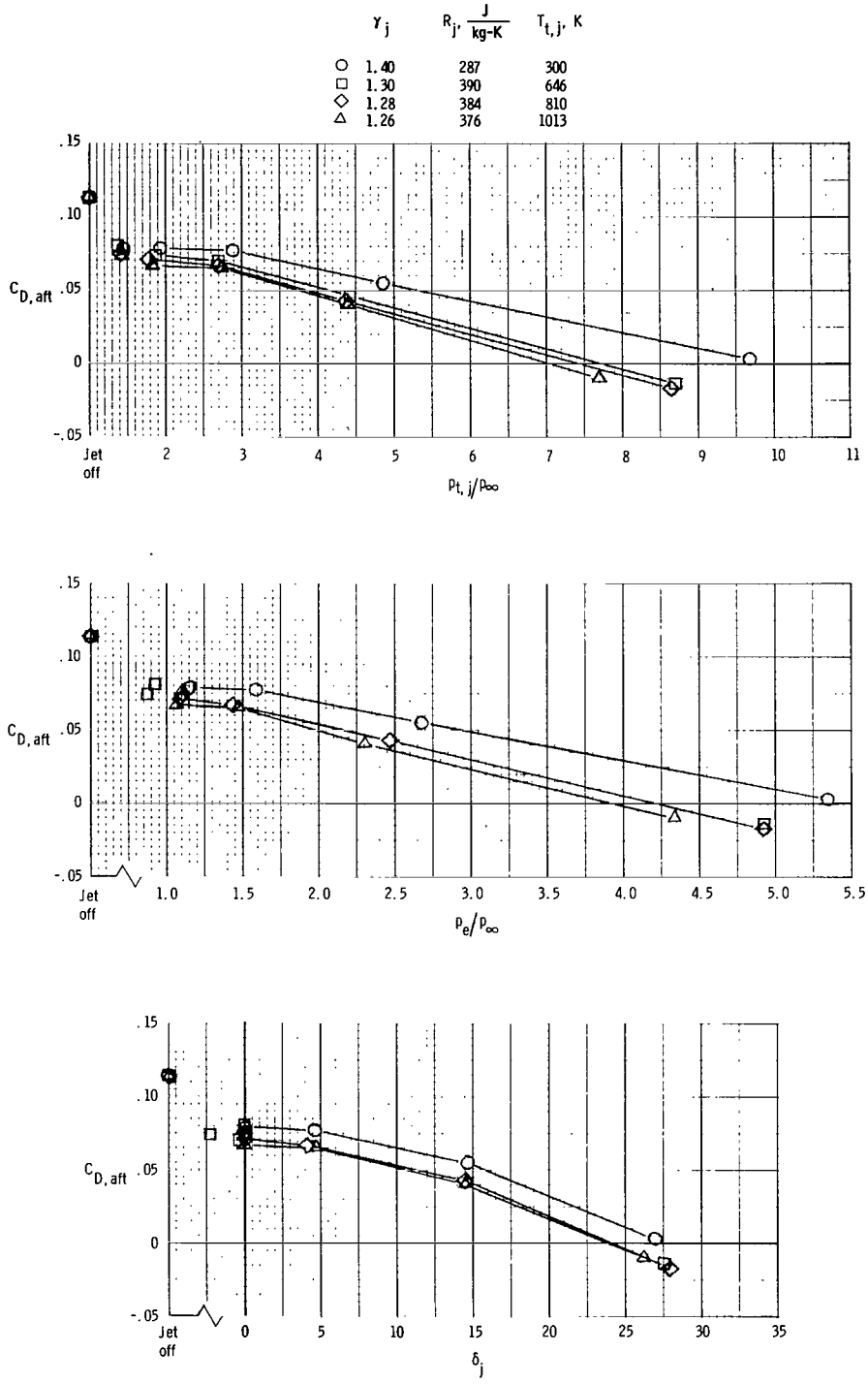

(d) $M_\infty = 0.95$.

Figure 11.- Continued.

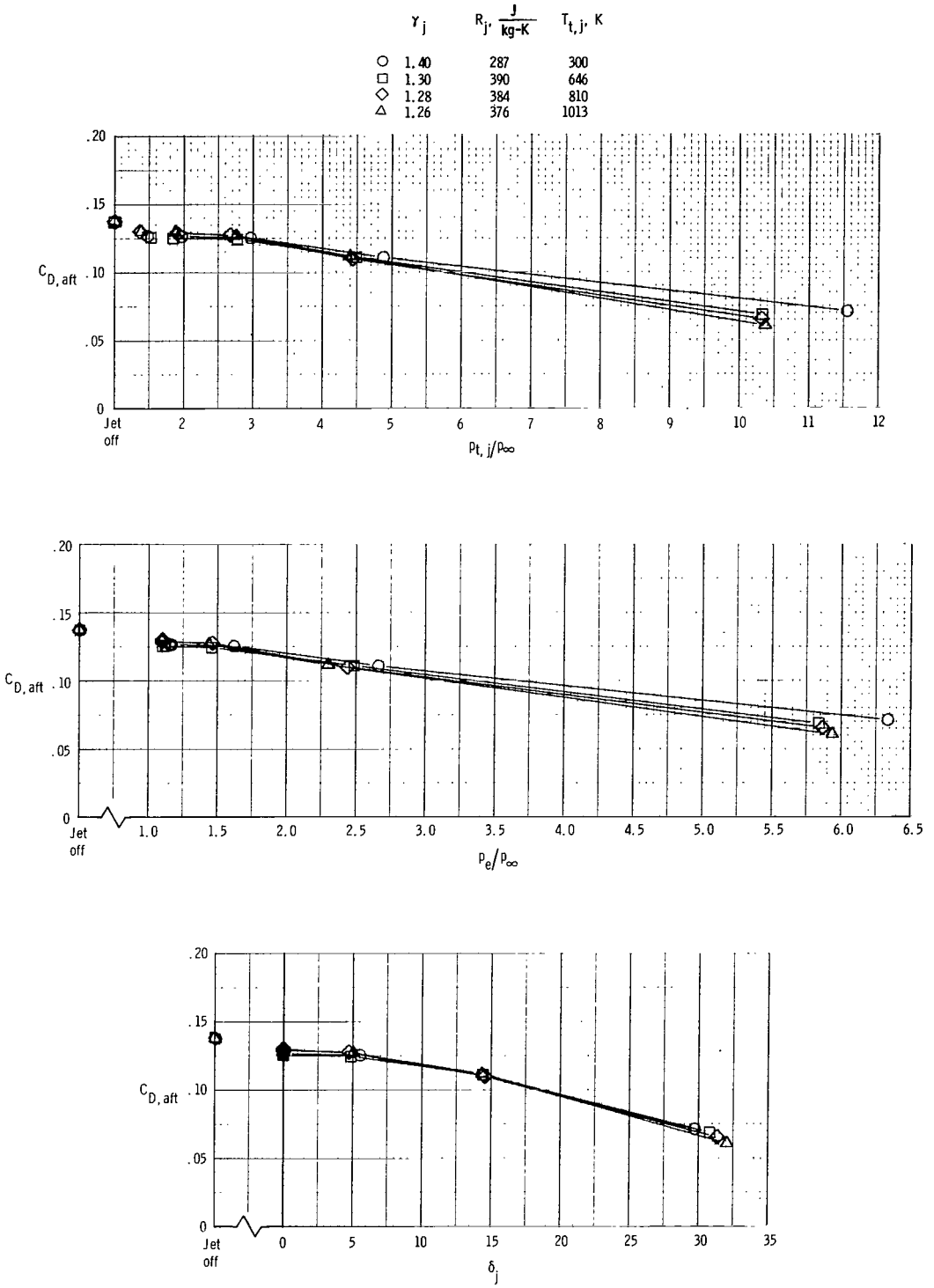

(e) $M_\infty = 1.20$.

Figure 11.- Concluded.

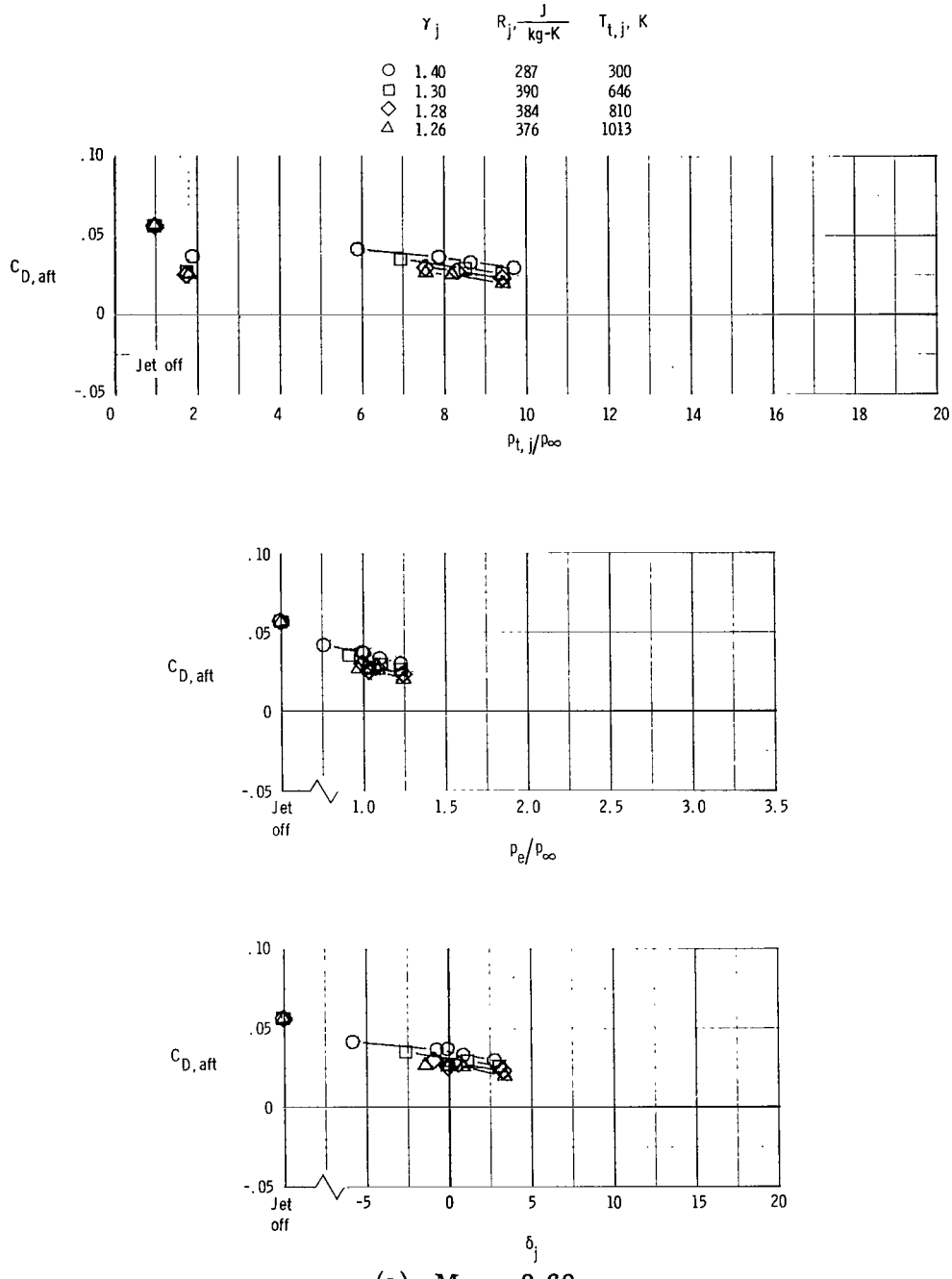

(a) $M_\infty = 0.60$.

Figure 12.- Corrected afterbody drag coefficient as a function of $p_{t,j}/p_\infty$, p_e/p_∞, and δ_j. $\beta = 20^o$; $M_e = 2$.

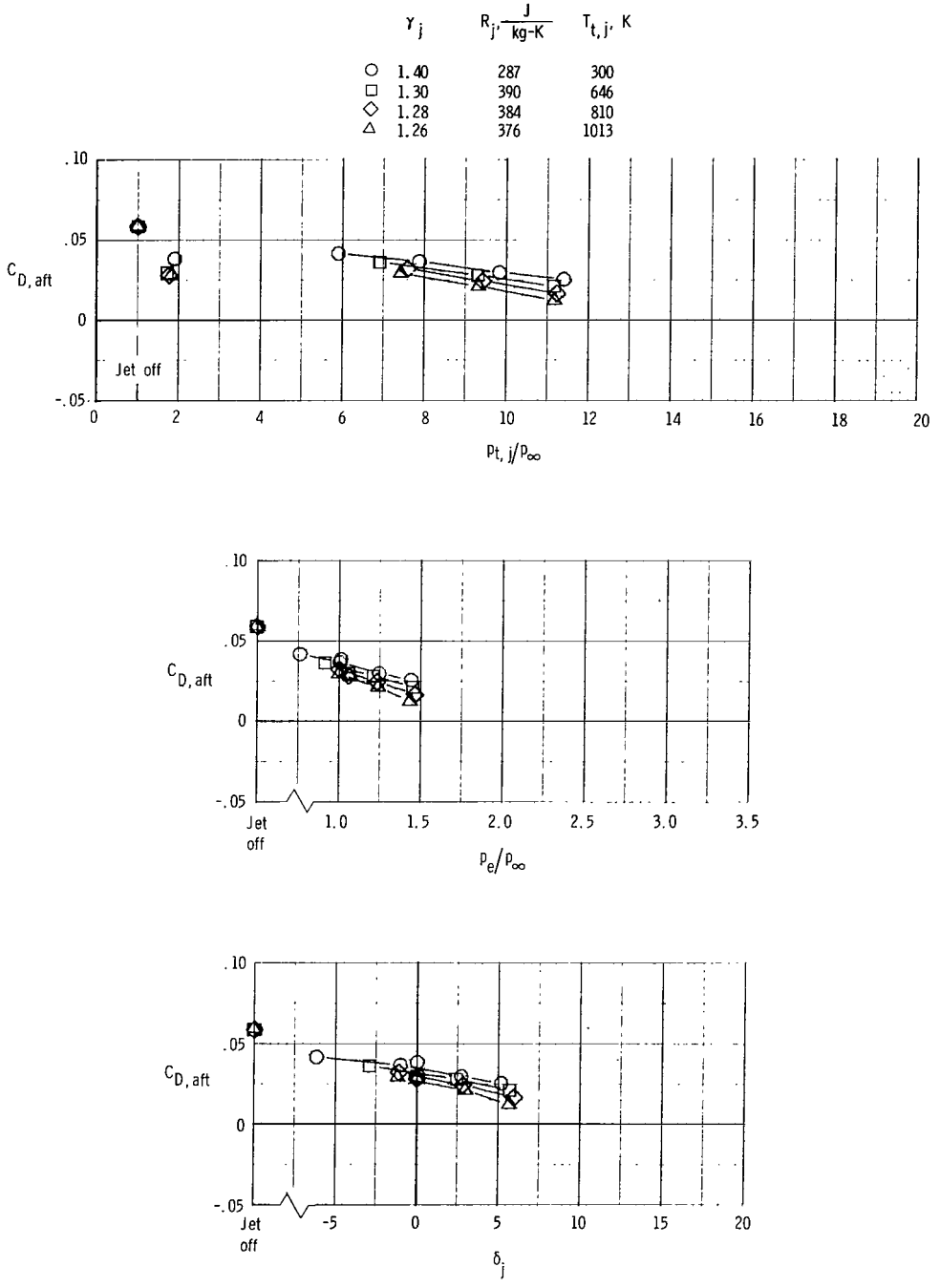

(b) $M_\infty = 0.80$.

Figure 12.- Continued.

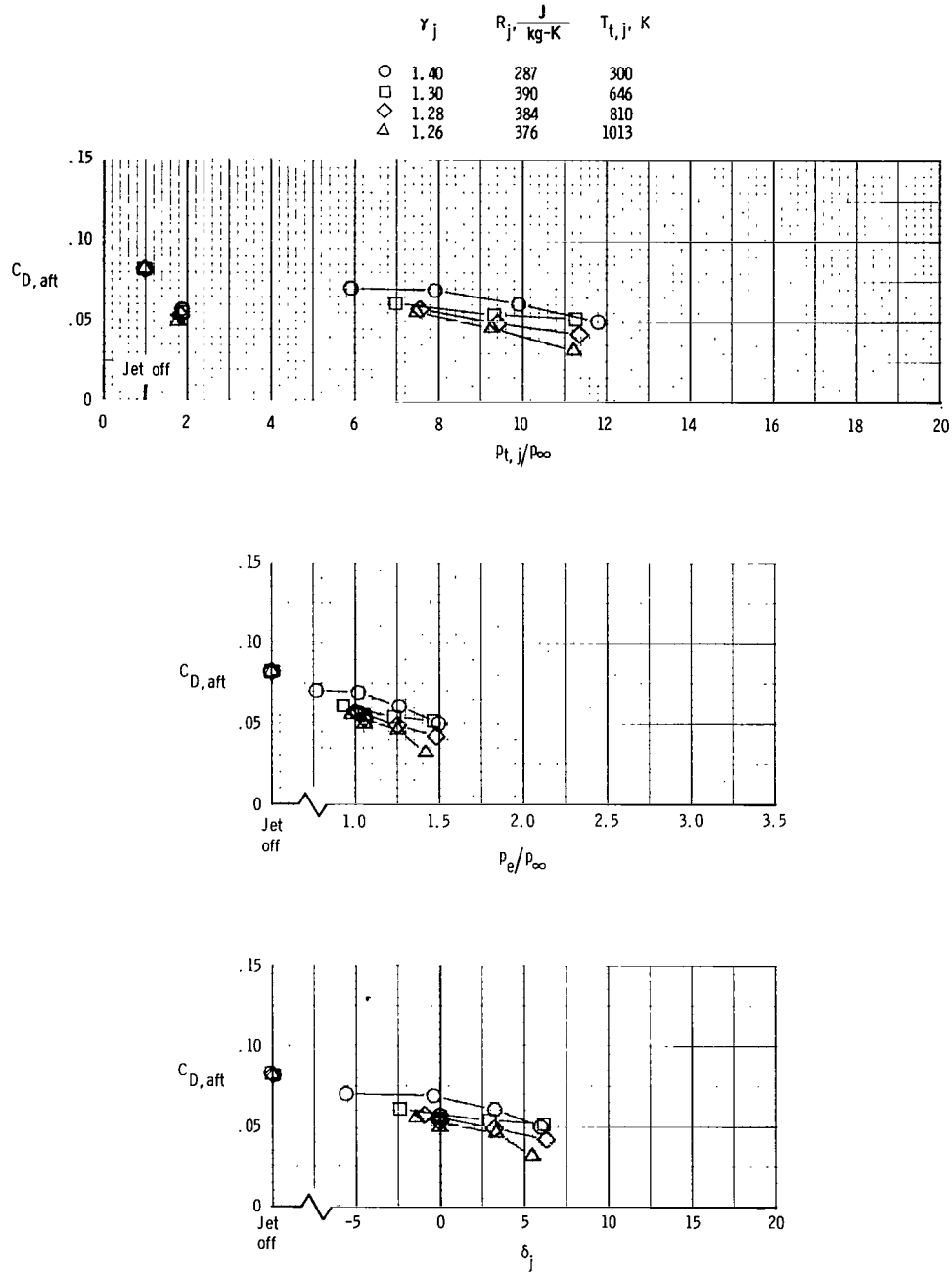

(c) $M_\infty = 0.90$.

Figure 12.- Continued.

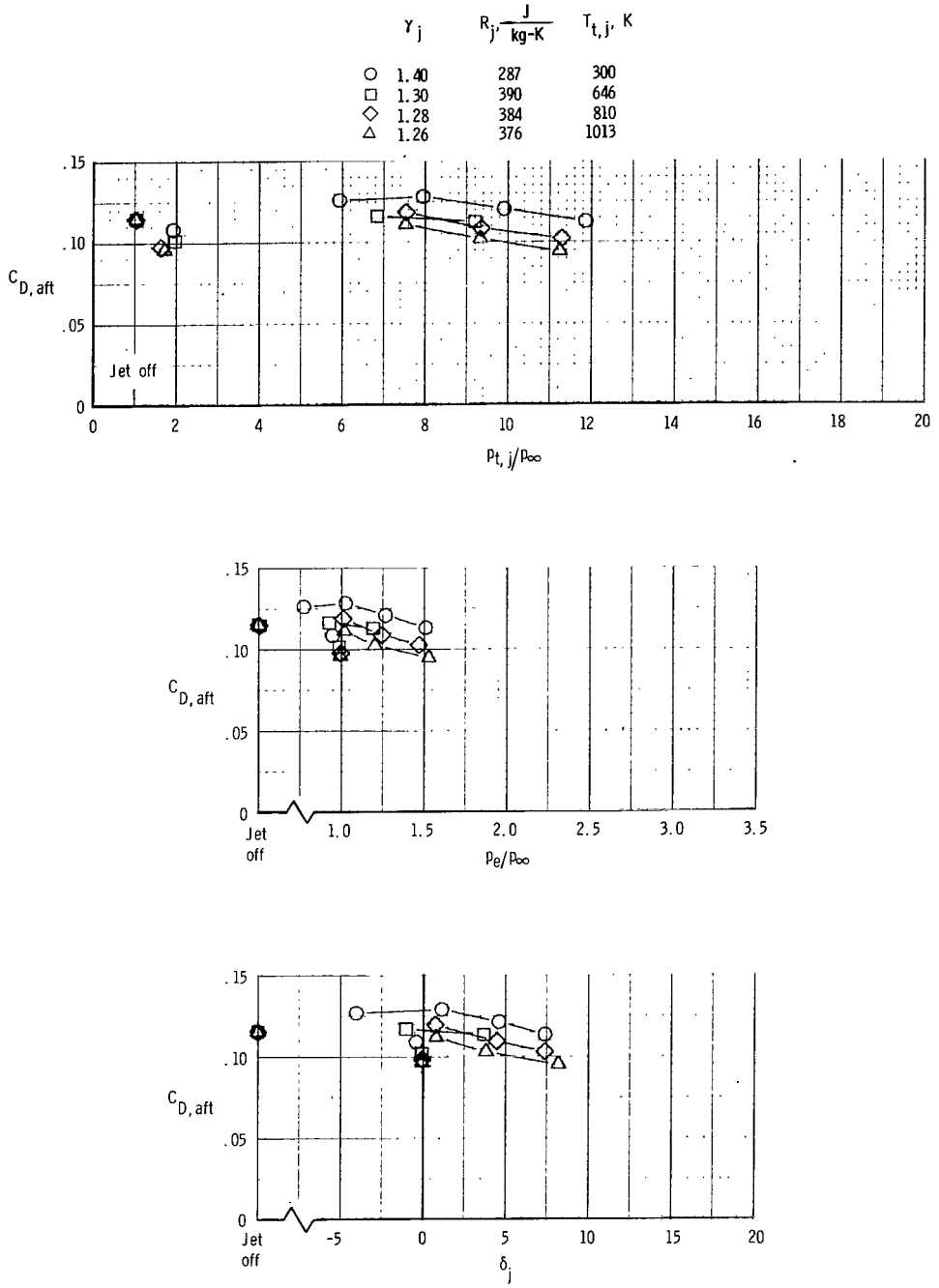

(d) $M_\infty = 0.95$.

Figure 12.- Continued.

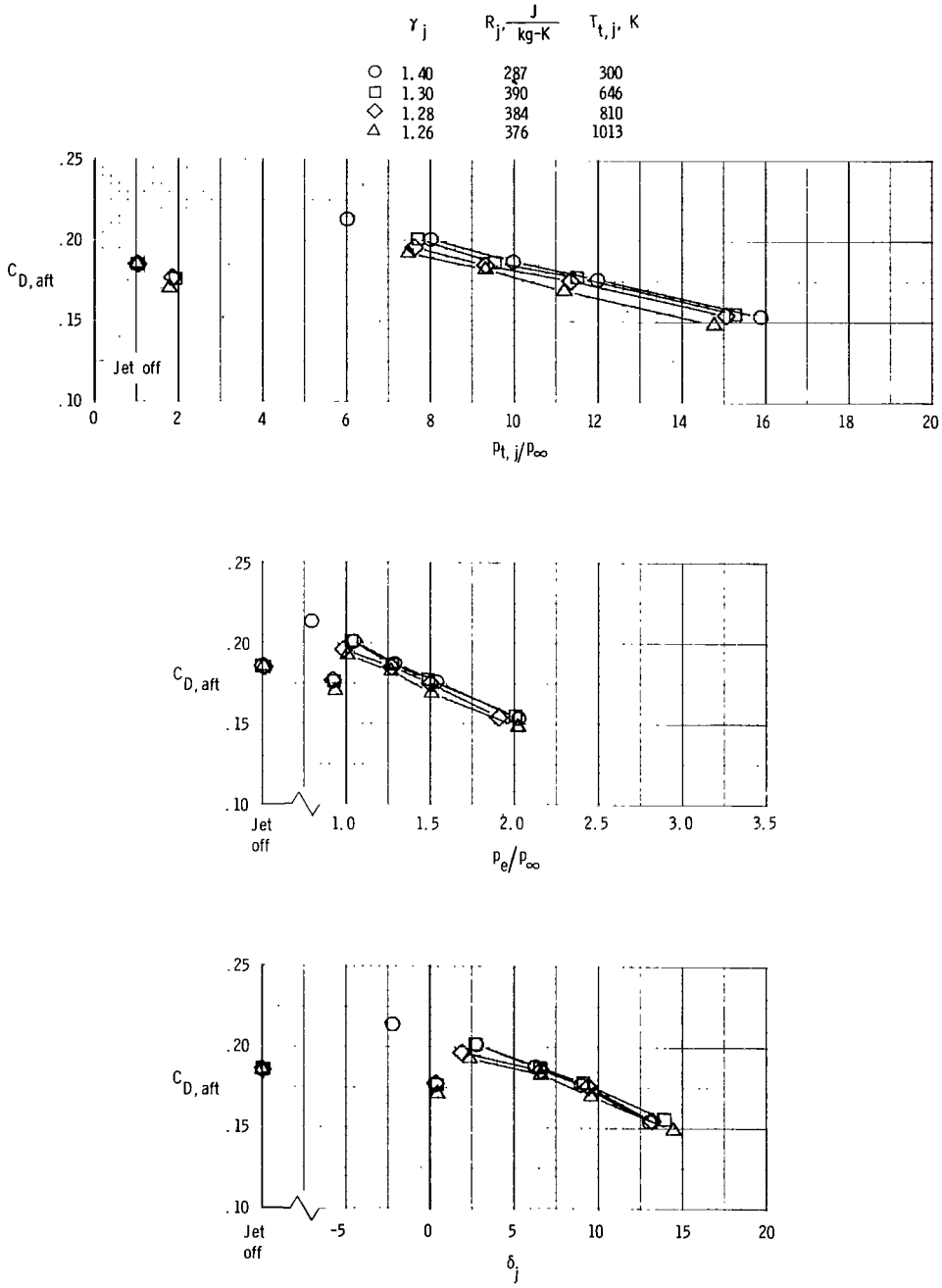

(e) $M_\infty = 1.20$.

Figure 12.- Concluded.

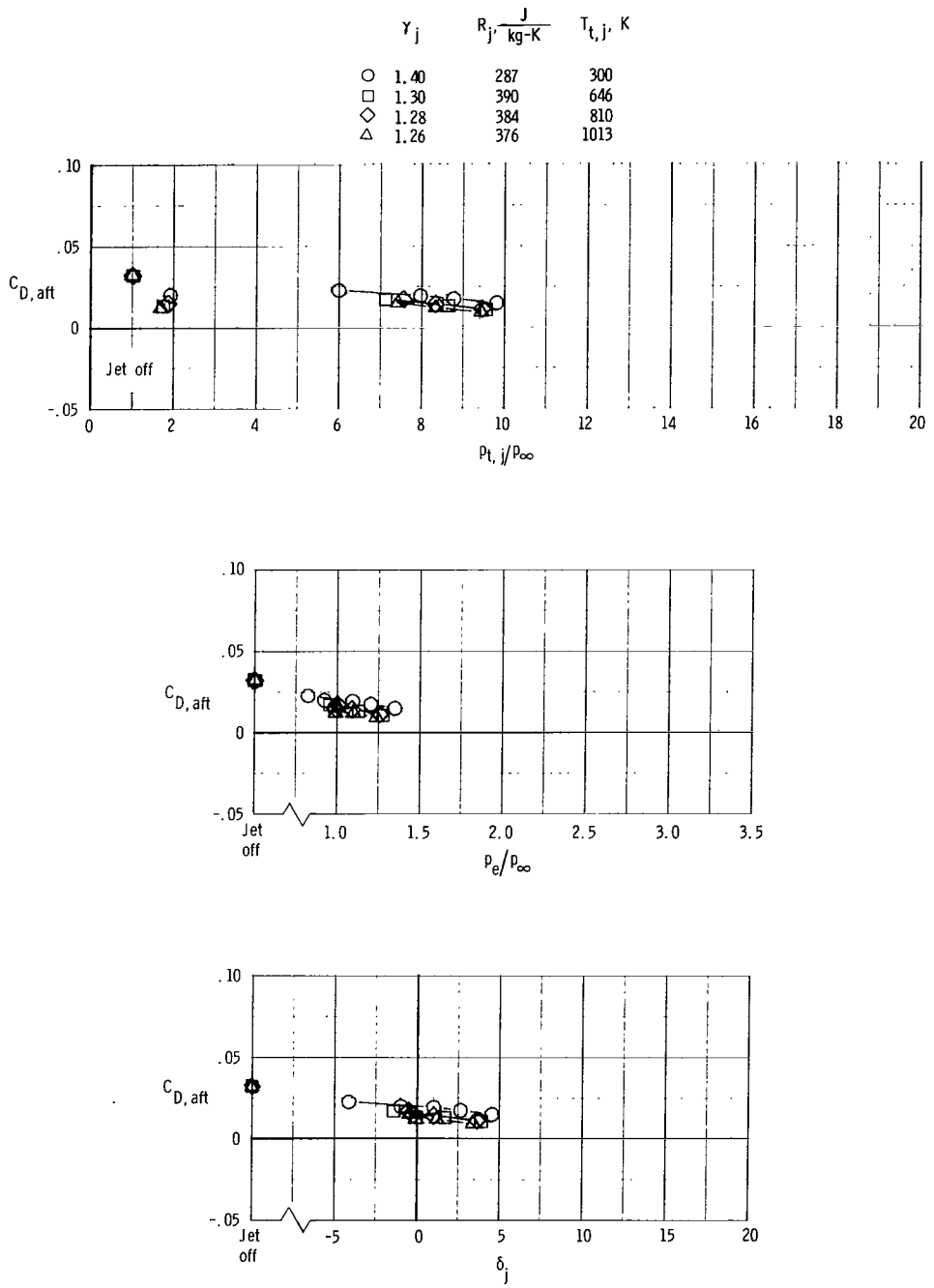

(a) $M_\infty = 0.60$.

Figure 13.- Corrected afterbody drag coefficient as a function of $p_{t,j}/p_\infty$, p_e/p_∞, and δ_j. $\beta = 10^o$; $M_e = 2$.

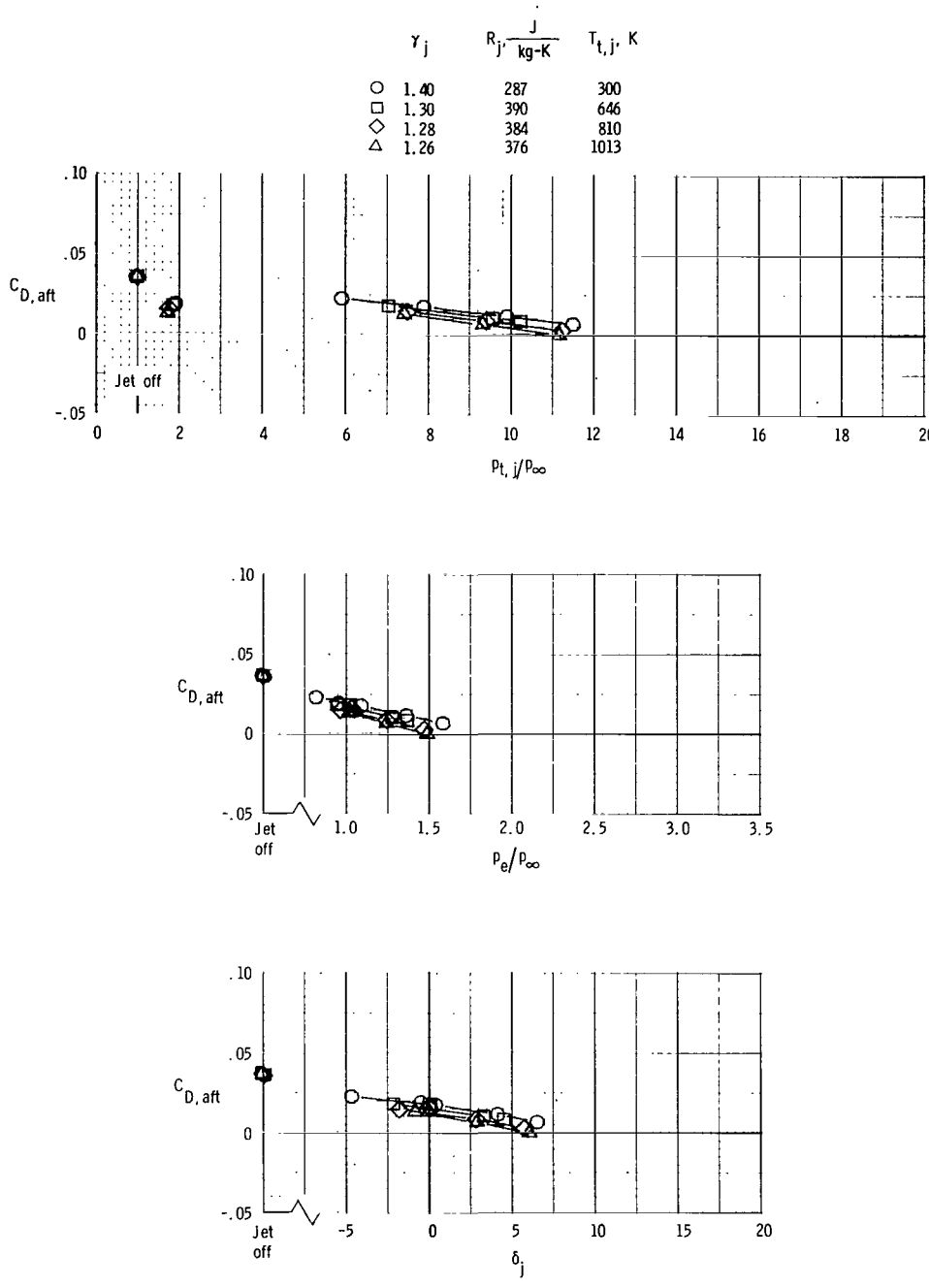

(b) $M_\infty = 0.80$.

Figure 13.- Continued.

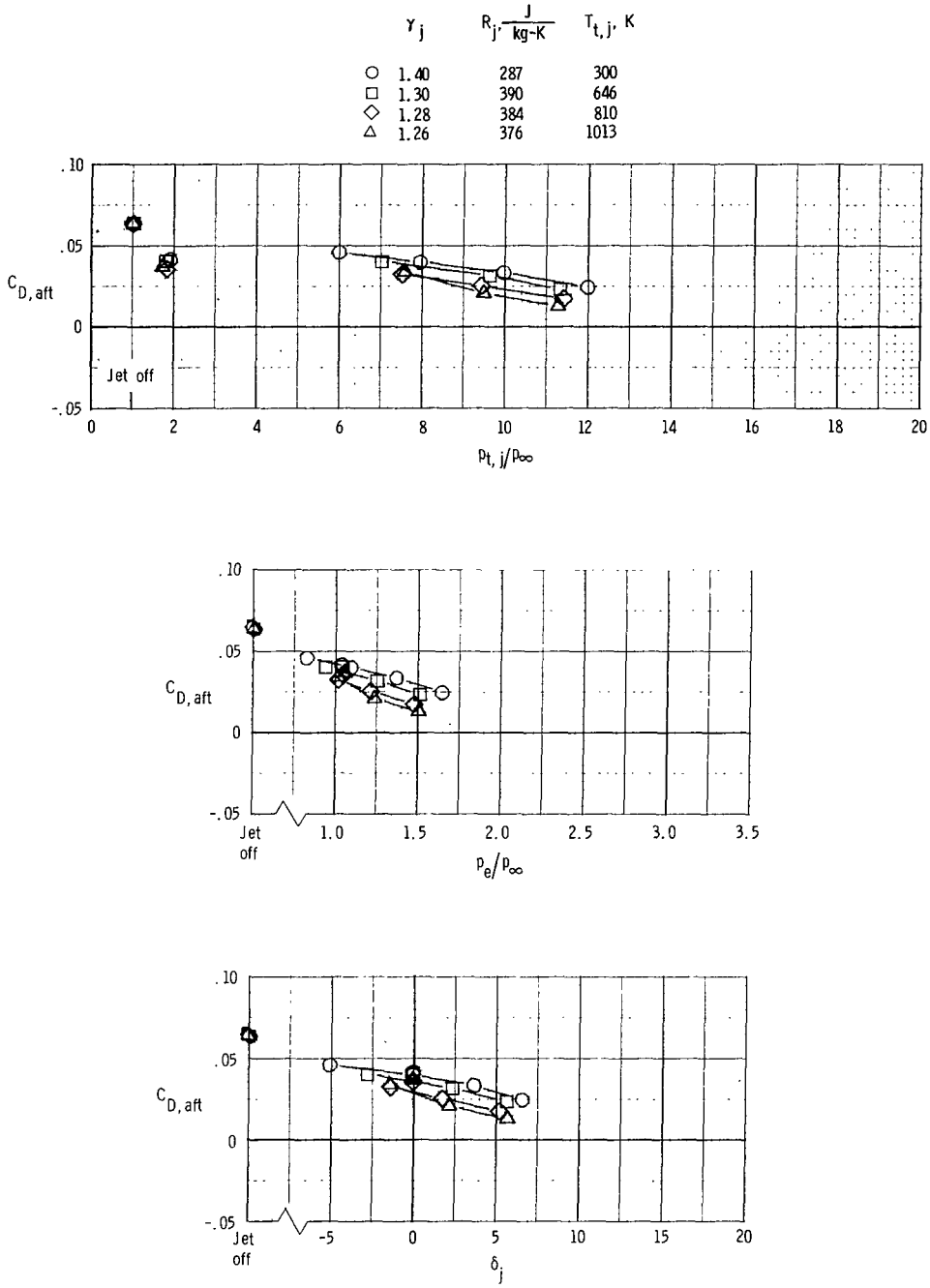

(c) $M_\infty = 0.90$.

Figure 13.- Continued.

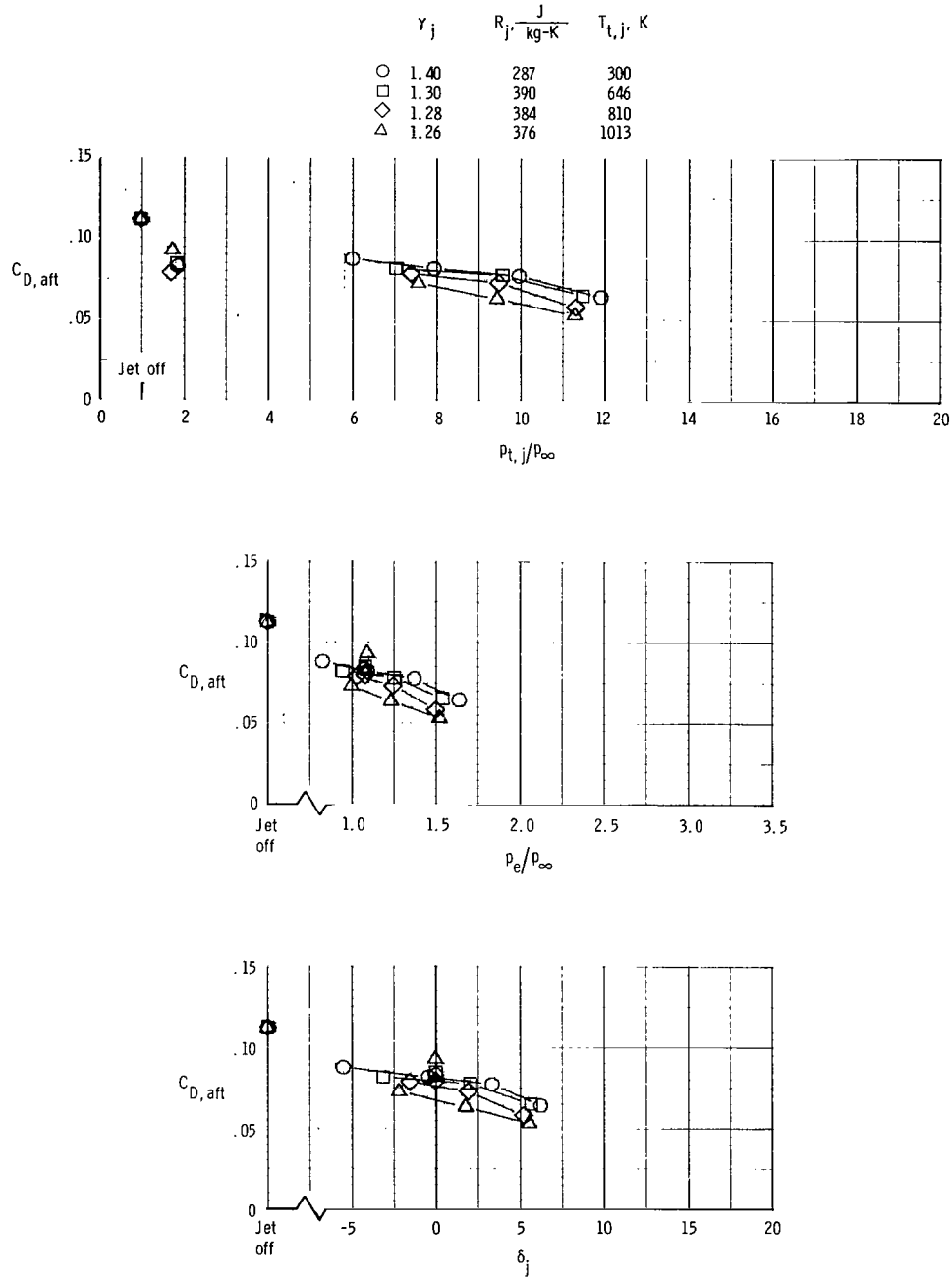

(d) $M_\infty = 0.95$.

Figure 13.- Continued.

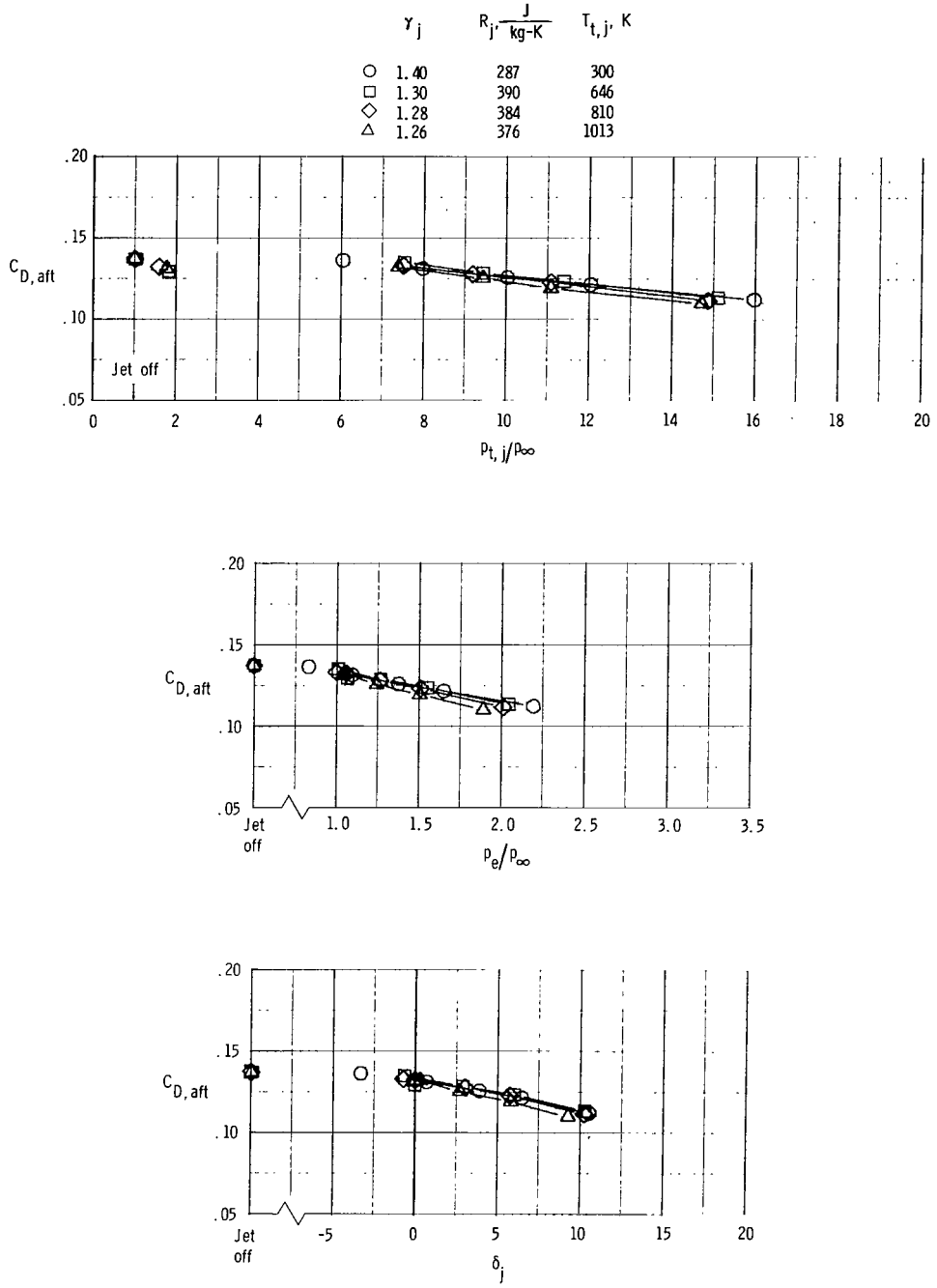

(e) $M_\infty = 1.20$.

Figure 13.- Concluded.

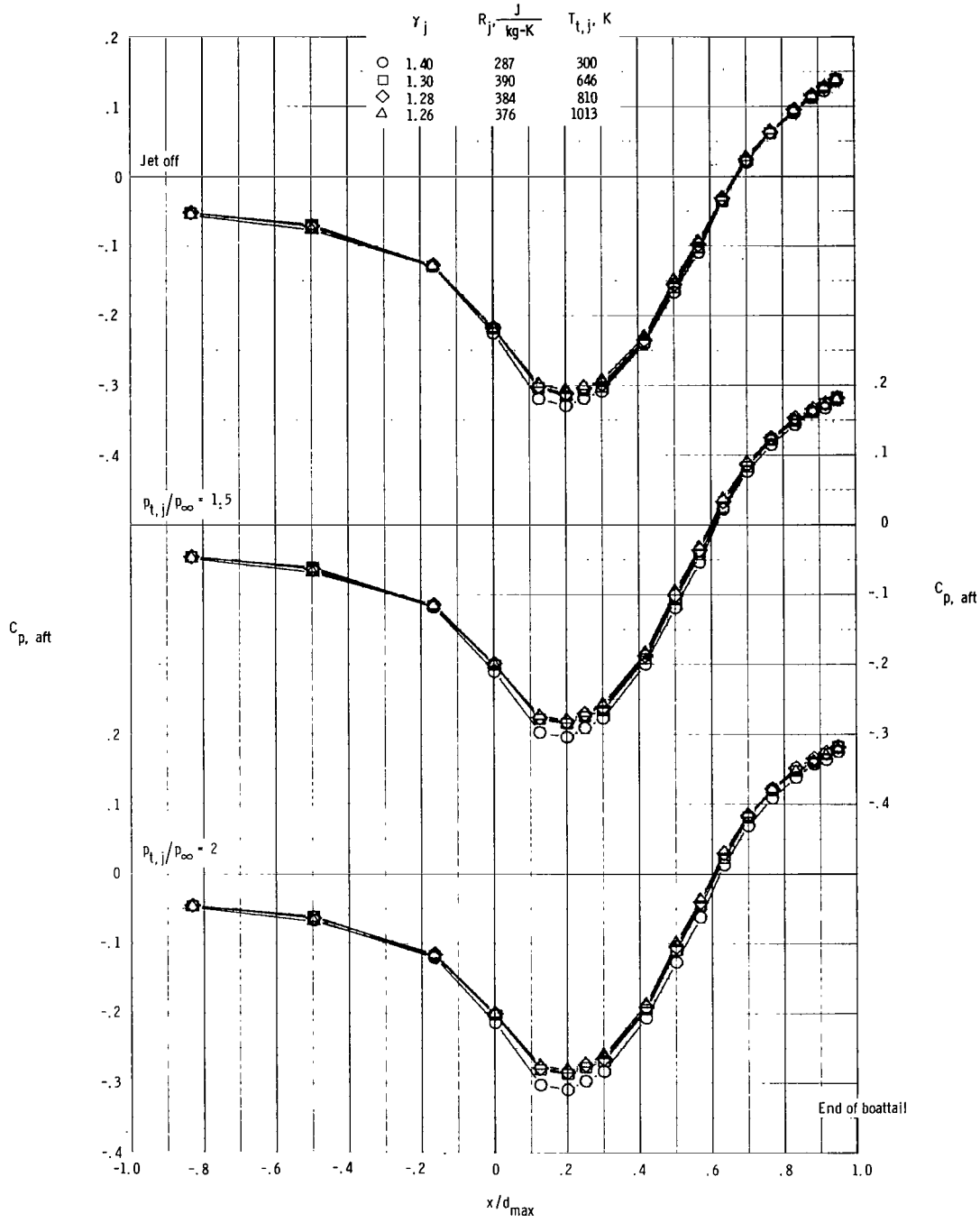

(a) $M_\infty = 0.60$; $p_{t,j}/p_\infty$ = Jet off to 2.

Figure 14.- Afterbody pressure coefficient distributions for each of the four jet exhaust gases. $\beta = 20^o$; sonic exit. (Each pressure coefficient is interpolated for exact values of jet total pressure ratio.)

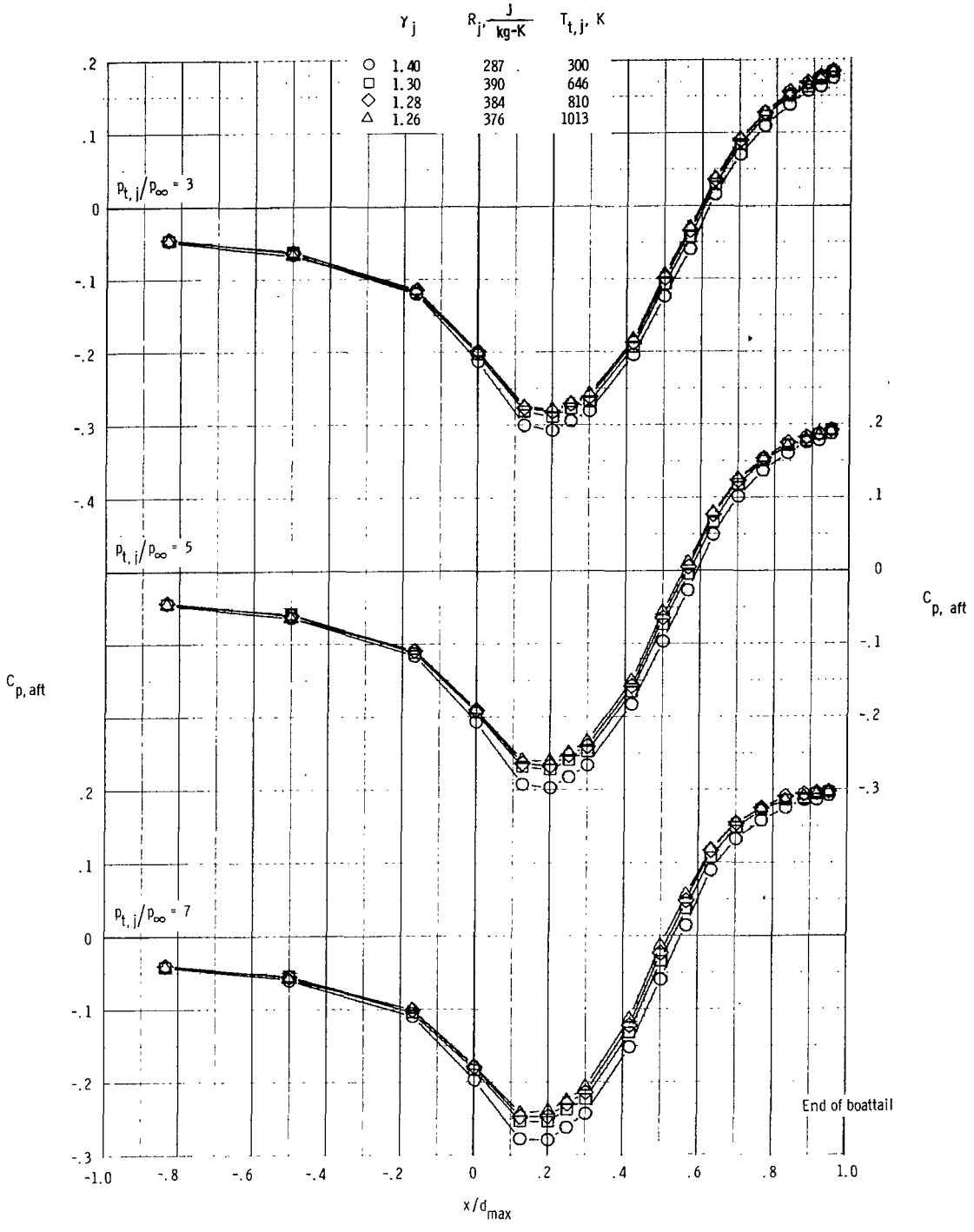

(b) $M_\infty = 0.60$; $p_{t,j}/p_\infty$ = 3 to 7.

Figure 14.- Continued.

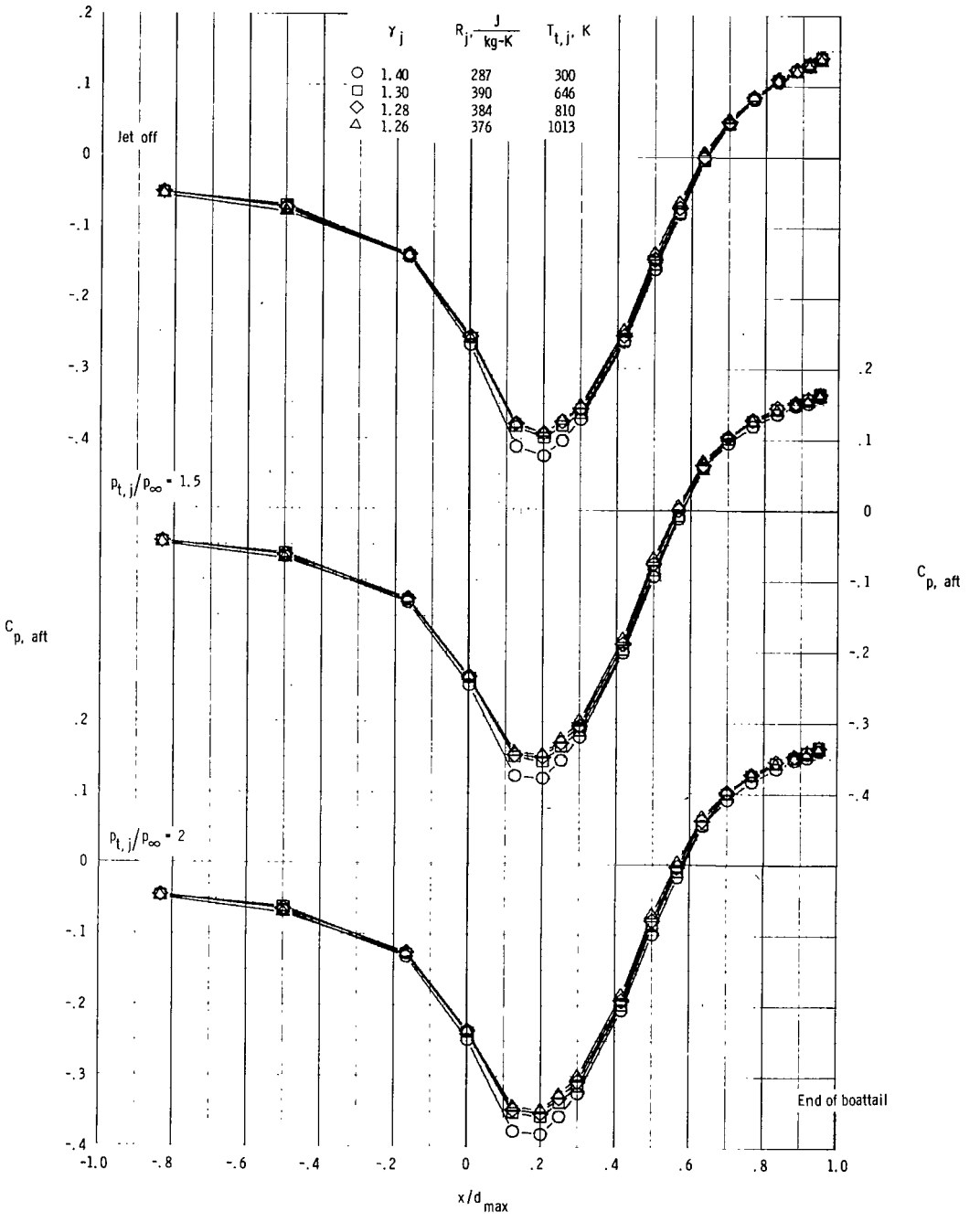

(c) $M_\infty = 0.80$; $p_{t,j}/p_\infty$ = Jet off to 2.

Figure 14.- Continued.

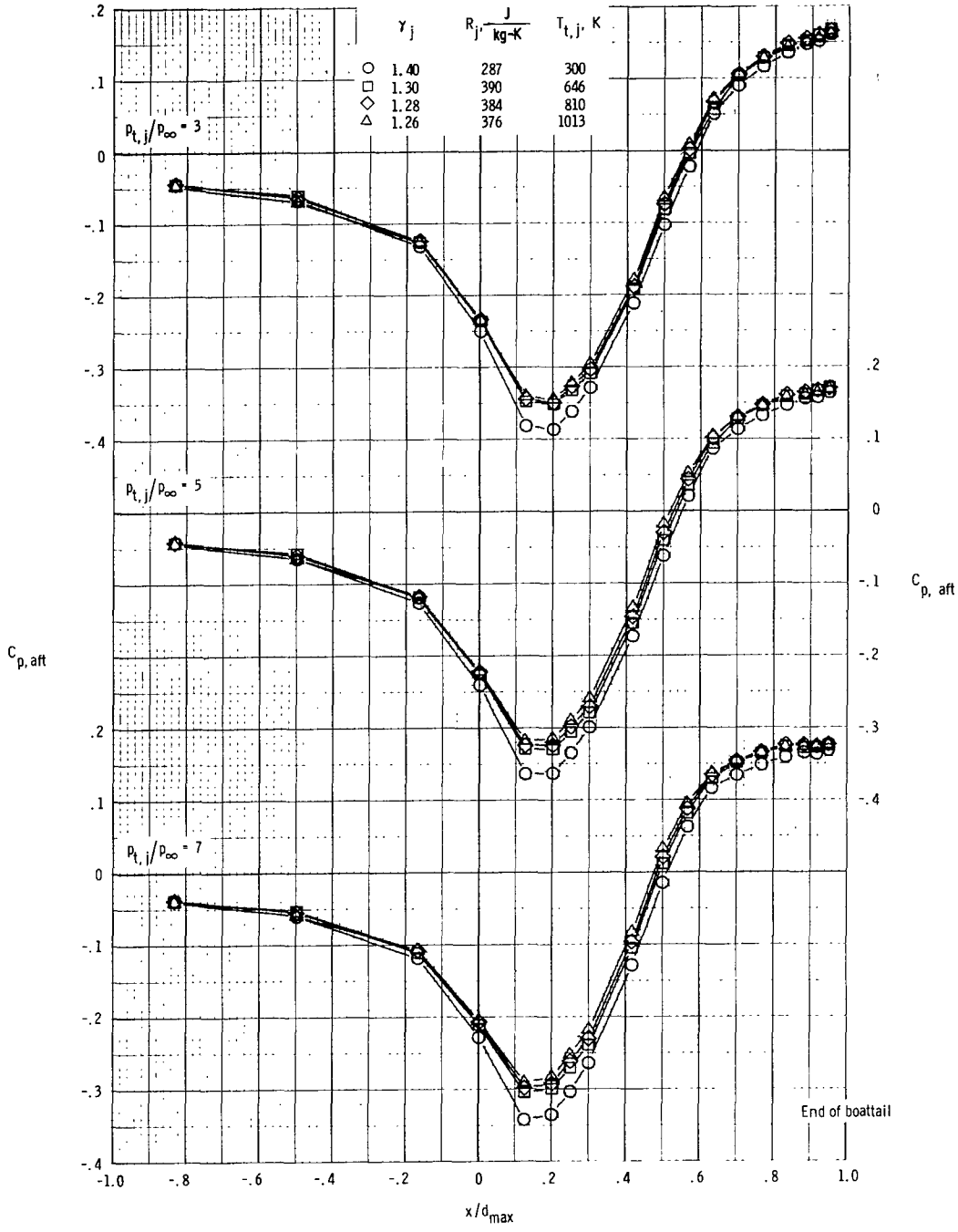

(d) $M_\infty = 0.80$; $p_{t,j}/p_\infty = 3$ to 7.

Figure 14.- Continued.

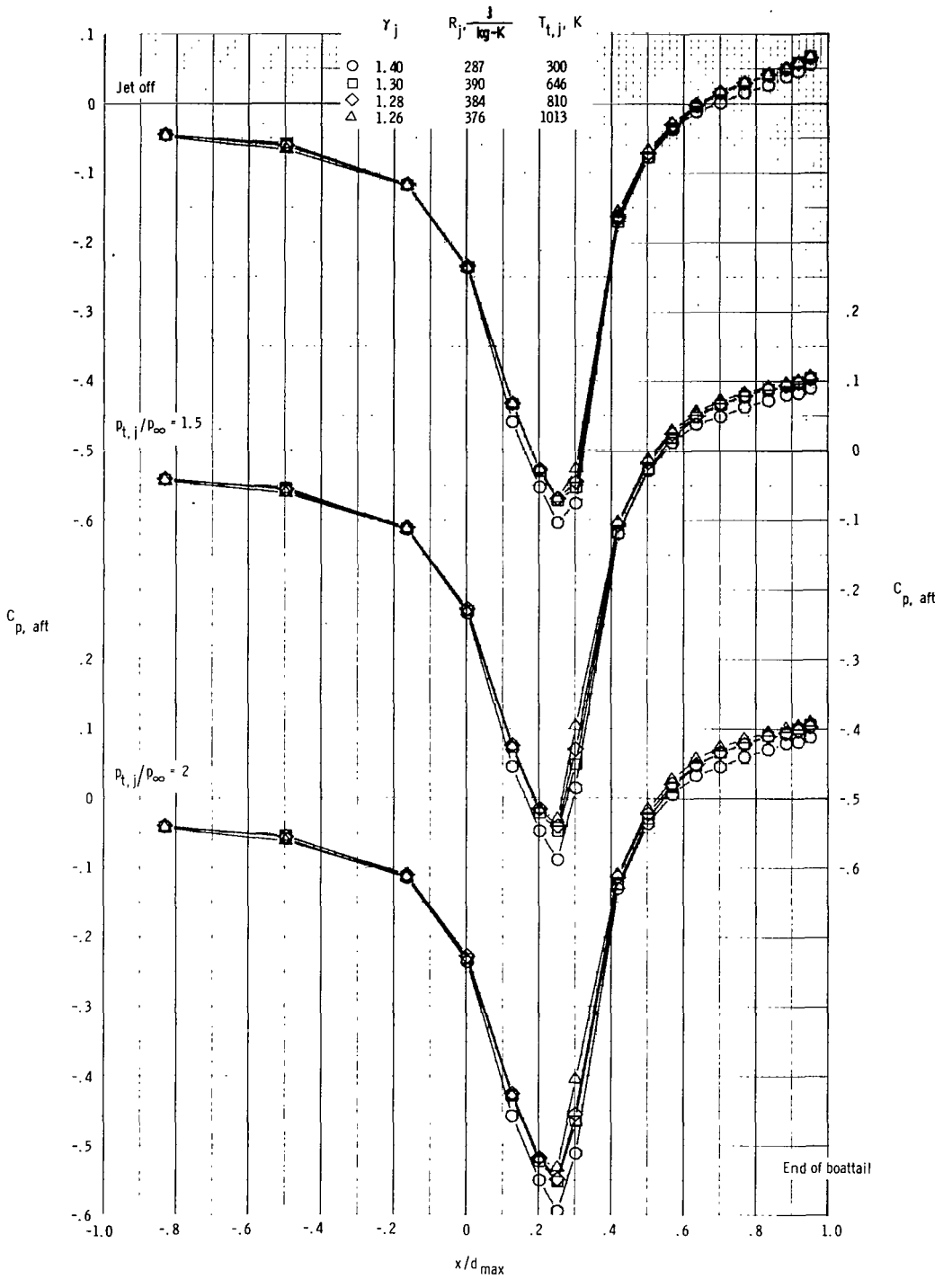

(e) $M_\infty = 0.90$; $p_{t,j}/p_\infty$ = Jet off to 2.

Figure 14.- Continued.

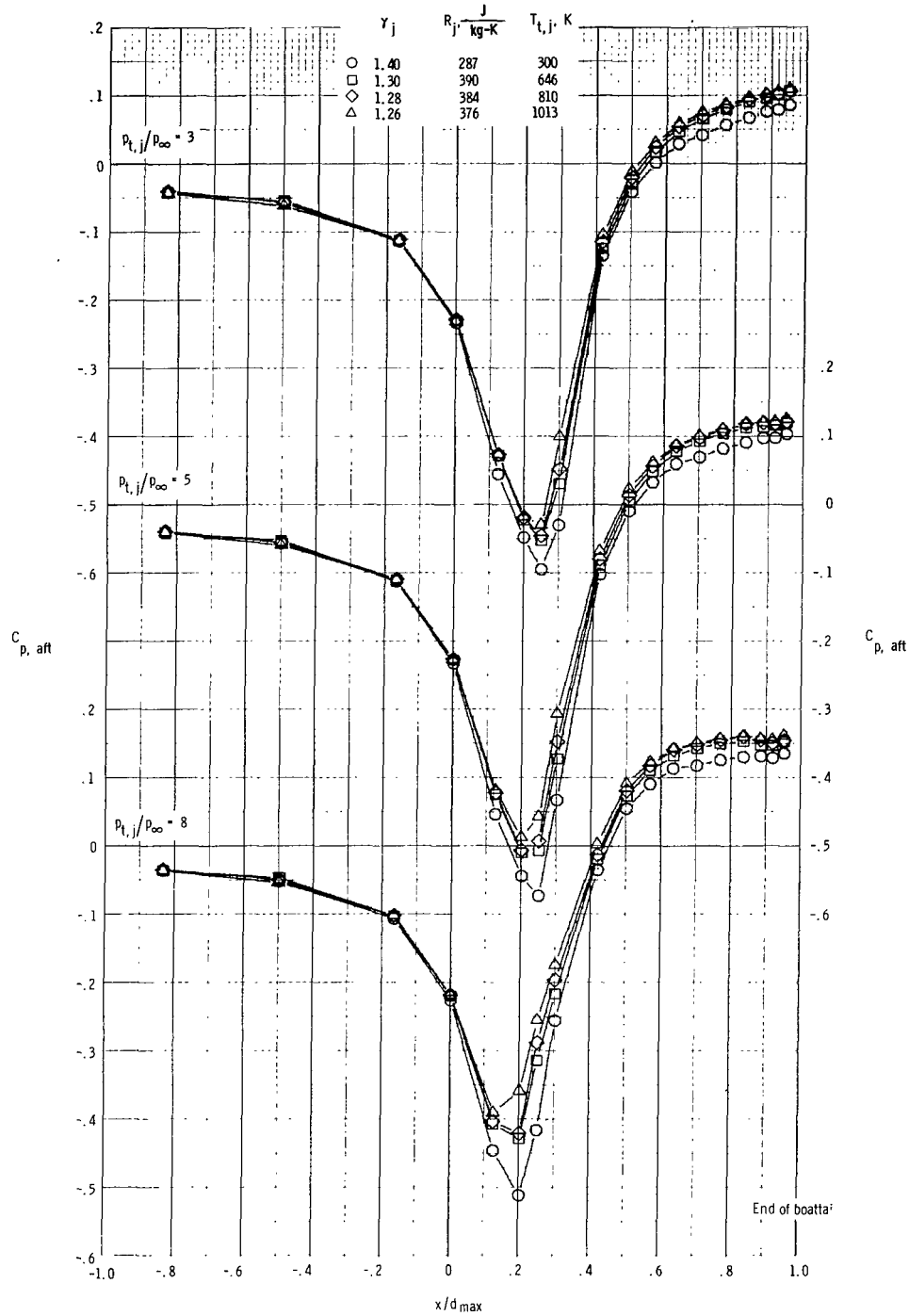

(f) $M_\infty = 0.90$; $p_{t,j}/p_\infty = 3$ to 7.

Figure 14.- Continued.

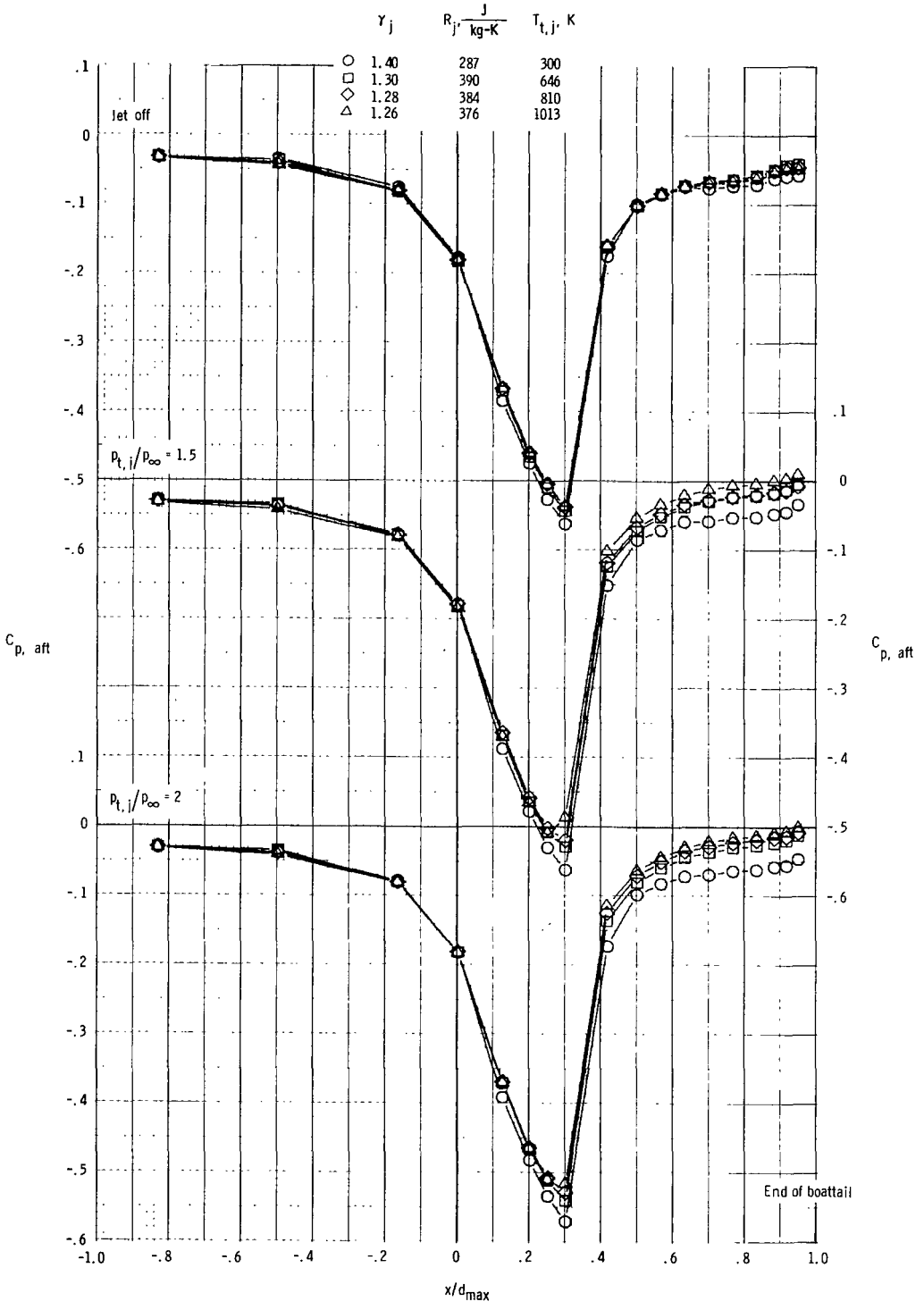

(g) $M_\infty = 0.95$; $p_{t,j}/p_\infty$ = Jet off to 2.

Figure 14.- Continued.

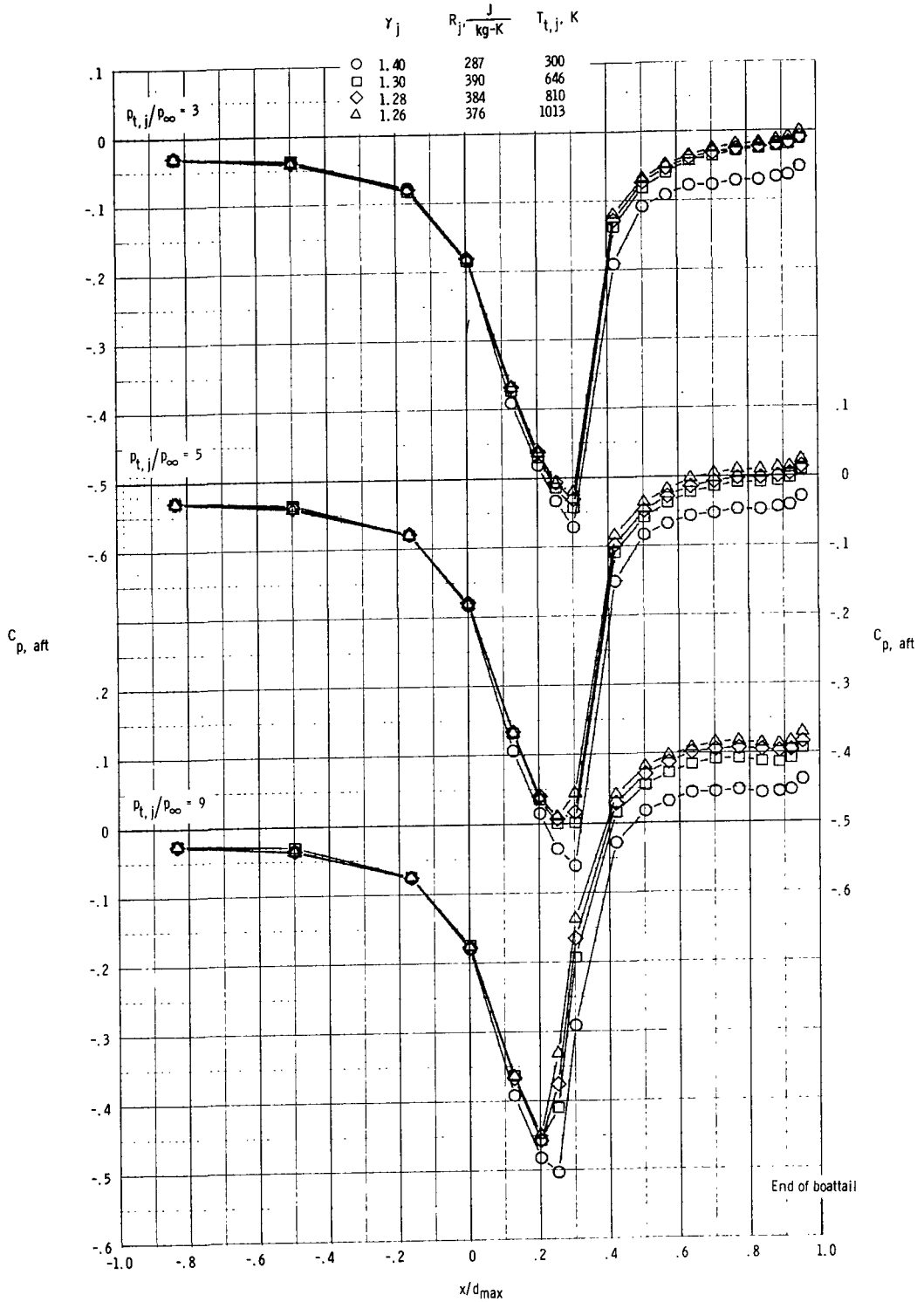

(h) $M_\infty = 0.95$; $p_{t,j}/p_\infty = 3$ to 9.

Figure 14.- Continued.

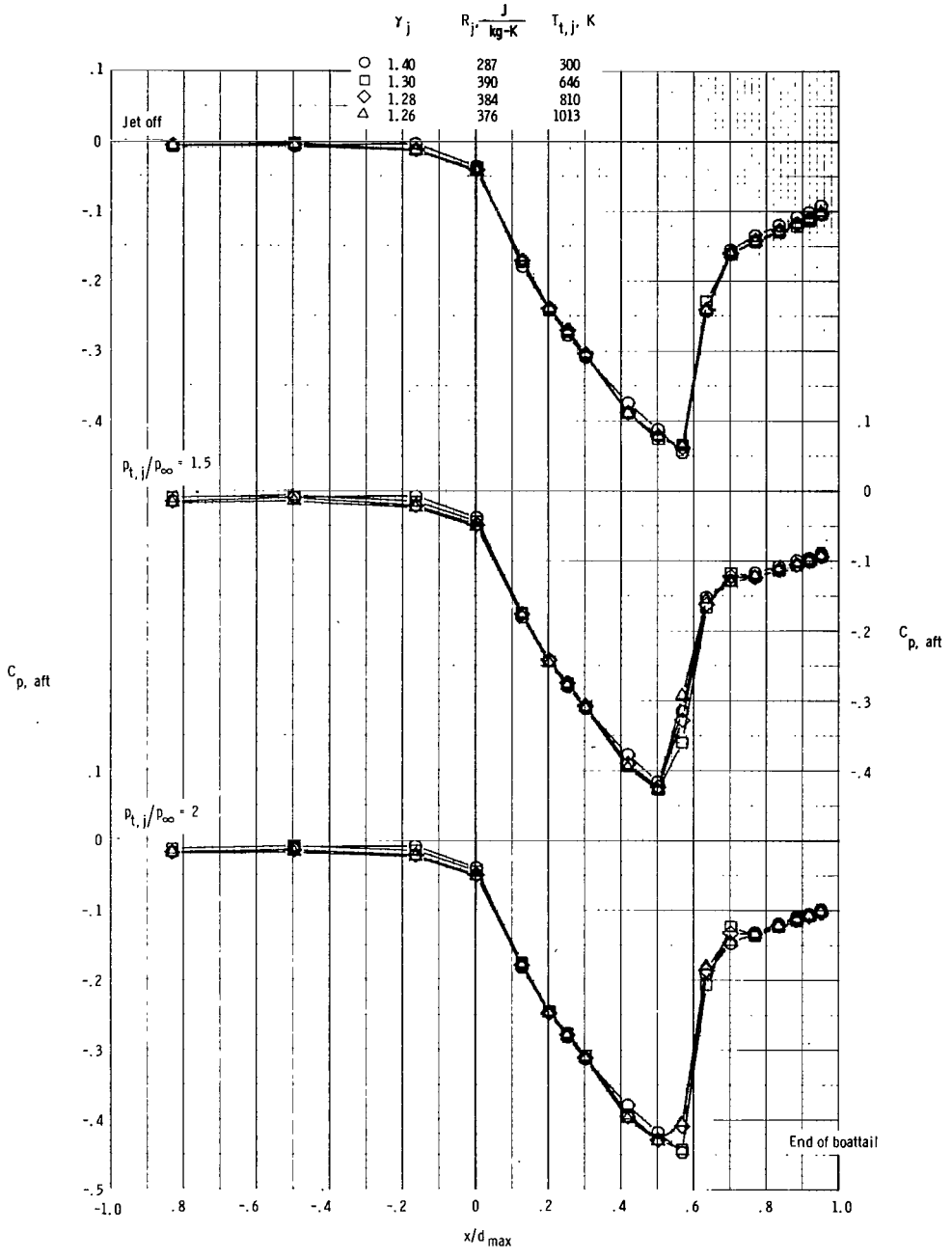

(i) M_∞ = 1.20; $p_{t,j}/p_\infty$ = Jet off to 2.

Figure 14.- Continued.

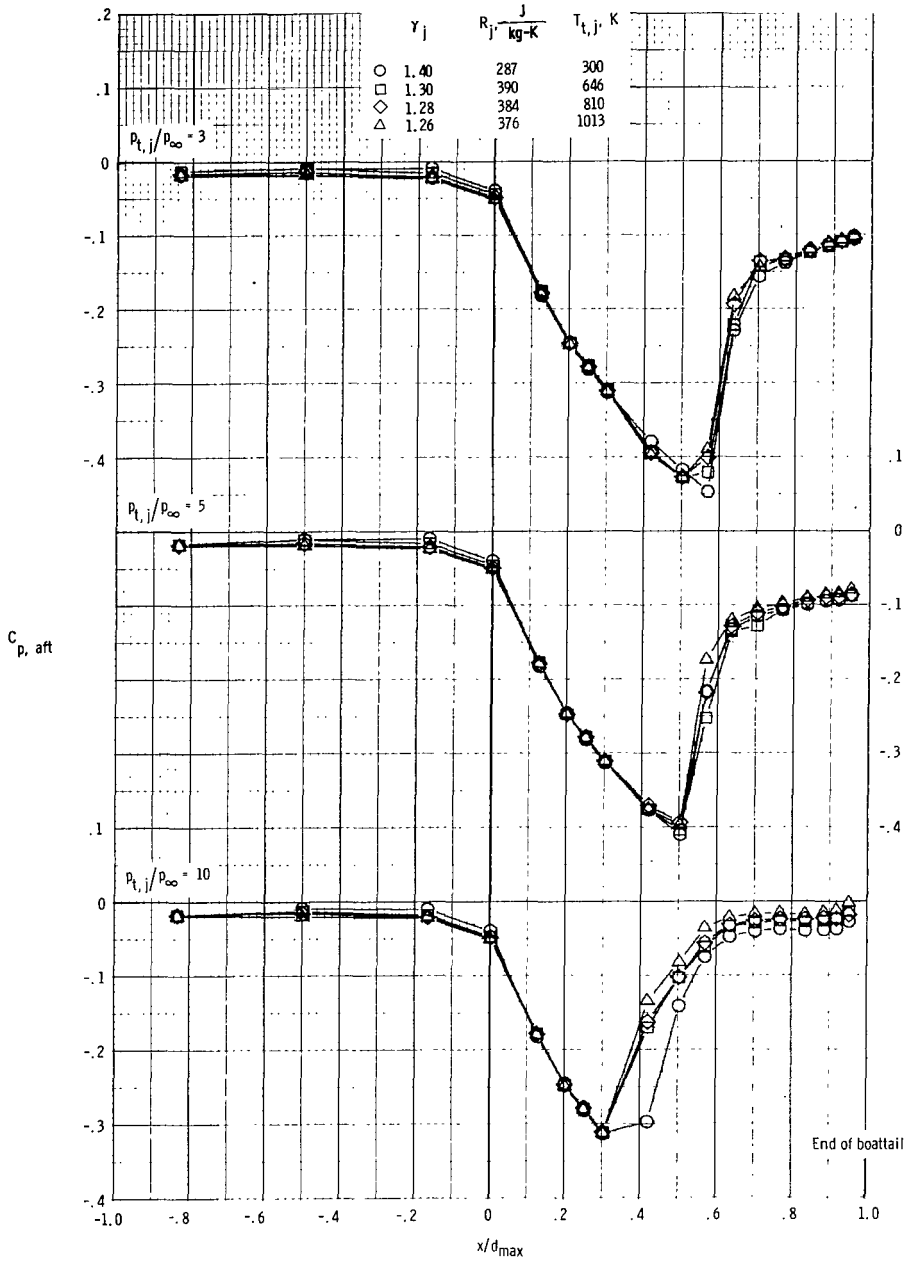

(j) $M_\infty = 1.20$; $p_{t,j}/p_\infty = 3$ to 10.

Figure 14.- Concluded.

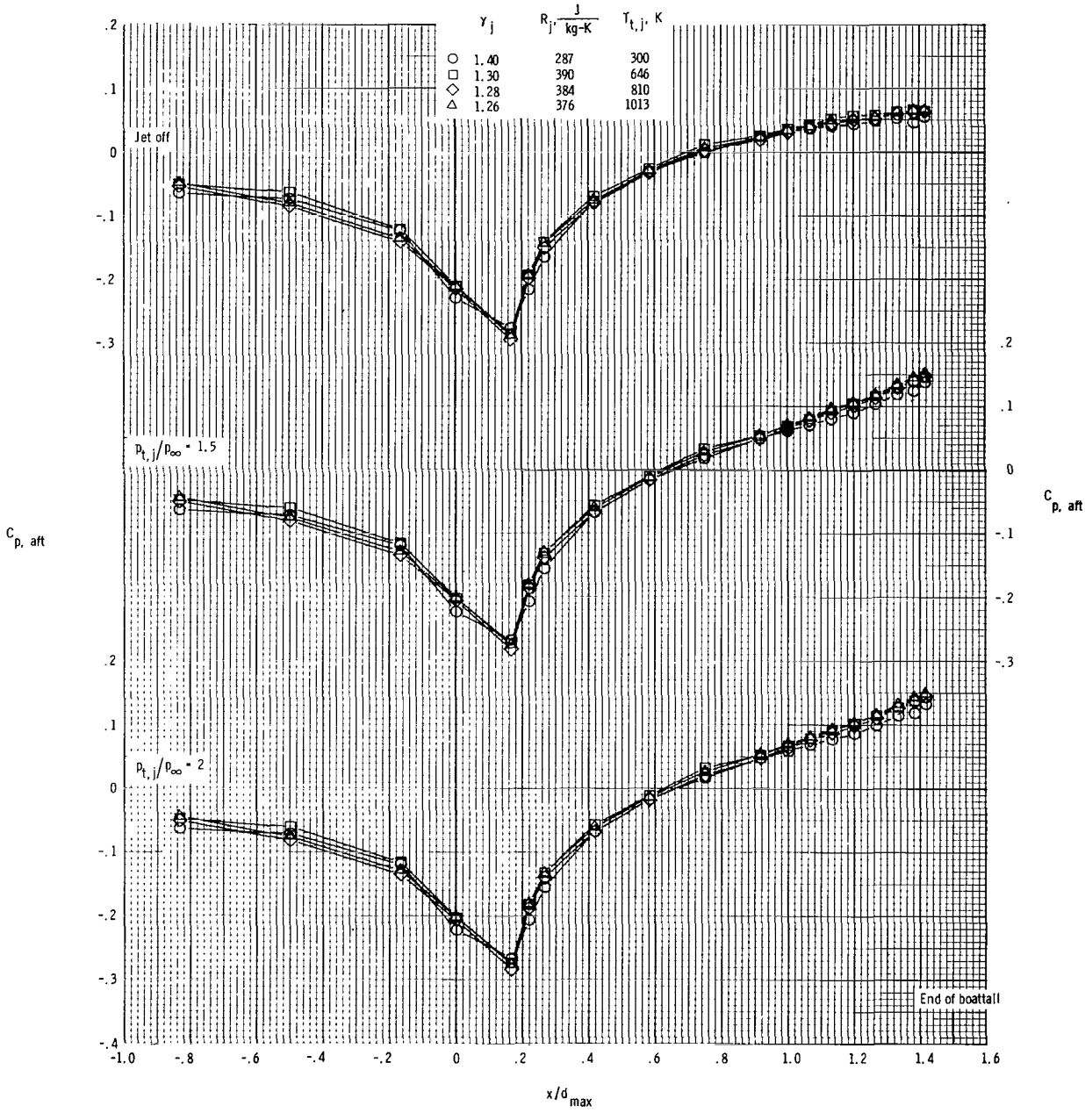

(a) $M_\infty = 0.60$; $p_{t,j}/p_\infty$ = Jet off to 2.

Figure 15.- Afterbody pressure coefficient distributions for each of the four jet exhaust gases. $\beta = 10^o$; sonic exit. (Each pressure coefficient is interpolated for exact values of jet total pressure ratio.)

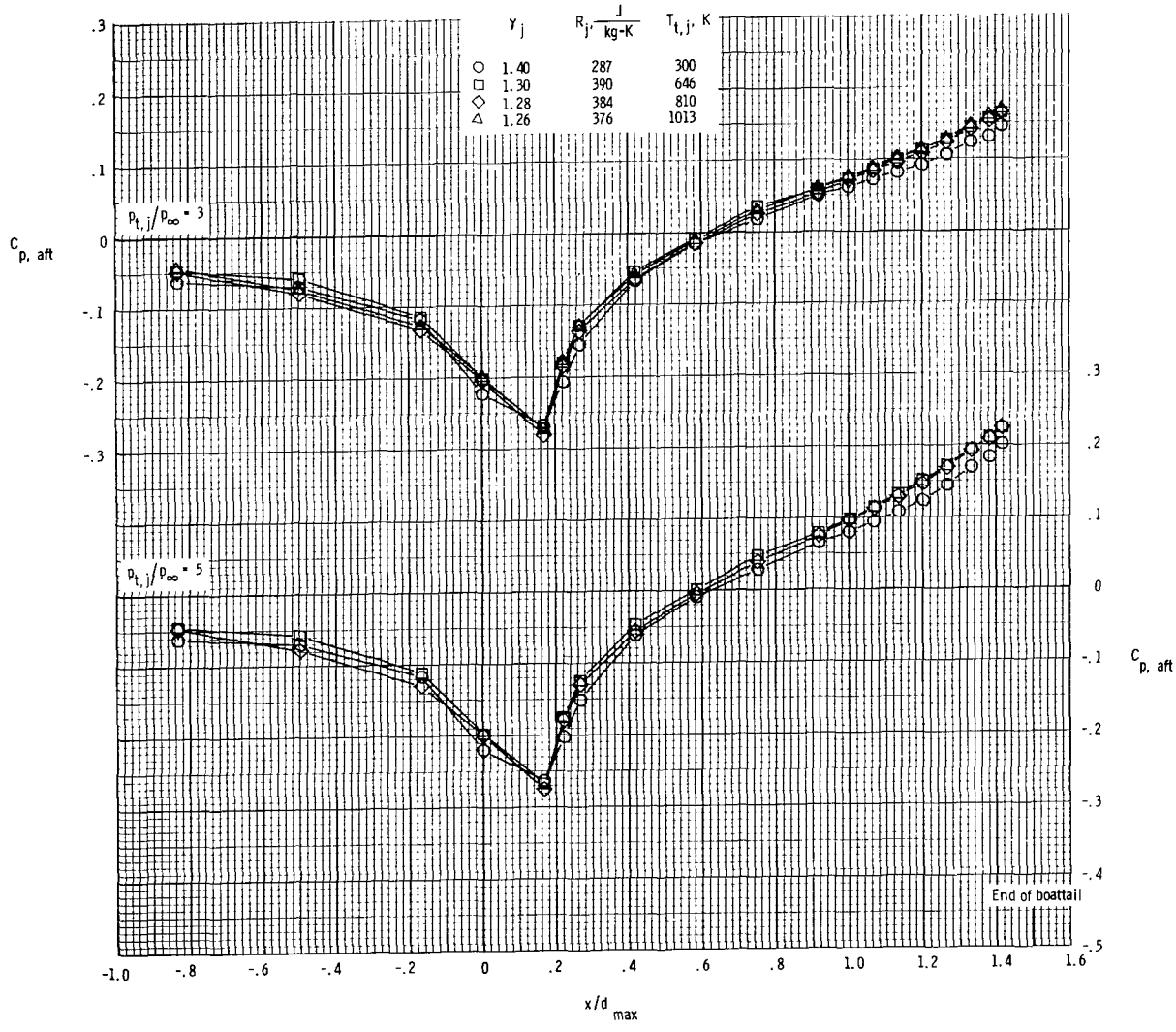

(b) $M_\infty = 0.60$; $p_{t,j}/p_\infty$ = 3 to 5.

Figure 15.- Continued.

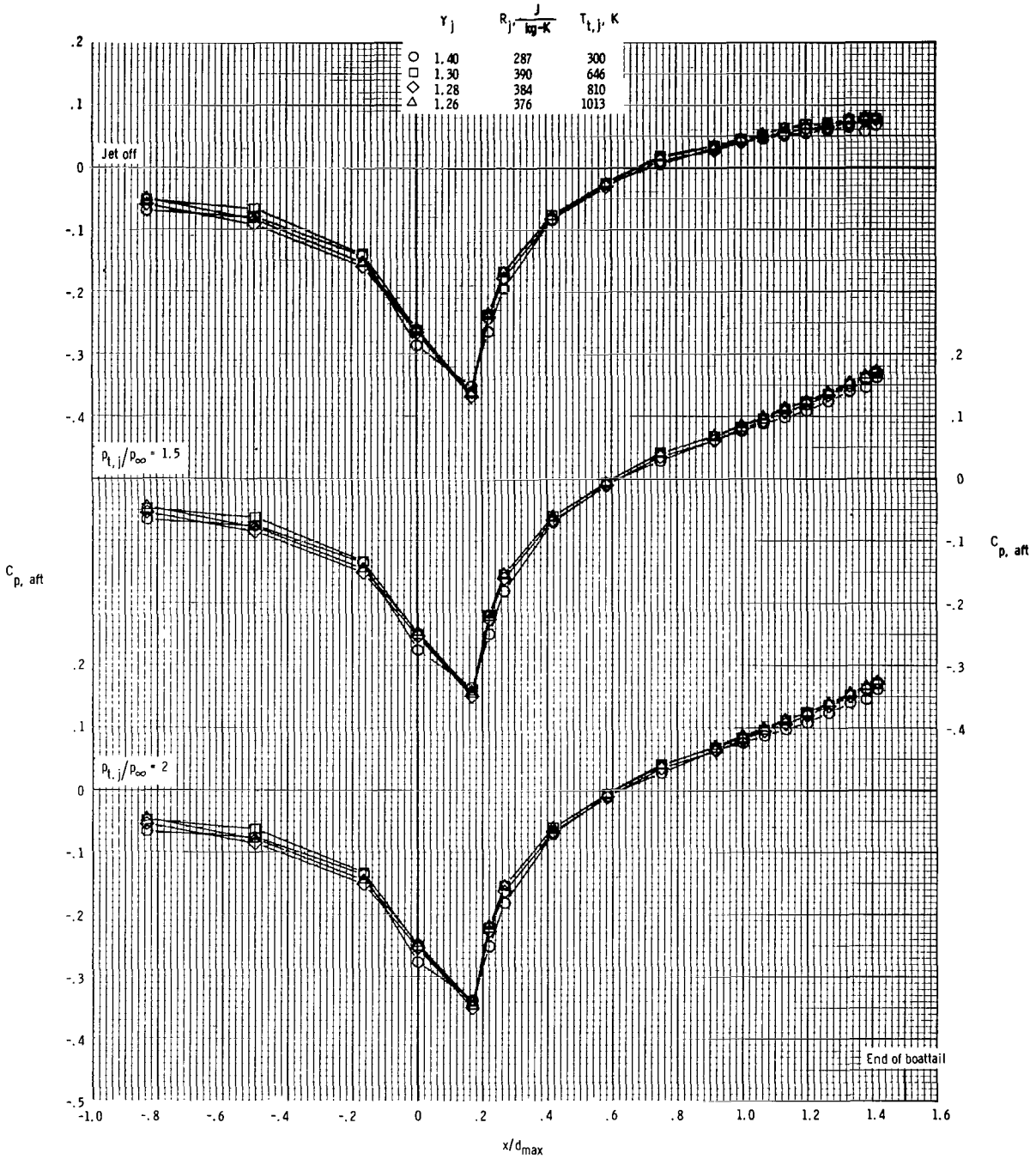

(c) M_∞ = 0.80; $p_{t,j}/p_\infty$ = Jet off to 2.

Figure 15.- Continued.

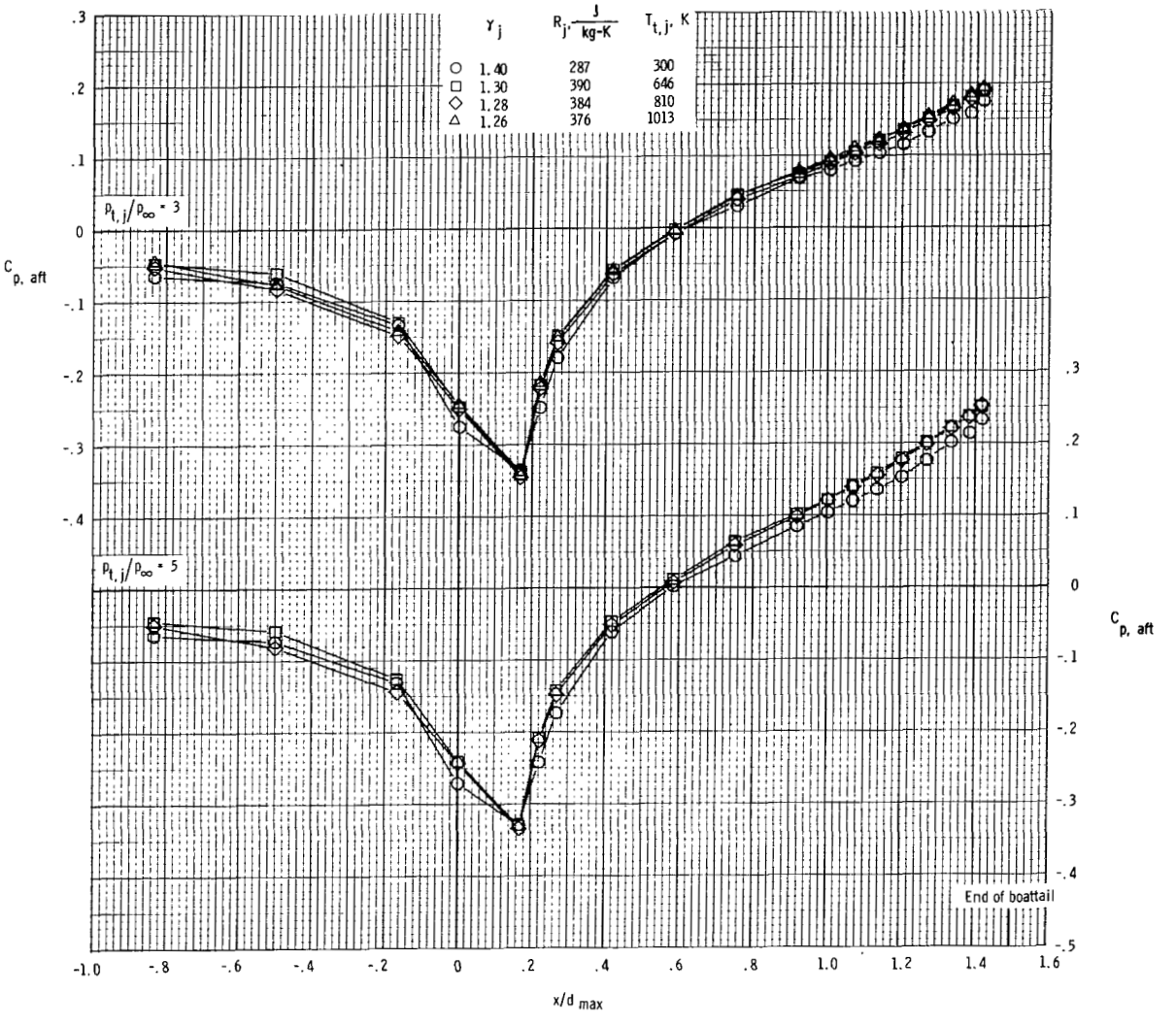

(d) $M_\infty = 0.80$; $p_{t,j}/p_\infty = 3$ to 5.

Figure 15.- Continued.

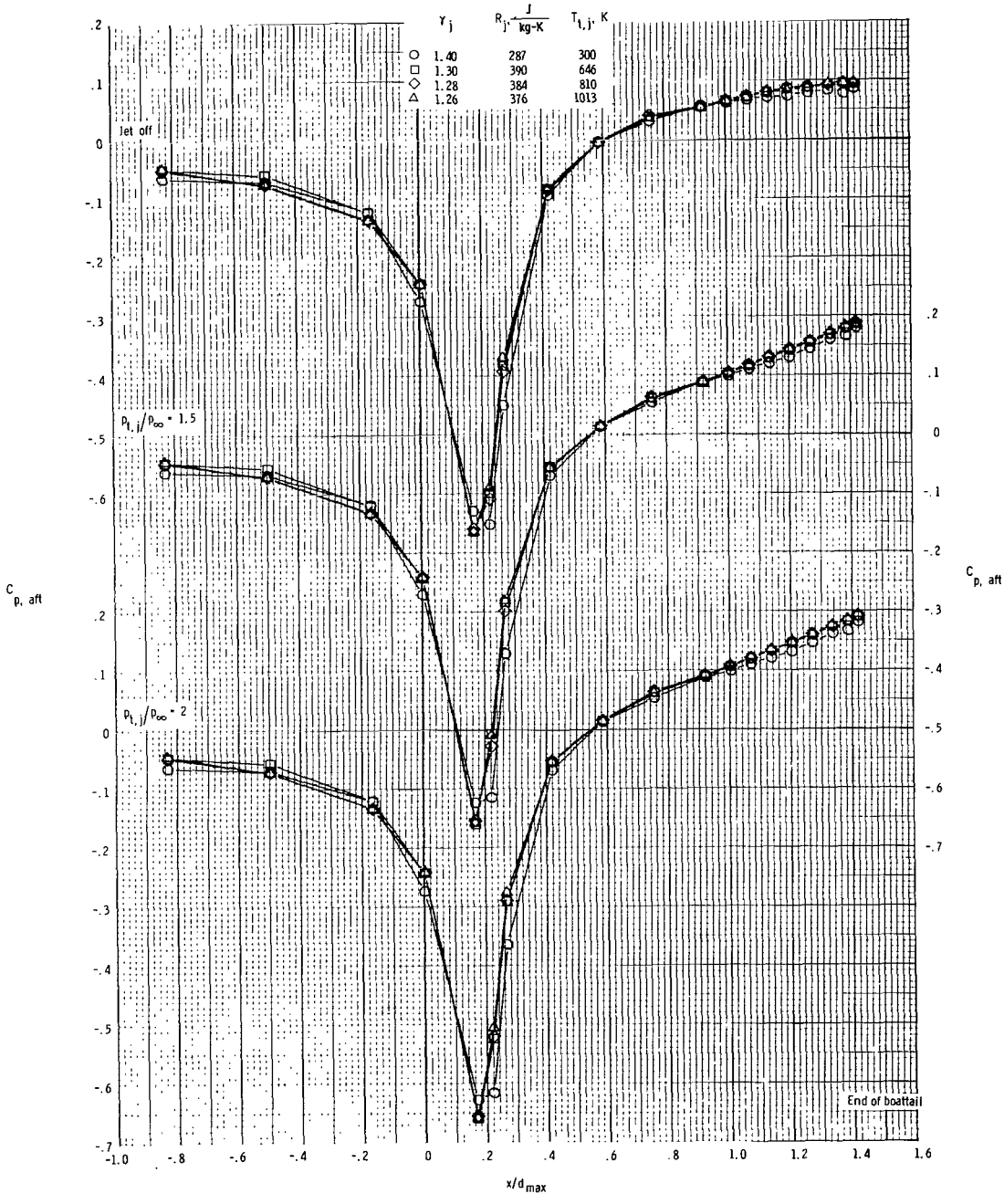

(e) $M_\infty = 0.90$; $p_{t,j}/p_\infty$ = Jet off to 2.

Figure 15.- Continued.

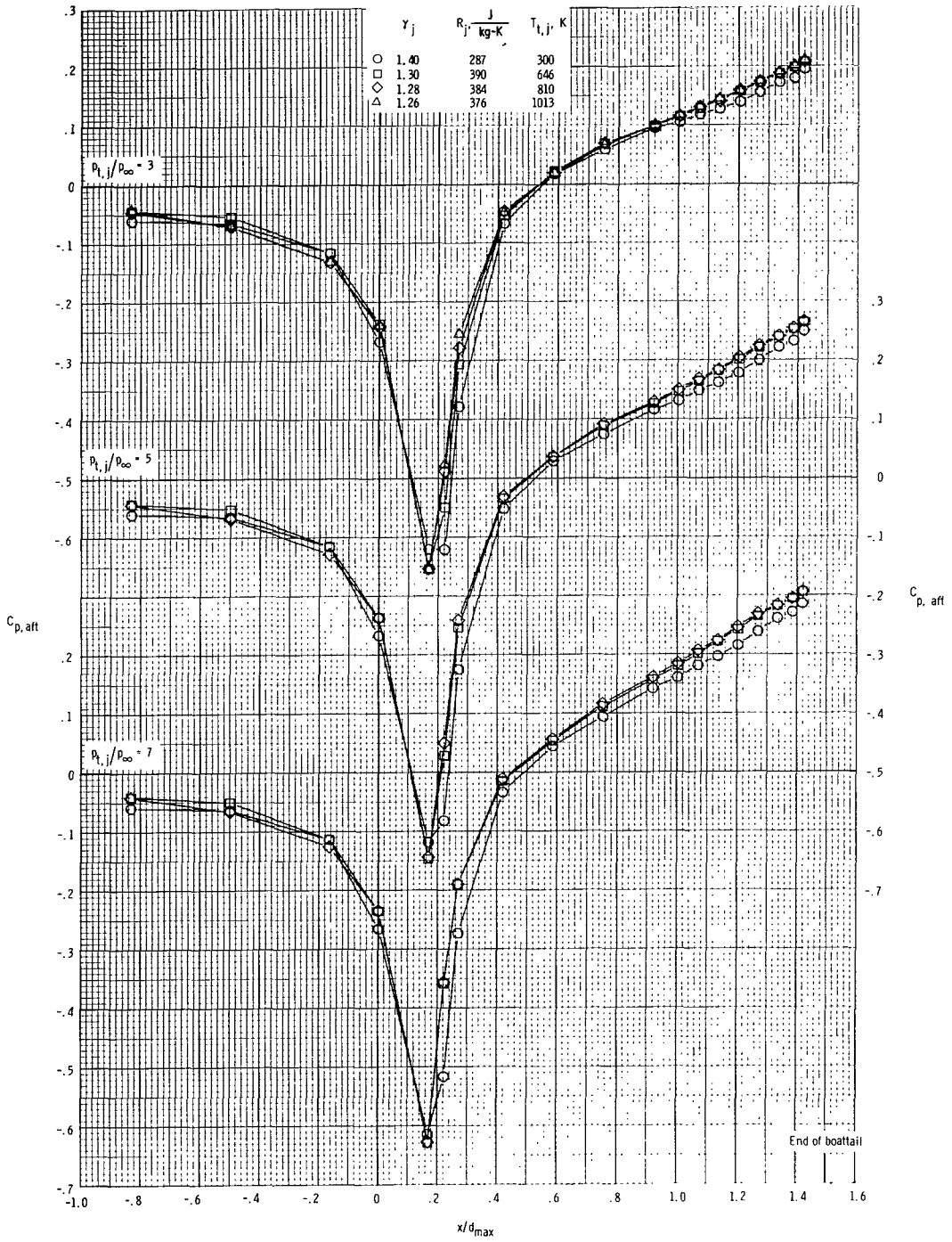

(f) $M_\infty = 0.90$; $p_{t,j}/p_\infty$ = 3 to 7.

Figure 15.- Continued.

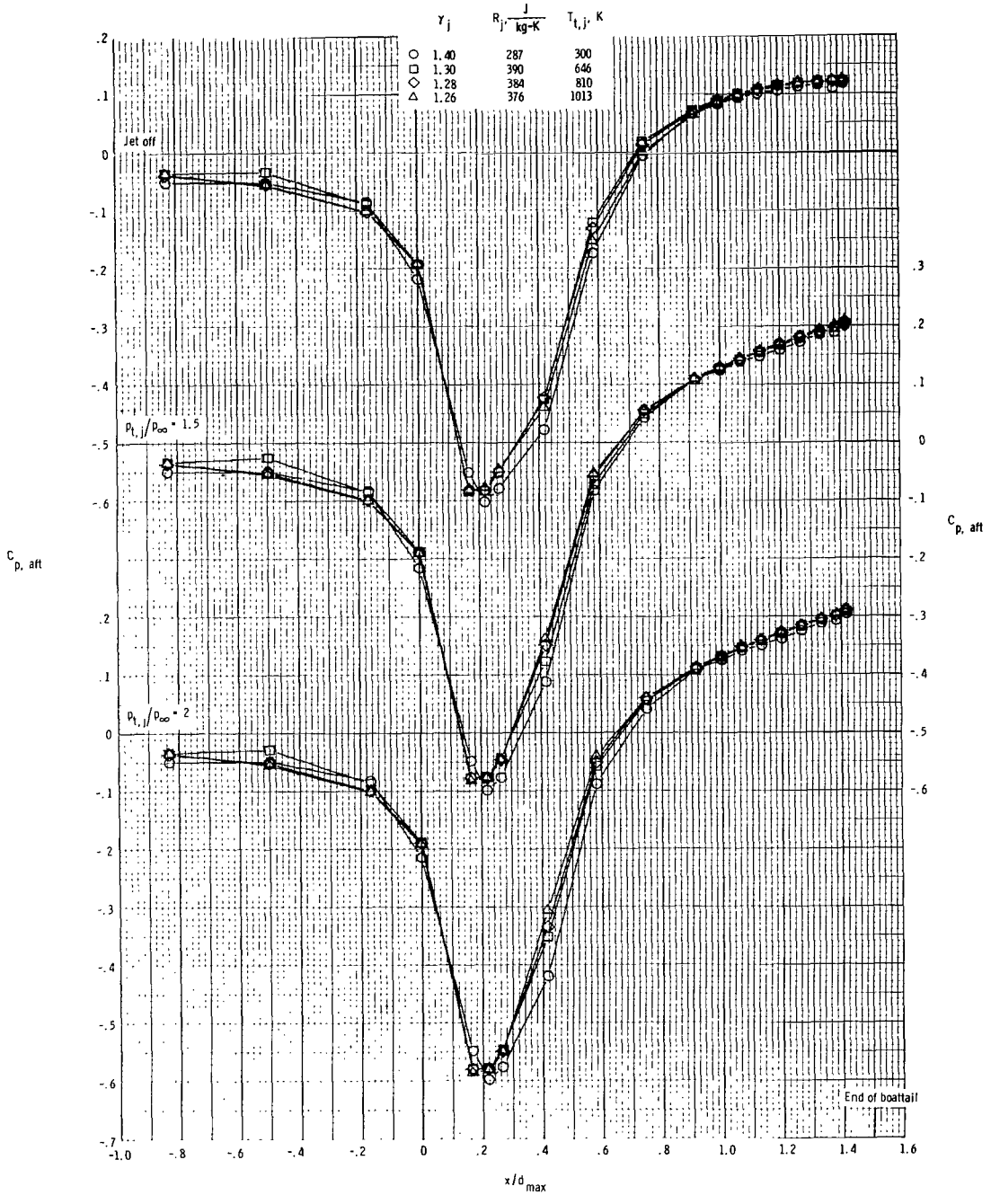

(g) $M_\infty = 0.95$; $p_{t,j}/p_\infty$ = Jet off to 2.

Figure 15.- Continued.

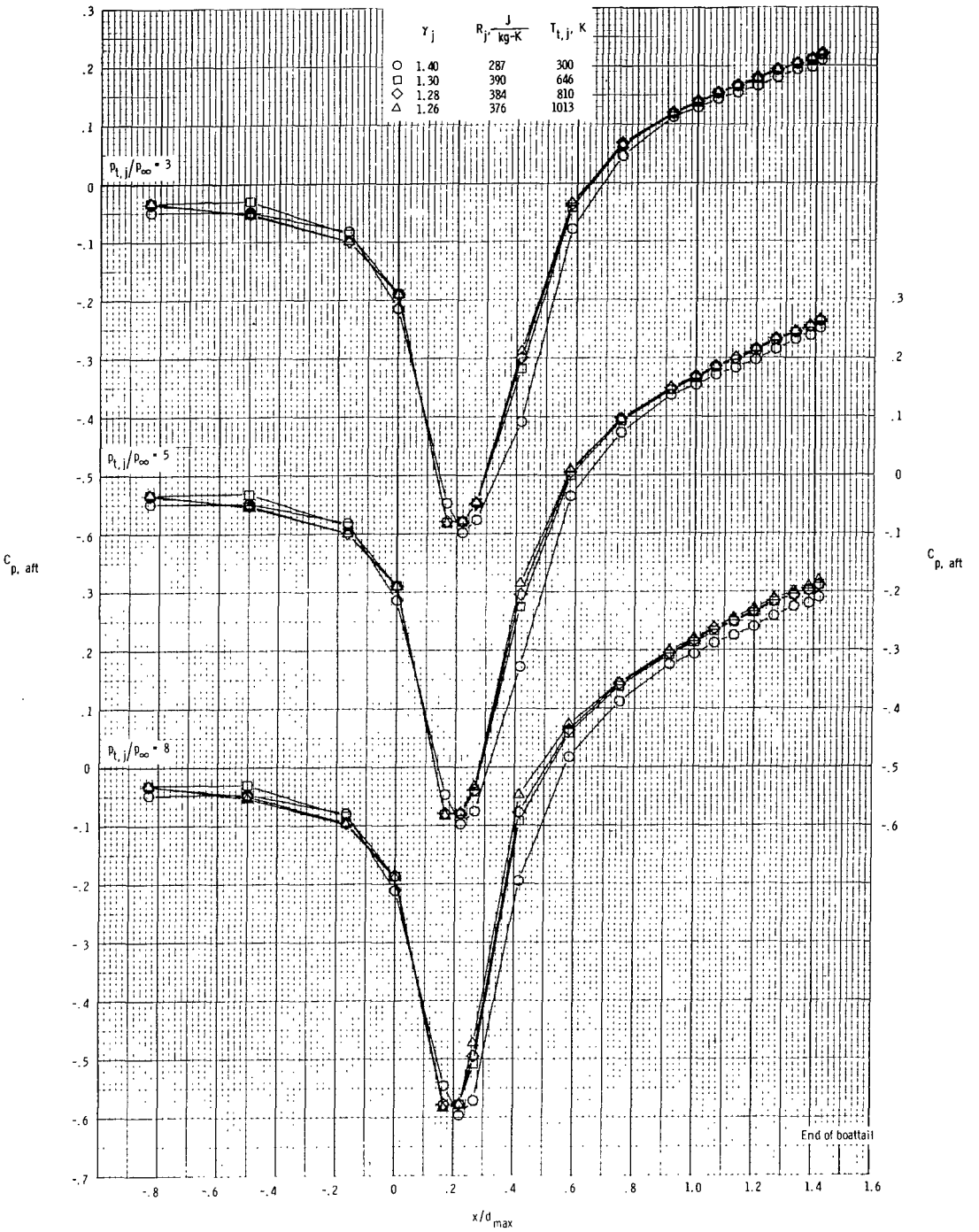

(h) $M_\infty = 0.95$; $p_{t,j}/p_\infty = 3$ to 8.

Figure 15.- Continued.

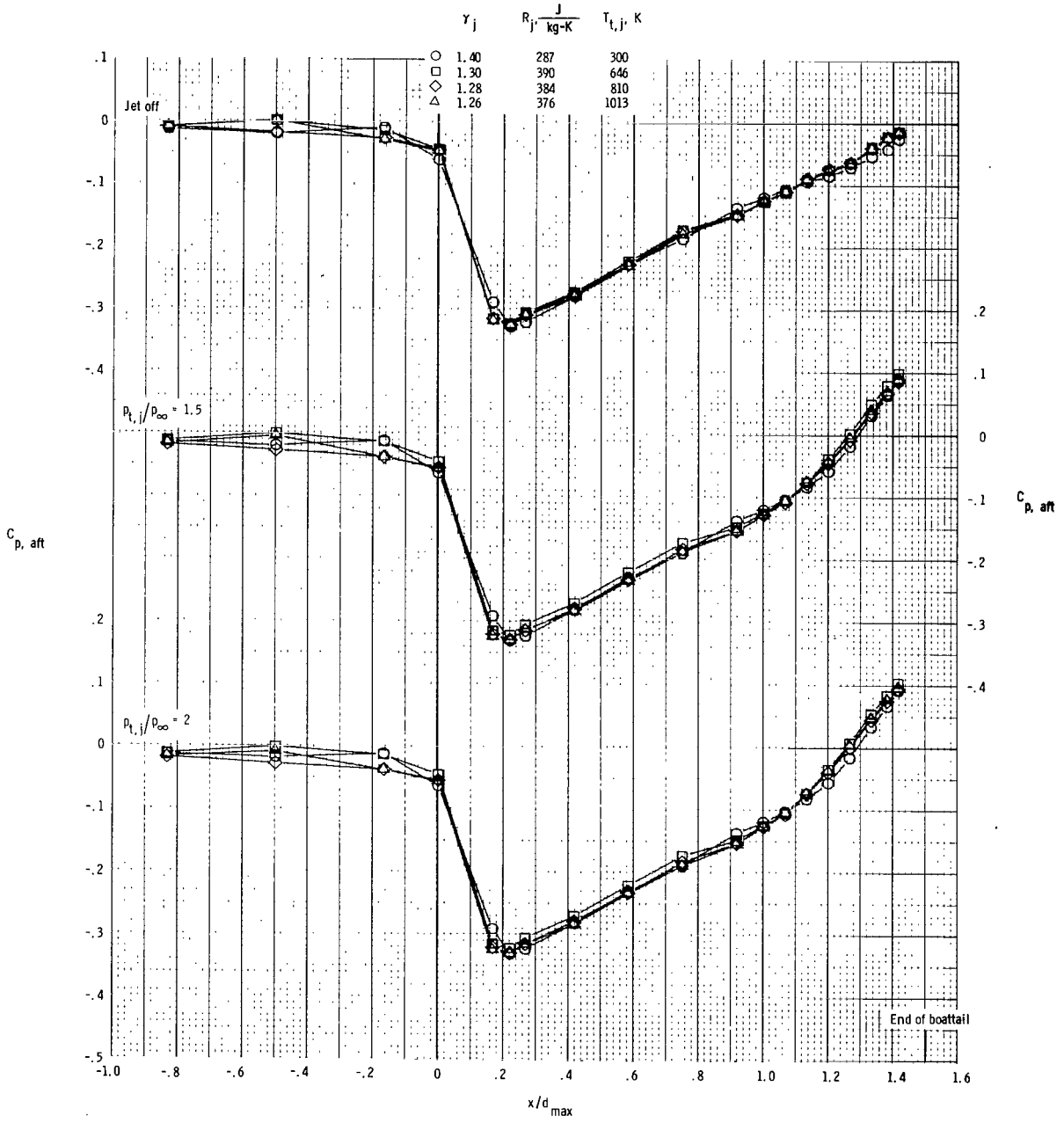

(i) $M_\infty = 1.20$; $p_{t,j}/p_\infty$ = Jet off to 2.

Figure 15.- Continued.

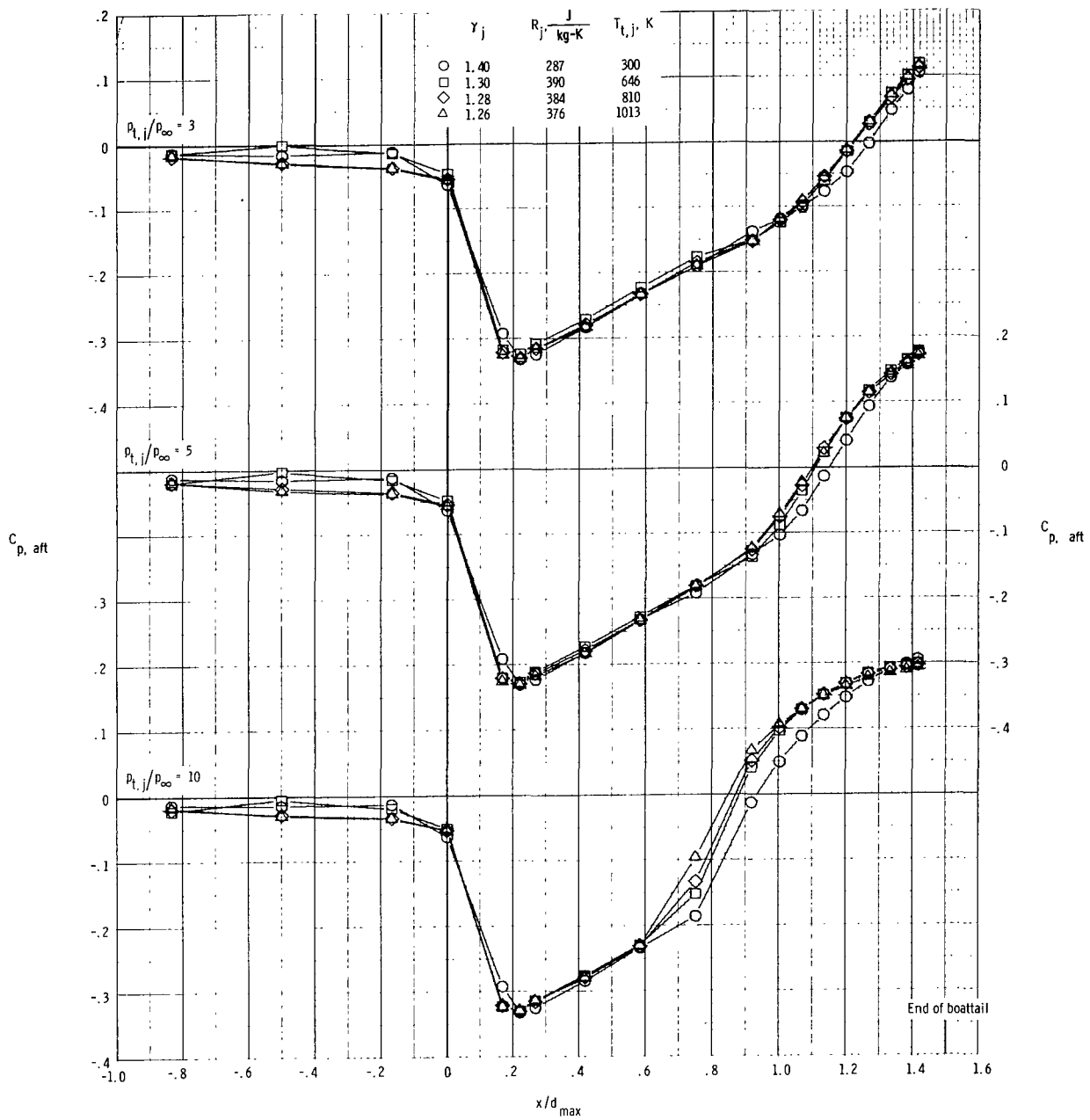

(j) $M_\infty = 1.20$; $p_{t,j}/p_\infty = 3$ to 10.

Figure 15.- Concluded.

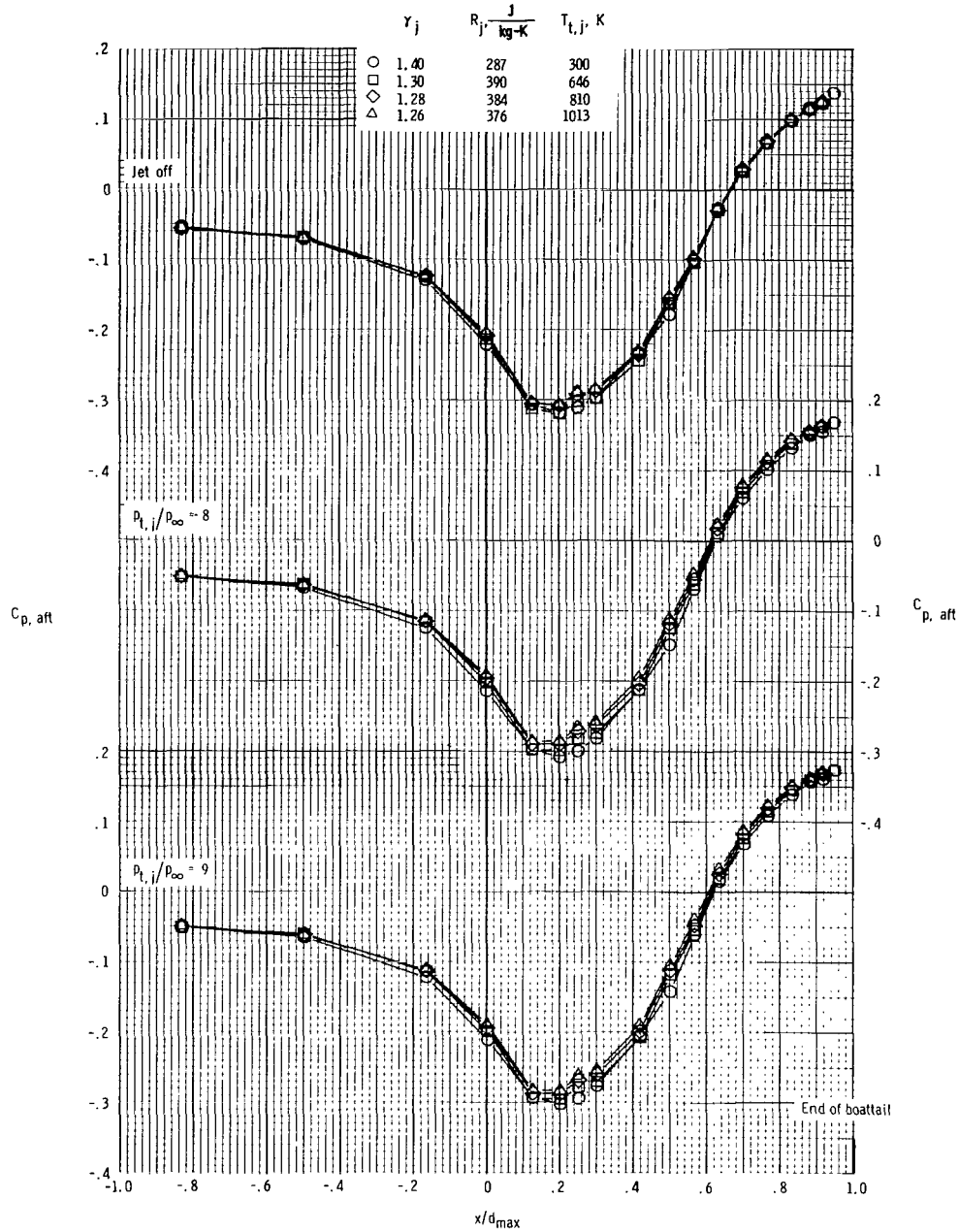

(a) $M_\infty = 0.60$; $p_{t,j}/p_\infty$ = Jet off to 9.

Figure 16.- Afterbody pressure coefficient distributions for each of the four jet exhaust gases. $\beta = 20^o$; $M_e = 2$. (Each pressure coefficient is interpolated for exact values of jet total pressure ratio.)

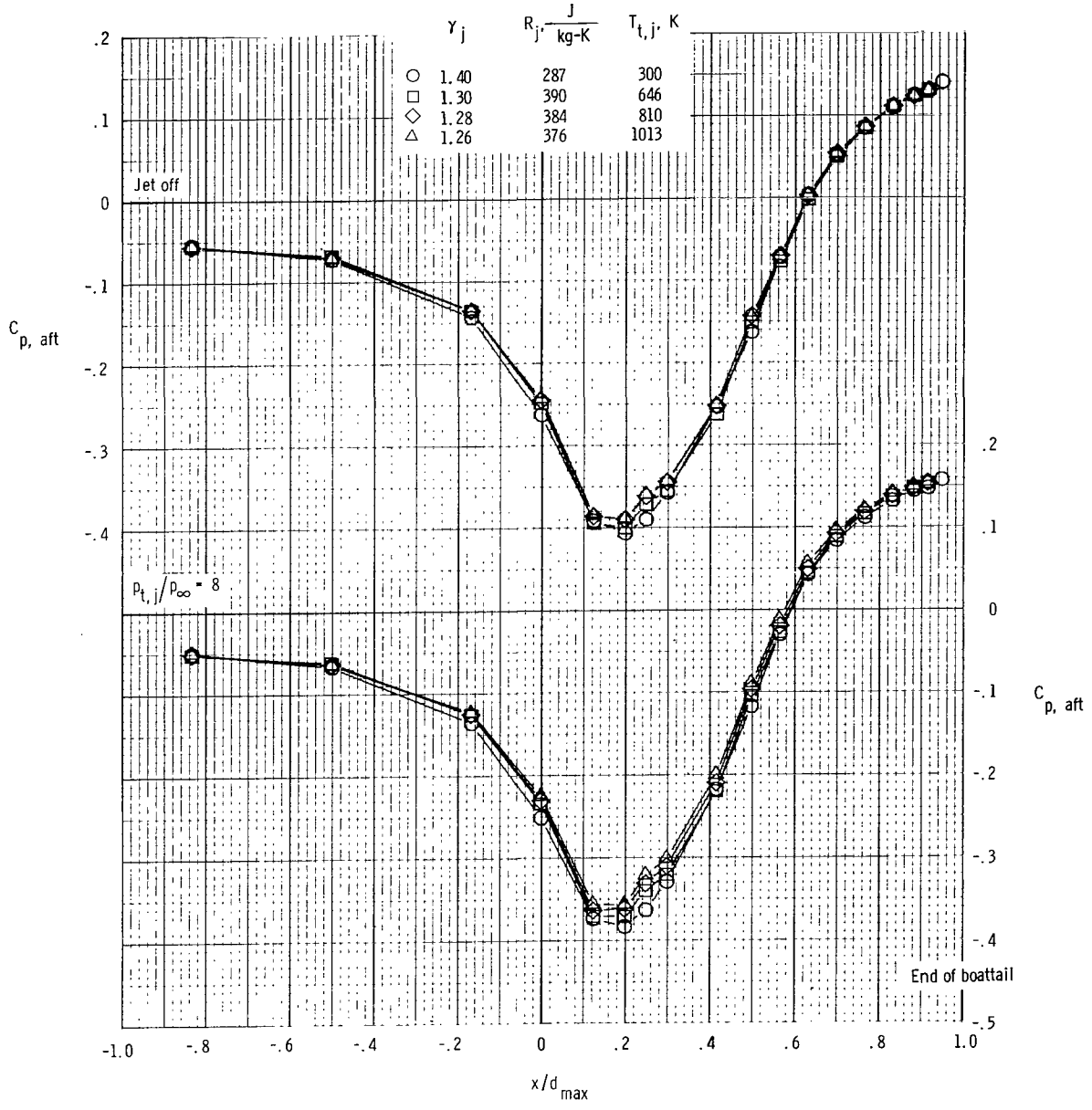

(b) M_∞ = 0.80; $p_{t,j}/p_\infty$ = Jet off to 8.

Figure 16.- Continued.

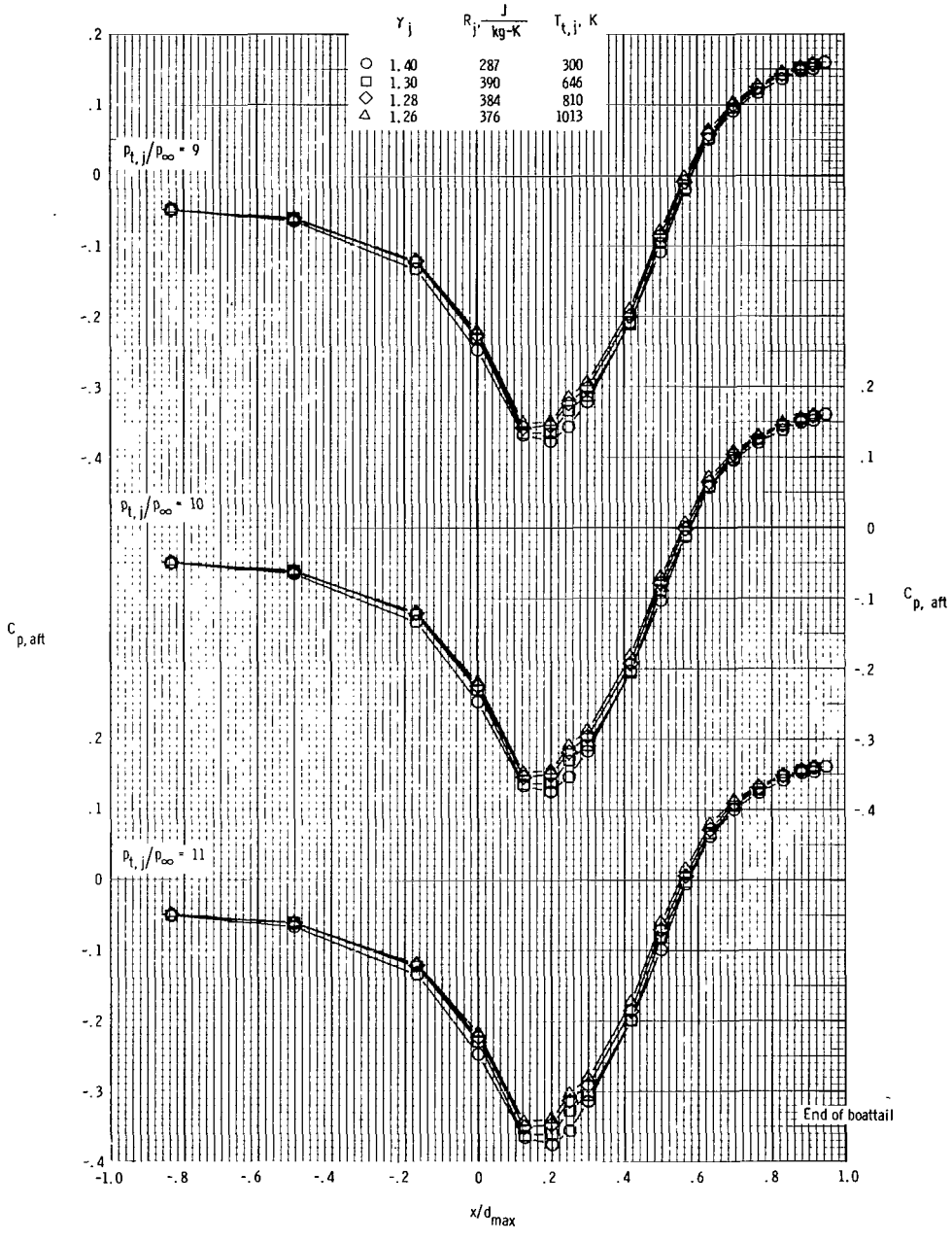

(c) $M_\infty = 0.80$; $p_{t,j}/p_\infty = 9$ to 11.

Figure 16.- Continued.

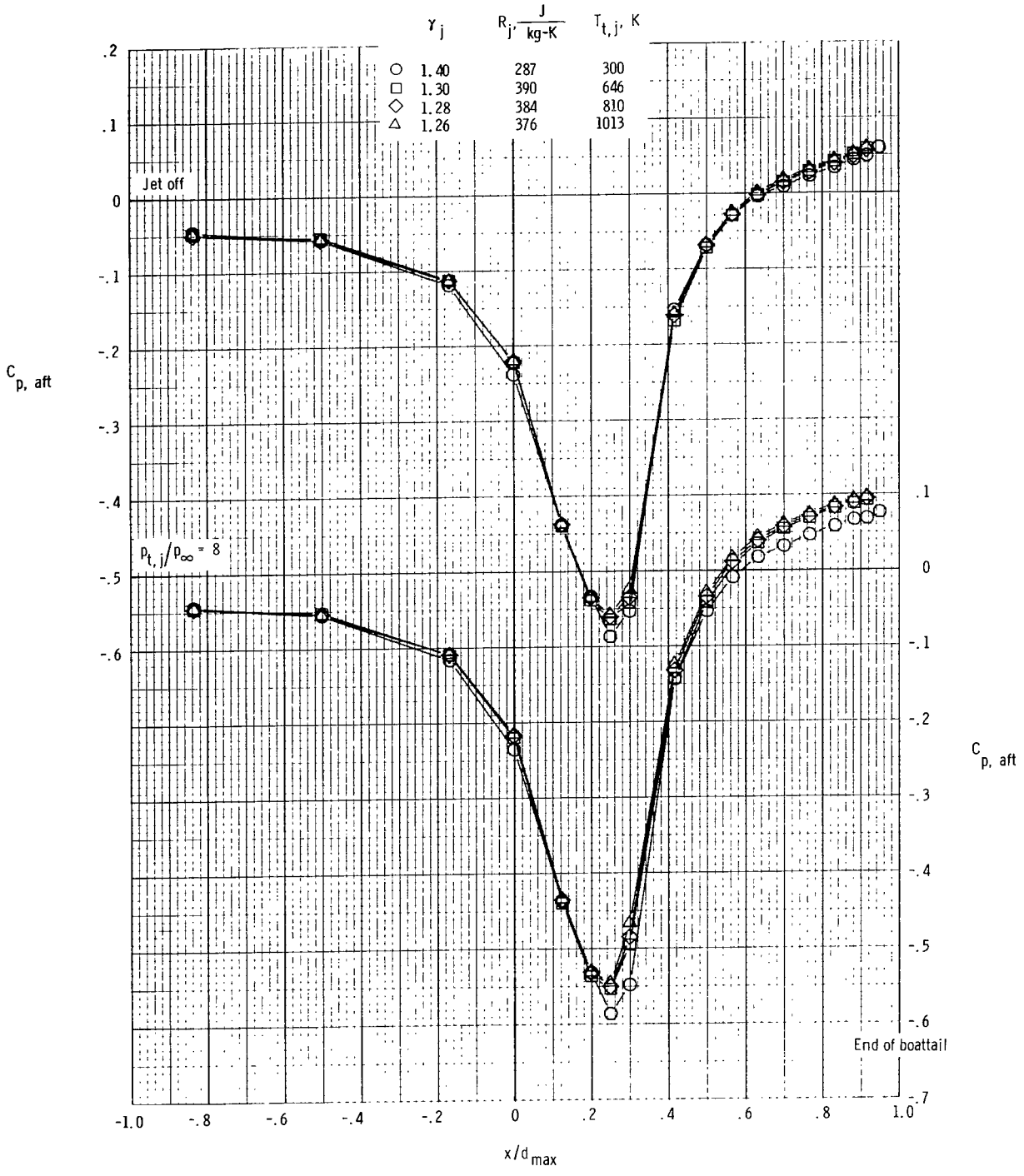

(d) M_∞ = 0.90; $p_{t,j}/p_\infty$ = Jet off to 8.

Figure 16.- Continued.

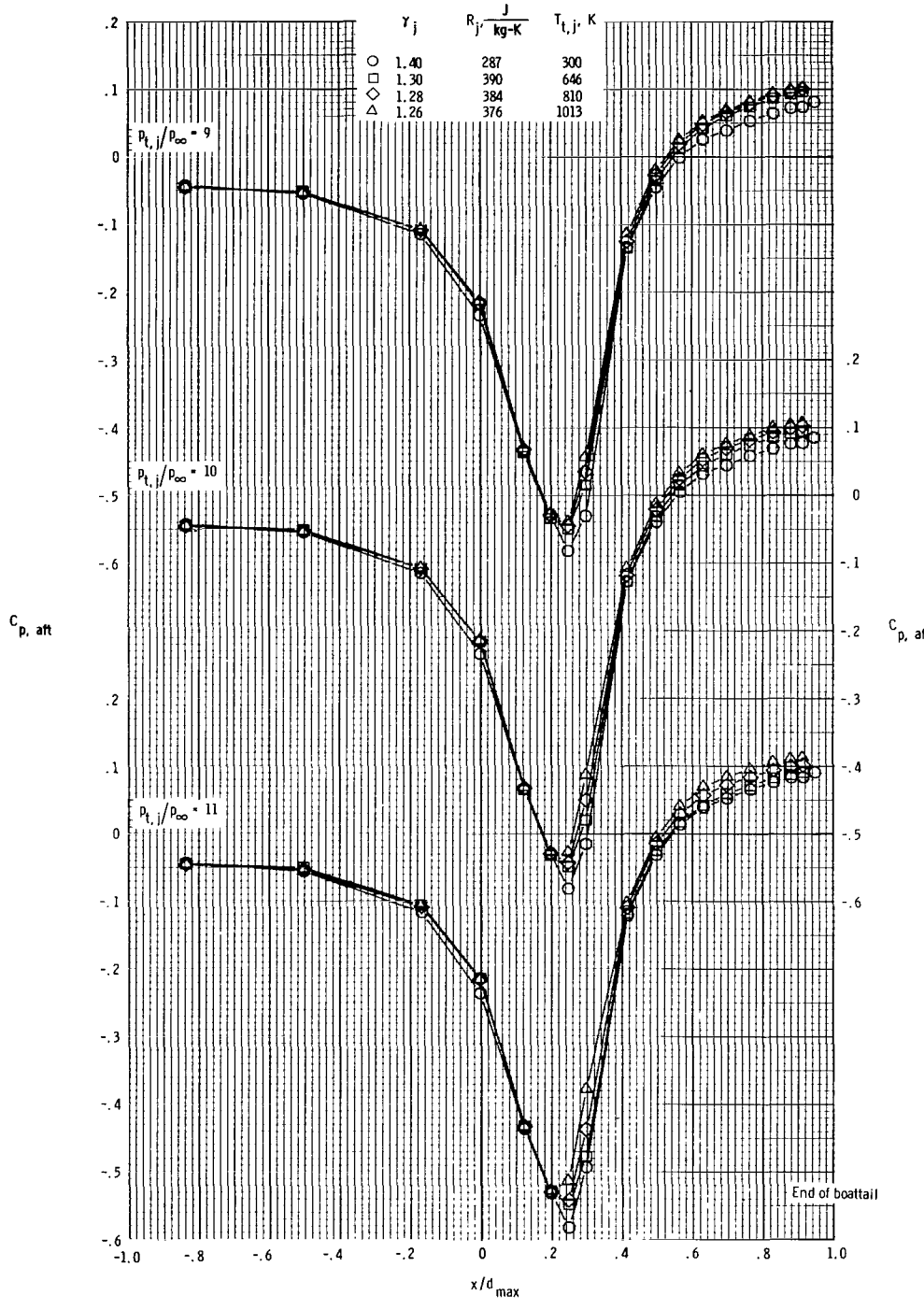

(e) $M_\infty = 0.90$; $p_{t,j}/p_\infty = 9$ to 11.

Figure 16.- Continued.

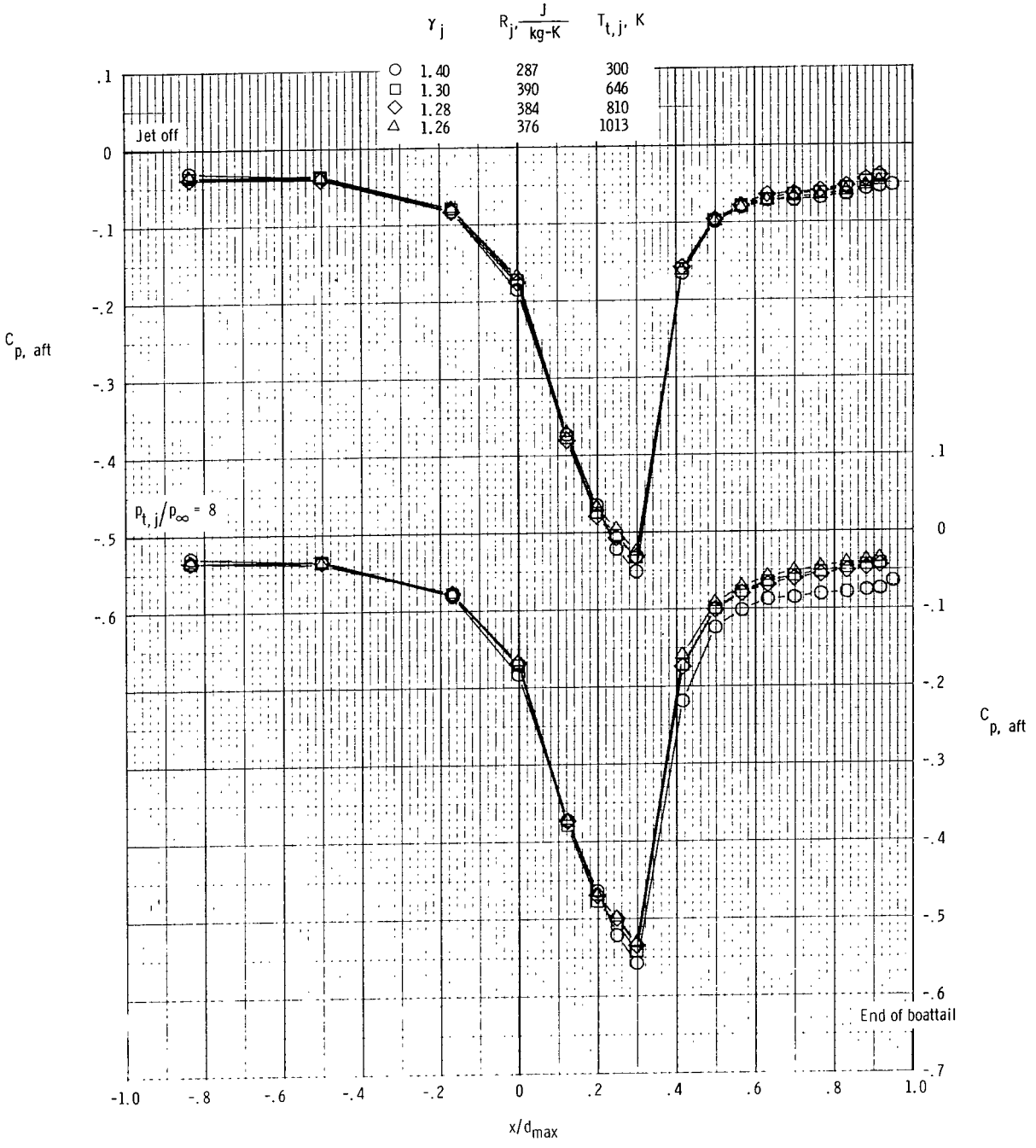

(f) M_∞ = 0.95; $p_{t,j}/p_\infty$ = Jet off to 8.

Figure 16.- Continued.

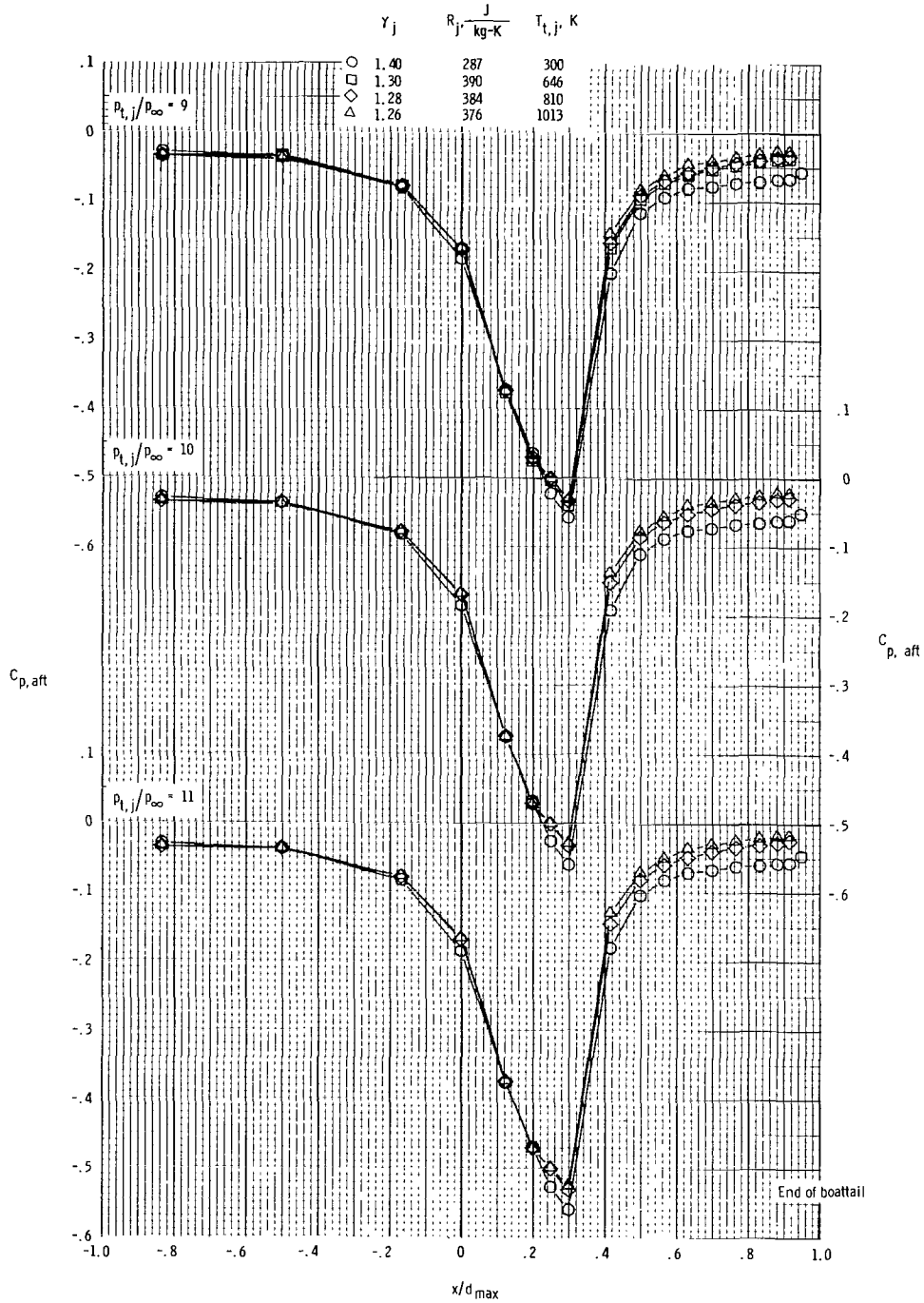

(g) $M_\infty = 0.95$; $p_{t,j}/p_\infty = 9$ to 11.

Figure 16.- Continued.

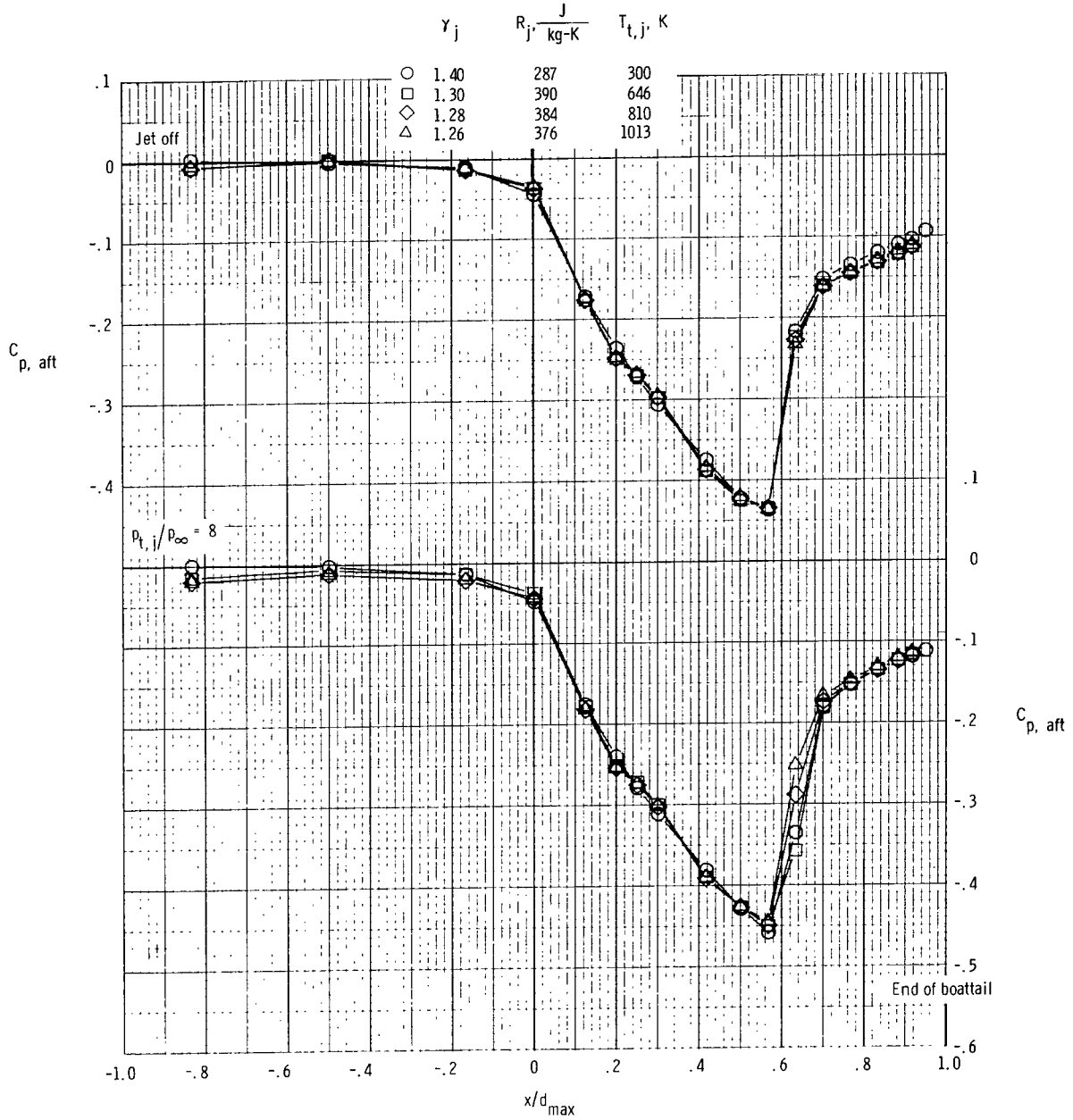

(h) M_∞ = 1.20; $p_{t,j}/p_\infty$ = Jet off to 8.

Figure 16.- Continued.

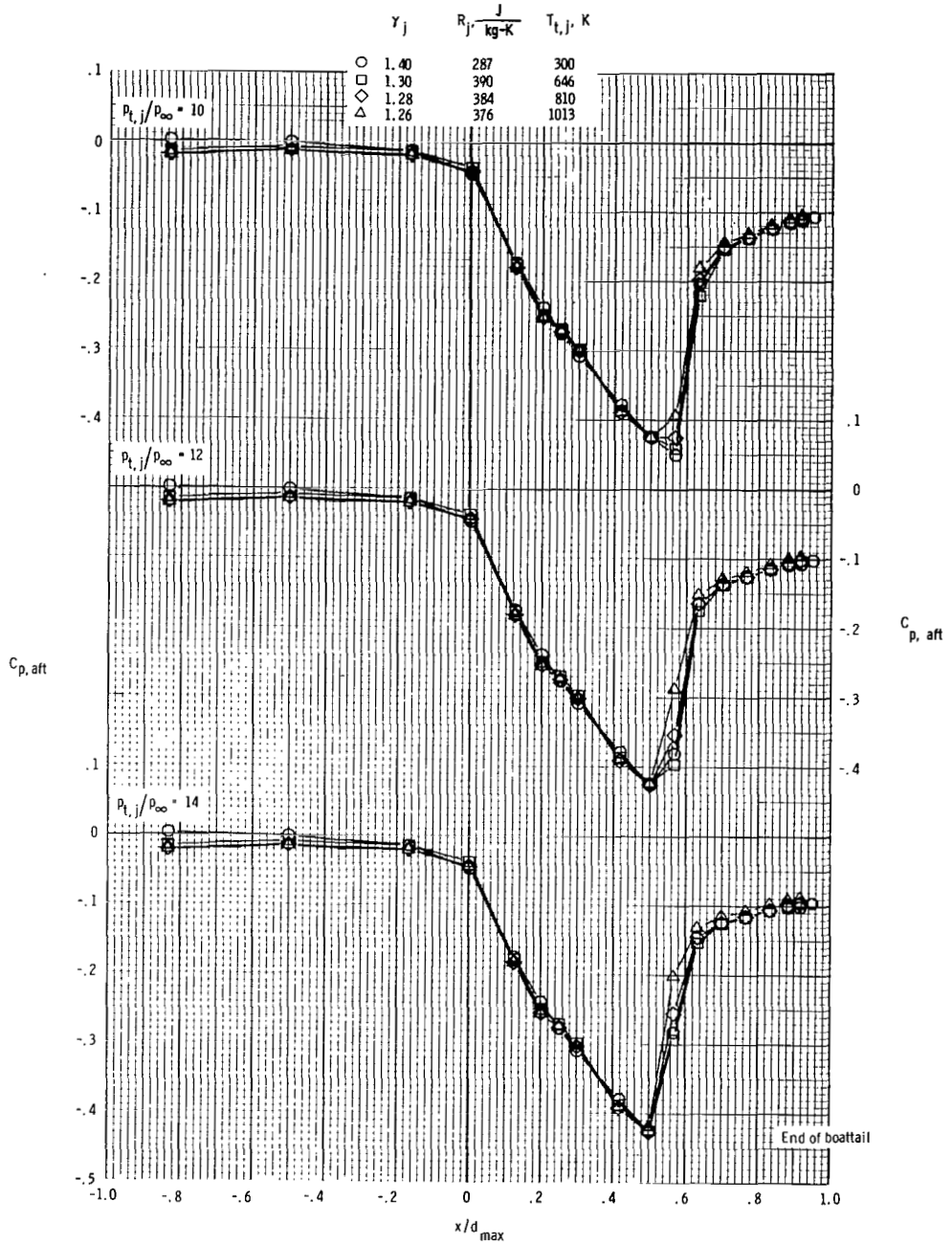

(i) $M_\infty = 1.20$; $p_{t,j}/p_\infty = 10$ to 14.

Figure 16.- Concluded.

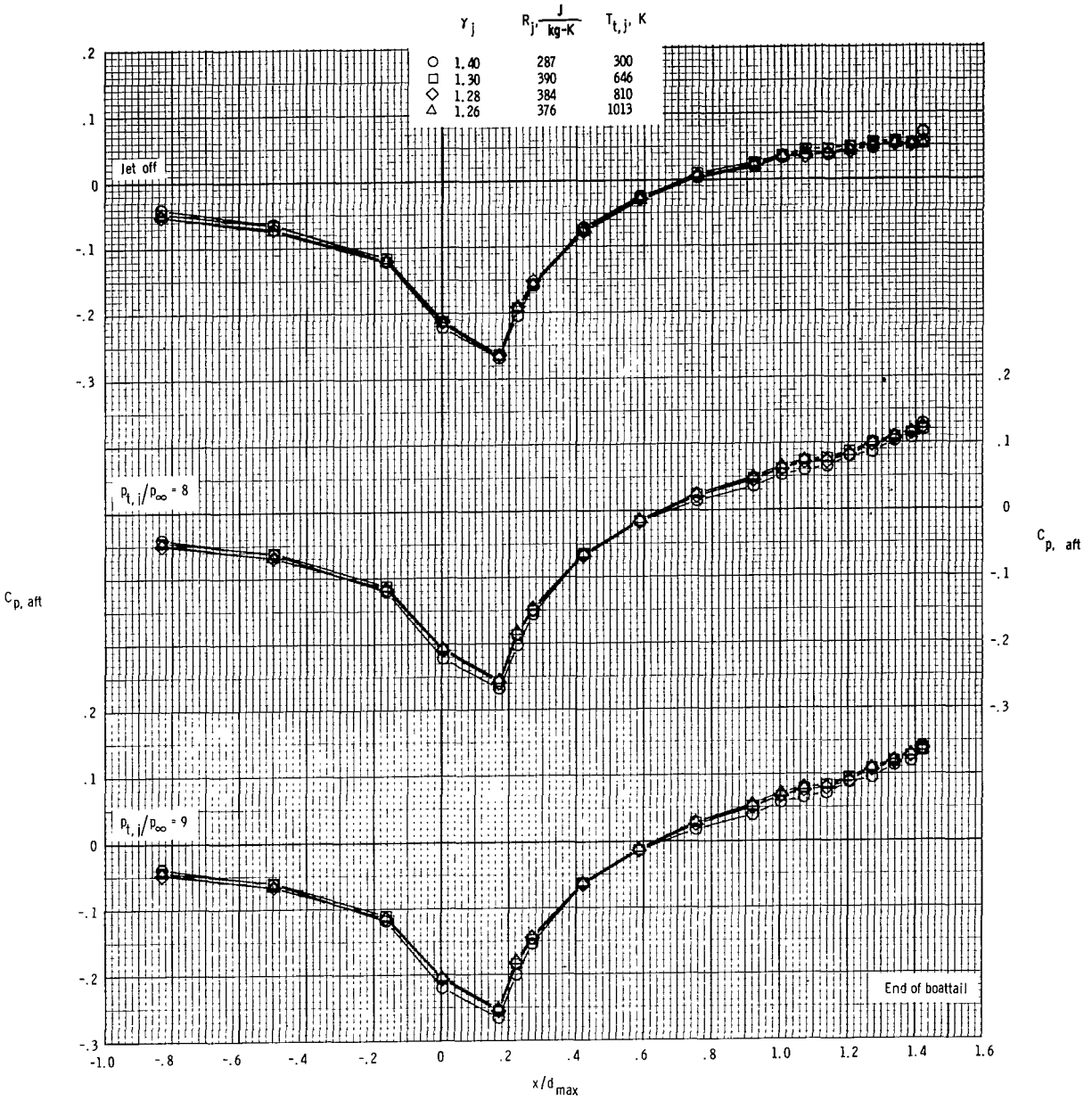

(a) $M_\infty = 0.60$; $p_{t,j}/p_\infty$ = Jet off to 9.

Figure 17.- Afterbody pressure coefficient distributions for each of the four jet exhaust gases. $\beta = 10^o$; $M_e = 2$. (Each pressure coefficient is interpolated for exact values of jet total pressure ratio.)

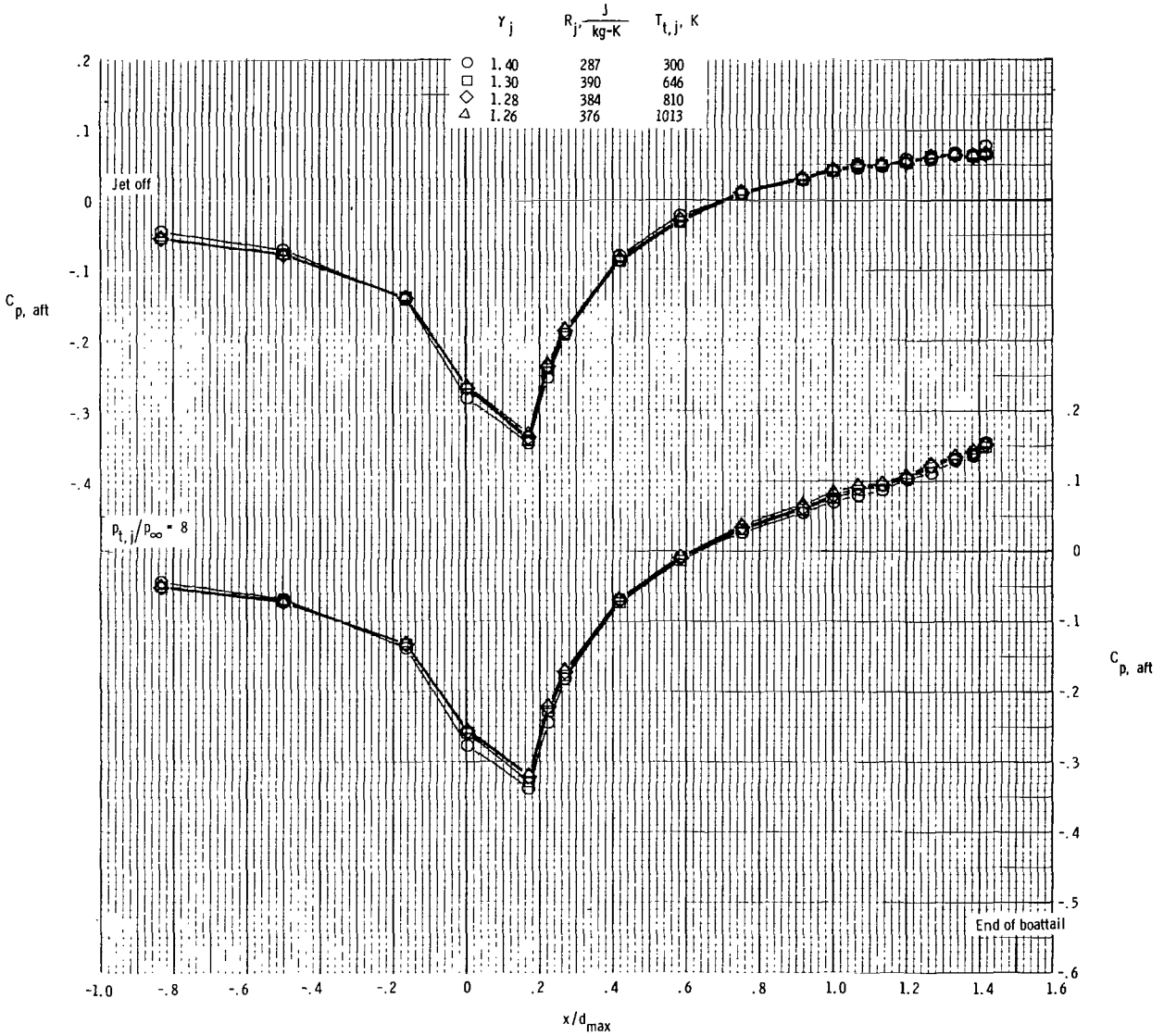

(b) $M_\infty = 0.80$; $p_{t,j}/p_\infty$ = Jet off to 8.

Figure 17.- Continued.

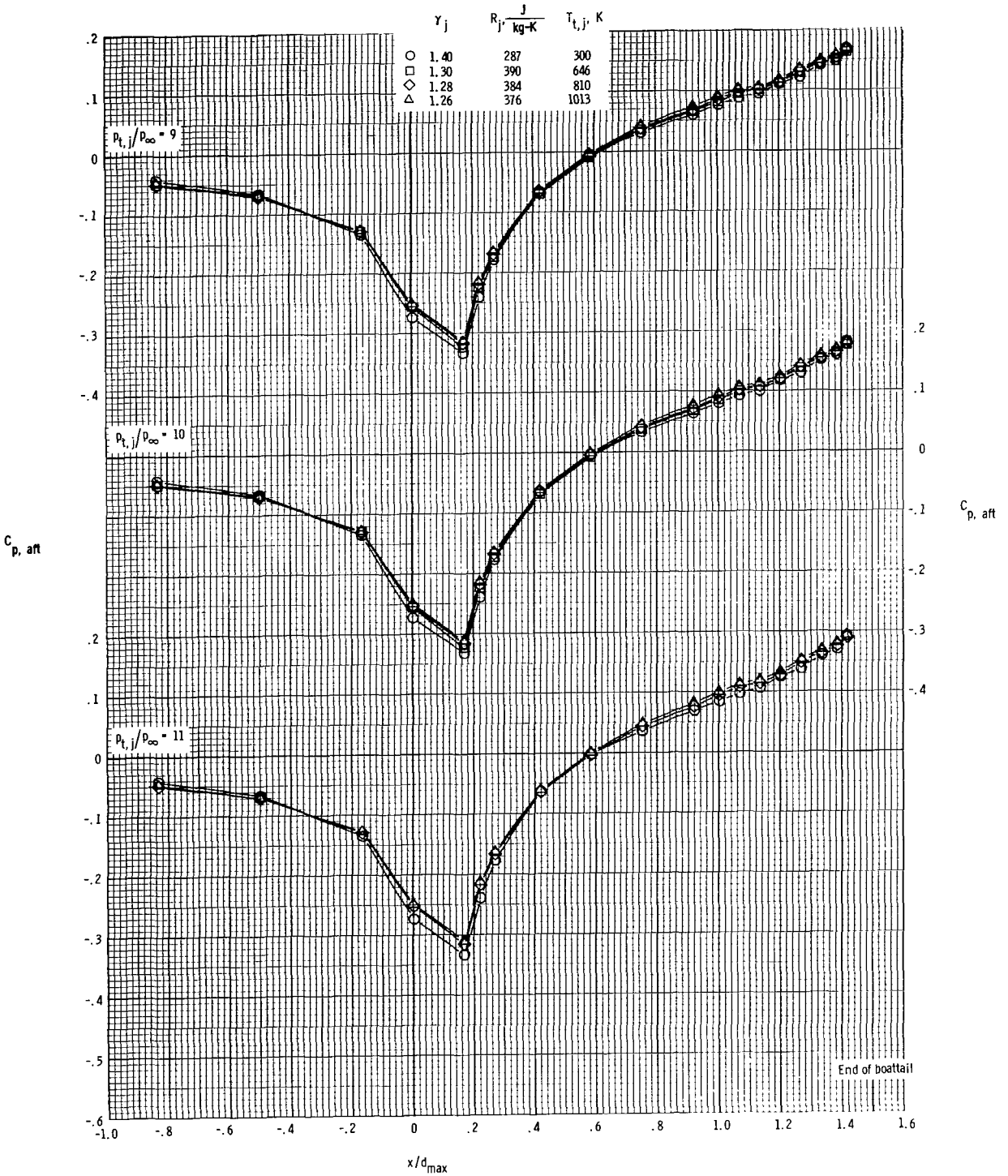

(c) $M_\infty = 0.80$; $p_{t,j}/p_\infty = 9$ to 11.

Figure 17.- Continued.

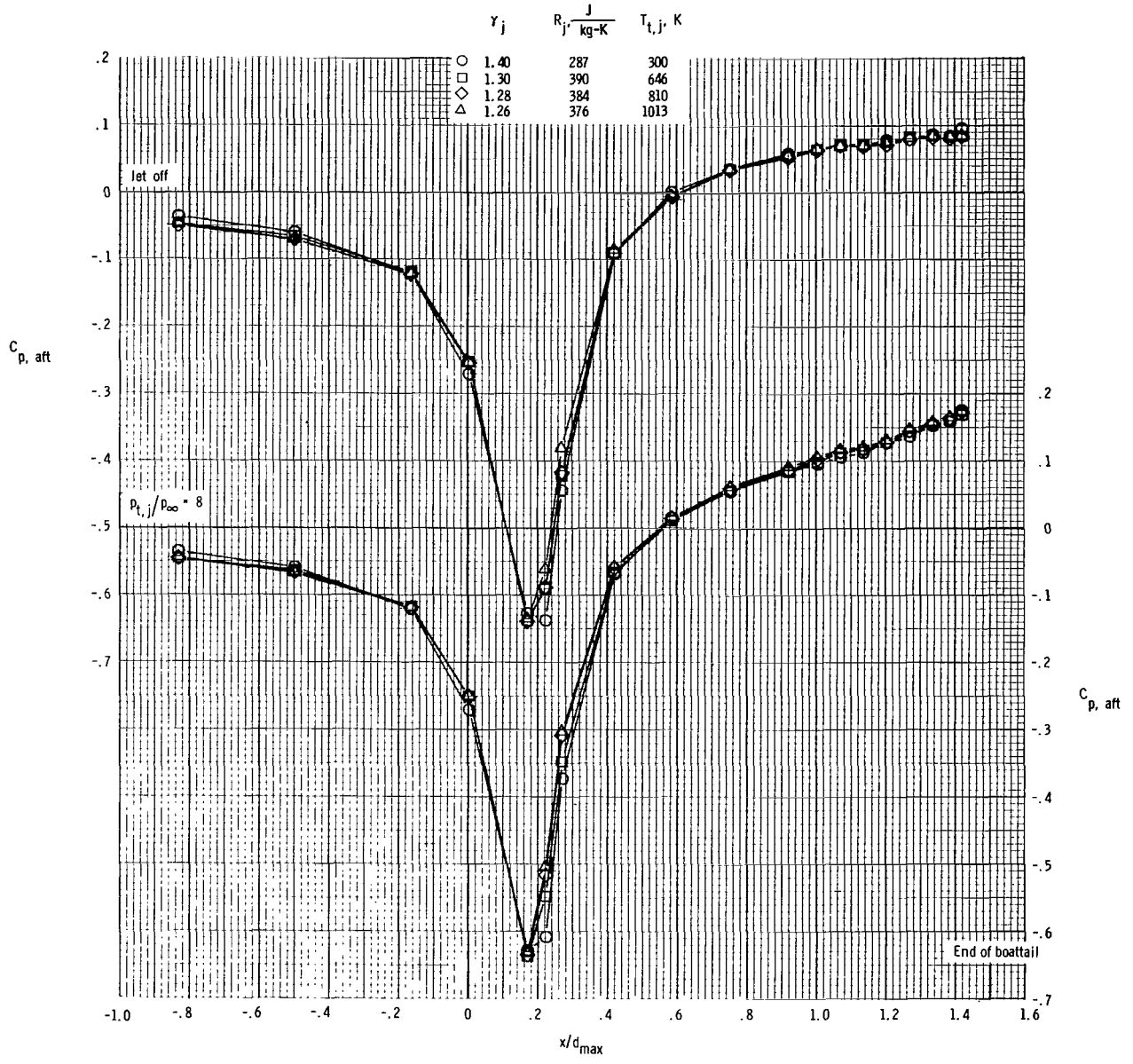

(d) $M_\infty = 0.90$; $p_{t,j}/p_\infty$ = Jet off to 8.

Figure 17.- Continued.

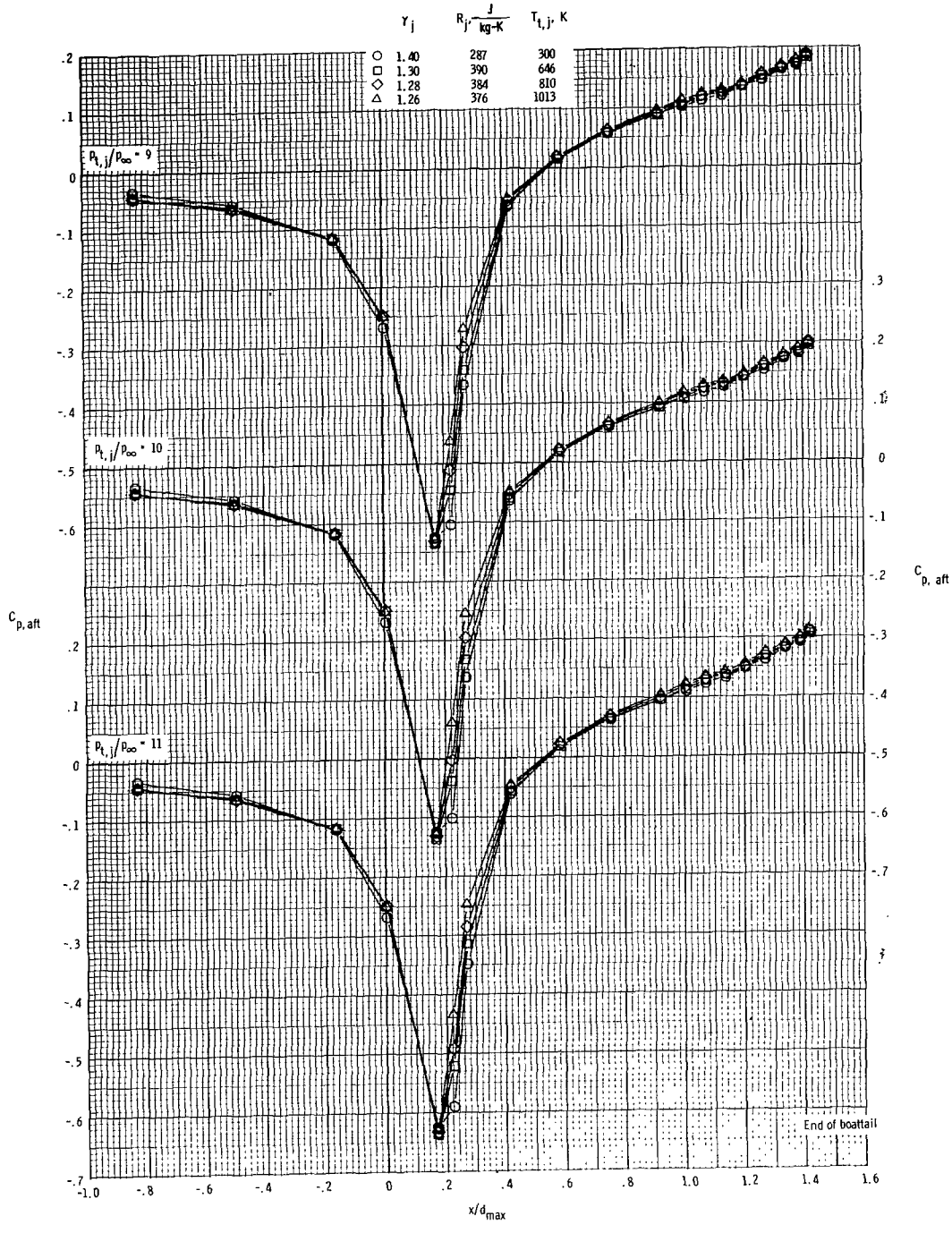

(e) $M_\infty = 0.90$; $p_{t,j}/p_\infty = 9$ to 11.

Figure 17.- Continued.

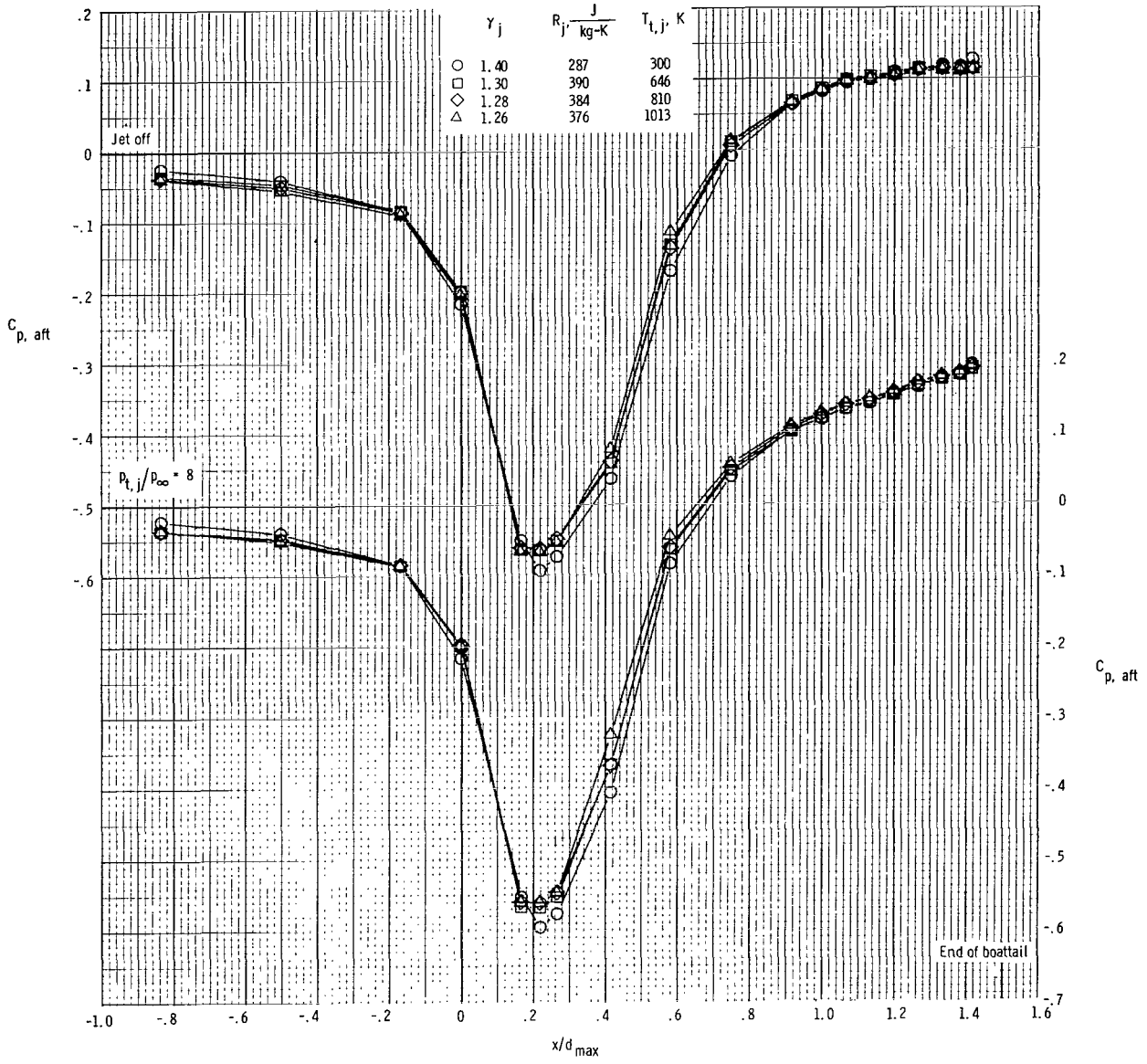

(f) $M_\infty = 0.95$; $p_{t,j}/p_\infty$ = Jet off to 8.

Figure 17.- Continued.

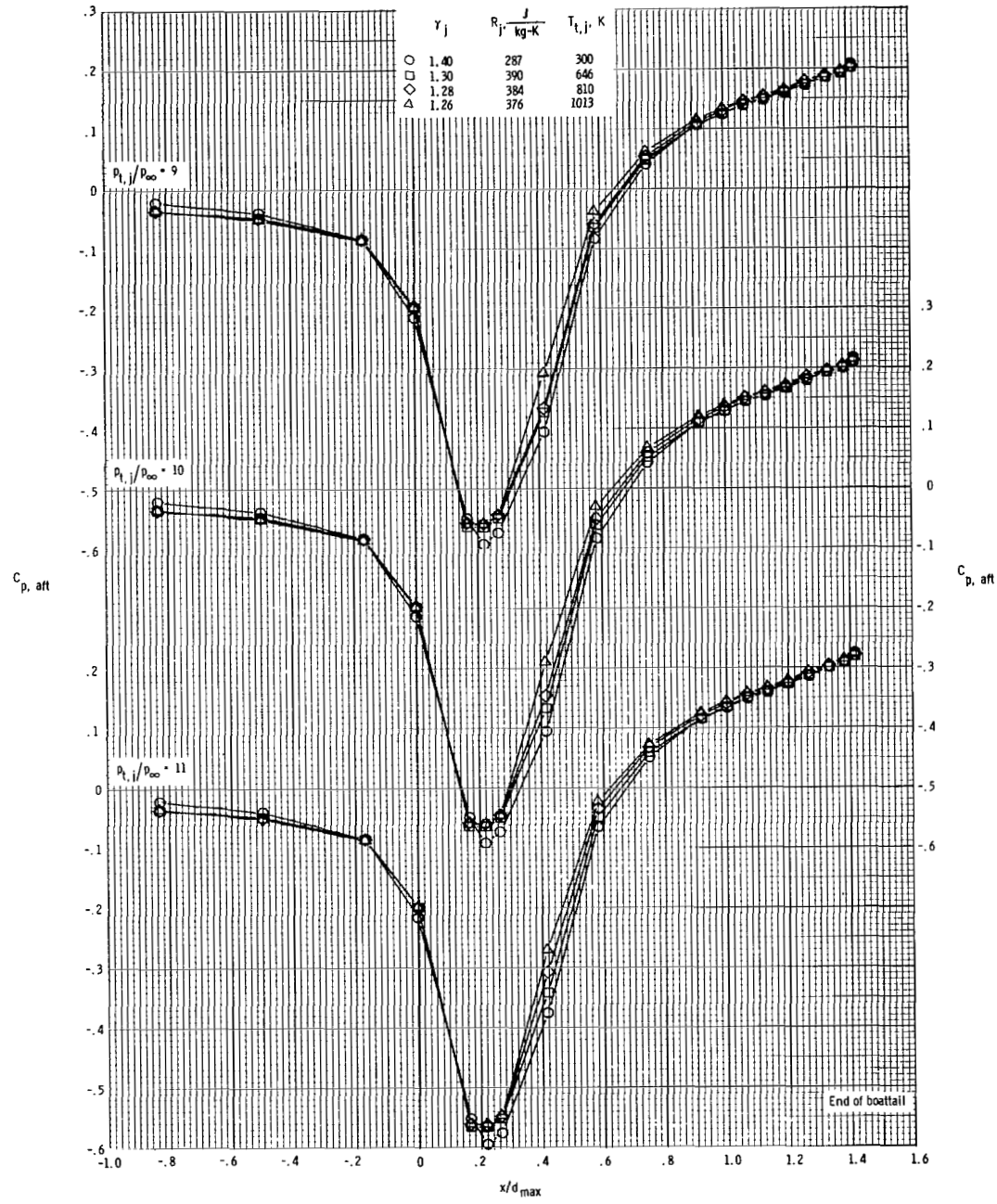

(g) $M_\infty = 0.95$; $p_{t,j}/p_\infty = 9$ to 11.

Figure 17.- Continued.

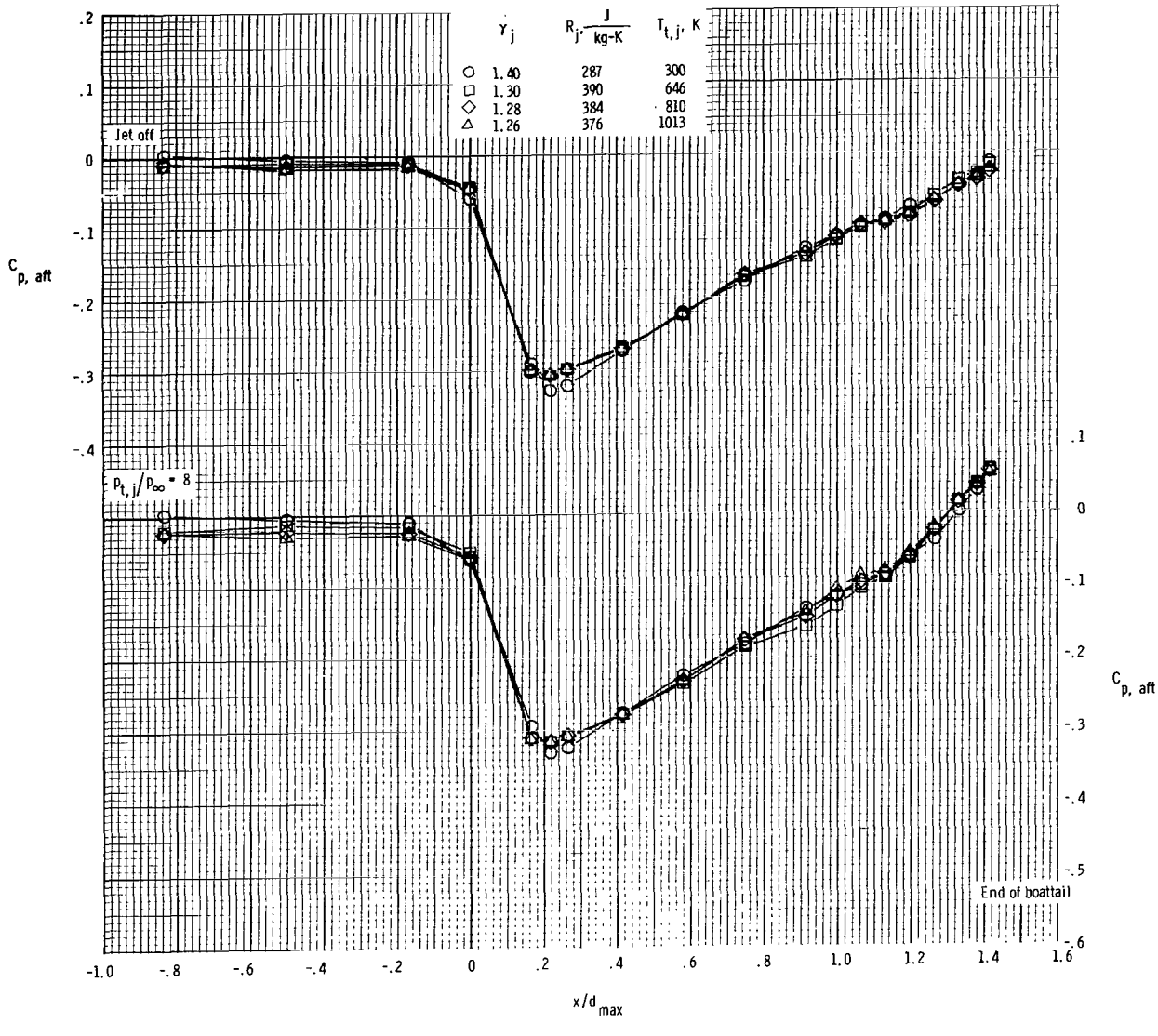

(h) $M_\infty = 1.20$; $p_{t,j}/p_\infty$ = Jet off to 8.

Figure 17.- Continued.

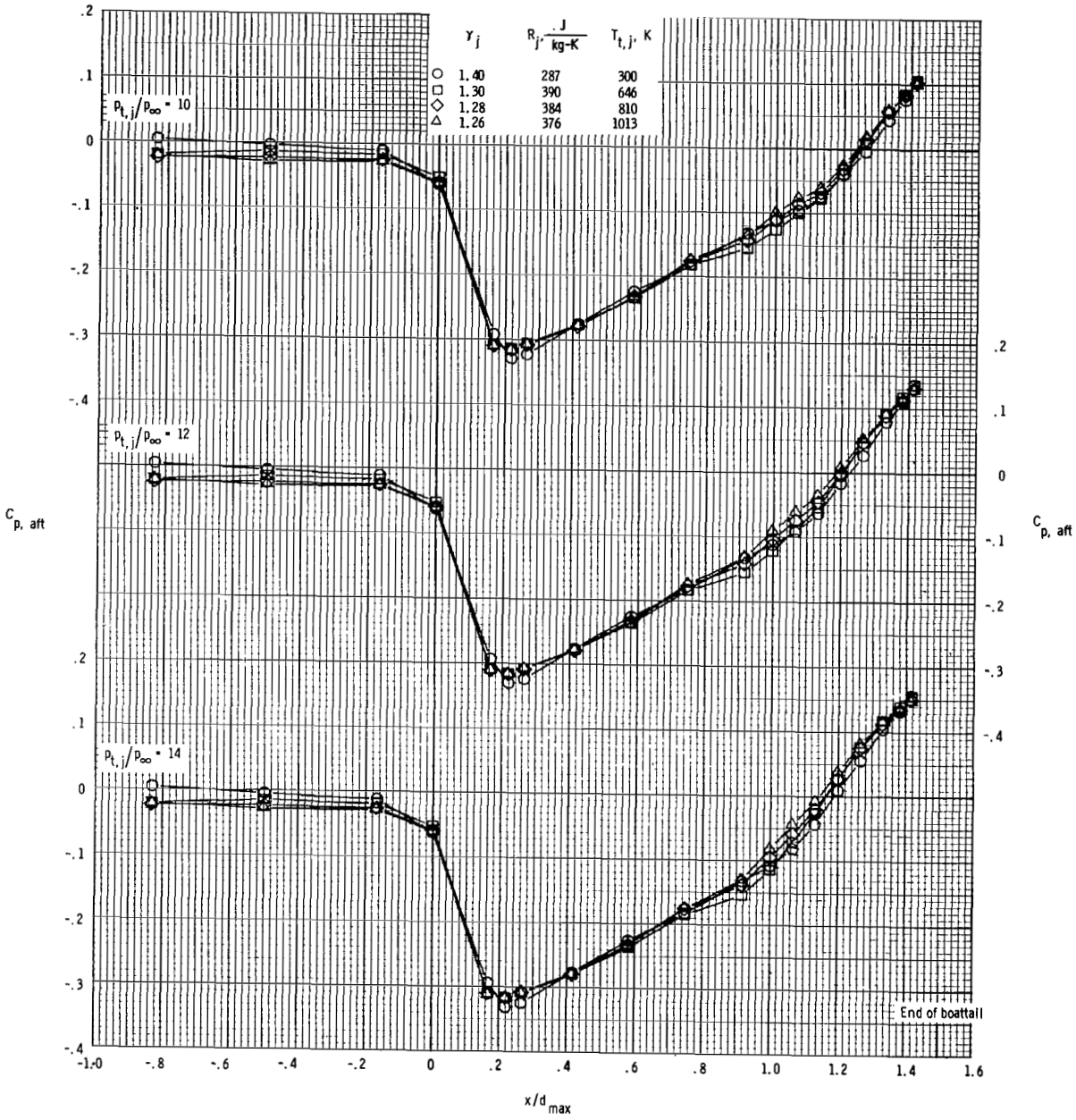

(i) $M_\infty = 1.20$; $p_{t,j}/p_\infty = 10$ to 14.

Figure 17.- Concluded.

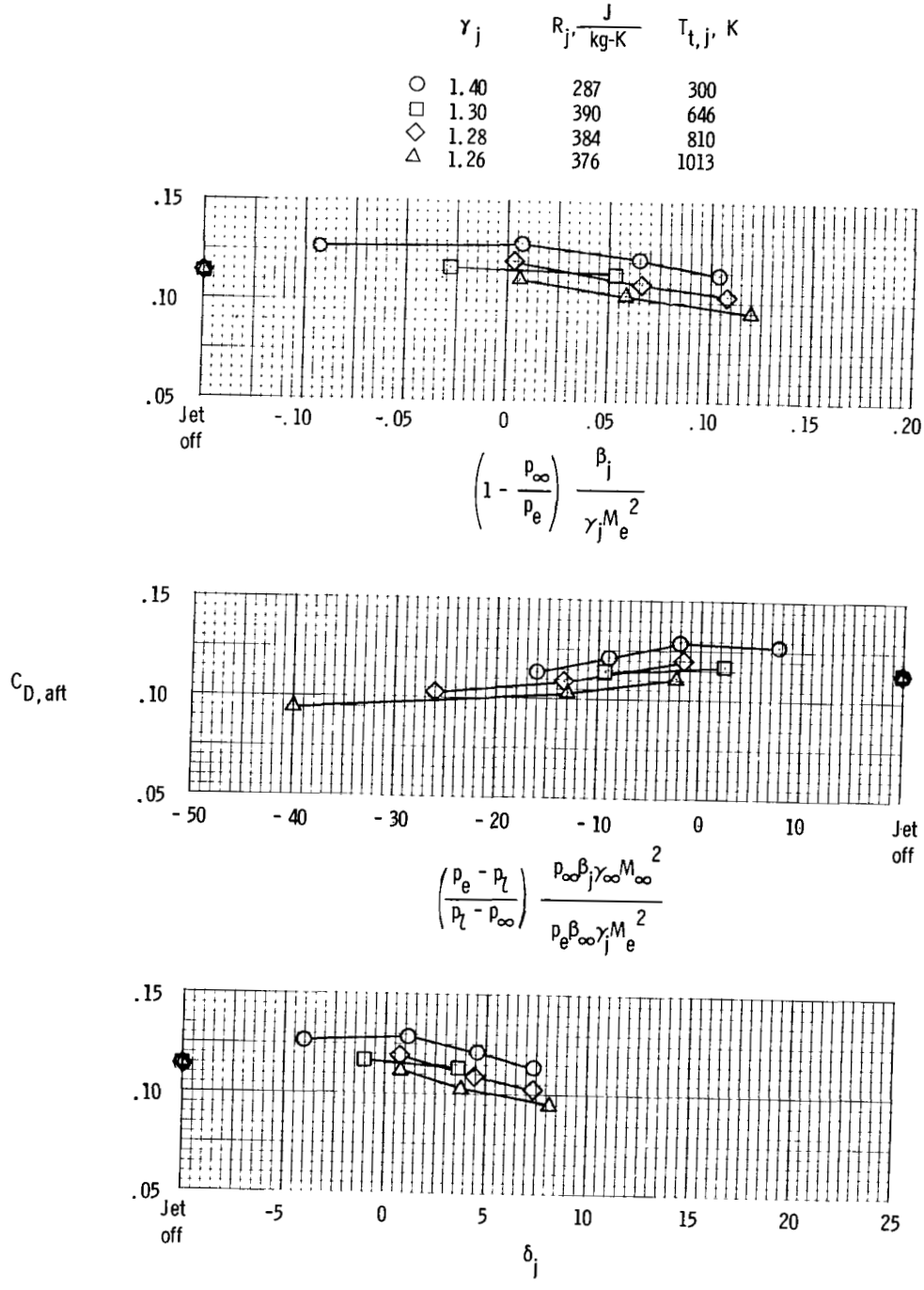

Figure 18.- Comparison of jet boundary simulation parameters. $\beta = 20^{O}$; $M_e = 2$; $M_\infty = 0.95$.

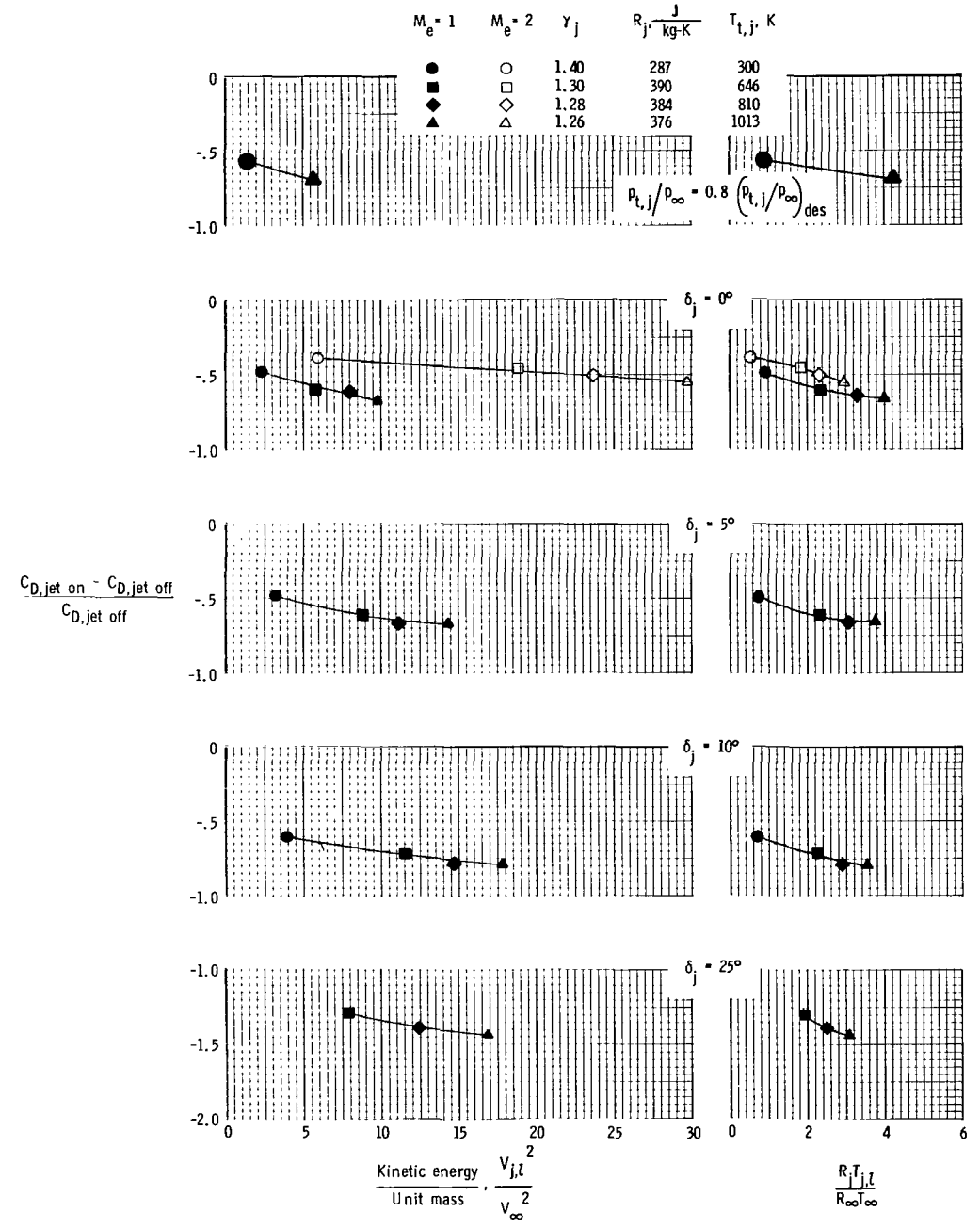

(a) $M_\infty = 0.60$.

Figure 19.- Incremental afterbody drag coefficient as a function of kinetic energy per unit mass and $R_j T_{j,\ell}/R_\infty T_\infty$. $\beta = 20^o$.

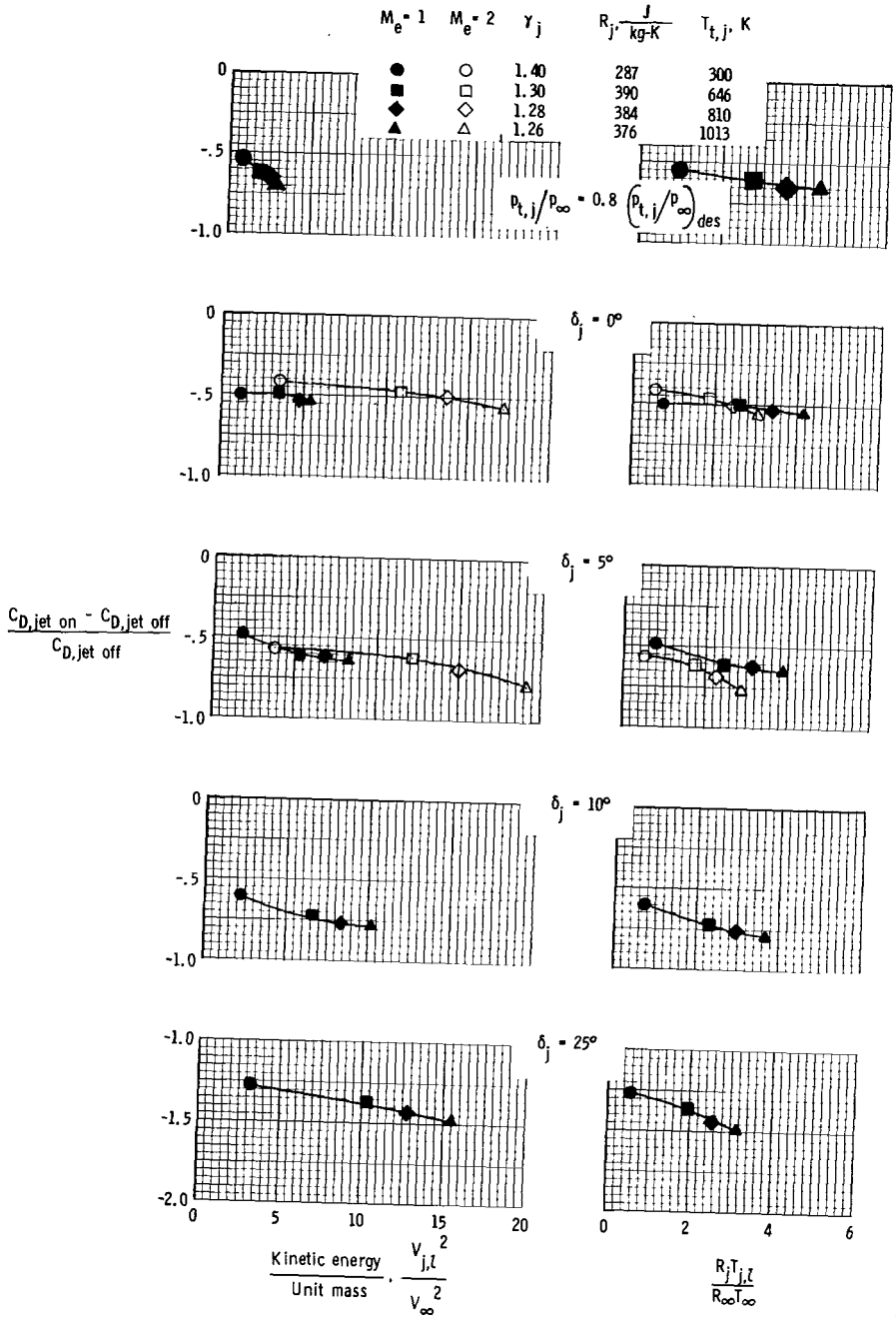

(b) $M_\infty = 0.80$.

Figure 19.- Continued.

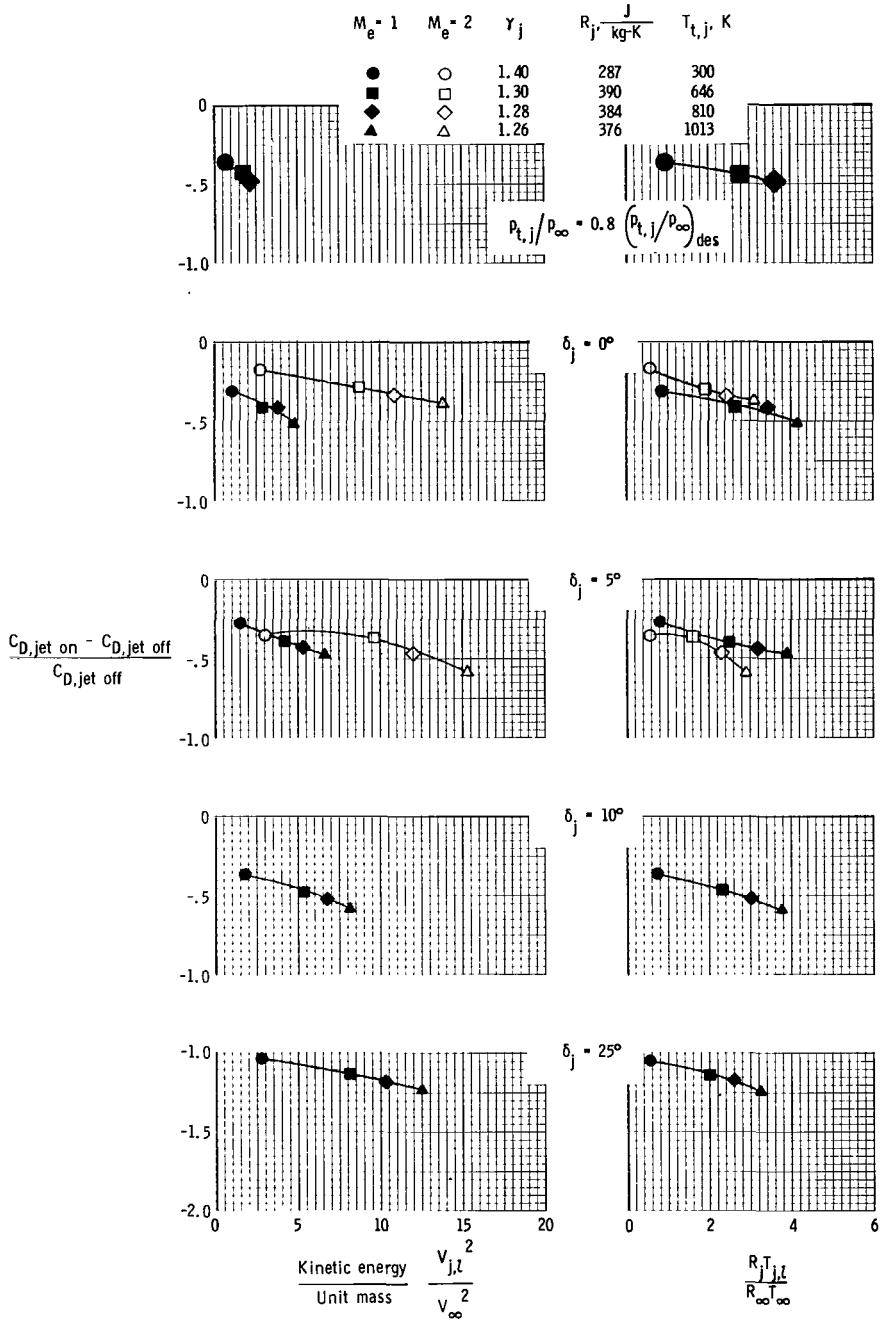

(c) $M_\infty = 0.90$.

Figure 19.- Continued.

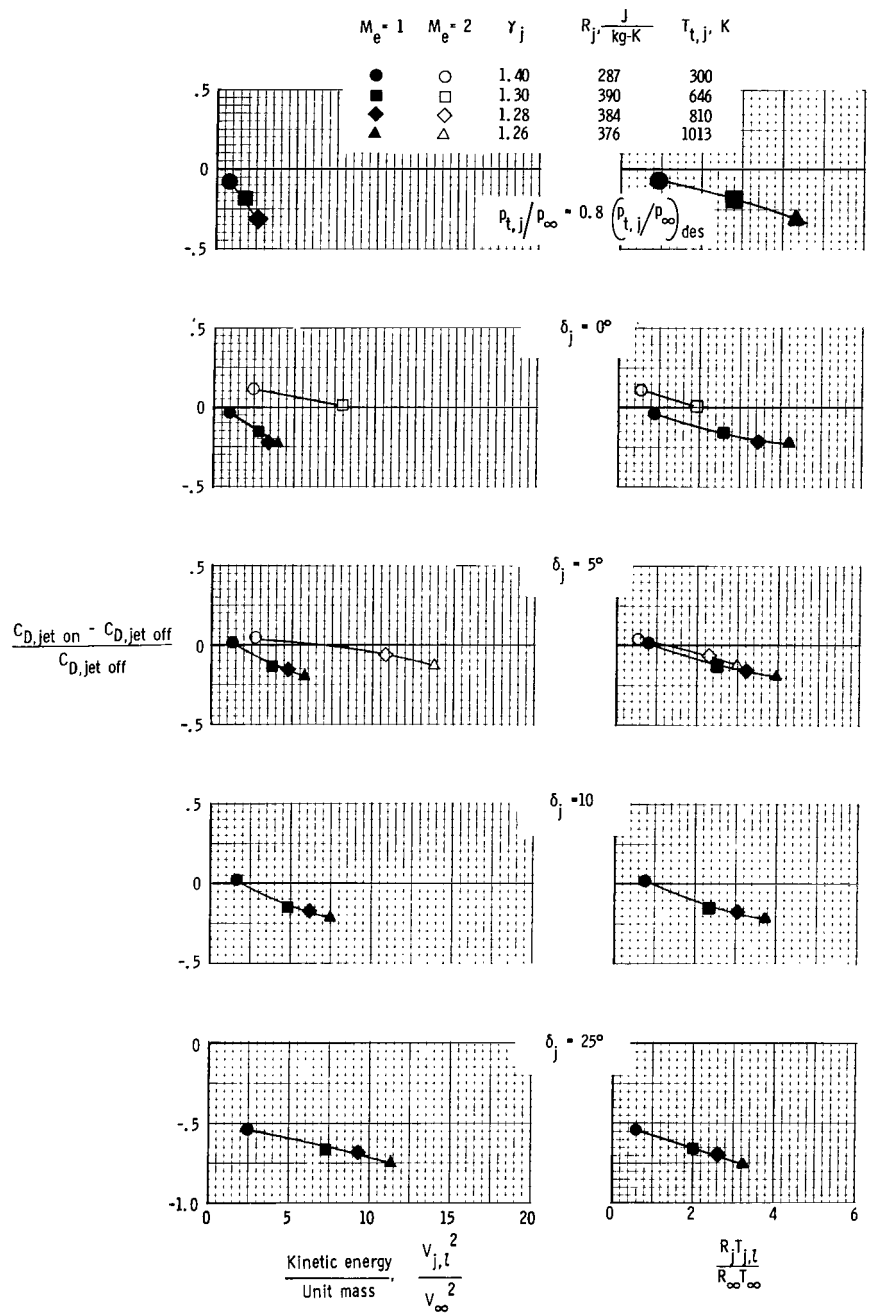

(d) $M_\infty = 0.95$.

Figure 19.- Continued.

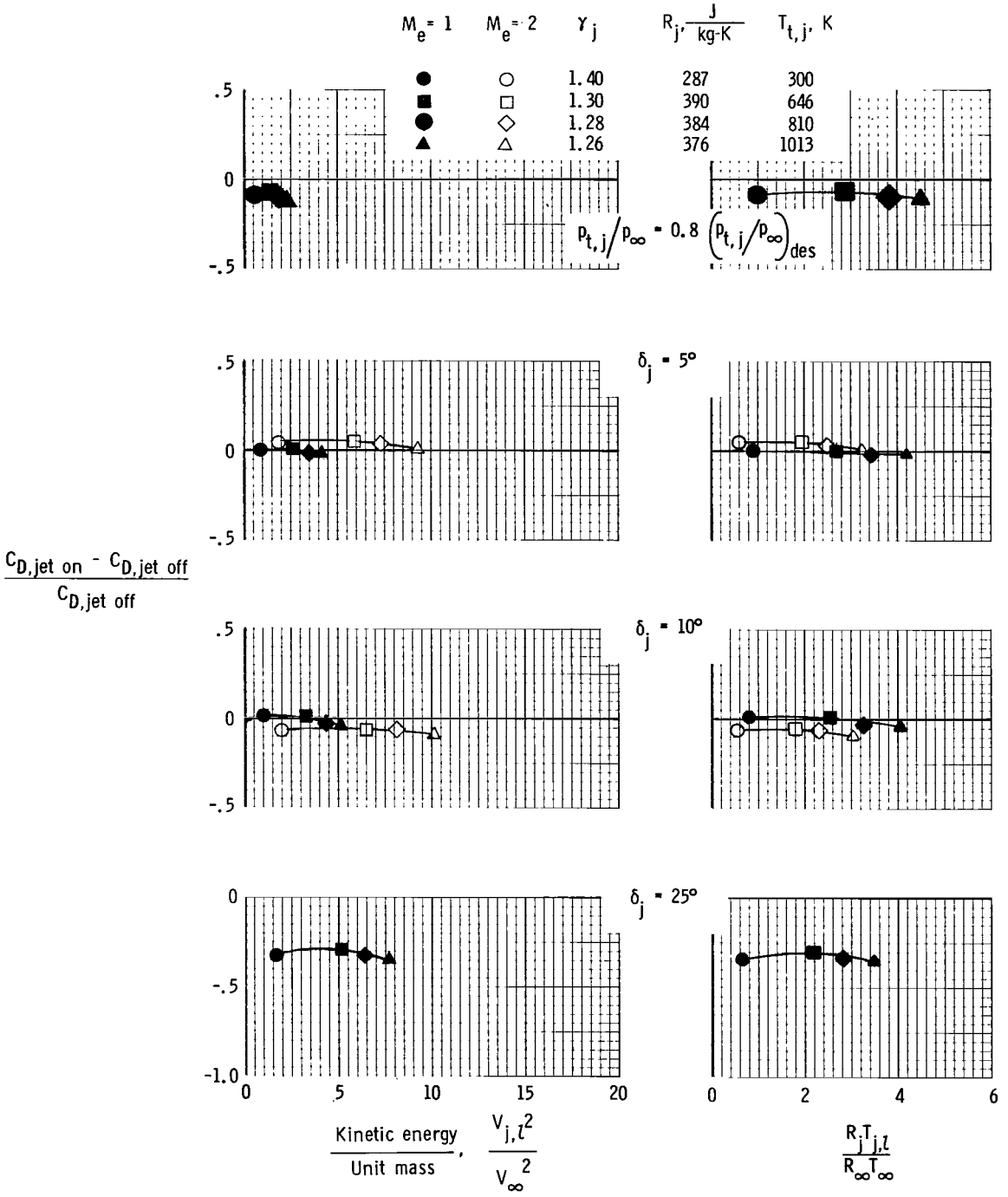

(e) M_∞ = 1.20.

Figure 19.- Concluded.

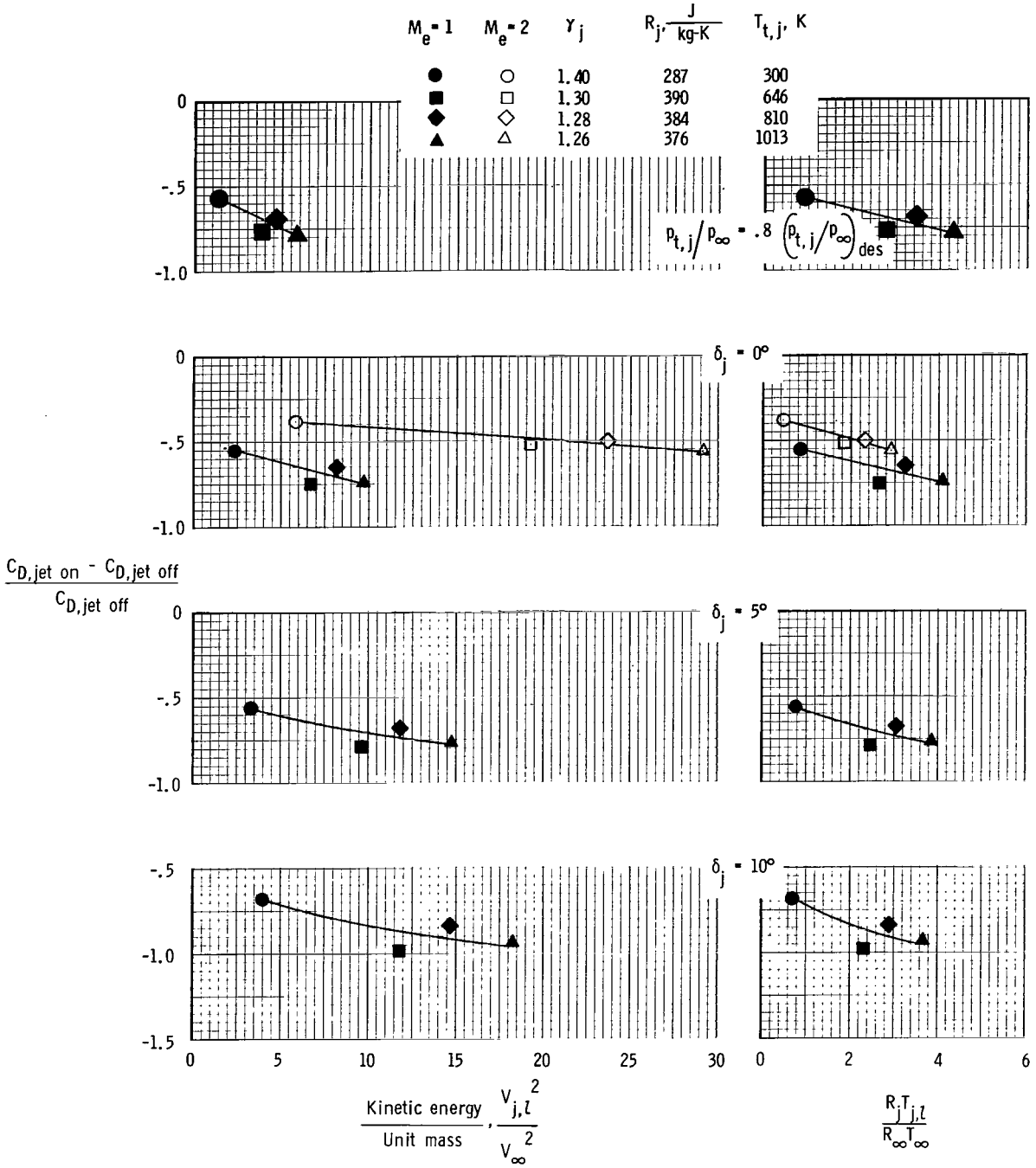

(a) $M_\infty = 0.60$.

Figure 20.- Incremental afterbody drag coefficient as a function of kinetic energy per unit mass and $R_j T_{j,\ell}/R_\infty T_\infty$. $\beta = 10^o$.

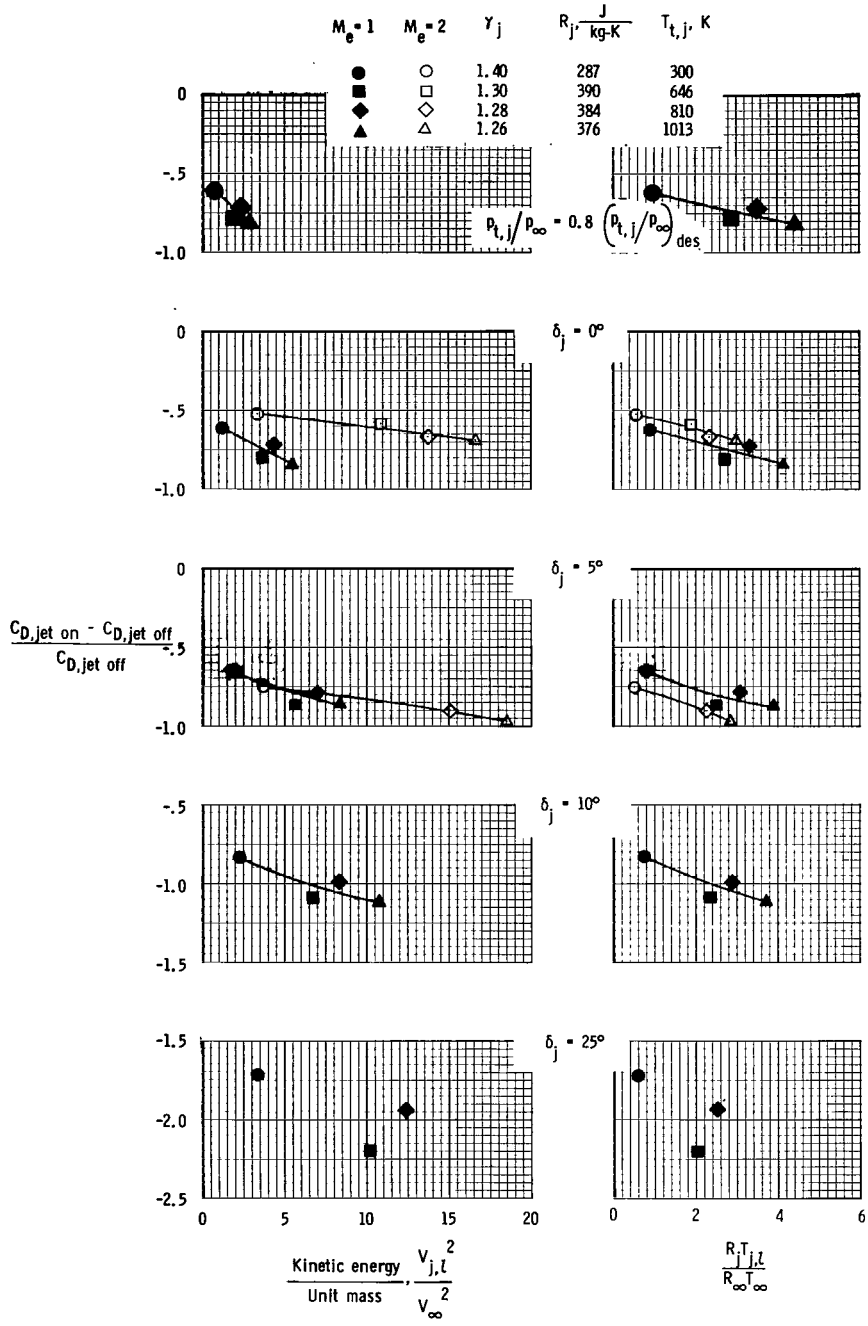

(b) $M_\infty = 0.80$.

Figure 20.- Continued.

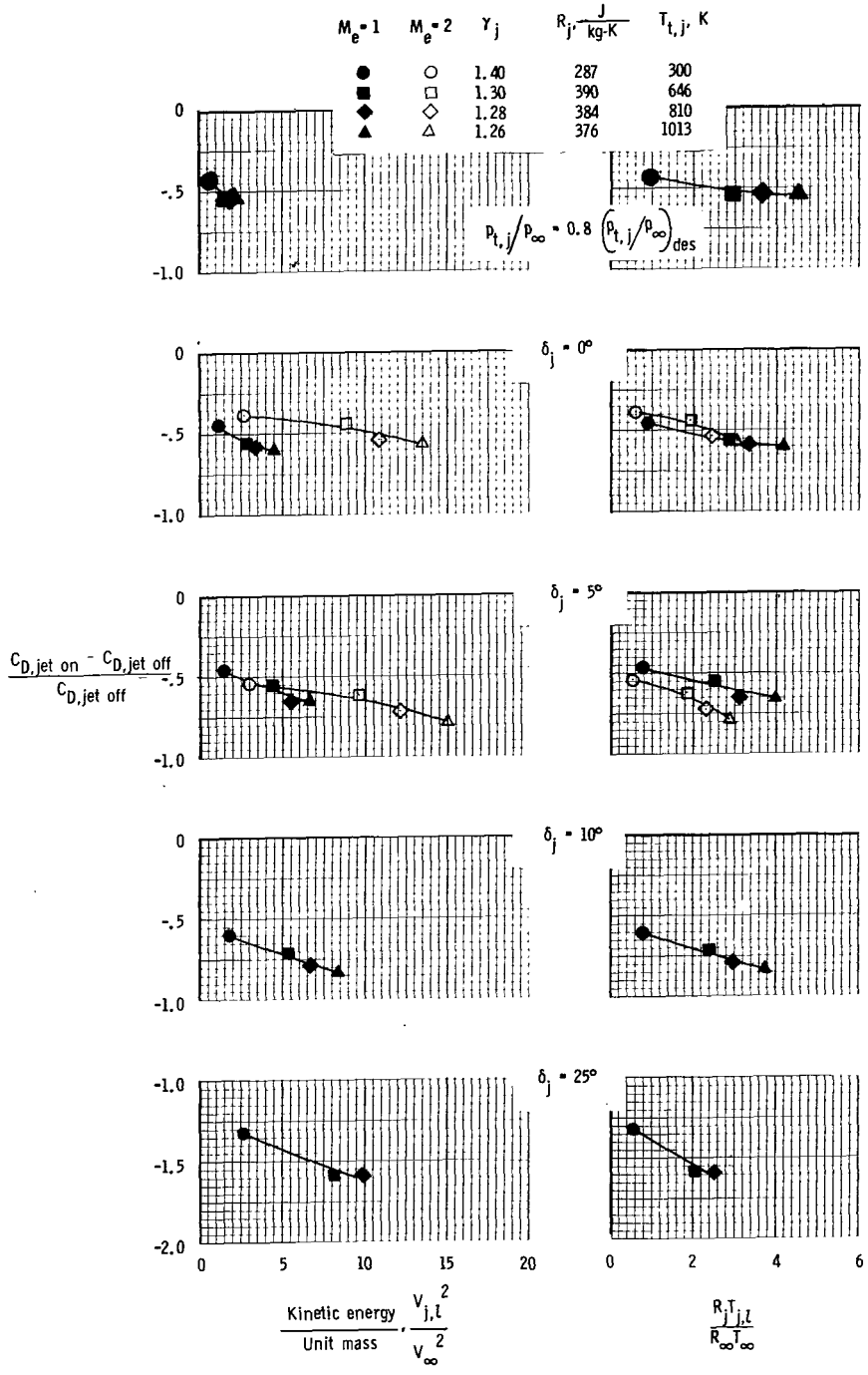

(c) $M_\infty = 0.90$.

Figure 20.- Continued.

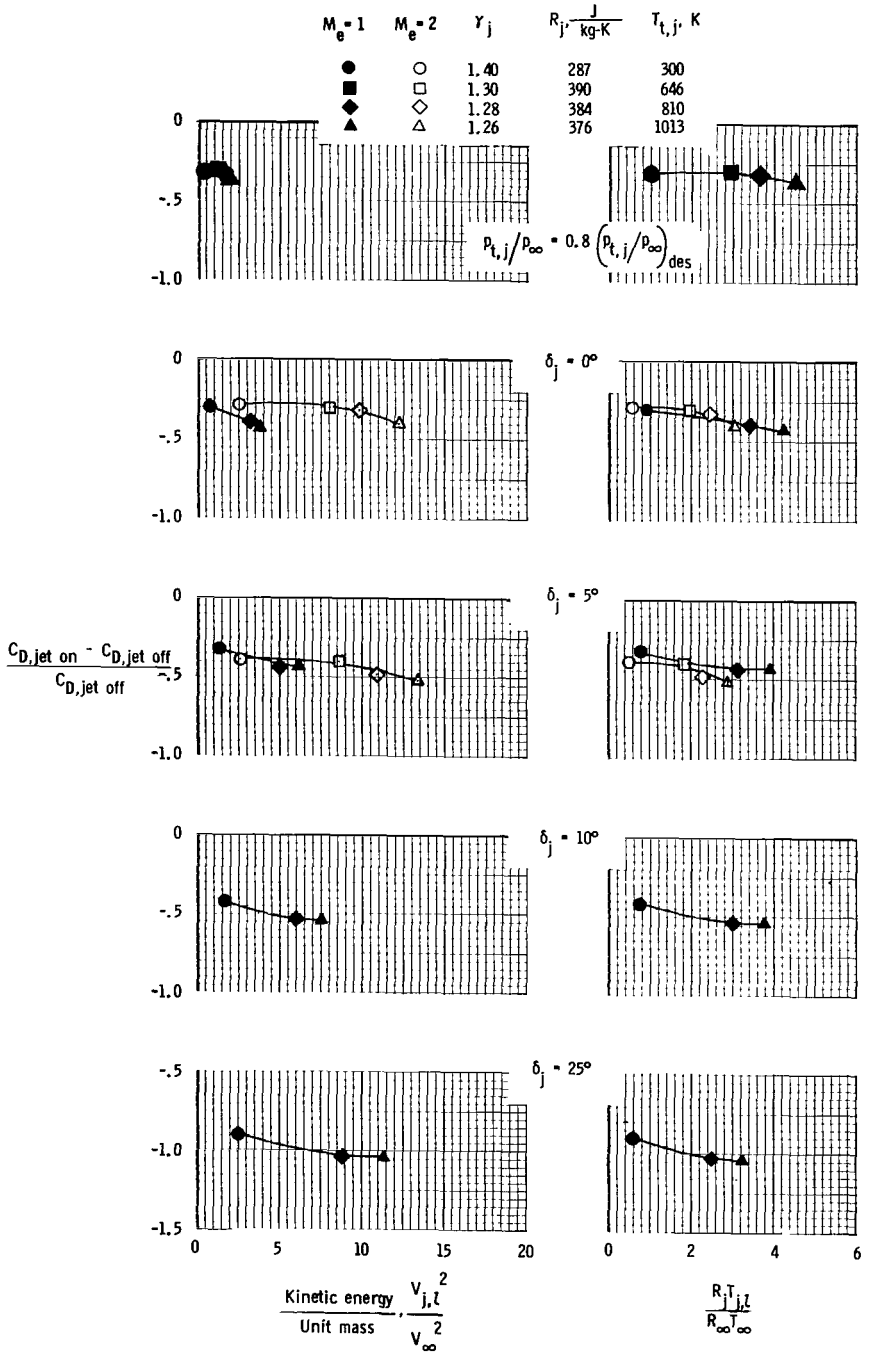

(d) $M_\infty = 0.95$.

Figure 20.- Continued.

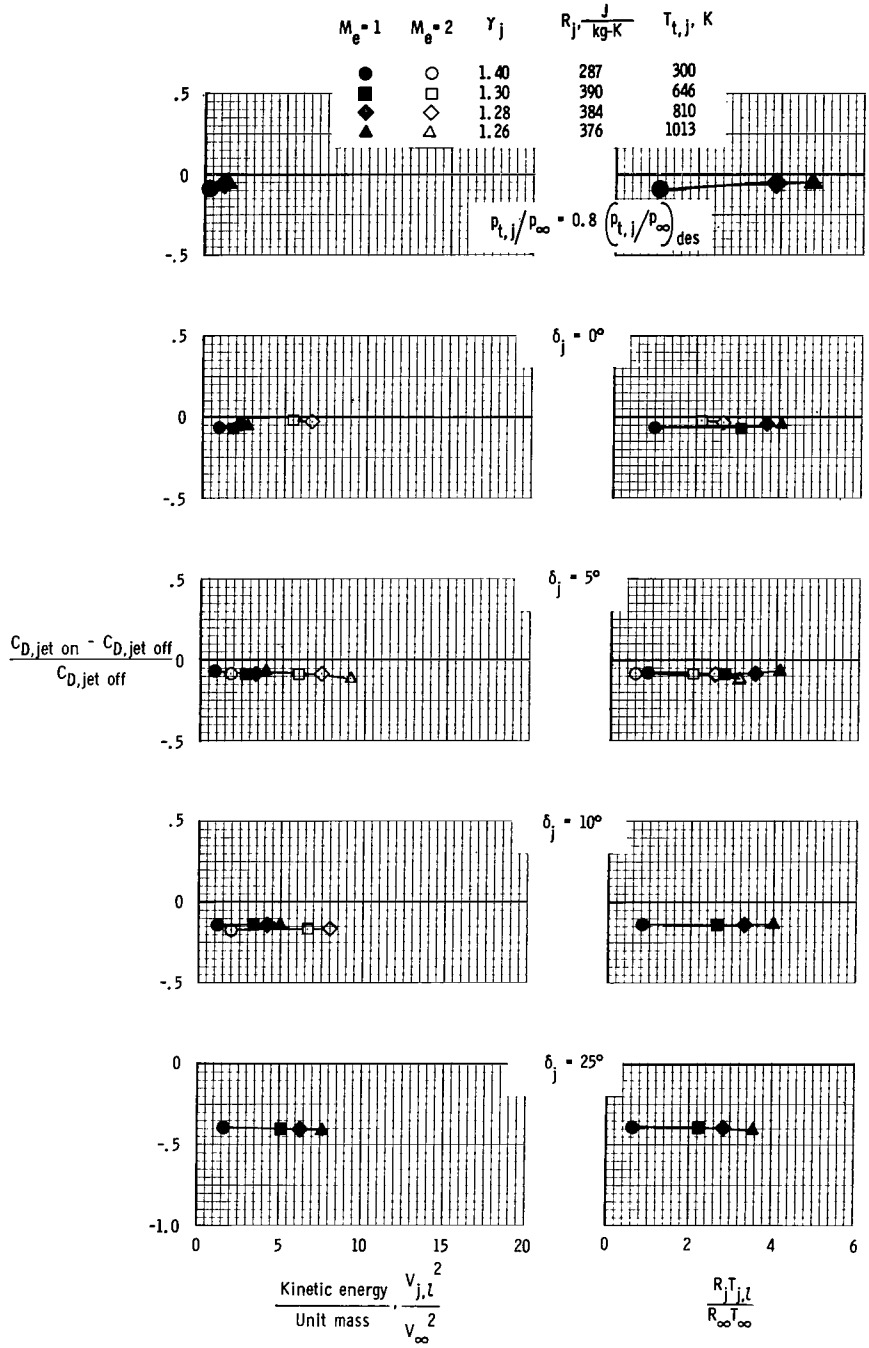

(e) $M_\infty = 1.20$.

Figure 20.- Concluded.

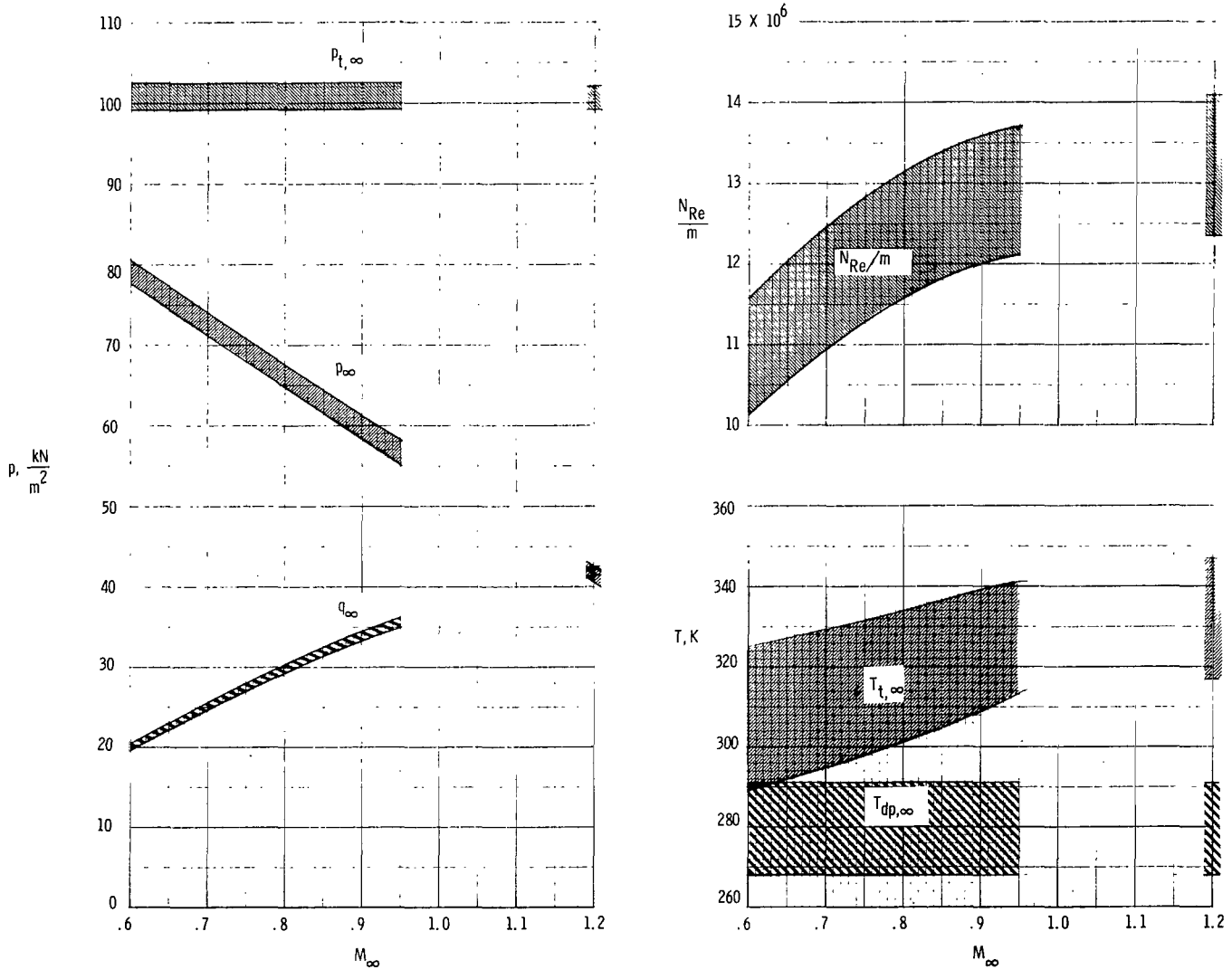

Figure 21.- Band of the free-stream parameters encountered during the investigation.

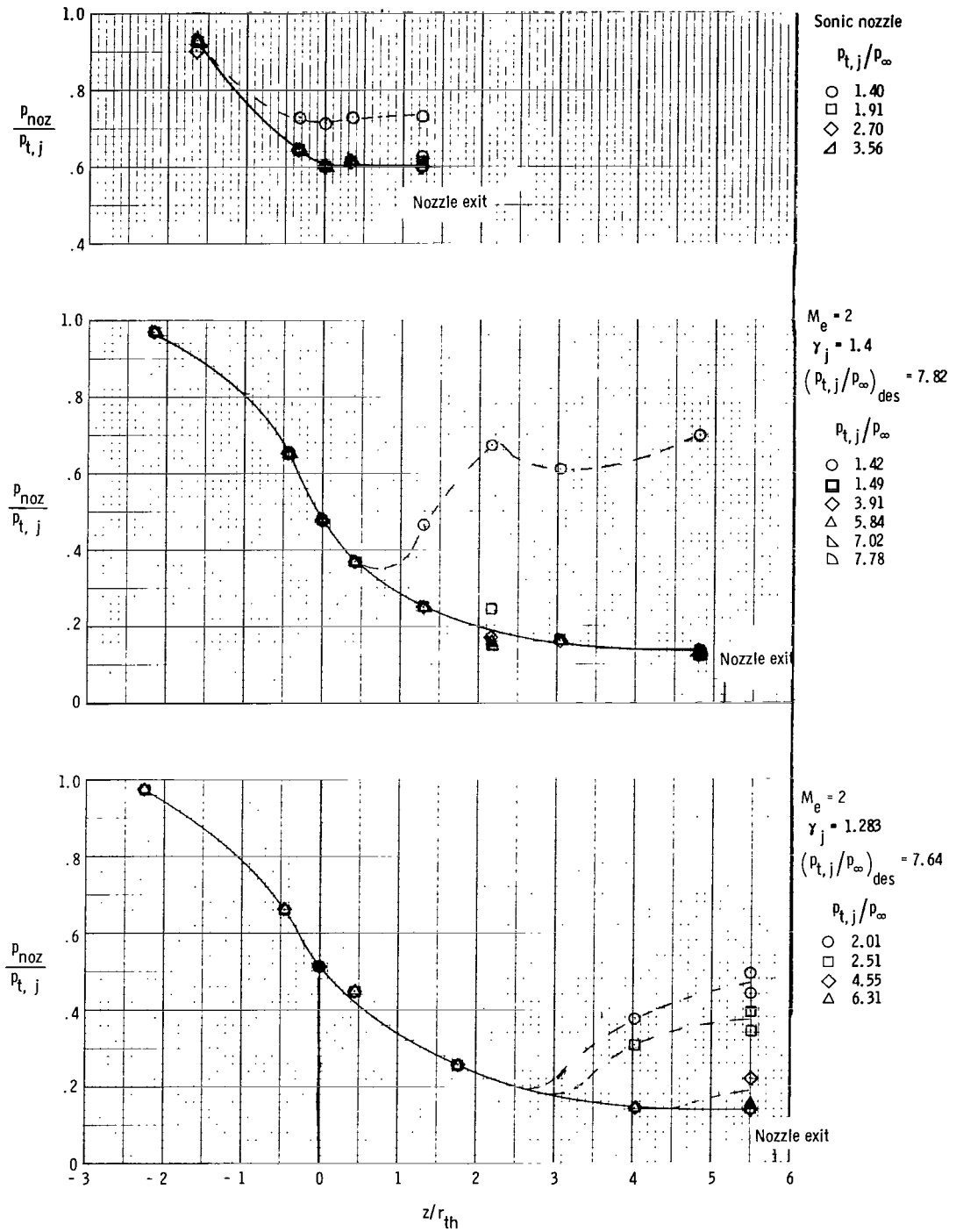

Figure 22.- Nozzle internal pressure distributions. $M_\infty = 0$.

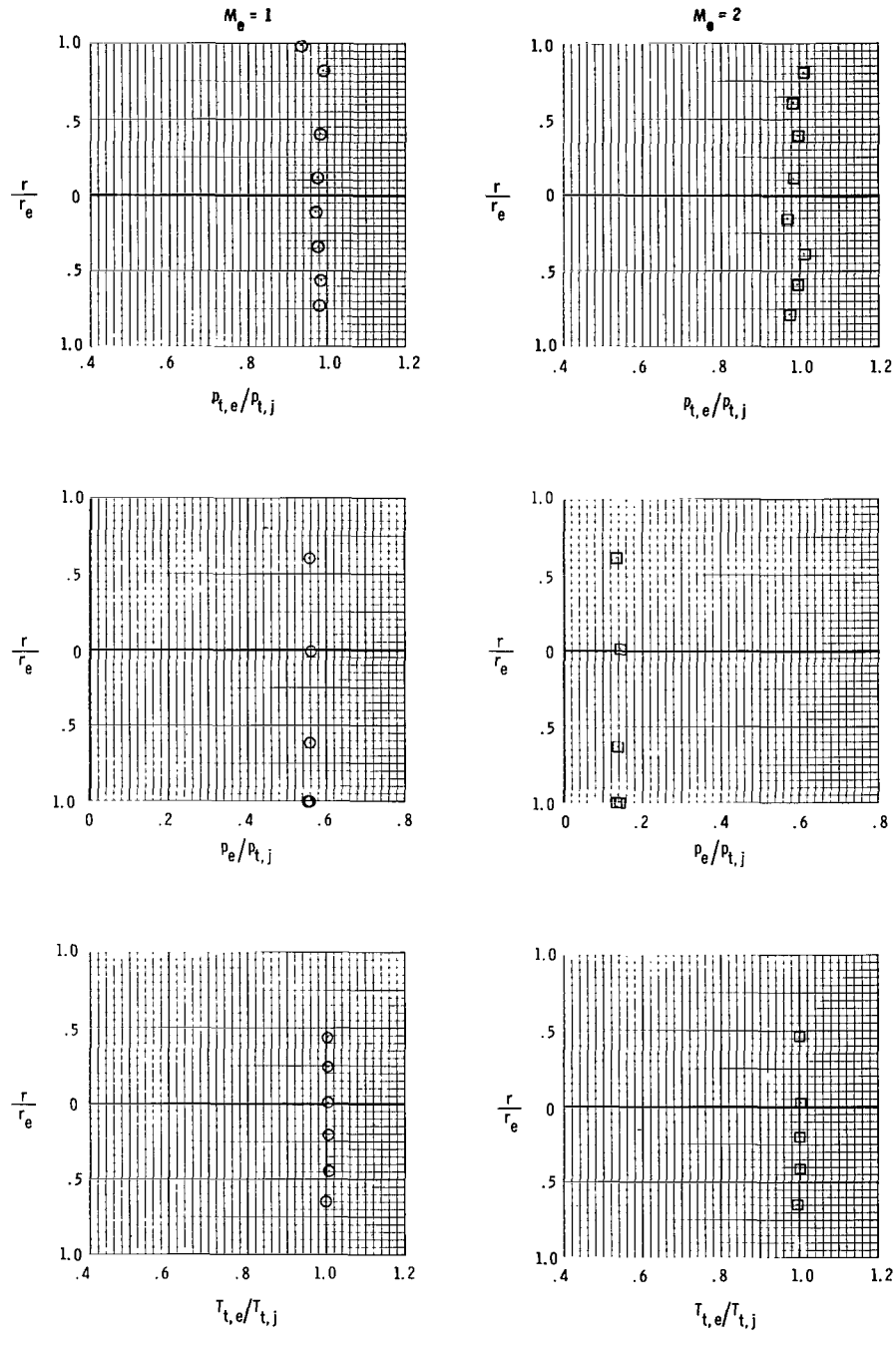

Figure 23.- Typical nozzle exit pressure and temperature profiles. $p_e/p_\infty \approx 1.0$; $\gamma_j = 1.283$; $M_\infty = 0$.

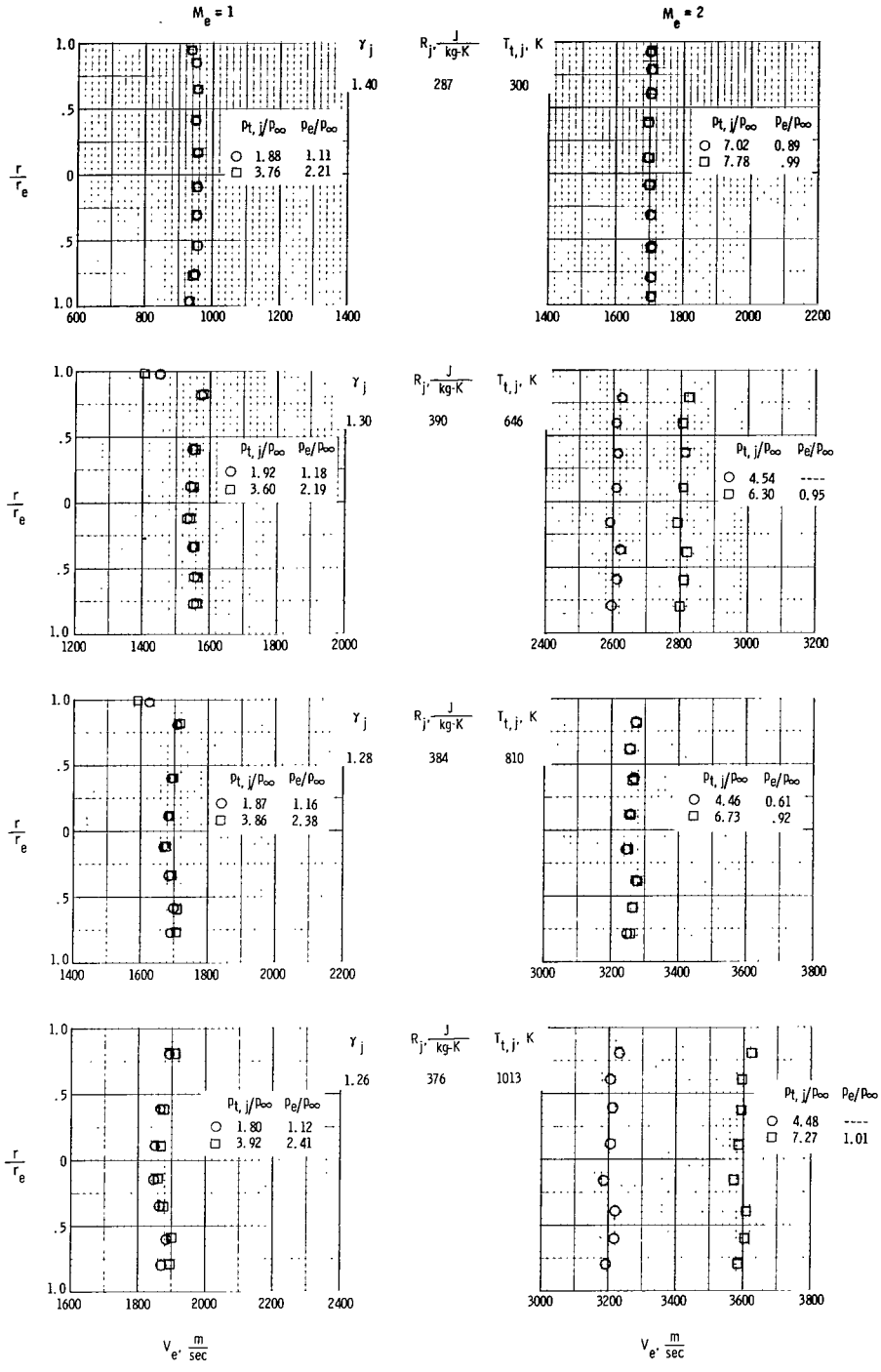

Figure 24.- Typical jet exit profiles for the sonic and supersonic internal contours. $M_\infty = 0$.

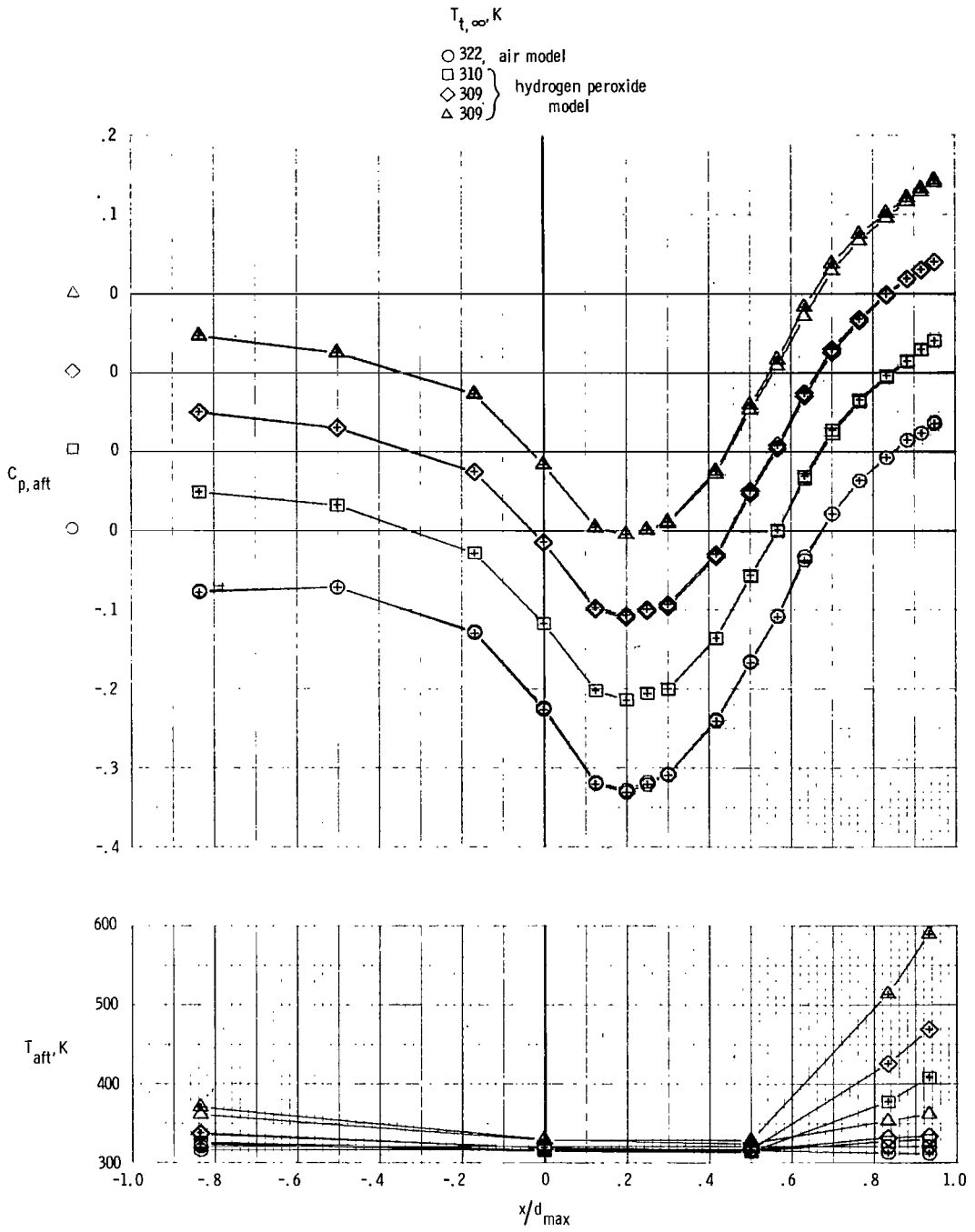

(a) Pressure coefficient and temperature distributions; $M_\infty = 0.60$.

Figure 25.- Jet-off pressure coefficient, temperature distributions, and boundary-layer profiles for the afterbody with $\beta = 20^o$ and $l/d_{max} = 1.0$. (Symbols with plus signs indicate data taken immediately after a jet pressure ratio sweep.)

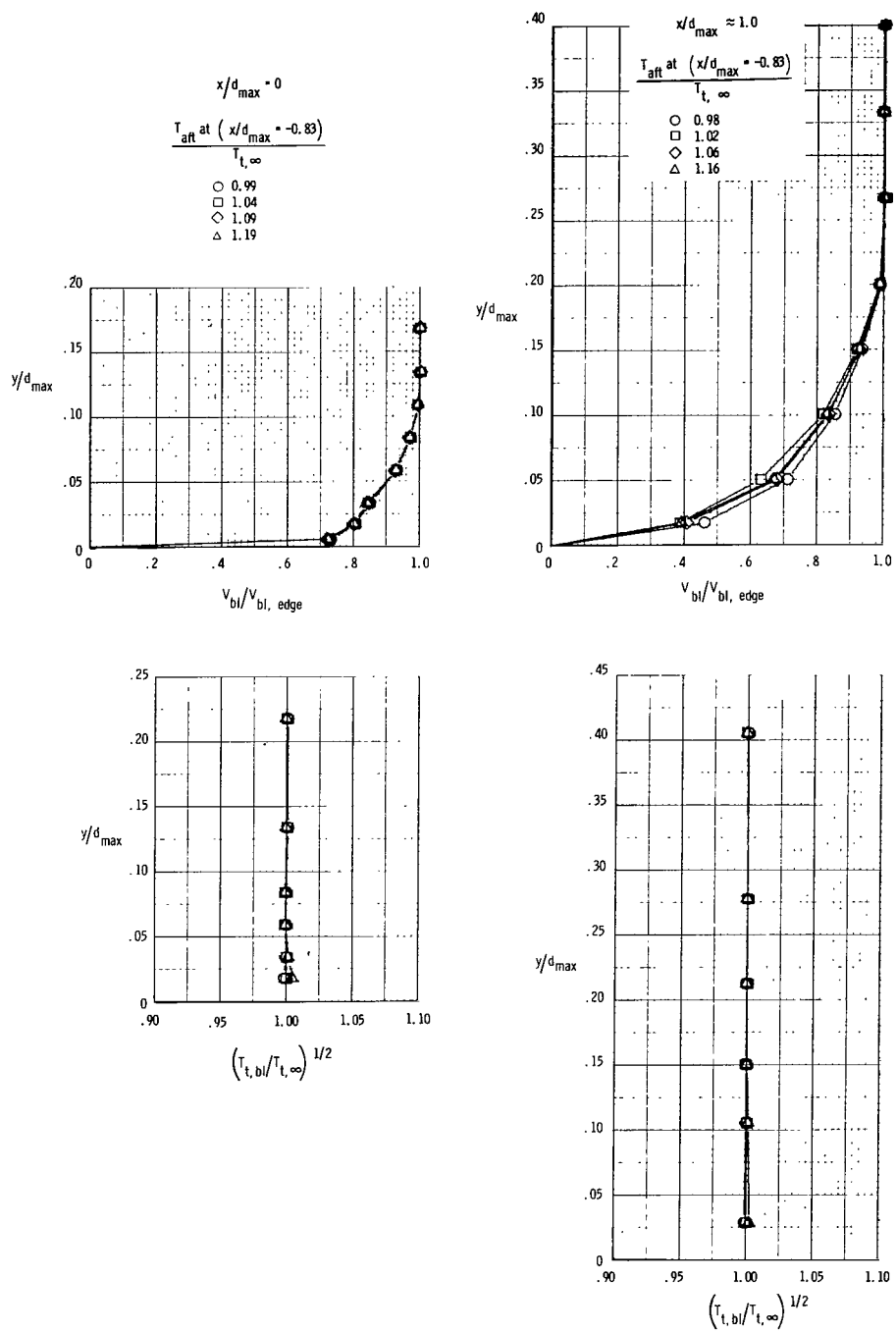

(b) Boundary-layer profiles; $M_\infty = 0.60$.

Figure 25.- Continued.

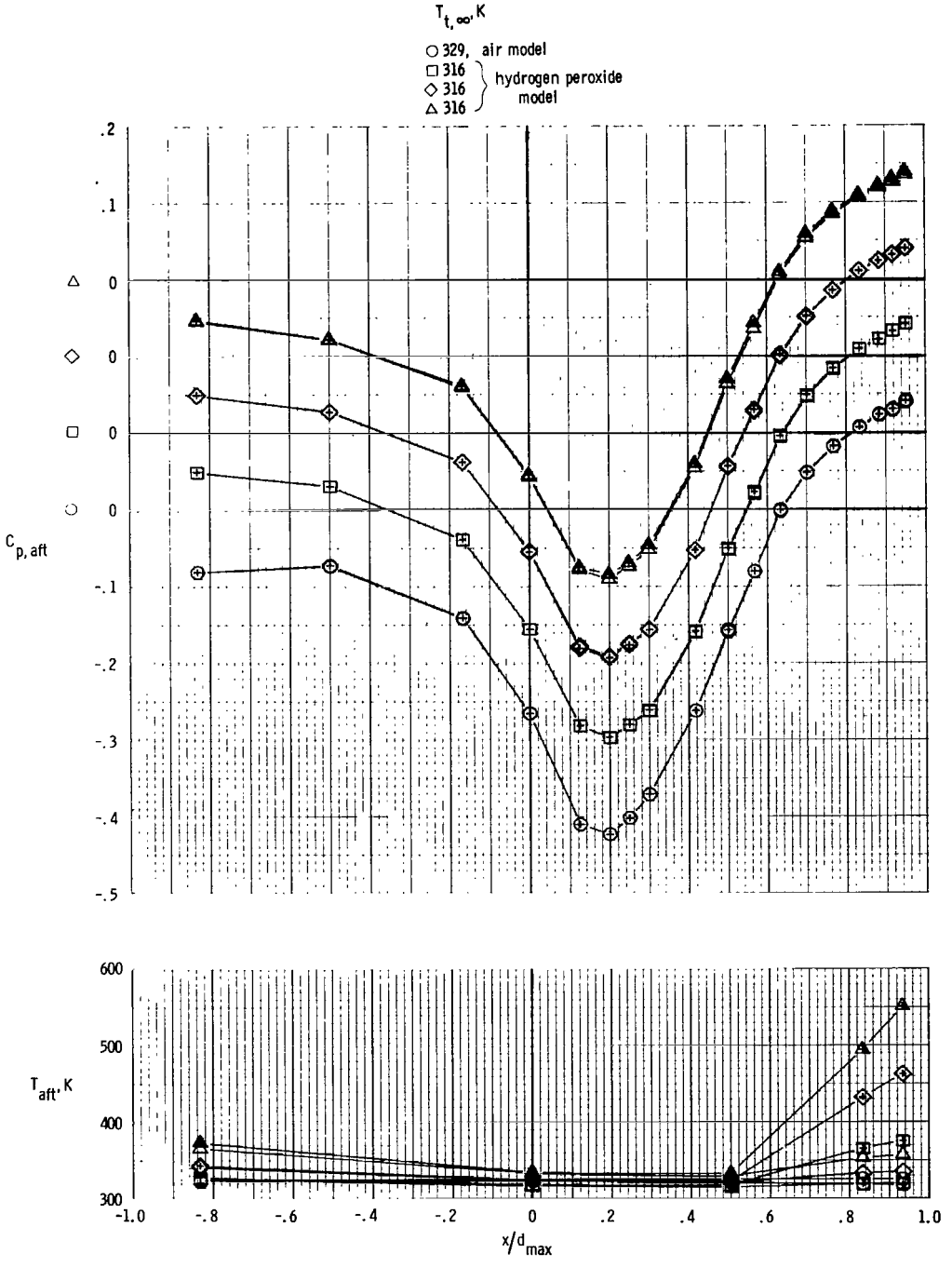

(c) Pressure coefficient and temperature distributions; $M_\infty = 0.80$.

Figure 25.- Continued.

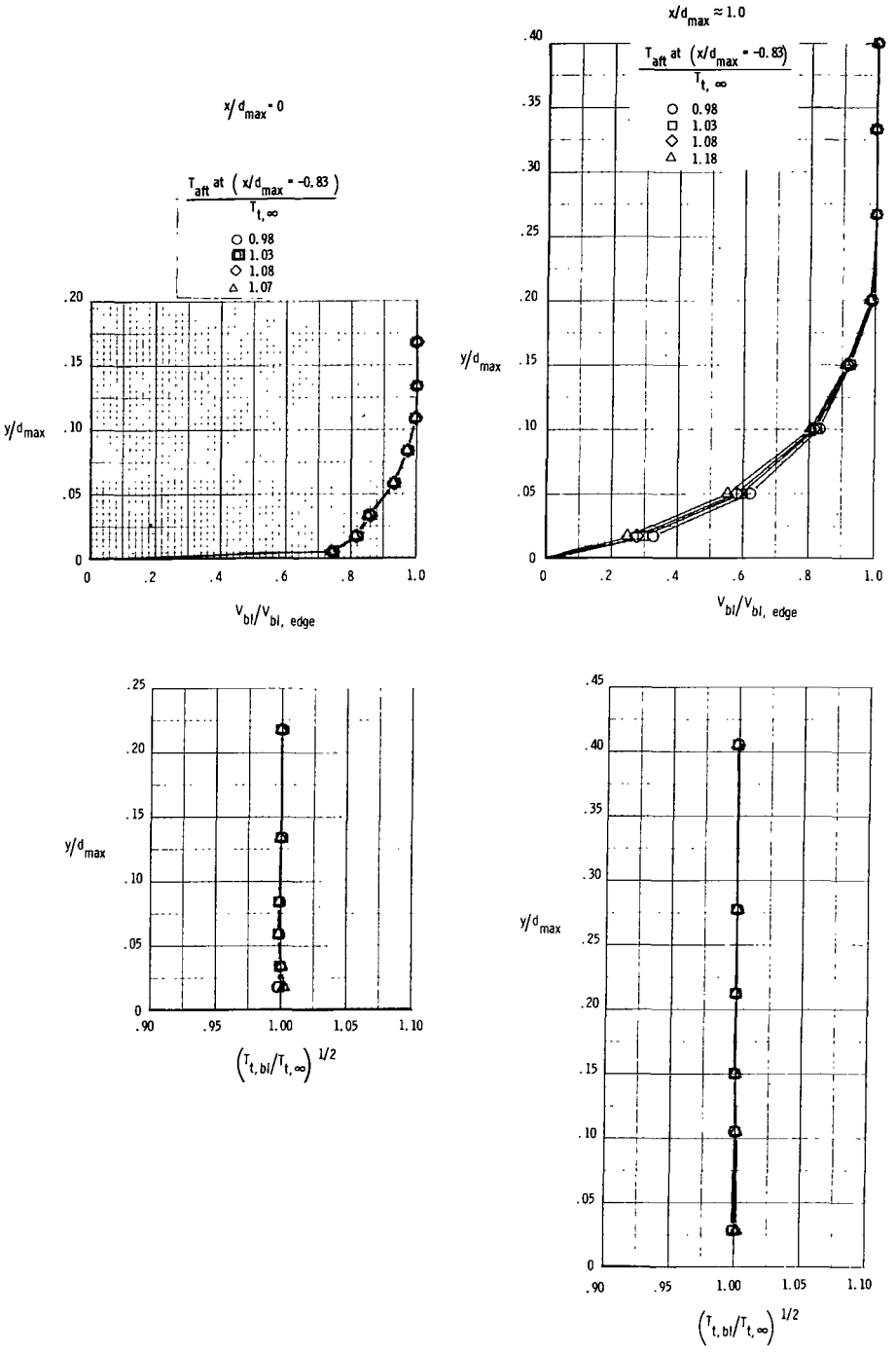

(d) Boundary-layer profiles; $M_\infty = 0.80$.

Figure 25.- Continued.

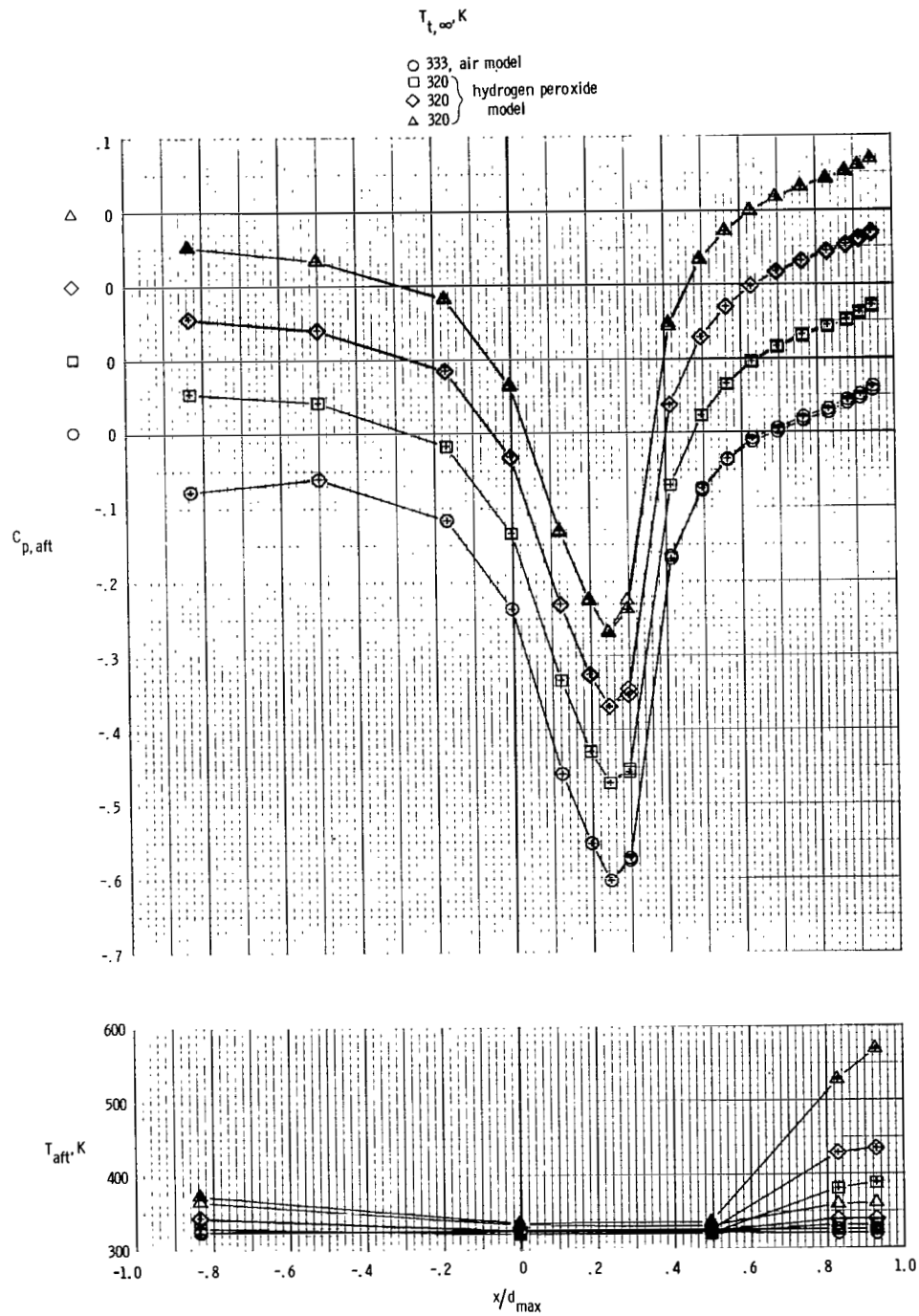

(e) Pressure coefficient and temperature distributions; $M_\infty = 0.90$.

Figure 25.- Continued.

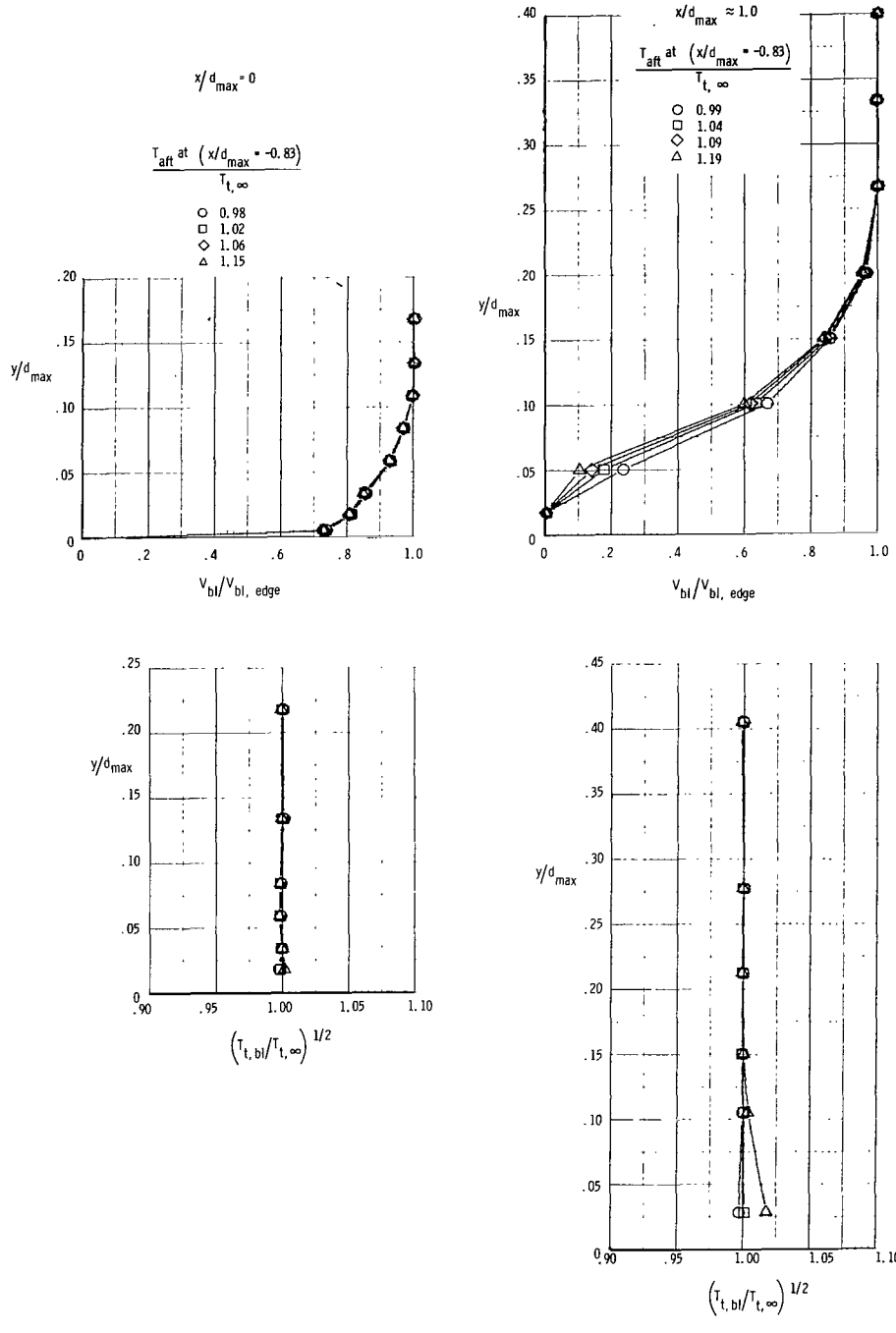

(f) Boundary-layer profiles; $M_\infty = 0.90$.

Figure 25.- Continued.

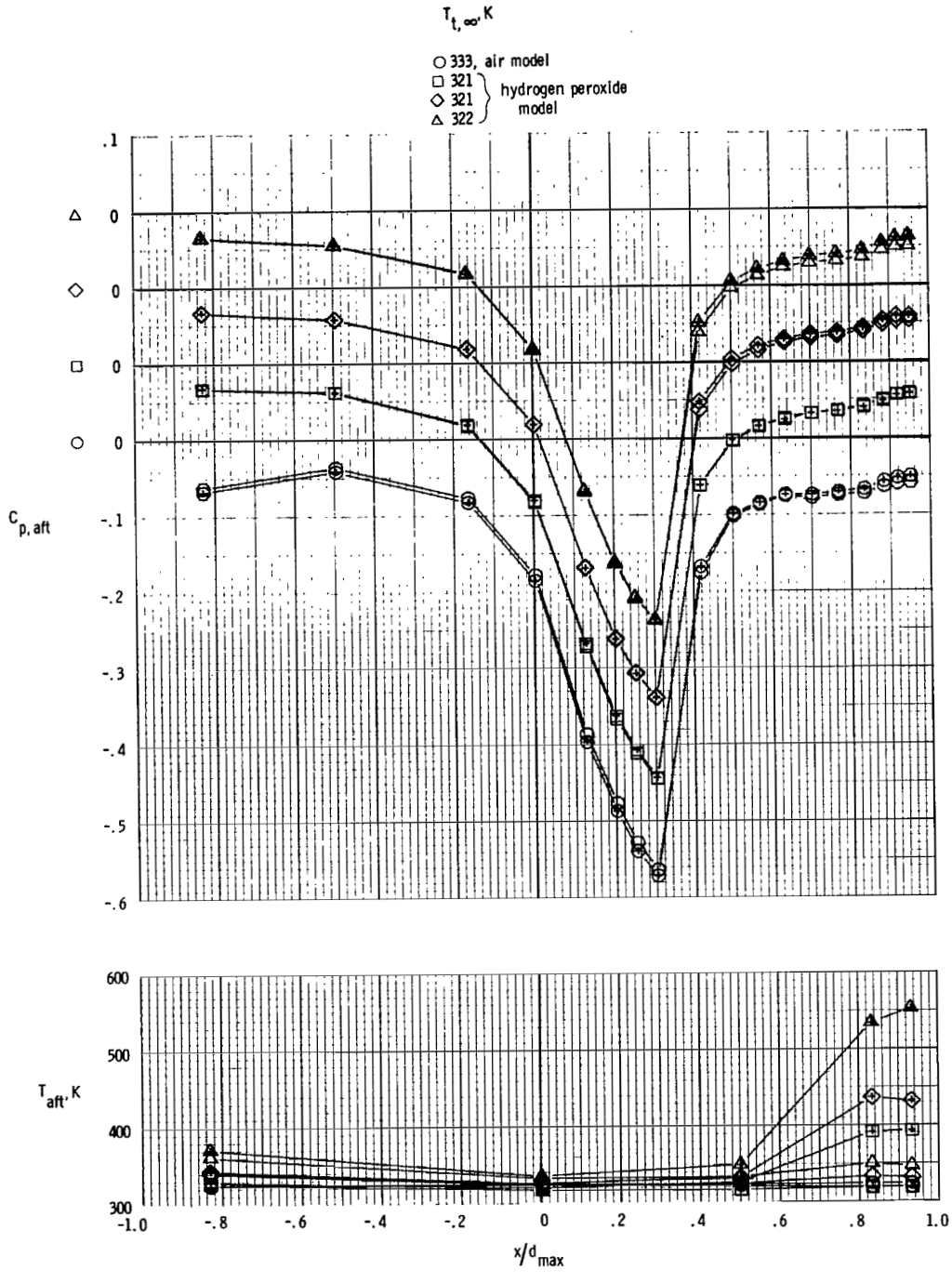

(g) Pressure coefficient and temperature distributions; $M_\infty = 0.95$.

Figure 25.- Continued.

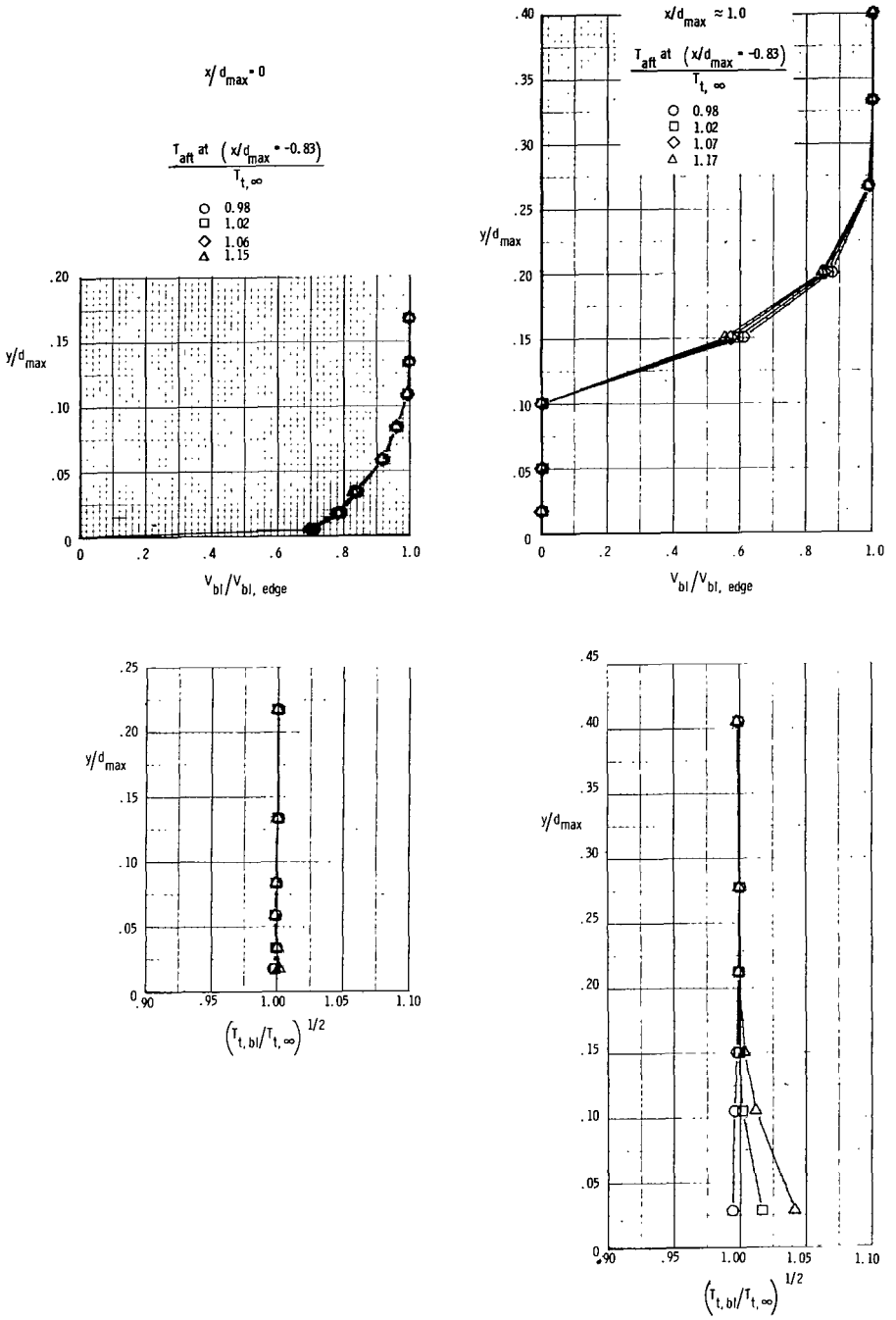

(h) Boundary-layer profiles; $M_\infty = 0.95$.

Figure 25.- Continued.

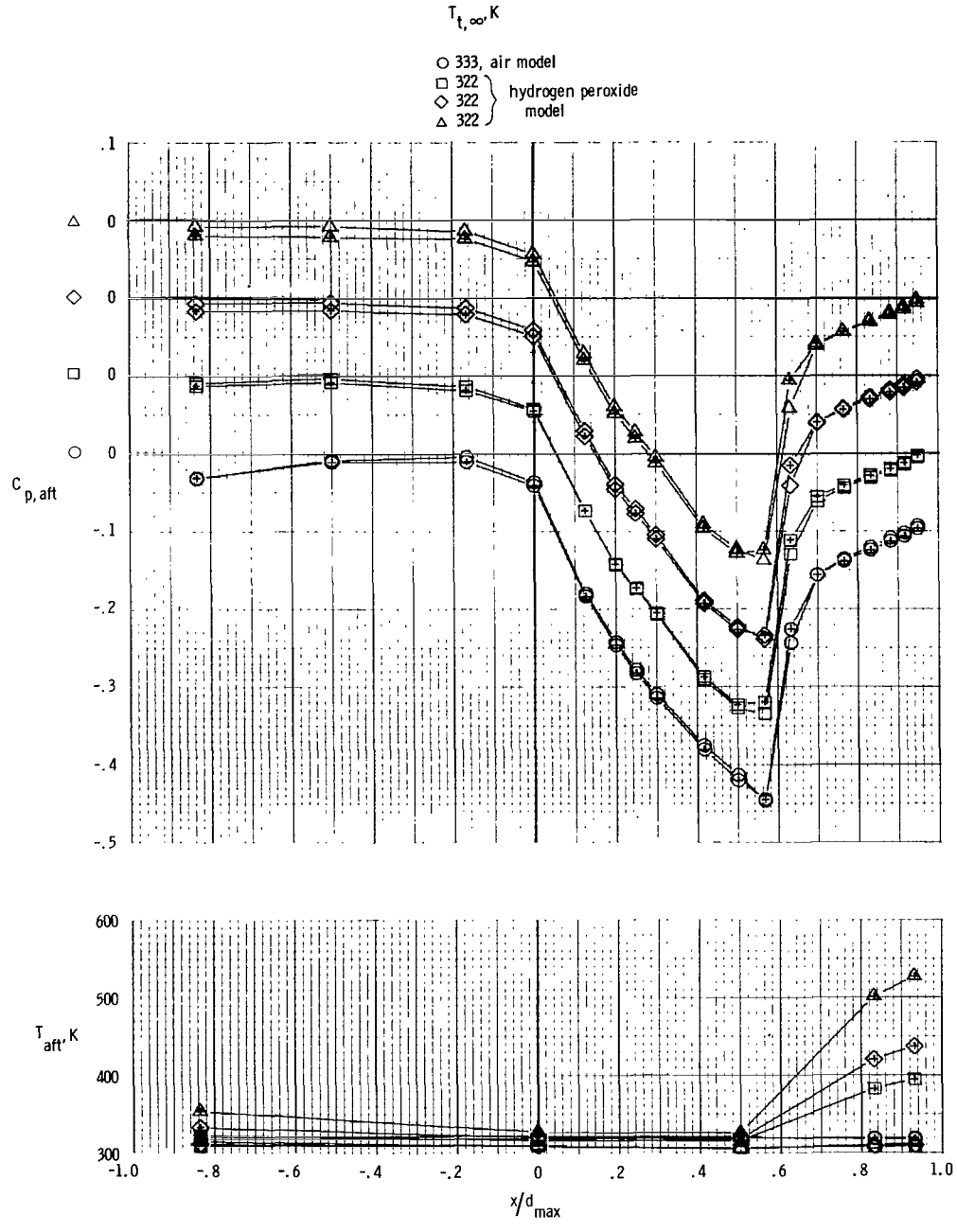

(i) Pressure coefficient and temperature distributions; $M_\infty = 1.20$.

Figure 25.- Continued.

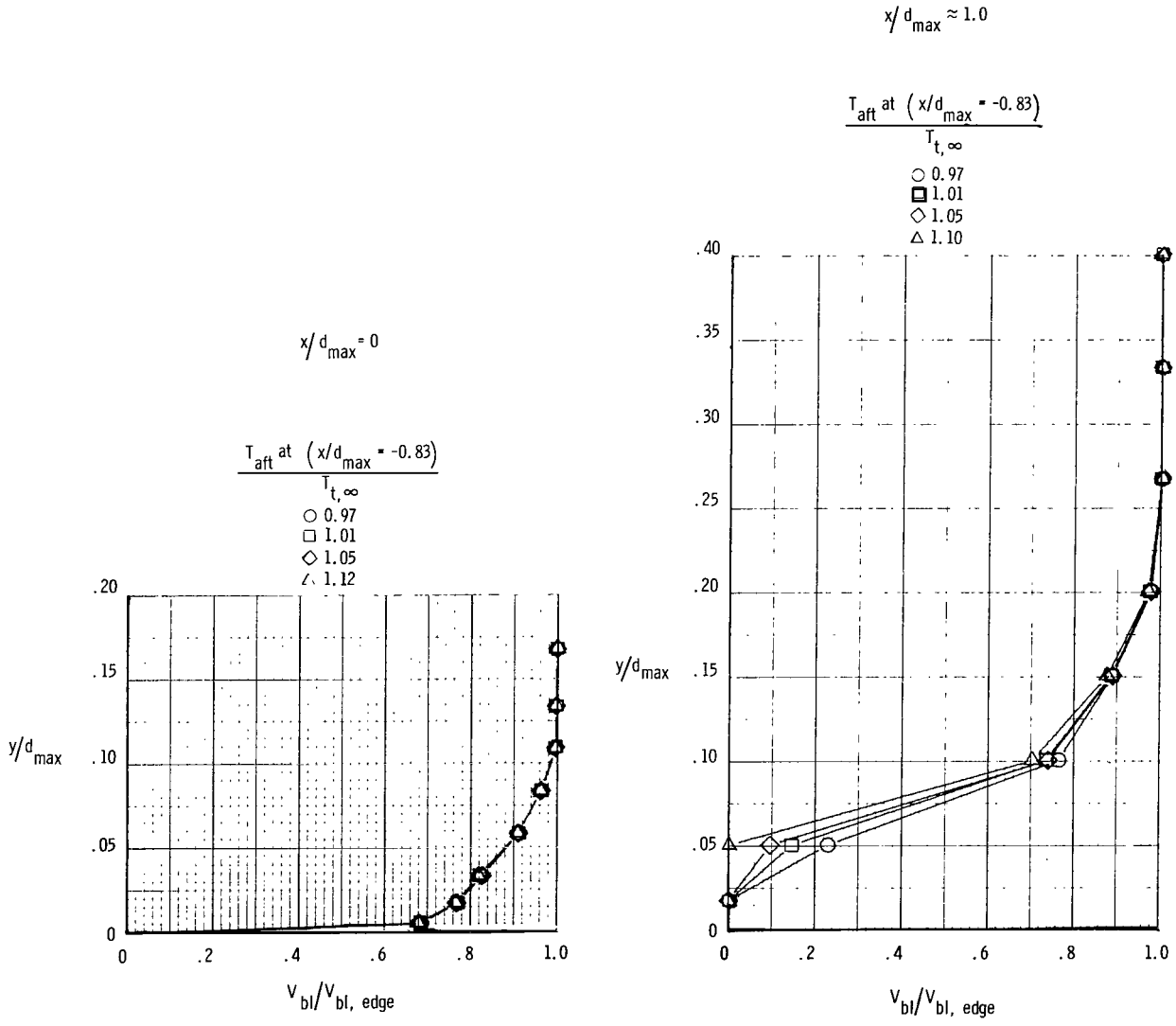

(j) Boundary-layer profiles; $M_\infty = 1.20$.

Figure 25.- Concluded.

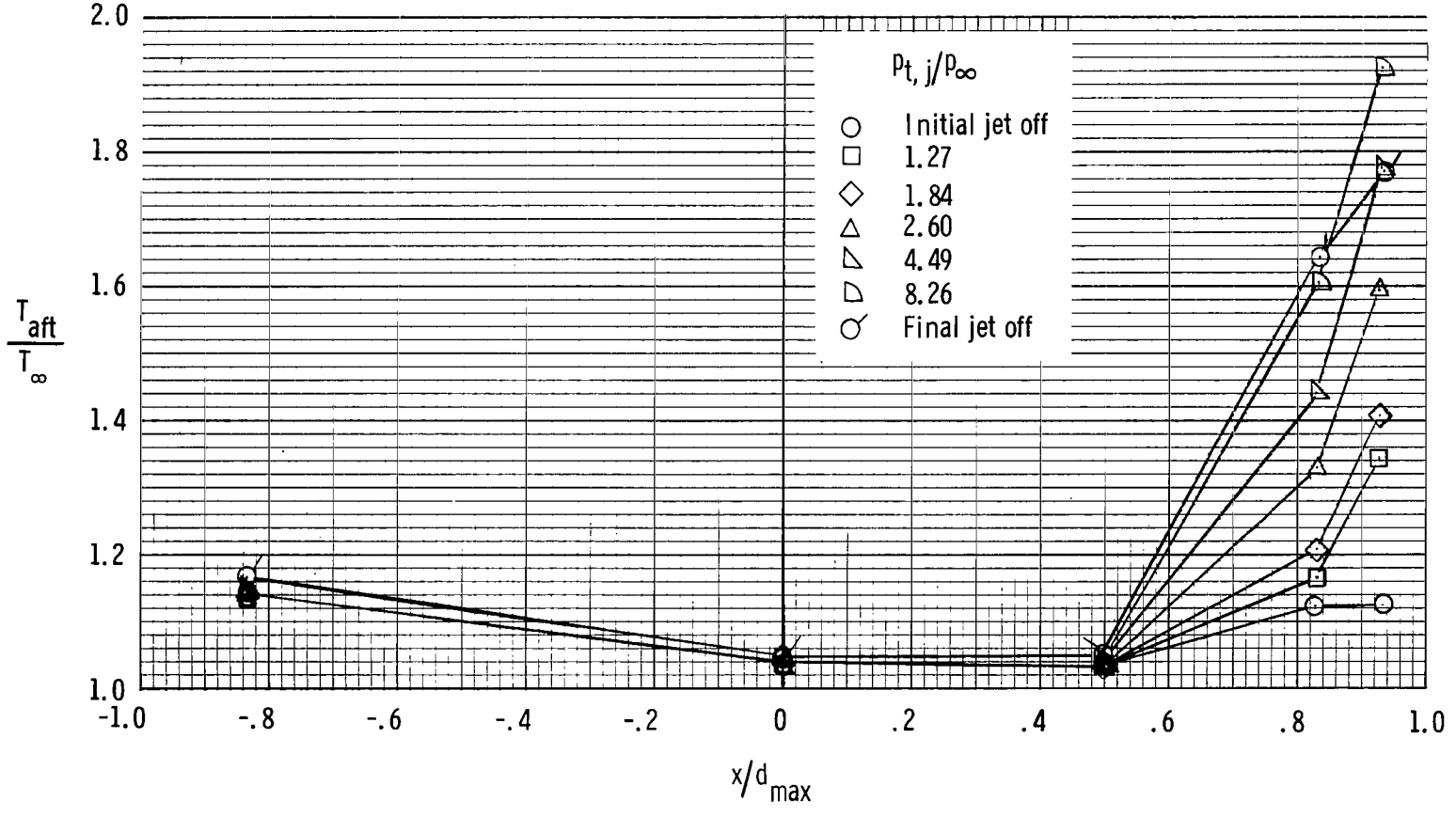

Figure 26.- Typical variation of afterbody skin temperature ratios during a jet pressure ratio sweep. $M_\infty = 0.90$; $T_{t,j} = 1013$ K.

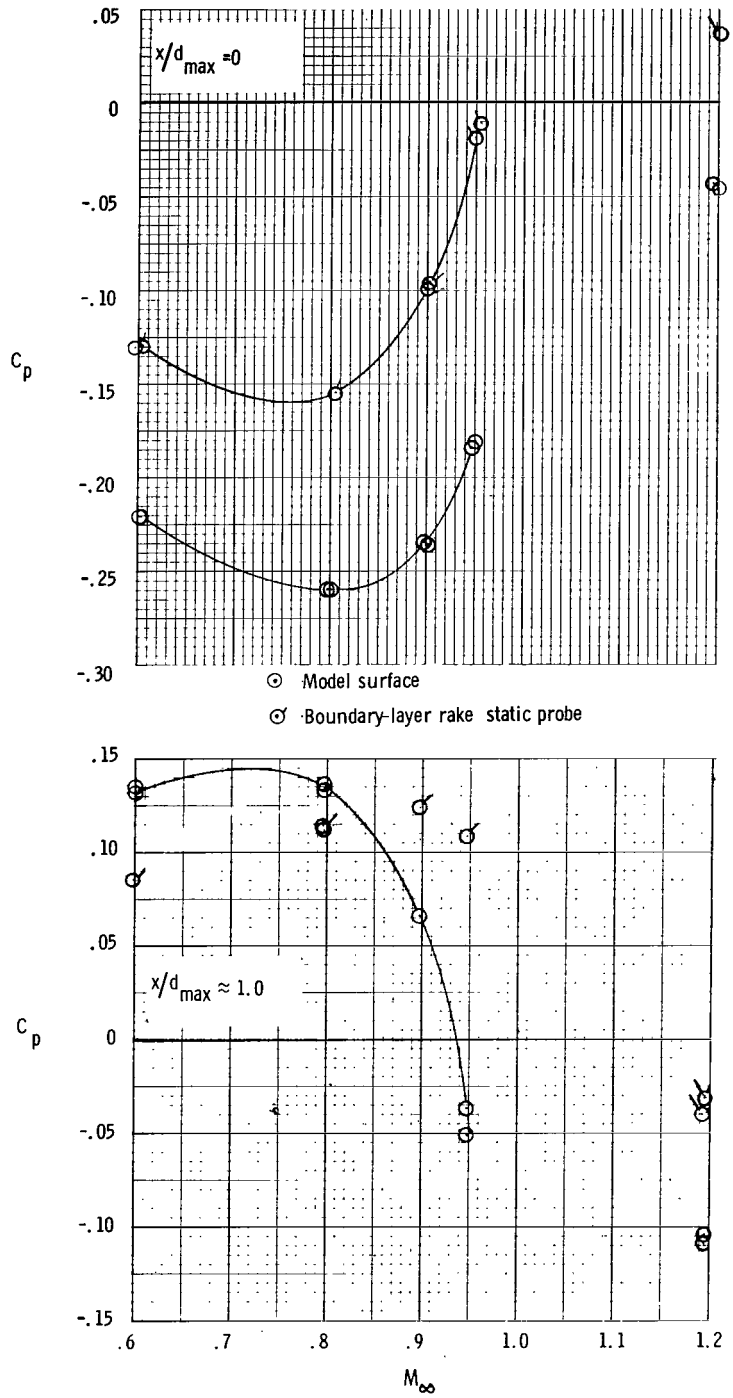

Figure 27.- Comparison of static pressure coefficients measured on model surface with boundary-layer rakes removed with those measured with boundary-layer rake static probes.

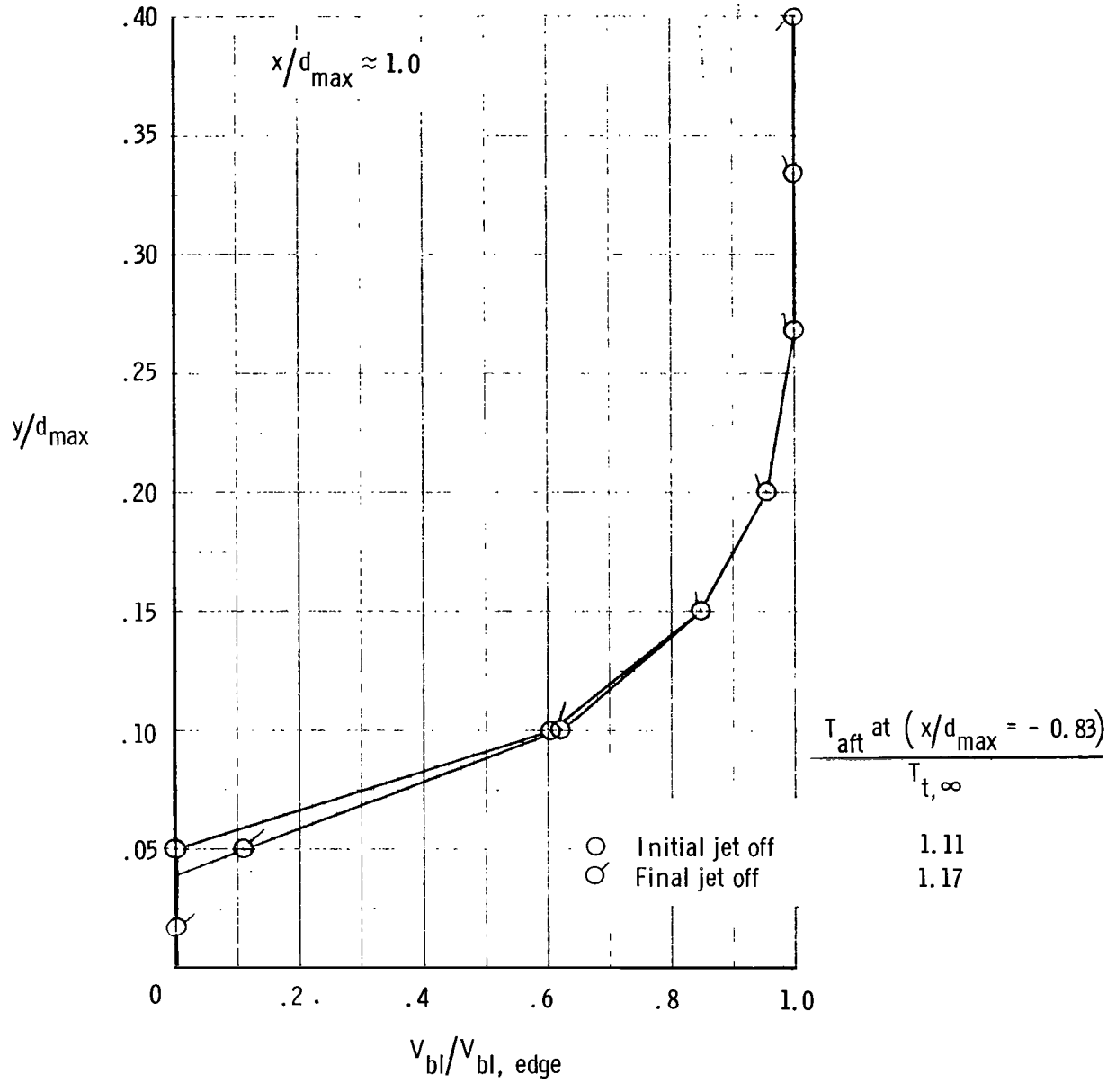

Figure 28.- Comparison of trailing-edge boundary-layer profiles immediately before and after a jet pressure ratio sweep. $M_\infty = 0.90$.

"The aeronautical and space activities of the United States shall be conducted so as to contribute . . . to the expansion of human knowledge of phenomena in the atmosphere and space. The Administration shall provide for the widest practicable and appropriate dissemination of information concerning its activities and the results thereof."

—NATIONAL AERONAUTICS AND SPACE ACT OF 1958

NASA SCIENTIFIC AND TECHNICAL PUBLICATIONS

TECHNICAL REPORTS: Scientific and technical information considered important, complete, and a lasting contribution to existing knowledge.

TECHNICAL NOTES: Information less broad in scope but nevertheless of importance as a contribution to existing knowledge.

TECHNICAL MEMORANDUMS: Information receiving limited distribution because of preliminary data, security classification, or other reasons. Also includes conference proceedings with either limited or unlimited distribution.

CONTRACTOR REPORTS: Scientific and technical information generated under a NASA contract or grant and considered an important contribution to existing knowledge.

TECHNICAL TRANSLATIONS: Information published in a foreign language considered to merit NASA distribution in English.

SPECIAL PUBLICATIONS: Information derived from or of value to NASA activities. Publications include final reports of major projects, monographs, data compilations, handbooks, sourcebooks, and special bibliographies.

TECHNOLOGY UTILIZATION PUBLICATIONS: Information on technology used by NASA that may be of particular interest in commercial and other non-aerospace applications. Publications include Tech Briefs, Technology Utilization Reports and Technology Surveys.

Details on the availability of these publications may be obtained from:

SCIENTIFIC AND TECHNICAL INFORMATION OFFICE

NATIONAL AERONAUTICS AND SPACE ADMINISTRATION

Washington, D.C. 20546